

# Engineering synthetic adhesins for biophysical investigation and rewiring of host-microbe interactions

Présentée le 1<sup>er</sup> avril 2022

Faculté des sciences de la vie  
Unité du Prof. Persat  
Programme doctoral en biotechnologie et génie biologique

pour l'obtention du grade de Docteur ès Sciences

par

**Xavier Jean-Yves PIERRAT**

Acceptée sur proposition du jury

Prof. P. D. Barth, président du jury  
Prof. A. L. A. Persat, directeur de thèse  
Prof. J.-W. Veening, rapporteur  
Prof. G. Duménil, rapporteur  
Prof. B. Correia, rapporteur



# ACKNOWLEDGMENTS

---

First, I want like to thank my thesis advisor, Alex Persat, for offering me to join his newly created lab. Along the years, he has given me an ideal amount of freedom and guidance, of trust and constructive feedback to conduct this challenging thesis. Also, he has created a positive atmosphere in the lab and patiently helped me develop critical thinking, writing and presenting skills.

I am naturally grateful to the members of my thesis jury for the dedication they have put in evaluating this report and my oral defense, and to my candidacy exam jury for early key suggestions.

I am grateful to Jeremy Wong and Zainebe Al-Mayyah, who directly contributed to some experiments reported here, to Marco Kühn and Lorenzo Talà, who commented this manuscript. Also, this thesis could not have been done without precious help from numerous other scientists who provided me with tips, technical help, cell lines, strains and genetic material, listed at the end of this manuscript.

I would also like to thank my other colleagues from the Persat lab for always finding ways to joke about anything around a coffee or a drink, and Janet Van der Graaf and Terry Vuignier (former MSc and BSc students, EPFL) for hardworking with me on projects not included in this thesis.

I thank my family for always warmly welcoming me back in Alsace, my future in-laws and my friends, those from kindergarten to the more recent ones, for helping me decompress from time to time.

Last but not least, I would like to thank my fiancée, Camille Chagnon, for supporting me on every single aspect during the entirety of this PhD.

## ABSTRACT

---

Host attachment is often a critical step in the onset of pathogenesis. To attach to host cells, bacteria have evolved a range of adhesins that bind to specific receptors. Some of these adhesins have been thoroughly characterized using biochemical techniques. However, how adhesins engage with their receptors in a realistic context of host colonization remains obscure. For instance, how target cell surface properties regulate attachment has been overlooked. This hinders our understanding of pathogenicity, thereby limiting our ability to develop new therapeutic approaches.

Here, we aimed at characterizing the biophysical rules underlying bacterial attachment to live cells. In this context, we displayed synthetic adhesins on both bacterial and mammalian target cell surfaces to study how the mammalian membrane microenvironment regulates attachment. By leveraging microfluidics and high-temporal resolution confocal microscopy, we tracked the early adhesion of bacteria to target cells and compared it to abiotic surfaces. We modeled the distribution of residence times and uncovered that the binding to mammalian cells is a two-step process, as opposed to one-step binding to an abiotic surface. In particular, we highlight the impact of the mammalian cell glycocalyx and of the actin-mediated cell remodeling. Altogether, our results demonstrate that adhesin-ligand binding is not the only regulator of bacterial adhesion, due to the host mechanical microenvironment playing a critical role on the initiation of infection.

With a better knowledge of *in vivo* adhesion, we repurposed the synthetic adhesin system as a tool for bacterial-based therapy. Our plan consists in using adhesion to rewire host-pathogen interactions. By analogy with pathogenic viruses transformed into therapeutic gene delivery vectors, we focused on pathogenic bacteria injecting DNA to eukaryotic cells. *Agrobacterium tumefaciens* is a pathogen that delivers DNA to plants using its type IV secretion. It is widely used for gene editing in plants, and sometimes in yeast and fungal cells. It is therefore an attractive candidate as a human gene delivery vector. However, some cell types such as plant monocots or animal cells show extremely low transformation efficiency. Studies demonstrated a positive correlation between adhesion to recalcitrant plants and transformation efficiency. Hence, would a synthetic binding of *A. tumefaciens* to non-natural target cells increase delivery?

To measure the impact of adhesion on delivery efficiency, we repurposed an endogenous autotransporter of *A. tumefaciens* to display the previously characterized synthetic adhesin. This significantly increased the binding to yeast and mammalian cells displaying the target surface receptor. In addition, we developed a split luciferase assay to quantify the transfer of

helper proteins to target mammalian cell. This allowed us to optimize *A. tumefaciens*-mediated delivery to mammalian cells and to refine hypotheses concerning the translocation mechanisms involved in mammalian cells. Altogether, we show that synthetic adhesins are a valuable tool to improve our understanding of host-microbe interactions and for repurposing pathogens into therapeutic tools.

Keywords: autotransporter, intimin, adhesin, synthetic, display, bacteria, mammalian, microenvironment, interaction, microfluidics, tracking, biophysical, membrane, glycocalyx, nanobody, VHH, GFP, Agrobacterium, tumefaciens, yeast, HeLa, rewiring, delivery, injection, transfer, T-DNA, VirE2, gene therapy

## RÉSUMÉ

---

L'attachement à l'hôte est souvent une étape clé pour initier la pathogénèse. Les bactéries ont développé un éventail d'adhésines (protéines adhésives) pour s'attacher à des récepteurs spécifiques. Certaines de ces adhésines ont été caractérisées en détail grâce à des techniques biochimiques. Toutefois, la manière dont les adhésines se lient avec leur récepteur dans un contexte de colonisation de l'hôte reste obscure. Par exemple, la manière dont les propriétés de la surface de la cellule cible régulent l'adhérence a été ignorée. Cela entrave notre compréhension de la pathogénicité, et limite notre capacité à développer de nouvelles approches thérapeutiques.

Ici, nous avons voulu caractériser les lois biophysiques sous-jacentes à l'attachement des bactéries à des cellules vivantes. Dans ce contexte, nous présentons des adhésines synthétiques à la surface des bactéries et des cellules mammaliennes ciblées, pour étudier comment le microenvironnement de la membrane mammalienne régule l'attachement. En mobilisant microfluidique et microscopie confocale à haute résolution temporelle, nous avons suivi l'adhérence de bactéries aux cellules cibles et comparé celle-ci à l'adhérence à des surfaces abiotiques. Nous avons modélisé la distribution des temps de résidence et découvert que l'adhérence aux cellules mammaliennes est un processus en deux temps, comparé à l'adhérence en un temps sur les surfaces abiotiques. En particulier, nous mettons en évidence l'impact du glyco-calice mammalien et du remodelage de la cellule par l'actine. En somme, nos résultats démontrent que l'adhérence adhésine-ligand n'est pas l'unique régulateur de l'adhérence bactérienne, car le microenvironnement mécanique de l'hôte joue un rôle clé dans l'initiation de l'infection.

Grâce à une meilleure compréhension de l'adhérence *in vivo*, nous avons réaffecté le système d'adhérence synthétique en outil pour thérapie à base de bactéries. Notre plan consiste à rediriger des interactions microbe-hôte. Par analogie avec les virus pathogéniques transformés en vecteurs d'ADN pour la thérapie génique, nous nous sommes concentrés sur les bactéries pathogènes qui injectent de l'ADN dans des cellules eucaryotiques. *Agrobacterium tumefaciens* est un pathogène qui transfère de l'ADN dans des plantes blessées grâce au système de sécrétion de type IV. Il est communément utilisé pour l'édition génétique dans les plantes, et parfois dans les cellules fongiques et de levure. C'est donc un candidat intéressant en tant que vecteur de transfert de gènes aux humains. Toutefois, dans certains types cellulaires tels que les monocotylédones ou les cellules animales, l'efficacité du transfert d'ADN est très limitée. Des études ont montré une corrélation positive entre l'adhérence aux cellules récalcitrantes et l'efficacité du transfert d'ADN. Une adhérence

synthétique augmenterait-elle le transfert d'ADN d'*A. tumefaciens* à des cellules cibles non naturelles ?

Pour mesurer l'influence de l'adhésion sur l'efficacité de transfert, nous avons recyclé un autotransporteur endogène d'*A. tumefaciens* pour présenter l'adhésine synthétique que nous avons précédemment caractérisée. Ceci a considérablement augmenté l'adhérence à des cellules de levures et mammaliennes lorsque ces dernières présentent le récepteur-cible à leur surface. De plus, nous avons développé un système pour mesurer la quantité de protéines co-transférées lors de l'injection. Ceci nous a permis d'optimiser le transfert médié par *A. tumefaciens* et de raffiner les hypothèses concernant les mécanismes de transfert dans les cellules mammaliennes. En somme, nous démontrons que les adhésines synthétiques sont un outil de valeur pour améliorer notre compréhension des interactions hôte-microbe et pour recycler des pathogènes en outils thérapeutiques.

Mots-clés : autotransporteur, synthétique, présentation, adhésine, adhérence, bactérie, cellule mammalienne, interaction, microfluidique, traçage, biophysique, membrane, glyco-calice, anticorps camélidé, protéine fluorescente verte, intimin, *Agrobacterium tumefaciens*, levure, recyclage, transfert d'ADN, injection, HeLa, VirE2, thérapie génique

# CONTENTS

---

<b>Acknowledgments.....</b>	<b>3</b>
<b>Abstract .....</b>	<b>4</b>
<b>Résumé .....</b>	<b>6</b>
<b>Contents.....</b>	<b>8</b>
<b>List of Figures .....</b>	<b>11</b>
<b>List of tables .....</b>	<b>13</b>
<b>Glossary of frequently used terms and acronyms.....</b>	<b>14</b>
<b>1 Introduction .....</b>	<b>15</b>
1.1 Bacterial colonization .....	15
1.1.1 Adhesion to abiotic vs. biotic surfaces.....	15
1.1.2 Adhesion in fluid flow.....	15
1.1.3 Long-range appendages .....	16
1.1.4 Short-range appendages: focus on autotransporters.....	17
1.1.5 Bacterial lectins .....	21
1.2 Repurposing pathogens into therapeutic bacteria.....	21
1.2.1 Upgrading bacteria using synthetic biology .....	21
1.2.2 Repurposing bacterial injection machineries .....	22
1.3 Gene delivery .....	23
1.3.1 Gene therapies.....	23
1.3.2 Viral gene delivery vectors .....	23
1.3.3 Physico-chemical gene delivery .....	24
1.4 <i>Agrobacterium tumefaciens</i> .....	24
1.4.1 <i>A. tumefaciens</i> in the wild.....	24
1.4.2 <i>A. tumefaciens</i> is the gold standard organism for plant engineering.....	25
1.4.3 <i>A. tumefaciens</i> adhesins .....	26
1.4.4 <i>A. tumefaciens</i> ' type IV secretion system .....	26
1.5 Split protein reporters developed for bacterial injection .....	29
1.5.1 Split fluorescent proteins .....	29
1.5.2 Split luciferase.....	29
1.6 Synthetic bacterial adhesins: nanobodies (VHH).....	29
1.6.1 Structure .....	29
1.6.2 Engineering and applications .....	30
1.6.3 Nanobody display.....	31
1.7 Overall aims and organization of the thesis .....	31
1.7.1 Aim 1: Identify physical principles ruling bacterial early adhesion to tissues ....	31
1.7.2 Aim 2: Rewire <i>A. tumefaciens</i> to yeast and human cells .....	32
<b>2 The mammalian membrane microenvironment regulates the sequential attachment of bacteria to host cells. ....</b>	<b>33</b>
2.1 Abstract.....	34
2.2 Introduction .....	35
2.3 Synthetic adhesion to characterize bacterial attachment to host cells. ....	37

2.4	Bacteria attach to host cells in two successive steps.....	40
2.5	Bacteria attach to abiotic surfaces in a single specific step.....	43
2.6	Host cell membrane mechanics regulate bacterial adhesion .....	45
2.7	The glycocalyx shields the host from receptor-specific bacterial adhesion .....	48
2.8	Flagella and flow counteract the glycocalyx shield .....	51
2.9	Discussion.....	53
2.9.1	Context .....	53
2.9.2	Two steps adhesion to mammalian cells .....	54
2.9.3	The mammalian surface has a significant impact on bacterial adhesion.....	55
2.9.4	Impacts of fluid flow on bacterial adhesion to cells .....	55
2.9.5	Pathogens can target the mammalian glycocalyx.....	56
2.9.6	Timely adhesin deployment.....	56
2.9.7	Conclusion .....	56
2.10	Material and methods 1 .....	57
<b>3</b>	<b>Development of an adhesin display system at the surface of <i>A. tumefaciens</i> .....</b>	<b>64</b>
3.1	Abstract.....	64
3.2	Introduction .....	64
3.2.1	Synthetic multicellular assemblies .....	64
3.2.2	<i>Agrobacterium tumefaciens</i> .....	65
3.2.3	Motivation / aim .....	65
3.2.4	Overview .....	66
3.3	Identification of a potential synthetic adhesin scaffold in <i>A. tumefaciens</i> .....	67
3.4	Induction systems for <i>A. tumefaciens</i> engineering.....	70
3.5	Monitoring display using a tag fusion.....	73
3.6	FimH display in <i>A. tumefaciens</i> .....	76
3.7	Enzymatic display in <i>A. tumefaciens</i> .....	79
3.8	Nanobody display in <i>A. tumefaciens</i> .....	81
3.9	Other adhesins: display of RGD peptide at the surface of <i>A. tumefaciens</i> .....	84
3.10	Discussion.....	86
3.10.1	Summary.....	86
3.10.2	Limitations.....	86
3.10.3	Conclusion .....	87
3.11	Material and methods 2.....	88
<b>4</b>	<b><i>A. tumefaciens</i> targeted adhesion and delivery using synthetic adhesins.....</b>	<b>92</b>
4.1	Abstract.....	92
4.2	Introduction .....	93
4.2.1	<i>A. tumefaciens</i> T-DNA transfer.....	93
4.2.2	Motivation.....	93
4.3	Synthetic binding to yeast.....	95
4.4	Synthetic binding to mammalian cells.....	98

4.5	<i>A. tumefaciens</i> -mediated T-DNA transfer in mammalian cells .....	101
4.5.1	ssDNA can be processed and transcribed by mammalian cells.....	101
4.5.2	<i>A. tumefaciens</i> T-DNA transfer in HEK and HeLa cells .....	104
4.6	Repair template for CRISPR/Cas9 cuts.....	107
4.7	Helper protein localization in mammalian cells .....	109
4.8	Helper protein transfer monitoring .....	110
4.8.1	Split mCherry .....	110
4.8.2	Split NanoLuc.....	114
4.9	Synthetic binding of <i>A. tumefaciens</i> to <i>Chlamydomonas reinhardtii</i> .....	118
4.10	Discussion.....	122
4.10.1	Summary.....	122
4.10.2	Yeast gene transfer limitations and outlook .....	122
4.10.3	Transfer to mammalian cells: limitations and outlook .....	123
4.10.4	Conclusion .....	124
4.11	Material and methods 3.....	125
<b>5</b>	<b>Conclusion and perspectives.....</b>	<b>132</b>
5.1	The mammalian membrane microenvironment regulates the sequential attachment of bacteria to host cells .....	132
5.1.1	Results summary .....	132
5.1.2	Future directions .....	132
5.2	Development of an adhesin display system at the surface of <i>A. tumefaciens</i> .....	133
5.2.1	Results summary .....	133
5.2.2	Future directions .....	134
5.3	<i>A. tumefaciens</i> protein and T-DNA transfer to yeast and mammalian cells.....	136
5.3.1	Results overview .....	136
5.3.2	Summary of future directions.....	136
5.3.3	Safety.....	137
5.4	General conclusion .....	138
<b>6</b>	<b>Appendix 1: <i>Pseudomonas aeruginosa</i> EstA-based VHH display.....</b>	<b>139</b>
6.1	Engineering approach .....	139
6.2	Optimization .....	140
6.3	Application .....	142
<b>7</b>	<b>Appendix 2: Attempted characterization of wild-type Atu5364 and prevention of oxidation .....</b>	<b>143</b>
7.1	Investigating disulfide bond's removal in WT Atu5364.....	143
7.2	Does WT Atu5364 mediate binding to roots? .....	145
7.3	Prevention of periplasmic oxidation by knockout of the <i>dsbA</i> homolog in <i>A. tumefaciens</i> .....	147
	<b>Additional acknowledgements .....</b>	<b>150</b>
	<b>Supplementary information .....</b>	<b>151</b>
	<b>References.....</b>	<b>169</b>
	<b>Curriculum vitae.....</b>	<b>191</b>

## LIST OF FIGURES

Figure 1: Overview of the extracellular appendages of Gram-negative bacteria.....	16
Figure 2: Schematic of the main T5SS autotransporter topologies.....	18
Figure 3: A working model for hairpin-mediated passenger display.....	19
Figure 4: Two autotransporters used in this study.....	20
Figure 5: <i>A. tumefaciens</i> DNA transfer in the wild.....	25
Figure 6: Overview of <i>A. tumefaciens</i> ' T4SS and T-DNA's mode of entry into the target cell.....	27
Figure 7: Comparison of conventional IgG with camelid heavy-chain antibody. ....	30
Figure 8: Synthetic VHH adhesins and GFP receptor constructs.....	37
Figure 9: A synthetic adhesin-receptor system reveals a two-step mechanism of bacterial attachment to host cells.....	39
Figure 10: Functional validation and bacterial attachment as a function of VHH affinity to GFP. ....	42
Figure 11: Specificity of adhesion of <i>E. coli</i> -VHH to GFP-coated glass coverslips.....	43
Figure 12: Attachment of bacteria to abiotic surface is a single step process.....	44
Figure 13: Regulation of bacterial adhesion by host cytoskeleton. ....	46
Figure 14: HeLa cells actively remodel plasma membrane around bacteria.....	47
Figure 15: The membrane glycocalyx inhibits bacterial attachment. ....	49
Figure 16: Deglycosylation activity in mammalian cell culture medium. ....	50
Figure 17: Longer VHH linker does not improve binding in flow. ....	51
Figure 18: Flagella and flow attenuate the glycocalyx shield. ....	52
Figure 19: A model for mechanically-regulated, two-step bacterial attachment to host cells.....	54
Figure 20: Concept of a synthetic adhesin display to bind to surface features of target cells.....	66
Figure 21: <i>in silico</i> analysis of the two putative autotransporters in <i>A. tumefaciens</i> . ..	67
Figure 22: Atu5364 is not induced in different lab conditions. ....	70
Figure 23: The pVirE promoter requires low pH and acetosyringone. ....	71
Figure 24: The synthetic cumic acid-inducible promoter offers tight control of gene expression.....	72
Figure 25: 6xHis-tag prevents but HA tag enables PAO1 LecA and LecB display. ....	74
Figure 26: LecA and LecB display does not enable <i>A. tumefaciens</i> to bind to plates coated with their respective sugar.....	75

Figure 27: FimH's disulfide bond removal increases display efficiency and bacterial viability.....	76
Figure 28: FimH's disulfide bond removal impairs binding to mannose-coated surfaces. ....	78
Figure 29: <i>B. subtilis</i> LipA cannot be displayed using Atu5364. ....	80
Figure 30: VHH's disulfide bond removal improves display and viability and maintains affinity to GFP.....	82
Figure 31: pVirE is a potent inducible promoter for VHH display, both on binary vector and Tumor-inducing megaplasmid. ....	83
Figure 32: Successful inducible RGD display at the surface of <i>A. tumefaciens</i> .....	85
Figure 33: Synthetic adhesion to rewire the T4SS of <i>A. tumefaciens</i> to new target cells. ....	94
Figure 34: Synthetic adhesion of <i>A. tumefaciens</i> VHH display to GFP-displaying yeast cells.....	96
Figure 35: Synthetic binding does not increase stable T-DNA integration. ....	98
Figure 36: Synthetic adhesins increase binding of <i>A. tumefaciens</i> to HeLa cells.....	99
Figure 37: Synthetic adhesion of <i>A. tumefaciens</i> to HEK cells.....	100
Figure 38: ssDNA-transfected cells produce a GFP reporter.....	102
Figure 39: Hairpins favoring self-priming of ssDNA in cells slightly increase signal .	103
Figure 40: Monitoring <i>A. tumefaciens</i> -mediated DNA transfer using a fluorescent reporter shows limited impact of VHH.....	104
Figure 41: ssDNA FISH concept.....	105
Figure 42: ssDNA FISH gives low signal and does not allow precise T-DNA localization nor distinction from noise. ....	107
Figure 43: Agrobacterial T-DNA is not used as ssDNA repair template for CRISPR-Cas9-induced cuts. ....	108
Figure 44: VirE2 and VirD2 properly localize mammalian cell compartments. ....	110
Figure 45: Identification of the fusion-permissive site in VirE2(pTiC58). ....	111
Figure 46: Split sfCherry concept and control of the target cell line.....	112
Figure 47: Split sfCherry does not give a clear VirE2 transfer readout. ....	113
Figure 48: Monitoring and optimizing VirE2 transfer using the split luciferase system. ....	115
Figure 49: VHH display causes some GFP-binding-independent VirE2 transfer.....	116
Figure 50: VirE2 transfer is cell-cell contact dependent but mostly T4SS-independent. ....	117
Figure 51: Mammalian cells uptake VirE2 from bacterial lysate. ....	118

Figure 52: <i>A. tumefaciens</i> VHH binds to recombinant mVenus and to some extent to mVenus-displaying <i>C. reinhardtii</i> under agarose pad. ....	120
Figure 53: VHH(F98) is in close proximity with GFP(A206). ....	121
Figure 54: The predicted structures of Atu5354 and Atu5364 scaffolds are highly similar. ....	134
Figure 55: Crystal structure of <i>E. coli</i> Hemoglobin Protease .....	135
Figure 56: Design of the VHH display in PAO1. ....	140
Figure 57: Titration of the VHH display in PAO1 in different media.....	141
Figure 58: Atu5364's disulfide bond removal promotes even surface distribution of the passenger domain.....	144
Figure 59: <i>A. tumefaciens</i> binding to <i>Arabidopsis thaliana</i> roots is independent of Atu5364. ....	145
Figure 60: <i>atu0800</i> knockout impairs bacterial shape and viability but enables Atu5364 display.....	148
Figure 61: <i>atu0800</i> knockout does not improve VHH display. ....	149

## LIST OF TABLES

---

Table 1: Overview of the top templates used by SwissModel and I-Tasser homology-model modeling software with Atu5364(35-501) as input.....	68
Supplementary table 2: plasmids used in this study.....	151
Supplementary table 3: strains used in this study .....	165
Supplementary table 4: Raw data of the mathematical models for characteristic residence times. ....	167

## GLOSSARY OF FREQUENTLY USED TERMS AND ACRONYMS

---

**AAV:** adeno-associated virus

**Adhesin:** adhesion protein

**ANOVA:** Analysis of variance to analyze the differences among means.

**BamA:** beta-barrel associated machinery that help beta-barrel insertion into the outer membrane, including autotransporters

**CRISPR/Cas9:** clustered regularly interspaced short palindromic repeats / Cas9, system enabling targeted double-strand DNA breaks

**Cys-free:** cysteine free

**dsDNA:** double-stranded DNA

**EstA:** esterase A autotransporter from *Pseudomonas* spp.

**gRNA:** guide RNA, for CRISPR/Cas9 targeting

**HA tag:** hemagglutinin tag of sequence YPYDVPDYA

**HiBit:** 11 amino acid-long peptide complementing LgBit for split NanoLuc luciferase assay

**K<sub>D</sub>:** dissociation constant

**LgBit:** large part of the split NanoLuc luciferase assay

**MOI:** multiplicity of infection

**NanoLuc:** *Oplophorus gracilirostris* engineered luciferase

**NLS:** nuclear localization signal

**PI:** propidium iodide staining dead cells

**pTiC58:** tumor-inducing plasmid of *A. tumefaciens* strain C58

**ssDNA:** single-stranded DNA

**T-DNA:** *A. tumefaciens* transfer-DNA

**T3SS:** type III secretion system, which translocates proteins

**T4SS:** type IV secretion system, for DNA transfer

**T5SS:** type V secretion system, that mostly consists in autotransporters

**UPP:** unipolar polysaccharide that mediates polar adhesion in *A. tumefaciens*

**VirD2:** relaxase/nickase binding to the right and left border to produce linear ssDNA T-DNA, and driving T-DNA towards the eukaryotic cell nucleus.

**VirE2:** ssDNA binding protein, helper protein for T-DNA transfer, various other hypothetical functions

**VHH:** nanobody, adhesin derived from camelid immune system

# 1 INTRODUCTION

---

## 1.1 BACTERIAL COLONIZATION

Microorganisms have evolved the capacity to colonize almost any surface. This includes the human skin and gut, where commensal bacteria can synergize with the host metabolism. On the other hand, many pathogenic bacterial species use adhesion to colonize most of the human tissues.

### 1.1.1 Adhesion to abiotic vs. biotic surfaces

Bacteria adhering to indwelling medical device are responsible for more than half of nosocomial infections and contribute to the spread of resistant strains<sup>1,2</sup>. Consequently, the understanding of bacterial adhesion to abiotic surfaces is of clinical importance to prevent or to remove pathogens from the medical equipment. Bacteria use different adhesion strategies depending on the target substrate. To bind to abiotic surfaces, they will deploy adhesive forces mostly based on electrical charges or hydrophobicity of the surface<sup>3</sup>. Other parameters such as substrate stiffness can impact adhesion efficiency. For instance, *Escherichia coli* and *Pseudomonas aeruginosa* bind respectively 7 and 27-fold better on soft vs. stiff polydimethylsiloxane (PDMS), while *Staphylococcus aureus* adhered similarly on both surfaces<sup>4</sup>.

It is usually hard to draw analogies from bacterial adhesion to abiotic surfaces to explain binding to biological surfaces. The physical and biological complexity of the microenvironment is often overlooked. For instance, in mammalian cells, the soft plasma membrane is packed with transmembrane glycoproteins and glycolipids forming the glycocalyx<sup>5</sup>. Sometimes the glycocalyx contains the biomarker targeted by the bacteria. In other cases, bacteria need to find their way through a “forest” of sugars to reach the targeted surface protein<sup>6</sup>. Additionally, the membrane is not passive but actively rearranges itself under forces generated from the cytoskeleton, the extracellular space or from bacteria themselves<sup>5,7,8</sup>. Consequently, analogies from abiotic material and biochemical studies only partially explain biophysical processes involved in bacterial adhesion to mammalian cells.

### 1.1.2 Adhesion in fluid flow

In both biotic and abiotic scenarios, bacteria are often subject to fluid flow at low Reynolds number. Flow generates forces on bacteria that are tangential to the surface and in the direction of the flow<sup>9</sup>. To resist to such forces, bacteria need to switch from transient to

irreversible binding. For instance, *Caulobacter crescentus* secretes its own glue to rapidly establish a nearly irreversible stalk<sup>10</sup>. Cellular advective-diffusion of daughter cells promotes the emergence of morphological patterns<sup>11</sup>. On a longer timescale, bacteria generate their own multicellular microenvironment (biofilm) that retain nutrients and protect them from flow and other chemical or biological aggressions<sup>12</sup>. In a biotic scenario, fluid flow also acts on the target cells. For instance by shearing the glycocalyx, flow improves the access of the bacterium to the cell membrane<sup>13</sup>.

### 1.1.3 Long-range appendages

Flagella grant bacteria the ability to swim in liquids at low Reynolds number<sup>14</sup>. Since they are up to one order of magnitude longer than the cell body, flagella are one of the first features encountering a surface. Flagellar subunits (flagellins) have a dual role as they can also promote adhesion to surfaces of interest<sup>15</sup>. For instance in *P. aeruginosa*, an opportunistic lung pathogen, the flagellar capping protein binds to Lewis X antigen of lung mucins<sup>16</sup>.

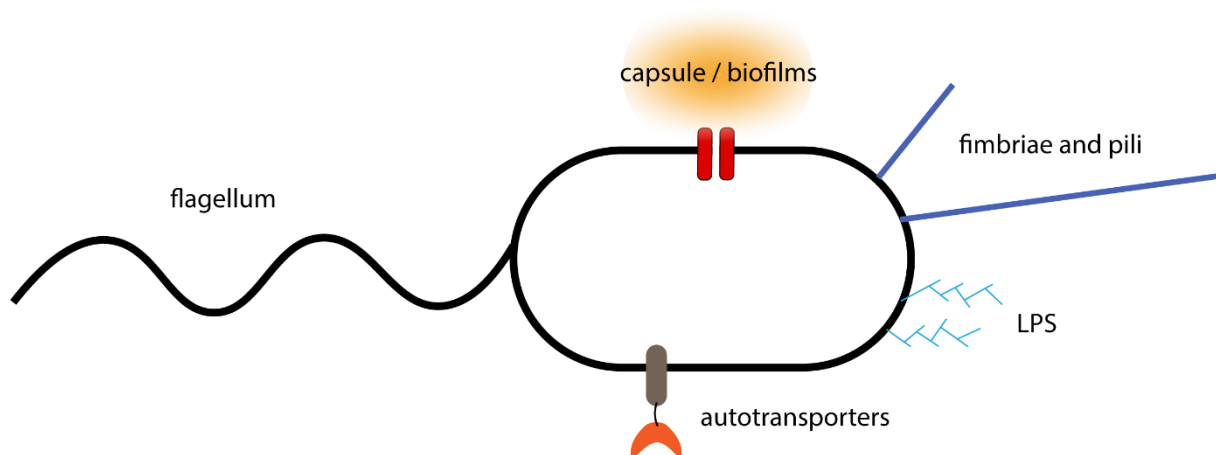


**Figure 1: Overview of the extracellular appendages of Gram-negative bacteria.**

Bacteria can harbor one or several flagella, secrete components of capsule and biofilms, project fimbriae and pili, they are decorated with lipopolysaccharides and can display outer-membrane-anchored autotransporters of various functions.

Pili and fimbriae represent another important family of long-range bacterial appendages (Figure 1). They are thread-like polymers of repeated pilin subunits<sup>17</sup>. They can confer bacteria the ability to move by twitching motility, contribute to biofilm formation and adhere to surfaces. One of the best characterized pili is the type 1 fimbriae of uropathogenic *E. coli*. The pilus is capped with a lectin called FimH. FimH notoriously forms a catch bond with mannose residues of surface glycoproteins from the uroepithelial layer, allowing *E. coli* to strengthen adhesion in the urinary tract under flow<sup>18–20</sup>. Pili can also mediate surface sensing through signal

mechanotransduction. For instance, obstruction of pilus retraction in *Caulobacter crescentus* triggers cyclic di-GMP increase leading to holdfast secretion for irreversible adhesion<sup>21</sup>. Similarly, pili-mediated surface-sensing in *P. aeruginosa* triggers increase in intracellular cyclic-AMP and virulence. Additionally, pili can mediate extracellular DNA uptake and contribute to the spread of antibiotics resistance in *Vibrio cholerae* and *Streptococcus pneumoniae*<sup>22,23</sup>. Finally, the adhesion forces of some pili allow them to trigger host cell remodeling. For instance, *Neisseria meningitidis* type IV pili were shown to trigger actin-independent host cell membrane protrusions along pili<sup>24</sup>.

#### **1.1.4 Short-range appendages: focus on autotransporters**

##### **1.1.4.1 Autotransporter biology**

Autotransporters belong to the type V secretion system (T5SS) family. They are anchored to the outer membrane of Gram-negative bacteria by a scaffold domain and display passenger domains of various functions (e.g. adhesion, enzymatic). As opposed to other secretion systems, they are expressed as a single polypeptide and require no chemical energy source (e.g. ATP or ion gradient) for insertion into and transport through the outer membrane<sup>25</sup>.

To date, four major topologies of autotransporters have been reported<sup>25,26</sup>. The type Va secretion system (T5aSS) autotransporter topology consists in a C-terminal outer-membrane beta-barrel holding a N-terminal passenger domain (Figure 2). The topology is also referred as “classical” autotransporter. In this nomenclature, the T5bSS is actually a Two-Partner Secretion system, as the “passenger” domain gets cleaved and non-covalently secreted. The T5cSS consists in trimeric autotransporters, such as NhhA of *N. meningitidis* allowing binding to macrophages<sup>27</sup>. The T5dSS is a hybrid version between T5aSS and T5bSS, where the scaffold resembles the one of T5bSS but holds the passenger domain instead of secreting it. Finally, the T5eSS, also called reverse autotransporter, harbors a reverse topology compared to T5aSS. A last autotransporter topology baptized T5fSS has recently been described in *Helicobacter pylori*. The passenger domain is however much smaller than in other autotransporters and mainly consists in an loop extending from the beta-barrel<sup>28</sup>.

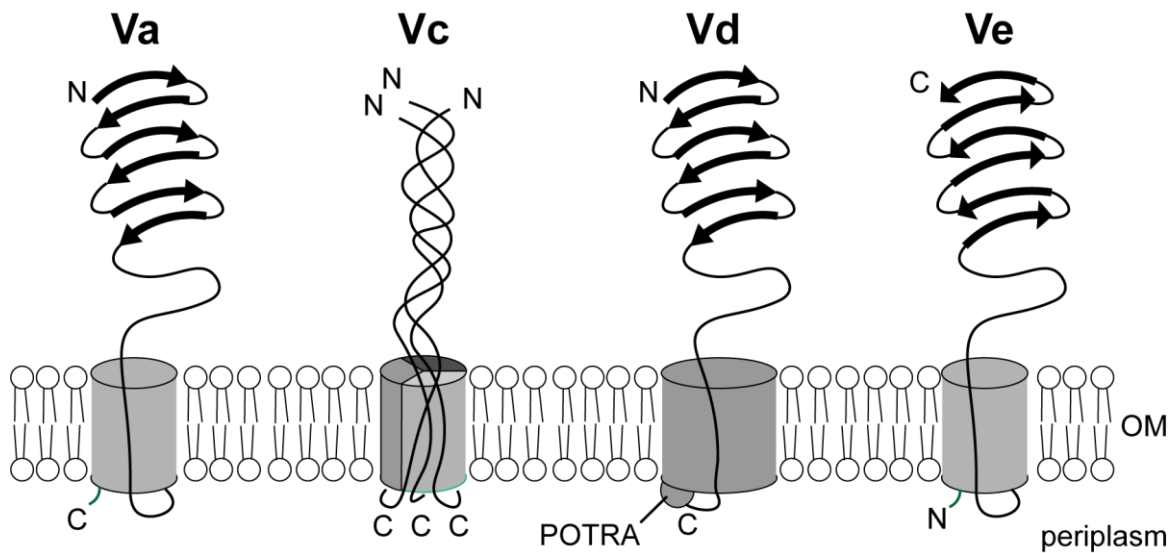


**Figure 2: Schematic of the main T5SS autotransporter topologies.**

Beta-barrels are shown in grey and are folded in the outer membrane (OM), linkers are black lines, and passengers drawn using arrows. “N” and “C” indicate the positions of the N- and C-termini. Polypeptide transport-associated (POTRA) is specific to T5dSS autotransporter and are derived from the T5bSS.

Despite their prefix “auto-”, autotransporters require chaperones for proper folding and export. After Sec-dependent translocation from the cytoplasm to the periplasm, passenger domains are kept in an unfolded state by chaperones such as Skp, FkpA, SurA and DegP in *E. coli*<sup>29</sup>. BamA located in the outer membrane helps membrane insertion of the autotransporter scaffold (Figure 3). The passenger domain translocation might be initiated almost concomitantly via the formation of a hairpin during assembly, yet it is unclear whether the hairpin is completely in the scaffold or partially in BamA lumen as shown in Figure 3<sup>30</sup>. The mechanism was demonstrated for classical and reverse autotransporters, and more recently for the trimeric autotransporter *Yersinia* Adhesin A (YadA)<sup>31</sup>.

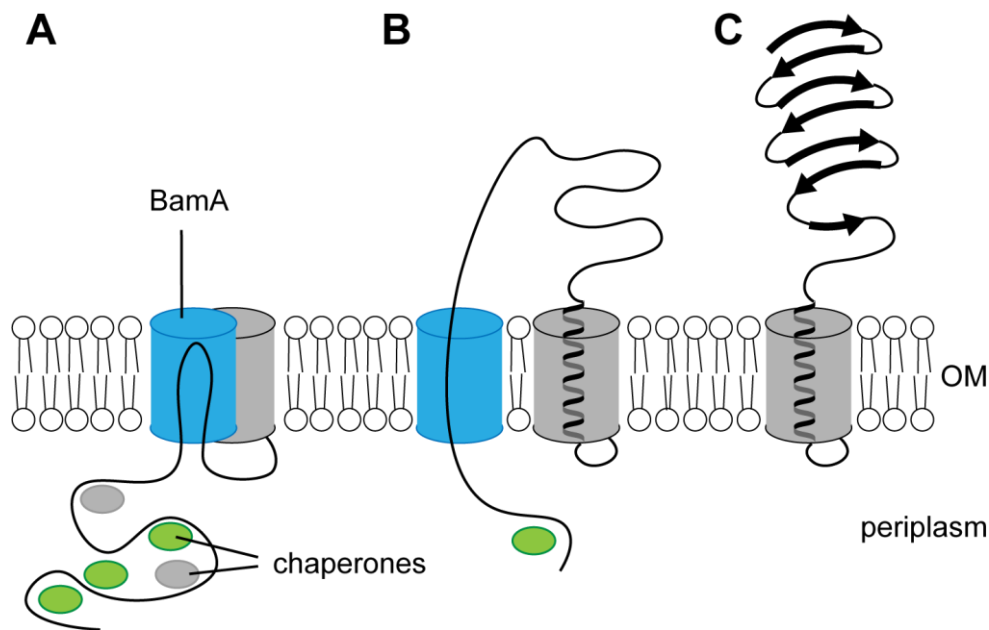


**Figure 3: A working model for hairpin-mediated passenger display.**

(A) Chaperones (green and grey ellipses) keep the passenger domain (black line) unfolded in the periplasm. In *E. coli*, the beta-barrel associated machinery (BamA) helps with the insertion of the autotransporter scaffold (grey cylinder) in the outer membrane (OM) and concomitantly initiates the hairpin formation of the passenger domain. (B) BamA and the scaffold separate and the part of the hairpin the most distant from the scaffold remains in BamA. The part residing inside the autotransporter beta-barrel is usually an alpha helix. The passenger domain export is driven by protein folding. (C) The passenger domain is completely folded in the extracellular space and covalently held by the scaffold.

Autotransporters transit through the oxidative periplasm where covalent disulfide bonds can be formed. In the periplasm of *E. coli*, the DsbA-DsbB complex forms disulfides in proteins and passes electrons to the respiratory chain, while the DsbC-DsbD pair uses electrons transferred through the inner membrane to isomerize mismatched disulfides<sup>32</sup>. An intra-chain disulfide bond creates a protein loop that can prevent export, depending on its size, as demonstrated in *E. coli*'s plasmid-encoded toxin autotransporter<sup>33</sup>.

Consequently, autotransporters contain a comparatively low number of cysteines, and when present, the removal of DsbA showed an increase in the display efficiency. For instance, the *V. cholerae* toxin B subunit was properly translocated by the Iga $\beta$  autotransporter in *E. coli* where the *dsbA* gene was knocked out<sup>34</sup>.

#### **1.1.4.2 Applications using engineered autotransporters**

Autotransporters are extremely versatile: we can relatively easily reuse them in other bacterial species and swap their passenger domain with other protein of interest for various applications including whole-cell biocatalysis, live vaccine development, protein-protein affinity screening and bioremediation<sup>35</sup>.

EstA is a T5aSS autotransporter expressed by *P. aeruginosa*. It was the first full-length structure solved (Figure 4A)<sup>36</sup>. Its catalytically active esterase passenger domain is involved in the production of rhamnolipids that modulate cell motility and biofilm formation<sup>37</sup>. Scientists successfully used the EstA scaffold for the display of lipase libraries in *E. coli*<sup>35</sup>. The passenger domain of EstA harbors a disulfide bond close to the alpha-helix linker.

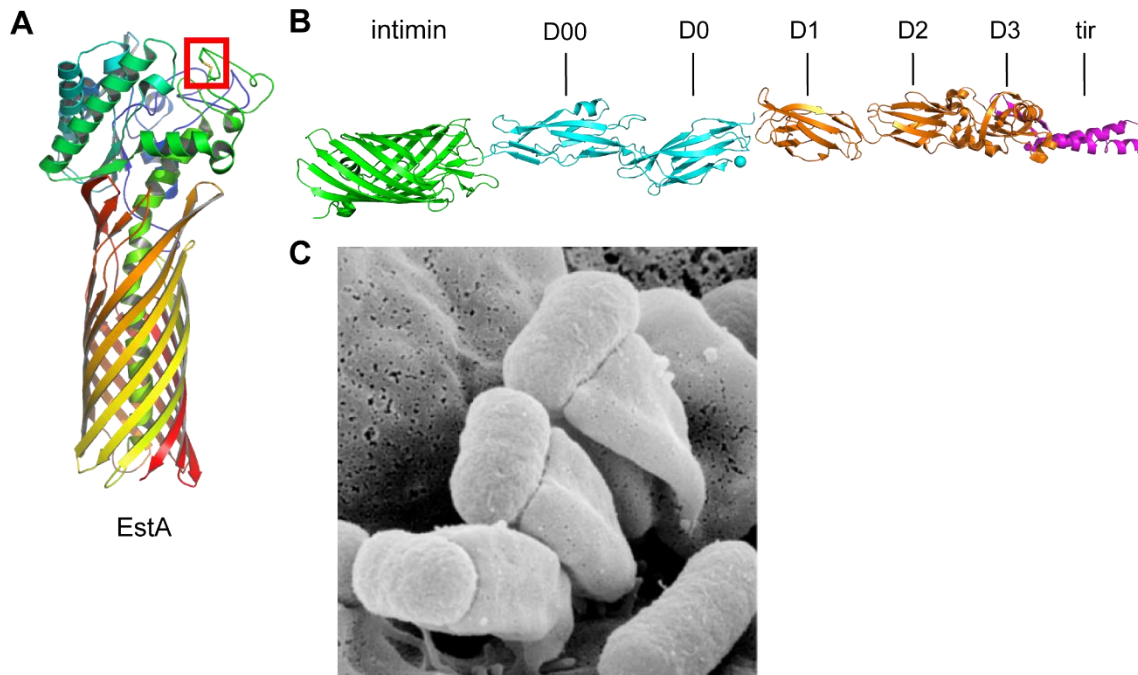


**Figure 4: Two autotransporters used in this study.**

(A) Crystal structure of the full-length *P. aeruginosa* EstA autotransporter of the T5aSS family (pdb 3KVN<sup>36</sup>). Disulfide bond is framed in red and is located at the top of the alpha-helix linker spanning through the beta-barrel. (B) Assembled crystal structures of *E. coli* intimin binding to the Tir receptor (pdb 4e1s<sup>38</sup>, 6tqd<sup>39</sup> and 1F02<sup>40</sup>). The reverse autotransporter scaffold (green) holds the D00-D3 domains (cyan and orange). D00-D2 consist in four bacterial immunoglobulin-like domains and D3 the C-type lectin-like domain binding to the Tir domain (magenta). (C) Scanning electron micrograph of enteropathogenic *E. coli* on top of pedestal-like structure on mammalian cells (Finlay and Cossart<sup>41</sup>).

Intimin is an inverse autotransporter adhesin from enteropathogenic and enterohemorrhagic *E. coli* (EPEC and EHEC) that mediates attachment to gut epithelial cells. It binds to Tir receptor at the host membrane that has been preemptively translocated by the bacterium (Figure 4B)<sup>42,43</sup>. Tir recruitment triggers local actin polymerization leading to the formation of pedestal-like structures at the surface of the host cell (Figure 4C)<sup>41</sup>. Intimin is homologous to *Yersinia pseudotuberculosis* and *Neisseria meningitidis* invasins, which bind to beta integrins present at the host cell membrane, to initiate host cell entry during infection<sup>44–46</sup>. Intimin was for instance successfully used to display nanobody libraries at the surface of *E. coli* (see section 1.6.3)<sup>47</sup>.

### 1.1.5 Bacterial lectins

Lectins are carbohydrate-binding proteins harboring affinity and specificity to certain sugar residues. Bacteria leverage lectins to target certain tissues enriched in defined sugars. They are sometimes displayed at the extremities of long-range appendages such as the aforementioned FimH at the tip of type 1 fimbriae.

Bacteria also secrete lectins as soluble proteins. For instance, LecA and LecB from *P. aeruginosa* respectively bind to galactose and fucose and are involved in biofilm formation and virulence in lung cell models<sup>48–50</sup>. They are regulated by quorum-sensing and might be released from dying cell as they don't have secretion signal discovered to date. Both lectins were crystalized as tetramers<sup>51,52</sup>.

In addition, some bacteria display lectin domains using autotransporters. Intimin's passenger domains for instance consists in several consecutive domains including a C-type lectin domain, yet to our knowledge its carbohydrate ligand remains to be identified<sup>53</sup>. A better characterized example is *Acinetobacter baumannii* trimeric autotransporter Ata that displays a more than 1700 amino-acid-long passenger domain with affinities to galactose, N-acetylglucosamine, and galactose ( $\beta$ 1–3/4) N-acetylglucosamine<sup>54</sup>.

## 1.2 REPURPOSING PATHOGENS INTO THERAPEUTIC BACTERIA

In plant as well as in animals, pathogenic bacteria need to compete with or escape the host immune system<sup>55,56</sup>. One common approach is the formation of biofilms, consisting in a complex three-dimensional matrix protecting them from chemical, environmental and mechanical stresses<sup>57</sup>. The immune-free microenvironment of some solid tumors offers a similar protection to bacteria<sup>58</sup>. Almost two hundred years ago, tumor retardation was observed following *Clostridia* infection<sup>59</sup>. Since then, the concept of recycling pathogenic bacteria for therapeutic purposes progressively emerged<sup>60</sup>.

### 1.2.1 Upgrading bacteria using synthetic biology

Chimeric antigen receptor T-cells (CAR-T) represent one of the most established and efficient method for personalized medicine in the oncologic field<sup>61</sup>. The patient's T-cells are harnessed *ex-vivo* with a cancer biomarker-recognition domain fused to cytosolic signaling domains that activates T-cells upon contact, and by-passes the endogenous T-cell receptor signaling domains.

Similarly, synthetic biology tools allow researchers to gear up bacteria with additional features. As motile and sensing living organisms, they were implemented with chemotaxis motility towards low pH, cytotoxic drug release triggered in anaerobic condition, quorum-sensing-controlled lysis or targeted adhesion to specific biomarkers<sup>62</sup>. While using engineered bacteria provides all advantages synthetic biology can offer, the use of living and replicating organisms in humans naturally raises a number of safety concerns. For instance, uncontrolled growth of immunogenic bacteria would lead to lethal septic shock. Besides removing virulence factors such as toxins, several strategies were developed to increase the safety features of therapeutic bacteria. For instance, one can reduce immunogenicity by engineering the lipopolysaccharide composition, include an inducible suicide safety switch or stop bacterial growth *in vivo* by pre-evolving bacteria towards synthetic auxotrophy<sup>63–65</sup>.

### 1.2.2 Repurposing bacterial injection machineries

Scientists have also rewired pathogenic injection machineries for therapeutic purposes. For instance, bacteria use the type III secretion system (T3SS) to inject toxins to eukaryotic cells and release their metabolites<sup>66</sup>. Ittig *et al.* leveraged *Yersinia enterocolitica*'s T3SS to deliver various proteins by fusion to the translocation signal of the toxin YopE. The engineered *Y. enterocolitica* is now under clinical evaluation for treating solid tumors at T3 pharmaceuticals (Basel, Switzerland)<sup>67</sup>. The T3SS can also be transferred to other better studied bacterial scaffolds such as *E. coli*<sup>68</sup>.

Another important secretion system is the type IV secretion system (T4SS). It is usually used for horizontal gene transfer between bacteria, causing the spread of social traits, virulence and resistance genes among species. Pathogens such as *Bartonella*, *Legionella*, *Coxiella*, *Brucella* and *Helicobacter* use their T4SS for trans-kingdom delivery of proteins and/or DNA to mammalian cells<sup>69</sup>. The first three species are intracellular pathogens and were used to infect mammalian cells with a transient transfection efficiency of about 5% *in vitro*, yet cell rounding reported high toxicity<sup>70</sup>. Could the bacterial T4SS compete with the current gene delivery methods used in the clinics?

## 1.3 GENE DELIVERY

### 1.3.1 Gene therapies

Today, the clustered regularly interspaced short palindromic repeats (CRISPR)/Cas9 technology enables targeted double or single-stranded cuts. Providing a repair template allows gene editing at the base pair level. Finally, the technology also allows down or up-regulation of genes in cells<sup>71</sup>. To date, a surprisingly low number of genetic diseases can be treated by gene therapies<sup>72,73</sup>. For *ex-vivo* gene editing like the production of CAR-T used in cancer therapies, large amount of DNA material can easily be transferred by chemical transfection or lentiviral transduction<sup>74</sup>. On the other hand, the treatment of genetic disorders or HIV would require to deliver and repair genes in humans, and the number of clinical trials is significantly lower<sup>75</sup>. The main limiting factor is the availability of safe DNA delivery methods able to efficiently deliver large DNA cargo<sup>76</sup>. Furthermore, the discovery of the CRISPR/Cas9 technology exacerbated the urge for new DNA vectors in the clinics<sup>74,77–79</sup>.

### 1.3.2 Viral gene delivery vectors

Unfortunately for human gene therapies, retroviruses failed in clinical trial more than 20 years ago due to random DNA integration events leading to leukemia<sup>80</sup>. At around the same period, lentiviruses were tried and induced a lethal immunogenic response in a 18-year old patient<sup>81</sup>. After an almost two-decade gap, adeno-associated viruses (AAVs) became the preferred choice for viral gene delivery in humans. The injected DNA remains as episome in nuclei and AAVs are little immunogenic<sup>82</sup>. Several serotypes of AAVs exist and target different tissues, for instance AAV2 and AAV9 for retinal and neuronal cells, respectively. AAVs surface capsid can be evolved or “mixed” to generate mosaicism in order to tailor tropism<sup>83,84</sup>. To this date there have been three non-CRISPR/Cas9 clinically-approved AAV-based gene therapies, why such a low number<sup>85</sup>?

The major limitation of AAVs for CRISPR/Cas9 gene editing is their packaging capacity: 4.7kb<sup>86</sup>. For instance, a promoter driving guide RNA (gRNA) expression followed by a promoter driving *Streptococcus pyogenes* Cas9 expression is 5.4 kilobases-long in a standard vector. Together with a repair DNA template for precise gene editing, the size requirements largely exceed the AAVs' capacity<sup>86</sup>. Different strategies are investigated to overcome such limitation such as smaller Cas9 orthologs or dual transductions<sup>87,88</sup>. Another limitation of AAV-based therapies is the pre-existing immunity to AAVs. Despite not being reported to cause any disease, the viruses can spread in the population and trigger a mild immune response. The

presence of pre-existing antibodies reduces gene delivery efficiency<sup>89</sup>. In addition, studies reported a cytotoxic effect of T-cells against AAV capsid-presenting cells<sup>90</sup>.

### **1.3.3 Physico-chemical gene delivery**

Alternatively, when the target tissue is accessible, chemical, nanoparticles-based transfection or lipofection of the gene-editing machinery are investigated in preclinical studies. For instance, Cas9-gRNA-lipid complexes were used to restore genetic hearing loss in neonatal mice<sup>91</sup>. Other physical transfection such as electroporation, magnetofection, laser or acoustic-based methods remain too invasive for their implementation in humans<sup>92</sup>.

## **1.4 AGROBACTERIUM TUMEFACIENS**

### **1.4.1 *A. tumefaciens* in the wild**

The ability to transfer DNA to eukaryotic cells is not limited to viruses. *Agrobacterium tumefaciens* (also known as *A. fabrum*<sup>93</sup>) is famous for trans-kingdom DNA delivery into plants. It is a Gram-negative alphaproteobacterium and the causal agent of crown gall disease. The disease results in plant tumors and is caused by the random integration of ~25 kb-long single-stranded transfer DNA (T-DNA). Because plant cells are protected by thick cell walls, the bacterium usually senses and opportunistically attacks wounded sites, where it uses its T4SS to transfer its T-DNA into plant cells (Figure 5). The T-DNA contains plant-promoter-driven genes encoding enzymes producing opines, which are special amino acids derivatives that *A. tumefaciens* can metabolize as a nitrogen source<sup>94</sup>. The bacterium co-injects helper proteins that facilitate T-DNA transport through the T4SS, protection in the cytosol, nuclear import and chromosomal integration. Following random integration in the plant genome, some T-DNA-encoded oncogenes lead to uncontrolled growth and to the onset of the tumor<sup>95</sup>.

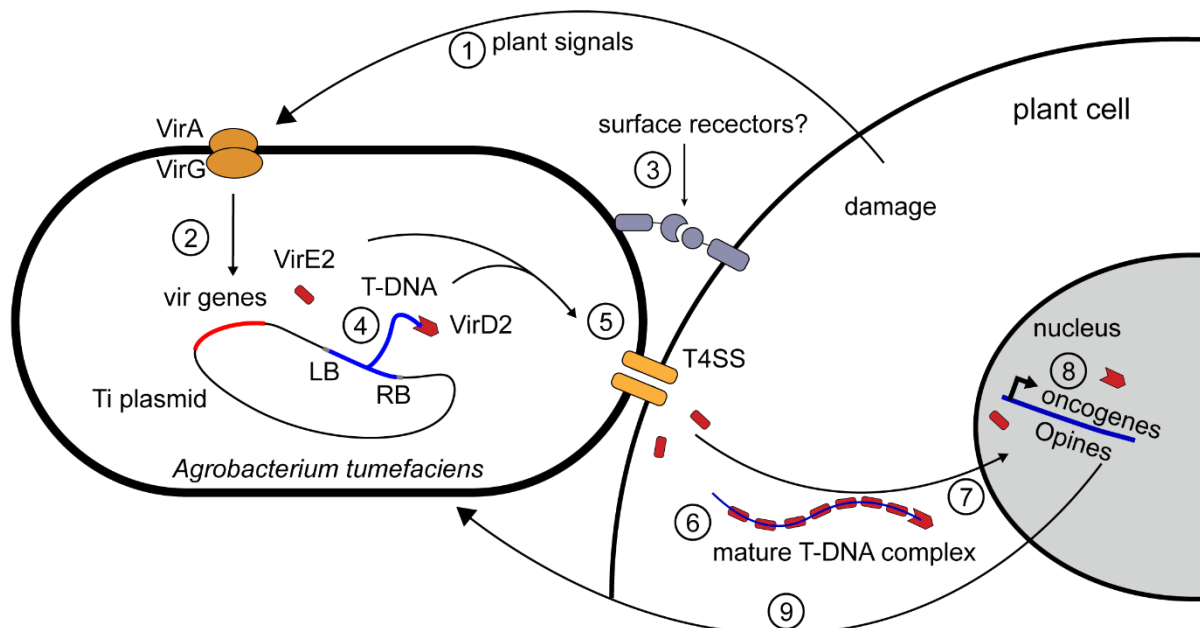


**Figure 5: *A. tumefaciens* DNA transfer in the wild.**

In the wild, damaged plant cells acidify the microenvironment and produce phenolic compounds sensed by the VirA-VirG two-components system in *A. tumefaciens* (1). This induces the transcription of new vir genes coding for the type IV secretion system (T4SS), the DNA nickase VirD2 and the single-stranded DNA-binding protein VirE2, among other helper proteins not depicted here for clarity (2). Concomitantly, bacteria bind to the plant cell, a process poorly characterized (3). The transfer DNA (T-DNA) is produced by nicking of the T-DNA sequence at the 25-bp long right and left borders (RB and LB, respectively) flanking the genes to be transferred to the plant cell (4). VirD2 brings the T-DNA to the T4SS for translocation to the target cell (5). VirE2 coats the T-DNA for protection from ssDNA endonucleases (6). VirD2 contains nuclear localization signals (NLS) for nuclear import (7). Other vir and endogenous proteins help ssDNA to integrate into the plant genome (8), for the transcription of oncogenes and genes involved in opines biosynthesis, that are in return beneficial for the bacterial growth (9).

#### 1.4.2 *A. tumefaciens* is the gold standard organism for plant engineering

Beyond the pathogenic trait of *A. tumefaciens*, plant biologists have assessed the potential of the bacterium for biotechnological applications. Using disarmed strains lacking pathogenic T-DNA, crop engineers were able to introduce new genes in plants, either by random integration or more recently by targeted integration using zinc-finger nucleases, transcription activator-like effector nucleases (TALENs) or CRISPR/Cas9 technologies<sup>96</sup>.

*A. tumefaciens*' T-DNA region is delimited by two 25 base-pairs-long left and right borders (LB, RB, respectively)<sup>97</sup>. Crop engineers generated disarmed strains by deleting such regions from the tumor-inducing plasmid<sup>98–102</sup>. These strains can be retransformed with binary vectors encoding any T-DNA of interest. Such vectors contain broad host range origin of replication for cloning in *E. coli* (or one of each ori).

GV3101::pMP90 used in this study consists in *A. tumefaciens* C58 background, contains a linear and a circular chromosome, the cryptic megaplasmid pAtC58 and pMP90, a disarmed version of the 214 kilobases-long tumor-inducing plasmid pTiC58<sup>102</sup>. Genes located on the pAt plasmid are dispensable and poorly characterized but in general facilitate metabolic activities in the plant root microenvironment and bulk soil, such as the ability to breakdown plant exudates<sup>103</sup>. The tumor-inducing plasmid contains virulence genes encoding the T4SS and other virulence-related genes as well as its own origin of transfer for horizontal gene transfer<sup>104</sup>.

#### **1.4.3 *A. tumefaciens* adhesins**

*A. tumefaciens* developed adhesins to adhere to target materials, to grow as biofilm and to protect itself from environmental stresses. Up to date, five different exopolysaccharides have been characterized: cyclic-b-(1, 2)-glucan, cellulose, curdlan, succinoglycan, and the unipolar polysaccharide (UPP)<sup>105</sup>. Among those, UPP is the only one that mediates adhesion to biotic and abiotic surfaces upon contact. Its production is controlled by cyclic-di-GMP, localizes at the opposite pole from the flagella and coordinates with to a loss of flagellar motility<sup>10</sup>. The structure of UPP is unknown except the fact it contains N-acetylglucosamine and N-acetylgalactosamine<sup>106</sup>. Besides exopolysaccharides, *A. tumefaciens* harbors 4 to 6 flagella that promote frequency of surface contact<sup>107</sup>. It also projects Ctp pili (Cpa-type pilus, named after its homologue in *C. crescentus*), that mediate reversible attachment to surfaces<sup>108</sup>. Conjugative pili from the T4SS also mediate adhesion, even though their target is unknown and their lateral deployment does not correlate with the unipolar localization of UPP<sup>109</sup>. Apart from sugars and extracellular appendages, a single protein adhesin has been described in *A. tumefaciens*: Rhicadhesin is a Ca<sup>2+</sup>-binding protein released by the bacterium and involved in attachment pea root hairs<sup>110</sup>.

#### **1.4.4 *A. tumefaciens*' type IV secretion system**

The T4SS of *A. tumefaciens* is a complex machinery that requires the coordination of numerous Vir proteins. VirB4 is the motor ATPase and powers the formation of the T-pilus. The T-pilus is composed of cyclized VirB2 subunits, and is primed by VirB1 and VirB5 minor pilin (Figure 6)<sup>111</sup>. VirB1 has an additional N-terminal transglycosylase domain that performs localized lysis of the bacterial cell wall for extension of the pilus through the periplasm<sup>112</sup>. VirB5 is homologous to *Helicobacter pylori* CagL, which binds to beta-integrins at the surface of human epithelial cells<sup>113</sup>. The addition of soluble VirB5 increased T-DNA transfer from *A. tumefaciens* to plant cells<sup>114</sup>.

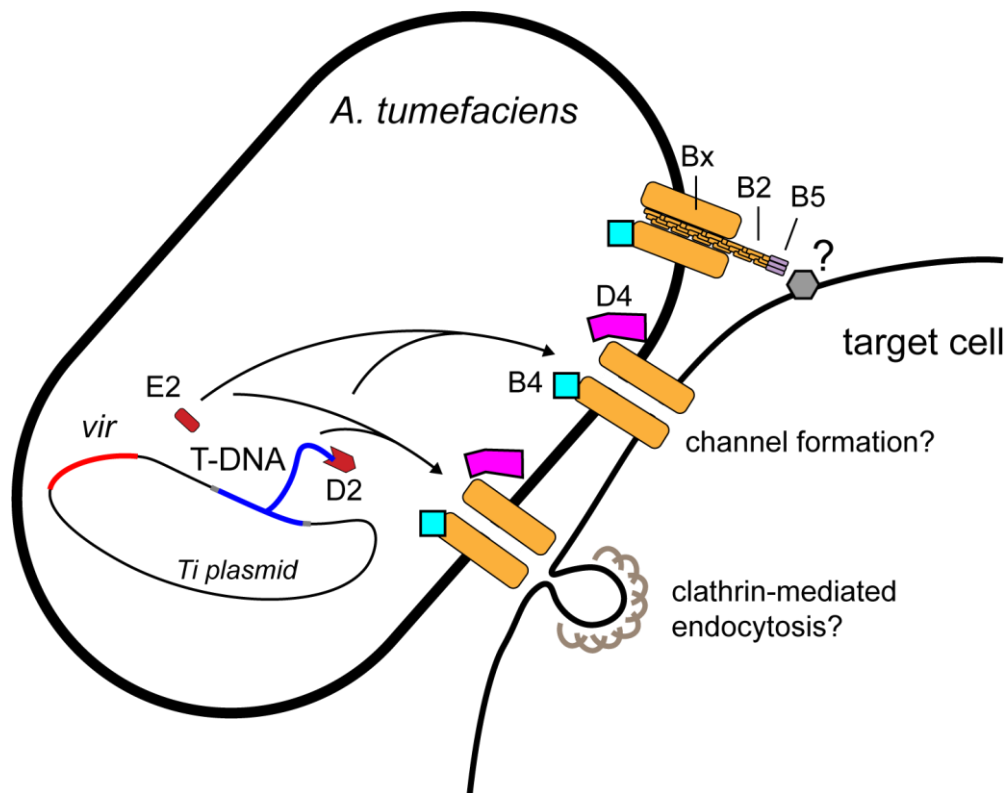


**Figure 6: Overview of *A. tumefaciens*' T4SS and T-DNA's mode of entry into the target cell.**

The T4SS is composed of several VirB proteins (Bx) including VirB10, a structural and signal mechanotransduction protein. The pilus is composed of VirB2 (B2) monomers capped by VirB5, which is suspected to increase transformation efficiency by binding to unknown target receptors. VirB4 (B4) powers the pilus polymerization and VirD4 couples helper proteins such as VirD2 (D2) and VirE2 (E2) to the T4SS. The T-DNA complex enters the target cell either by T4SS-mediated channel formation between both cytosols or by clathrin-mediated endocytosis triggered by VirE2 and facilitated by tight binding.

Among structural proteins, VirB10 harbors the additional role of a signal transducer, undergoing a conformational change upon activation to allow substrate translocation<sup>115,116</sup>. Some mutagenesis screens identified some T-DNA transfer competent but T-pilus-deficient strains, leading to two possible interpretations<sup>117</sup>. On the one hand, pili could be present but too short for detection, on the other hand, the pilus might predominantly act as an attachment organelle, leading to the formation of tight donor-target cell junction for T-DNA transfer, rather than a translocation through the pilus, which is sterically improbable<sup>118</sup>.

VirD4 is an ATPase containing a substrate receptor for coupling helper proteins to the assembled T4SS. To this purpose, the C-terminal domains of helper proteins contain a consensus motif R-X(7/10)-R-X-R-X-R-X-X(n)<sup>119</sup>. VirD4 mutants still produce pili but are transfer-deficient<sup>118</sup>. VirD4 couples at least VirD2, VirD5, VirE2, VirE3 and VirF to the base of the T4SS for translocation. VirD5 and VirF are implicated in T-DNA genomic integration in plant cell's nuclei by interacting with the target plant cell machinery, but at least VirF is dispensable

for yeast cell transformation<sup>120,121</sup>. Ambiguously, VirE3 was both demonstrated as a transcriptional activator and as a VirE2-companion localizing on the cytoplasmic side of the plant plasma membrane<sup>122,123</sup>.

VirD2 starts acting in the bacterium. It binds to the LB and RB of the T-DNA region for nicking DNA and production of linear, single-stranded T-DNA. It remains covalently linked to the 5' end of the T-DNA. Its C-terminal translocation motif is recognized by VirD4 and the T-DNA complex is translocated to the target cell. Furthermore, a C-terminal bipartite nuclear localization signal (NLS) interacts with host importin- $\alpha$  for nuclear import of the T-DNA complex<sup>124,125</sup>.

Last but not least, VirE2 is a sequence-unspecific single-stranded DNA (ssDNA) binding protein, that protects T-DNA in the target cell from host ssDNA endonucleases. Besides this undisputed function, literature attributes other and sometimes conflicting functions to VirE2. Scientists initially believed VirE2 drove nuclear import into host cells but more recently they reattributed it to a cytosolic localization<sup>126–128</sup>. VirE2 might be delivered into plant cells via clathrin-mediated endocytosis, but could also form channels in artificial membranes<sup>129,130</sup>. Once in the target cell, conflicting studies either locate VirE2 at the cytoplasmic side of the plasma membrane, or point its trafficking along the endoplasmic reticulum/actin network or show it interacting with the CG1 host nucleoporin to facilitate nuclear import<sup>128,131–133</sup>.

Overall, it is rather clear how T-DNA and helper proteins get exported using the T4SS, however, the efficient entry into a large range of plant cells remains obscure<sup>134</sup>. VirB2 depolymerization might cause membrane fusion in a process similar to bacterial fusion. The T4SS might first translocate helper proteins in the intercellular space, followed by VirE2-assisted uptake by the target cell. *VirE2*-mutant strains were however complemented by VirE2-producing plant cells<sup>135</sup>.

Once reaching the plant nucleus, we also poorly understand the mechanisms for T-DNA integration into the host genome. *A. tumefaciens* does not translocate a dedicated integrase, rather, T-DNA integration relies on host cell DNA repair pathways<sup>134</sup>. T-DNA might integrate as ssDNA using microhomology-mediated end joining<sup>136</sup>. But there is also evidence that T-DNA can integrate as double-stranded DNA (dsDNA) into double-strand breaks<sup>137,138</sup>. Finally, T-DNA can circularize and form dimeric T-circles (sometimes multimeric) in plant cells and are reminiscent of integration events<sup>139</sup>.

## 1.5 SPLIT PROTEIN REPORTERS DEVELOPED FOR BACTERIAL INJECTION

### 1.5.1 Split fluorescent proteins

Monitoring protein localization by fusing it to a fluorescent protein is the method of choice for conventional and super-resolution fluorescent microscopy. However, when it comes to follow proteins translocated through injection machineries, the relatively large size and robust beta-barrel structure of fluorescent proteins inhibits injection<sup>140,141</sup>.

To circumvent this, scientists must use smaller peptides. For instance, they developed a split-fluorescent GFP by separation of the last and 11<sup>th</sup> beta-strand (GFP11) from the 10 first ones (GFP1-10)<sup>142</sup>. This technology was applied to *A. tumefaciens*-mediated transformation in plant cells for VirE2 visualization<sup>143</sup>. VirE2 cannot be N- or C-terminally fused to peptides without decreasing transformation efficiency<sup>144</sup>: to overcome this, an internal permissive site of VirE2 was used to fuse GFP11, and target cells expressed GFP1-10. VirE2-GFP11 translocation could be monitored in yeast and plant cells, and movement was visible in plant cells<sup>129,133</sup>.

### 1.5.2 Split luciferase

The scientific community initially developed the split luciferase technology for the study of protein-protein interactions<sup>145</sup>. The *Gaussia* luciferase fragments were designed with low affinity to enable reversibility. More recently, scientists engineered NanoLuc from the deep sea shrimp *Oplophorus gracilirostris* and split it into two components of high affinity (HiBit and LgBit, 1.3 kDa and 18 kDa, respectively)<sup>146</sup>. In a similar fashion to split fluorescent proteins, protein translocation to mammalian cells was quantified with *Salmonella*'s T3SS and recently with *H. pylori*'s T4SS<sup>147,148</sup>.

## 1.6 SYNTHETIC BACTERIAL ADHESINS: NANOBODIES (VHH)

### 1.6.1 Structure

Nanobodies are immunoglobulins from the camelid adaptive immune system. Camelids produce both conventional heterotetrameric antibodies and homodimeric heavy-chain antibodies<sup>149</sup>. The latter lacks a constant domain responsible for dimerization with the light-chain and bind antigen using the variable heavy-chain (VHH) only (Figure 7). This property, in addition to their short length (less than 130 amino, or 15 kDa) and robust structure, make them appealing candidates for the development of new protein binders.

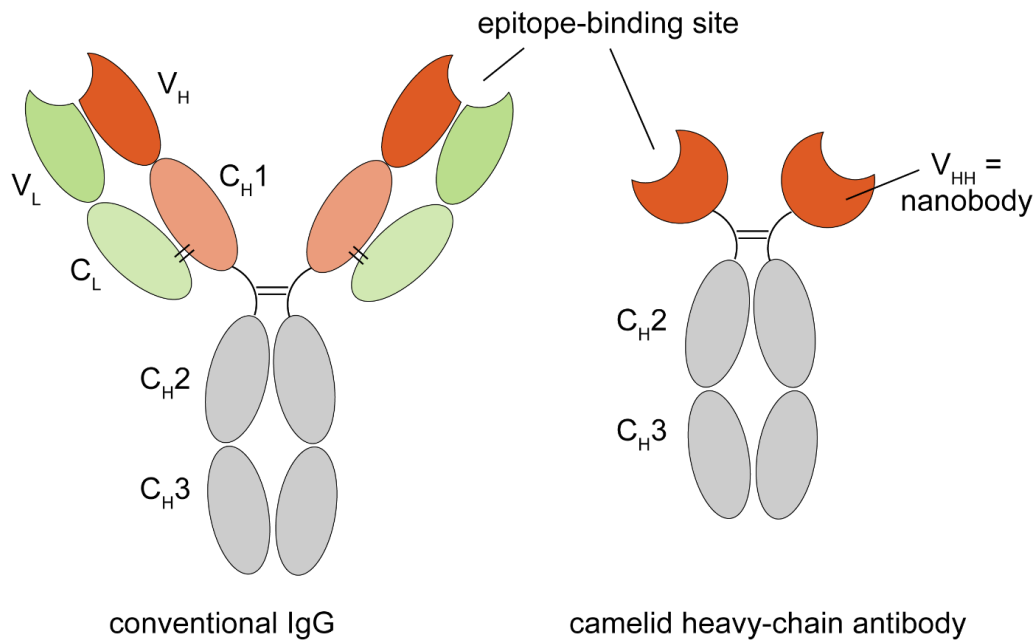


**Figure 7: Comparison of conventional IgG with camelid heavy-chain antibody.**

Conventional IgG are heterotetrameric structures bridged by disulfide bonds (black lines). The heavy chain is composed of four immunoglobulin domains: the variable domain conferring part of the epitope specificity and affinity ( $V_H$ ), and three constant structure domains ( $C_H1-3$ ). The light chain is composed of the variable light chain, completing the epitope specificity ( $V_L$ ), and the constant part ( $C_L$ ). In camelid heavy-chain antibody, the epitope specificity is entirely determined by the variable heavy chain of heavy-chain antibodies ( $V_{HH}$ ) domain, also called nanobody, mounted on  $C_H2-3$  scaffold.

Like other variable heavy chains, they harbor three variable complementarity-determining regions (CDR) that generate loops and specificity to the substrate. CDR3 is the longest of the loops, especially in camels. An excess of flexibility is usually entropically counterproductive, consequently, a conserved interloop disulfide bond is usually present between two cysteines on CDR1 and long CDR3<sup>149</sup>. In llamas, CD3 are shorter and the disulfide bond is less frequent. When present, removing the VHH disulfide bond does not systematically abolish binding to the target antigen: the removal of cysteines within a VHH anti-GFP maintained sub-nanomolar affinity, while a cysteine-free VHH anti-mCherry conserved mechanical strength to the antigen as measured by atomic force microscopy<sup>150,151</sup>. In the case of VHH anti-GFP, this is likely resulting from the fact the VHH binds in a non-canonical fashion to GFP, by engaging interactions with GFP from the side of the framework regions, rather than CDRs<sup>152</sup>.

### 1.6.2 Engineering and applications

Several methods exist for the development of VHH against new antigens. First, one can obtain a polyclonal library of nanobodies by immunizing camels or llamas with the antigen, and screen

clones of the desired properties from it. *Ab initio*, one can perform phage display starting from naïve DNA libraries<sup>153</sup>.

VHH have numerous applications in basic biology<sup>154</sup>. For instance we can fuse them to fluorescent proteins and express fluorescent fusions to track target proteins in dividing cells<sup>155</sup>. VHH are also potent candidates for diagnostics and therapeutic applications. Overall, they exhibit limited immunogenicity in animal models. Caplacizumab (Cablivi®) targets von Willebrand factor for the treatment of thrombotic thrombocytopenic purpura, a rare blood-clotting disorder, and was the first VHH-based therapy approved in 2018 in Europe<sup>156</sup>.

### 1.6.3 Nanobody display

Scientists displayed VHH at the surface of mammalian, yeast and bacterial cells<sup>154</sup>, where they functioned as adhesins. For instance, Salema *et al.* used a bacterial intimin-based display of VHH libraries against human epidermal growth factor receptor (EGFR) and performed selection on live human cells overexpressing this cancer biomarker<sup>157</sup>. They removed the intimin's passenger domains D1-D3 (Figure 4B) and replaced them with VHH libraries. Using the same scaffold, Glass *et al.* created adhesin toolbox that includes a tetracycline-inducible VHH anti-GFP system in *E. coli*<sup>47,158</sup>. This assembly represents an elegant proof of concept of synthetic cell assemblies but we believe the system has the potential to solve actual biological problems.

## 1.7 OVERALL AIMS AND ORGANIZATION OF THE THESIS

### 1.7.1 Aim 1: Identify physical principles ruling bacterial early adhesion to tissues

A key step in pathogenicity is the attachment of bacteria to target tissues, which also further triggers virulence. To bind to target cells with high specificity, bacteria decorate themselves with adhesins targeting host receptors. Biochemical assays can determine parameters such as the dissociation constant of the adhesin-receptor pair. They can be completed with microfluidics approaches for the characterization of bacterial adhesion to abiotic material, but these still do not illuminate the general biophysical rules of initial attachment to host cells. This often results in poor prediction of bacterial adhesion in an *in vivo* context, because how target cell surface properties regulate attachment is largely overlooked. In addition, it remains difficult to decouple adhesive from toxic effects when investigating pathogen adhesion<sup>41,159</sup>.

In [chapter 2](#), we tackled the issue from a target cell perspective. We investigated the contribution of the mammalian microenvironment mechanics in the early steps of bacterial adhesion to host cells and compared it to adhesion to abiotic surfaces. We fine-tuned adhesion using a synthetic adhesin displayed on a non-pathogenic *E. coli* targeting a synthetic mammalian cell surface receptor<sup>47</sup>. We tracked bacterial attachment and detachment in flow at high temporal resolution. We found that the specific attachment of bacteria to host cells occurs in two consecutive steps. A first adhesin-independent step takes place within the first few seconds following contact. This is followed by the onset of specific adhesion resulting in nearly irreversible attachment on longer timescale. We demonstrate that membrane mechanics, flow and glycocalyx, regulate each of the adhesion steps. Overall, we show that the biomechanical microenvironment of host tissues strongly regulates the adhesion behavior of bacteria to their target cells, indicating that this process cannot be solely reduced to adhesin-receptor interactions.

### **1.7.2 Aim 2: Rewire *A. tumefaciens* to yeast and human cells**

*A. tumefaciens* is the one of the preferred DNA vectors for plant engineering. However, the scientific community only has a partial understanding of bacterial adhesion processes and lacks tools to fine-tune adhesion of the bacterium to target surfaces. In this context, the limited attachment of the bacterium to non-natural hosts might limit transfer efficiency. Consistent with this, studies showed a positive correlation in transformation efficiency and adhesion in a monocot<sup>160,161</sup>. To date, there is no genetically-encoded tool to fine-tune adhesion of the bacterium to target surfaces. Hence can we leverage and broaden the nanobody display technology in *A. tumefaciens* to rewire it to recalcitrant target cells?

In [chapter 3](#), we provided *A. tumefaciens* with an adhesin display system to fine-tune adhesion of the bacterium in order to target cell surfaces. We investigated and repurposed an endogenous, previously uncharacterized autotransporter of the bacterium. We displayed adhesins of increasing complexity that highlighted the structural limitations of the passenger domain for this scaffold. This ultimately enabled us to robustly display synthetic adhesins such as VHH anti-GFP at the surface of *A. tumefaciens*.

In [chapter 4](#), we rewired *A. tumefaciens* to new cell types. Using our synthetic adhesin display system, we robustly bound the bacterium to yeast and mammalian cells. In addition, we investigated different existing tools to monitor the T4SS-mediated delivery of helper proteins and T-DNA into mammalian cells, with limited success. Instead, we developed a highly sensitive split NanoLuc system that reported an increase in VirE2 transfer from the bacteria to mammalian cells when inducing the autotransporter display system.

## 2 THE MAMMALIAN MEMBRANE MICROENVIRONMENT REGULATES THE SEQUENTIAL ATTACHMENT OF BACTERIA TO HOST CELLS.

---

This chapter is adapted from the post-print version of the article published in August 2021 in mBio (American society for microbiology Journal), volume 12, number 4 as:

Xavier Pierrat, Jeremy Wong, Zainebe Al-Mayyah, Alexandre Persat\*. *The Mammalian Membrane Microenvironment Regulates the Sequential Attachment of Bacteria to Host Cells*. MBio. 2021;12(4).<sup>162</sup>

Institute of Bioengineering and Global Health Institute, School of Life Sciences, Ecole Polytechnique Fédérale de Lausanne, CH-1015 Lausanne, Switzerland

\*Corresponding author: [alexandre.persat@epfl.ch](mailto:alexandre.persat@epfl.ch)

Authors contributions:

X.P. and A.P. conceived the work. X.P. designed and performed the experiments, except the ones involving glass surface functionalization with fluorescent proteins. J.W. designed and performed the glass functionalization with proteins and some of the bacterial attachment to the functionalized surfaces. Z.A-M. provided support for cell culture, DNA purification and colony PCR. The EPFL Flow Cytometry Core Facility performed single cell sorting. X.P. analyzed the data. X.P. and A.P. wrote and revised the paper, with the input from J.W. All authors approved the manuscript and declare no conflict of interest.

Supplementary movies S1-6 are available at:

<https://zenodo.org/record/5079719#.YdWPA1nTWuU>

## 2.1 ABSTRACT

Pathogen attachment to host tissue is critical in the progress of many infections. Bacteria use adhesion *in vivo* to stabilize colonization and subsequently regulate the deployment of contact-dependent virulence traits. To specifically target host cells, they decorate themselves with adhesins, proteins that bind to mammalian cell surface receptors. One common assumption is that adhesin-receptor interactions entirely govern bacterial attachment. However, how adhesins engage with their receptors in an *in vivo*-like context remains unclear, in particular under the influence of a heterogeneous mechanical microenvironment.

We here investigate the biophysical processes governing bacterial adhesion to host cells using a tunable adhesin-receptor system. By dynamically visualizing attachment, we found that bacterial adhesion to host cell surface, unlike adhesion to inert surfaces, involves two consecutive steps. Bacteria initially attach to their host without engaging adhesins. This step lasts about one minute during which bacteria can easily detach. We found that at this stage, the glycocalyx, a layer of glycosylated proteins and lipids, shields the host cell by keeping adhesins away from their receptor ligand. In a second step, adhesins engage with their target receptors to strengthen attachment for minutes to hours. The active properties of the membrane, endowed by the actin cytoskeleton, strengthen specific adhesion.

Altogether, our results demonstrate that adhesin-ligand binding is not the sole regulator of bacterial adhesion. In fact, the host cell's surface mechanical microenvironment mediates the physical interactions between host and bacteria, thereby playing an essential role in the onset of infection.

## 2.2 INTRODUCTION

In the wild, bacteria predominantly live associated with surfaces. Their sessile lifestyle confers fitness advantages such as protection from predators and improved access to nutrients<sup>163</sup>. In the context of host colonization, the transition between planktonic and sessile lifestyles plays a functional role in mediating host-microbe interactions. Indeed, attachment to host tissue, more specifically to cells, is often a critical first step towards infection or commensalism<sup>159,164</sup>. As a result, the dynamics of attachment of single bacteria to host cells can dramatically influence the outcome of infection or regulate host-microbiota homeostasis<sup>165</sup>.

Bacterial adhesion to abiotic materials greatly contributes to biofouling and contamination of indwelling medical devices. Multiple physicochemical properties of the surface mediate adhesion to inert materials, including charge, hydrophobicity and conditioning<sup>166</sup>. In addition, mechanical properties of the material such as stiffness and surrounding fluid flow regulate attachment strength and dynamics<sup>167–169</sup>. The understanding of adhesion to abiotic materials provides us with only rudimentary insights on adhesion to biological tissue. More specifically, the physical and biological complexity of biotic surfaces remains overlooked when making the analogy between living and inert materials. The surface of host mammalian cells is composed of a soft lipid bilayer densely packed with surface proteins<sup>170</sup>. In addition, it is a dynamic surface, permanently rearranging itself under the action of forces such as the ones generated by the cytoskeleton. Finally, in contrast with abiotic adhesion, bacterial attachment to host cell involves specific molecular interactions<sup>164</sup>. As a result, drawing analogies between biotic and abiotic adhesion can be informative, but may overlook critical physical and biological regulators.

Pathogens and commensals alike express proteins at their surfaces that specifically bind to host membrane receptors. These cell type-specific adhesins promote tissue tropism during infection or colonization<sup>171</sup>. These can be classified in categories that reflect their structure and molecular mechanism of display. Adhesins from the autotransporter family are exposed immediately near the bacterial cell envelope<sup>172</sup>. Their structure includes an outer-membrane beta-barrel scaffold and an inner alpha helix that holds a passenger domain. This domain often includes its ligand-binding domain<sup>35</sup>. Intimin is an autotransporter adhesin from enteropathogenic and enterohemorrhagic *Escherichia coli* (*E. coli*) that mediates attachment to gut epithelial cells. Intimin binds to Tir receptors at the host membrane that have been preemptively translocated by the bacterium<sup>42,43</sup>. *Yersinia pseudotuberculosis* uses invasin, which binds to beta integrins present at the host cell membrane, to initiate host cell entry during infection<sup>44,45</sup>. Similarly, *Neisseria meningitidis* uses NadA to invade host cells<sup>46</sup>.

How the microenvironment the host cell surface mediates the interaction between adhesins and their receptors remains unclear. Absolute bacterial count suggests that the membrane fluidity of host cells slightly decreases bacterial adhesion<sup>173</sup>. At the molecular level of single adhesins, force spectroscopy measurements have helped characterize bond mechanics both on abiotic materials and on live cells<sup>174</sup>. These have helped precisely identify exotic adhesin behavior such as the formation of catch bonds, which strengthen under an applied tensile force. The fimbriae tip adhesin FimH notoriously forms a catch bond, allowing uropathogenic *E. coli* to strengthen adhesion in the urinary tract under flow<sup>18–20</sup>. Studies of bacterial adhesion, including catch bonds, have mainly focused on detachment of bacteria, where adhesive force balances externally applied mechanical load<sup>175</sup>. How the physical environment regulates bacterial approach and attachment to mammalian cell surfaces has yet to be systematically investigated in context.

The structure and biochemistry of many adhesin-receptor interactions have been well-characterized<sup>159,164,176</sup>. Several studies showed a direct correlation between the molecular adhesin-receptor kinetics and attachment behavior of single bacteria to their target host cell<sup>20,166,167</sup>. In some pathogens, bacteria sequentially deploy multiple adhesins, thereby establishing a multi-step process. For example, *Salmonella* first reversibly attach the Fim adhesin, then irreversibly attach using the type III secretion system<sup>177</sup>. This two-step process involves active deployment of adhesins that also have an impact on host physiology. While the molecular mechanisms of adhesion are clear for specific adhesins, these do not illuminate the general biophysical rules of adhesions to host cells. In particular, it remains complex to decouple adhesive from toxic effects when investigating pathogen adhesion.

To investigate the intrinsic contributions of mechanics in the early steps of bacterial adhesion to host cells, we combined synthetic and biophysical approaches. We fine-tuned adhesion by engineering autotransporters for heterologous inducible display of a synthetic adhesin on a non-pathogenic strain of *E. coli*, targeting an inducible synthetic mammalian cell surface receptor<sup>47</sup>. We found that the specific attachment of bacteria to host cells occurs in two consecutive steps. A first step is non-specific, taking place within the first few seconds following contact. This is followed by the onset of specific adhesion resulting in nearly irreversible attachment on longer timescale. We found that mechanobiological factors of the host cell surface, including membrane mechanics, flow and glycocalyx, regulate each of the adhesion steps. Overall, we show that the biomechanical microenvironment of host tissues strongly regulates the adhesion behavior of bacteria to their target cells, indicating that this process cannot be solely reduced to adhesin-receptor interactions.

## 2.3 SYNTHETIC ADHESION TO CHARACTERIZE BACTERIAL ATTACHMENT TO HOST CELLS.

To systematically probe bacterial adhesion to host cells without relying on virulence factors, we engineered an exogenous adhesin in a non-flagellated *E. coli* and cognate receptor in HeLa cells. As adhesin, we display a tetracycline-inducible anti-GFP nanobody (camelid single-domain variable heavy chain, VHH) using a truncated intimin scaffold<sup>47,158</sup>. The N-terminal domain consists in a beta-barrel associated with the bacterial outer membrane, through which spans an alpha helix displaying the synthetic passenger domain (Figure 8A). Two out of four immunoglobulin-like structures and the lectin-like domain of the passenger domain of wild-type intimin are replaced with an HA tag and VHH domain (Figure 4B)<sup>39,47</sup>. By staining with recombinant GFP and quantifying the fluorescence signal at the surface of single bacteria induced with increasing tetracycline concentrations, we generated titration curves allowing us to fine-tune the density of displayed VHH (Figure 8D, E). To display receptor GFP ligand for the synthetic adhesin at the surface of HeLa, we displayed a doxycycline-inducible GFP fusion to a CD80 receptor anchored in the plasma membrane (Figure 8B)<sup>178</sup>. Direct visualization of the fluorescence signal localized at the cell plasma membrane can confirm and help quantify receptor density (Figure 8F).

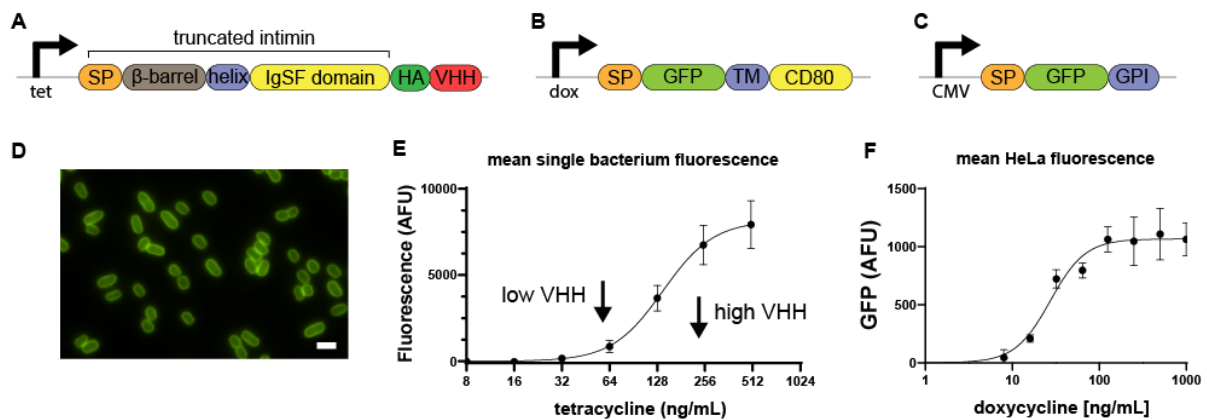


**Figure 8: Synthetic VHH adhesins and GFP receptor constructs.**

(A) Schematic of the VHH display genetic construct. *E. coli* display anti-GFP nanobodies (VHH) based on a tetracycline-inducible promoter (tet) and a truncated intimin that consists in a signal peptide (SP), a beta-barrel anchored in the outer membrane, an alpha-helix crossing the beta-barrel. The scaffold allows the display of an HA epitope tag (HA) and a nanobody anti-GFP (VHH). (B) Schematic of the GFP display construct. GFP was displayed at the surface of mammalian cells by the mean of a doxycycline-inducible promoter, a mammalian signal peptide (SP), and anchored in the plasma membrane with a CD80 transmembrane domain (TM) and its C-terminal cytosolic domain. (C) Schematic of the GFP display genetic construct devoid of cytosolic component. GFP was displayed at the surface of mammalian cells by the mean of a constitutive CMV promoter, an insulin signal peptide (SP), and anchored in the plasma membrane with a CD55 glycosylphosphatidylinositol anchor (GPI). (D) Widefield epifluorescence image of *E. coli* VHH stained with recombinant GFP. Scale bar: 2  $\mu$ m. (E) Tetracycline titration followed by staining with recombinant GFP. Error bars represent standard deviation of triplicate fields of view. The solid line represents a Hill function fit. (F) Doxycycline titration on HeLa

cells stably engineered with a doxycycline-inducible GFP display. Error bars represent standard deviation of triplicate fields. The solid line represents a Hill function fit.

We transiently transfected HeLa displaying CD80-anchored GFP, leading to a heterogeneous population of GFP positive and negative cells. We then mixed in *E. coli* with a high surface density of VHH (*E. coli* VHH) with HeLa GFP whose respective adhesin and receptor were induced separately. After washing, we visualized the co-culture by confocal microscopy. We observed that bacteria bound to GFP-positive HeLa, but not to GFP-negative cells (Figure 9A, B). This indicated that the synthetic system is specific, validating it as a model of bacterial adhesion. As a result, we generated a stable and clonal doxycycline-inducible HeLa GFP-display cell line (HeLa GFP) and grew cultures of this line in microchannels to investigate adhesion in flow conditions. We diluted bacteria in mammalian cell culture medium and loaded them on a syringe pump for flow control. We injected the bacterial suspension in the microchannel covered with HeLa GFP. After one hour under moderate flow, we imaged cells in the channel by confocal microscopy and quantified the number of bacteria per mammalian cell. The bacterial counts per HeLa GFP cell were larger when both constructs were highly induced compared to uninduced or low induction conditions (Figure 9C). Pre-incubation of *E. coli* VHH with recombinant soluble GFP decreased the bacterial count per HeLa GFP back to the non-induced condition (Figure 9C). Therefore, this system yields selective and dose-dependent bacterial adhesion of VHH-displaying bacteria to GFP-displaying HeLa both in static and flow conditions. Our initial characterization overall demonstrates that in tandem, *E. coli* VHH and HeLa GFP represent a realistic, tunable model for specific microbial adhesion to host mammalian cells.

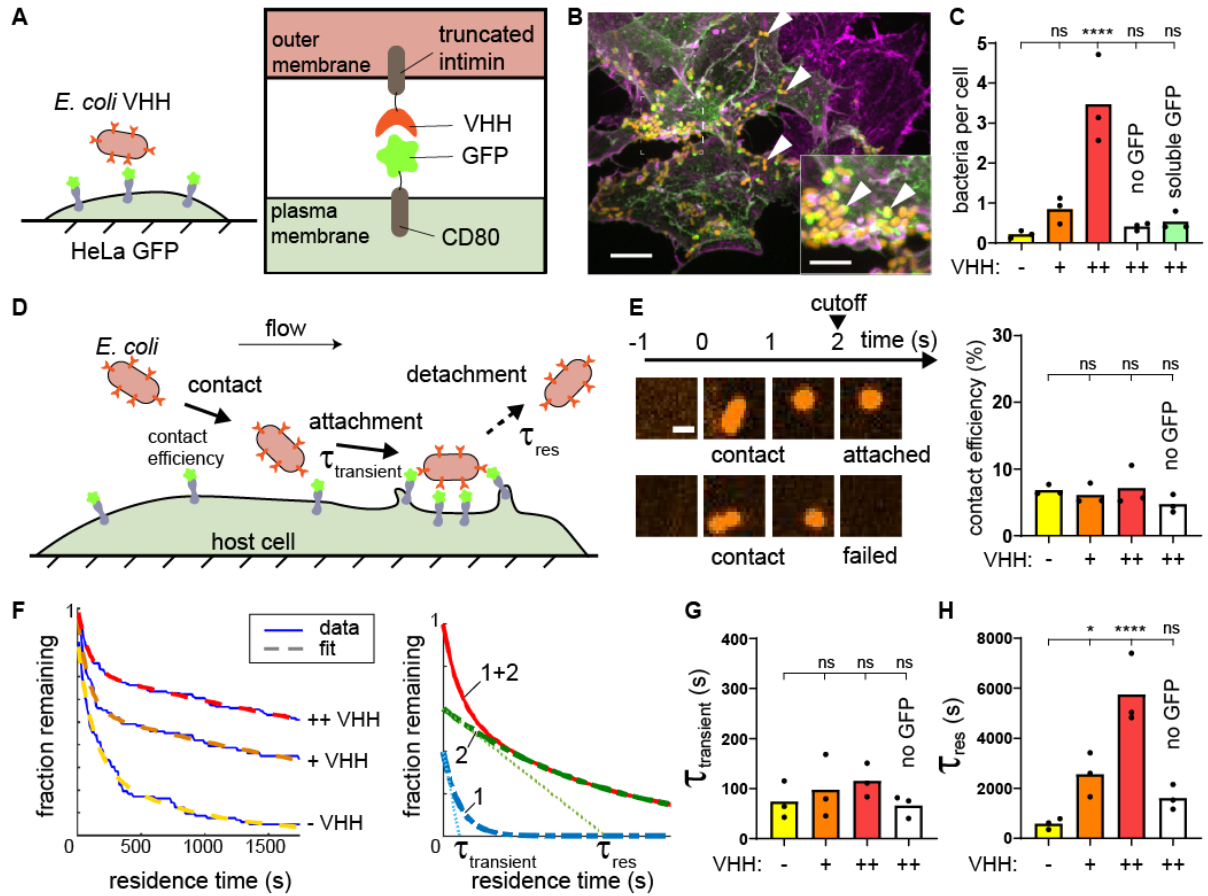


**Figure 9: A synthetic adhesin-receptor system reveals a two-step mechanism of bacterial attachment to host cells.**

(A) Schematic of the synthetic adhesin-receptor system. *E. coli* cells display nanobody targeting GFP (VHH) fused to a truncated intimin autotransporter scaffold. HeLa cells display GFP receptors by fusion with the membrane-anchored CD80 scaffold (HeLa GFP). (B) In a mixed population of GFP+ (green) and GFP- (purple) HeLa cells, *E. coli* (orange, indicated with white arrows) specifically binds to GFP+ cells. Actin stained with phalloidin (purple). Scale bars: 10  $\mu$ m (main) and 5  $\mu$ m (inset). (C) Bacterial count per HeLa cell increases with *E. coli* nanobody density. *E. coli* expressing VHH at low density, or expressing VHH at high density but preincubated with soluble GFP only rarely bind to HeLa cells displaying GFP ("–", "+" and "++" correspond to no- low- and high-VHH induction, respectively). (D) Dynamic visualizations of bacterial adhesion to HeLa cells under flow allows to simultaneously monitor attachment and detachment events at multiple timescales. (E) Bacterial contact efficiency is independent of VHH density and GFP display. High speed confocal imaging at 1 frame per second highlights bacterial populations that detach rapidly after contact. We considered bacteria as attached if they stayed on the HeLa cells surface for more than 2 s. Scale bar 2  $\mu$ m. (F) We constructed residence time distributions using long timescale tracking of attached bacteria (1 h). Bacteria adhering during the first 30 min were followed for 30 supplementary min in order to avoid artificial cropping of the data (see material and methods). Bare *E. coli* and *E. coli* displaying low and high VHH levels have largely different residence time distributions. We fit these distributions using the sum of two exponentials highlight two characteristic timescales  $\tau_{\text{transient}}$  and  $\tau_{\text{res}}$  (right illustrative graph). The single exponentials are shown in dashed green and blue and their sum is the continuous red line. (G) The model parameter  $\tau_{\text{transient}}$  is independent of the adhesin displayed. (H) In contrast, the characteristic residence time  $\tau_{\text{res}}$  increases with nanobody density. Statistical tests: one-way ANOVA followed by Dunnett's post hoc test (\*\*\*\*  $P < 10^{-4}$ , \*  $P < 0.05$ ).

## 2.4 BACTERIA ATTACH TO HOST CELLS IN TWO SUCCESSIVE STEPS.

Our initial results showed that the number of bacteria attached to host cells depends on the induction levels of both VHH adhesin and GFP receptor (Figure 9B, C). We wondered whether this was due to changes in the number of bacteria attaching or detaching from the host cell surface (Figure 9D). This question motivated us to inspect the dynamics of attachment to HeLa cells at the single bacterium level. We tracked attachment and detachment of single bacteria over the course of 1 h (Movie S1). These visualizations helped us identify two classes of attachment behaviors. First, a large proportion of bacteria were only visible on single frames, indicating that they were in contact with the membrane for a few seconds. Another population of cells stayed attached for much longer times. We were intrigued by this dichotomy in adhesion behaviors and performed multiscale imaging to characterize each step.

To inspect short timescale attachment events, we performed fast confocal imaging of attachment (1 frame per second). We found that a large proportion of bacteria only stayed on the membrane for about two seconds (one or two frames, Movie S2). We then quantified the proportion of bacteria that attached to the host surface for more than two seconds relative to the total number of contacts, which we call contact efficiency (Figure 9E). We found that the contact efficiency was in average only 7% when both VHH and GFP were induced. We then compared this contact efficiency between adhesin-receptor conditions. Surprisingly, we found that neither the presence of VHH adhesins nor of GFP receptors influenced the contact efficiency (Figure 9E). This suggests that this early stage is not specific.

We thus speculated that the adhesin-receptor interactions regulate bacterial attachment on a longer timescale. To test this hypothesis, we timed single bacteria residing the surface of host cells during a 1 hour-long movie (Movie S1). We thus built inverse cumulative residence time distributions (Figure 9F). We found that these distributions had exponential-like decays, which we could fit to the sum of two exponential functions (Figure 9F and Material and methods 1). This highlighted two characteristic timescales over which bacteria detached from the surface. The shortest timescale is on the order of 100 seconds, and was nearly identical between conditions (Figure 9G). The longest timescale  $\tau_{\text{res}}$ , associated with the second exponential, showed large variations between VHH or GFP configurations (Figure 9H). We measured a 10-fold increase in  $\tau_{\text{res}}$  when bacteria displayed a high VHH density compared to bacteria displaying an empty intimin scaffold (no VHH). In addition, we measured a 3.5-fold decrease when we did not induce GFP on HeLa cells. These results implicate that adhesin-receptor interactions only materialize over minutes. As a comparison to typical association rates, we estimated the on- and off-rates of adhesin-ligand based on known kinetics constants of VHH-GFP<sup>179</sup>. The off-rate of VHH reflects a characteristic time of 6900 s, which is of the same order

of magnitude as our  $\tau_{\text{res}}$  measurements. For an arbitrary GFP concentration of 1  $\mu\text{M}$ , the on-rate yields a reaction time on the order of 1 s, two order of magnitude shorter than our measurements. This suggests that other factors mediate the first adhesion step, before adhesins engage with their ligand. In summary, we highlighted that bacteria specifically attach to host cells by going through an initial non-specific attachment followed by adhesin-receptor docking, thereby promoting long lasting physical contact.

We then tested the contributions of biochemical properties of the adhesin in regulating attachment. We swapped the adhesin to two other VHH sequences coding for anti-GFP nanobodies of different affinities ( $K_D$ ) and kinetic rates ( $k_{\text{on}}$  and  $k_{\text{off}}$ )<sup>180</sup>. We checked that their expression levels were unaffected using anti-HA FITC-labeled antibodies (Figure 10A-Ci). We first verified that the fusion to intimin did not affect  $K_D$ . Titrating these alternate VHH forms on *E. coli* with GFP yielded  $K_D$  matching their *in vitro* measurements performed with soluble recombinant proteins (Figure 10A-Cii,iii)<sup>179,180</sup>. We thus performed adhesion experiments on HeLa GFP under flow with *E. coli* expressing the alternate VHH forms. We observed a slight positive correlation between bacterial load per HeLa and VHH affinity across three orders of magnitude of  $K_D$  and two order of magnitude of  $k_{\text{off}}$  (Figure 10A-D). Consistent with its non-specific nature, the contact efficiency was independent of the affinity of the nanobody to GFP (Figure 10E). On the longer timescale, we measured higher  $\tau_{\text{res}}$  and a statistically significant increase in the pre-exponential factor  $C_{\text{res}}$  at higher affinities (Figure 10F, G), explaining the differences in the bacterial load. Altogether, the dependence of the specific adhesion step on adhesin biochemistry was surprisingly weak compared to the changes induced by adhesin expression levels (Figure 9H and Figure 10F).

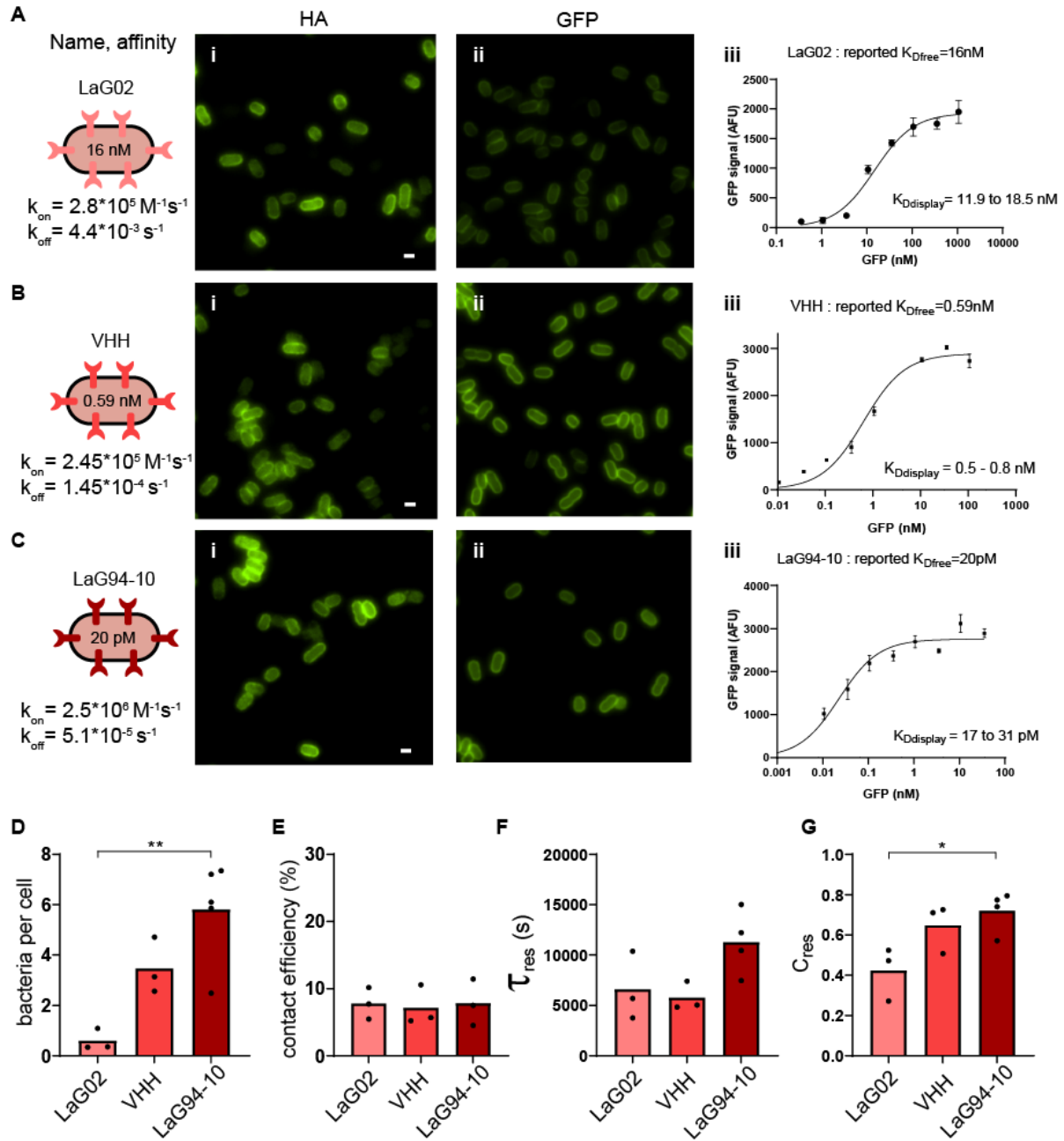


**Figure 10: Functional validation and bacterial attachment as a function of VHH affinity to GFP.**

(A-C) We displayed and compared VHH with two different anti-GFP nanobodies (LaG02 and LaG94-10) at the surface of *E. coli*. These have distinct biochemical properties including affinity ( $K_D$ ), on- and off-rates. (i) The level of expression was measured by HA staining. Scale bar: 1  $\mu\text{m}$ . (ii) Their functionality was then assessed by staining with excess amount of recombinant GFP. (iii) By titrating with recombinant GFP, we could determine the  $K_D$  of displayed nanobodies. These remain in the range of the published values obtained with soluble recombinant nanobodies. Bacteria were induced with 250 ng/mL tetracycline overnight prior to staining. Error bars represent standard deviation of triplicate fields. The solid line represents a function fit as described in supplementary methods. Image intensity scale is identical between samples. (D) Final *E. coli*-nanobody count per HeLa cell positively correlates with nanobody affinity in flow. Nanobody display induction level is high. (E) The contact efficiency does not depend on the nanobody affinity to GFP. (F) Comparison of the characteristic residence time  $\tau_{res}$  as a function of nanobody affinity. An outlier of value 775,000 s was excluded from further analysis. (G) Higher affinity increases the proportion of bacteria irreversibly binding to cells. Statistical tests: one-way ANOVA followed by Tukey post hoc test (\*\*  $P < 0.01$ , \*  $P < 0.05$ ).

## 2.5 BACTERIA ATTACH TO ABIOTIC SURFACES IN A SINGLE SPECIFIC STEP

We suspected that the complex of physical microenvironment the host cell membrane plays a role in either of the two successive steps of attachment. To provide additional insights on these factors, we compared the specific adhesion of *E. coli* to the surface of an abiotic material with the one on mammalian cells. We engineered specific adhesion to glass by conjugating receptors to a coverslip substrate. We conjugated N-terminally His-tagged recombinant GFP to nitrilotriacetic acid (Ni-NTA) functionalized glass, on which we bonded elastomeric microfluidic channels (see material and methods). We monitored the dynamics of specific adhesion to abiotic surface by flowing a bacterial suspension in the GFP-coated microchannel. We observed bacteria almost exclusively attaching to the GFP-coated areas, thereby validating adhesion specificity (Figure 11A-C and Movie S3). These experiments highlighted a blatant difference with mammalian cells: there were ten times more bacteria attached to the GFP-coated glass surface than on HeLa cells (Figure 12A, B). This difference was strictly dependent on VHH-GFP interactions as bacteria only sparsely attached to untreated glass, or to glass coated with mKate2, a red fluorescent protein that does not bind VHH (Figure 11D).

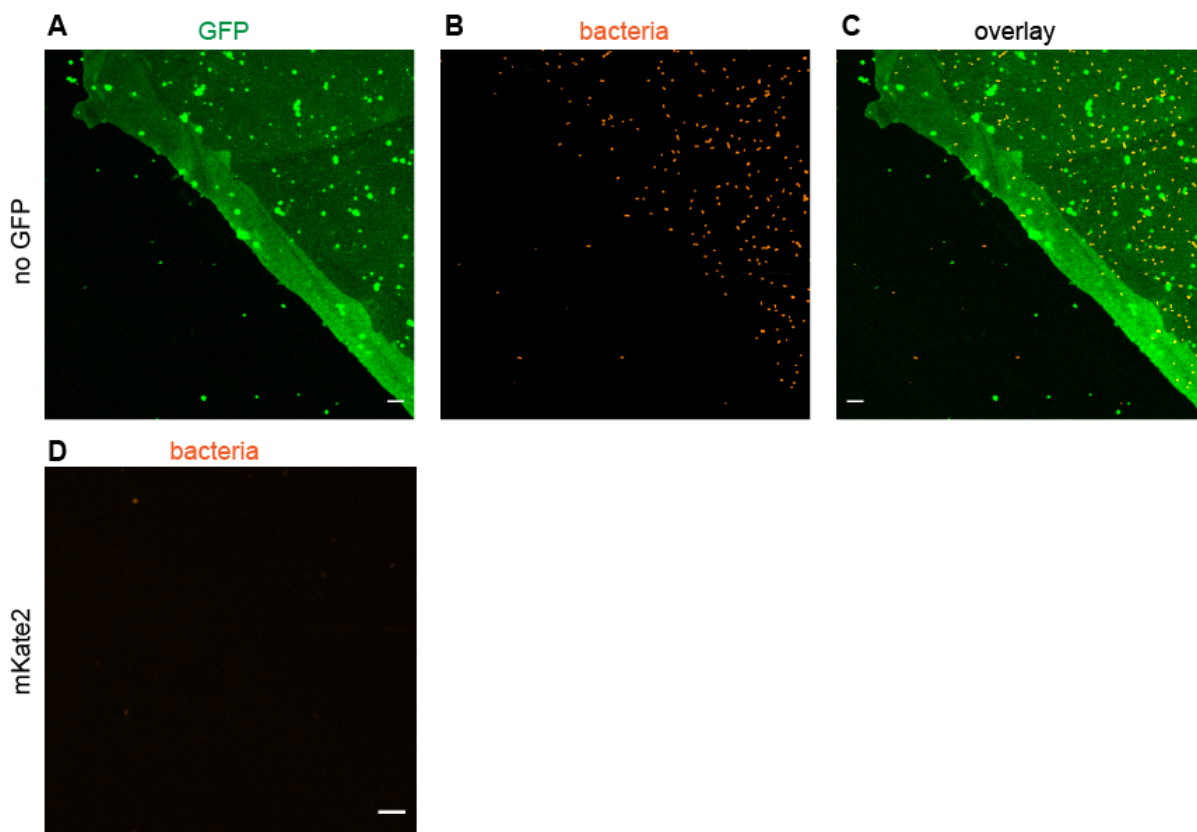


**Figure 11: Specificity of adhesion of *E. coli*-VHH to GFP-coated glass coverslips.**

(A) Microscopy image of the edge of a GFP-coated region on the coverslip. (B) Maximum intensity projection of the corresponding field showing bacterial attachment (red) after 10 min in flow. (C) Overlay of (A) and (B). (D) Maximum intensity projection of *E. coli* VHH (red) after 60 min in flow on mKate2-coated coverslips. Scale bars: 10  $\mu\text{m}$ .

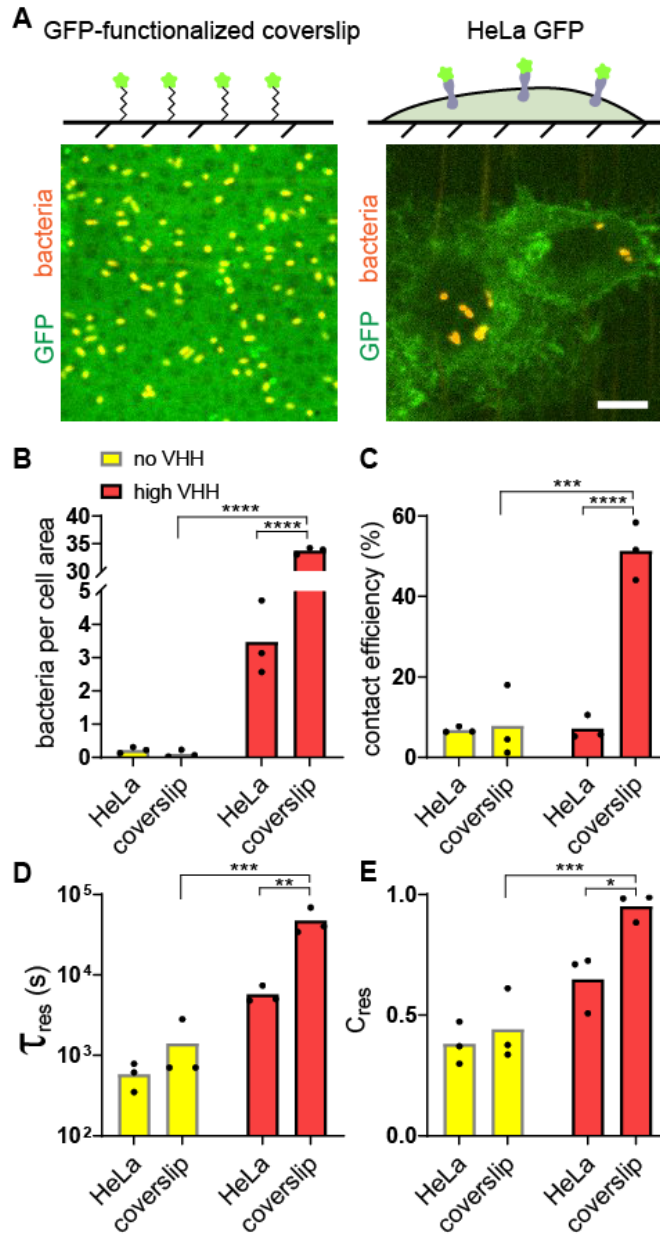


**Figure 12: Attachment of bacteria to abiotic surface is a single step process.**

(A) (Top) Controlled GFP-functionalized coverslips permits visualization of specific adhesion to hard, abiotic surface and quantitative comparison with adhesion to mammalian cells. (Bottom) Representative confocal microscopy images of bacterial binding to GFP-coated coverslips (left) and HeLa-GFP (right). Scale bar: 10  $\mu$ m. (B) Final bacterial count per cell area is about 10-fold larger on GFP-coated coverslips than HeLa cells in the presence of VHH. (C) Bacterial contact efficiency is higher on GFP-coated coverslips than HeLa cells in the presence of VHH. (D) The characteristic residence time  $\tau_{res}$  shows the VHH-dependent binding to coverslips is stronger than to HeLa cells. (E) Relative contribution of short and long timescale exponential fits shows that 95% of *E. coli* VHH strongly bind to GFP-coated coverslips. Statistical tests: two-way ANOVA and Sidak post-hoc test (\*\*\*\*  $P < 10^{-4}$ , \*\*\*  $P < 0.001$ , \*\*  $P < 0.01$ , \*  $P < 0.05$ ).

To further characterize the pronounced difference in adhesion between abiotic and biotic surfaces, we focused on attachment/detachment dynamics. We compared the early contact efficiencies and residence times of bacteria on glass with the ones on HeLa cells. First, we found that about 50% of *E. coli* VHH stayed attached to the GFP-coated glass surface upon initial contact, in contrast with the 7% of bacteria remaining on HeLa GFP cells (Figure 12C). This largely contributed to the differences in bacterial accumulation at the end of the experiment. In addition, the characteristic residence time of *E. coli* VHH on glass was more than eight times longer than on HeLa (Figure 12D). This characteristic time was also much longer than the duration of our visualizations so that most bacteria can be considered irreversibly attached to glass. Finally, on the longer timescale, very few bacteria transiently bound to coverslips, as highlighted by the relative contribution of  $\tau_{\text{transient}}$  (Figure 12E). This further supports a scenario where adhesin and receptor engage rapidly and efficiently when an abiotic surface supports the receptors.

In summary, specific adhesion to an abiotic surface is controlled by early attachment events within the first few seconds of surface encounter, consistent with *in vitro* reaction rates. Successful attachment beyond this step leads to nearly irreversible surface association. Thus, a single specific step mediates attachment on abiotic surfaces, while phenomena at both short and long timescales regulate specific attachment to host cells.

## 2.6 HOST CELL MEMBRANE MECHANICS REGULATE BACTERIAL ADHESION

Given the differences in material properties between inert and living substrates, we hypothesized that the mechanical microenvironment of host cells may play a key role in regulating attachment. Following this intuition, we investigated the role of cells mechanics in the process of adhesion to host cells. Host cell mechanics depend on the intrinsic membrane bilayer properties but also on emergent properties provided by the actin cytoskeleton.

We observed that bacteria attached to HeLa accumulate GFP at their surface, as if they were embedded into membrane invaginations (Figure 13Ai-ii). Given the role of the cytoskeleton in the shape and mechanics of eukaryotic cell membranes, we hypothesized that actin could play a role in bacterial attachment. To first explore this possibility, we visualized the actin cytoskeleton of bacteria-bound cells using fluorescent phalloidin staining. The actin density increased around individual attached bacteria, indicating a potential morphological remodeling of the membrane upon attachment (Figure 13Aiii-iv). Our GFP display construct is based on a truncation of the CD80 receptor that is overexpressed in macrophages with notoriously increased actin remodeling. To exclude the possibility that remodeling is an artefact of the C-

terminal CD80 anchor, we fused GFP to a glycosylphosphatidylinositol (GPI) membrane anchor devoid of cytosolic signaling components (Figure 8C)<sup>181</sup>. There, we could also observe a similar actin remodeling and membrane surrounding bacteria (Figure 13B and Figure 14A, B). The membrane remodeling occurred within minutes, on a similar timescale as the GFP uptake (Movie S4, S5, Figure 14C, D). Actin-dependent membrane remodeling could thus increase the contact area between bacteria and host cell, stimulating adhesin-receptor interactions and consequently increasing adhesion strength.

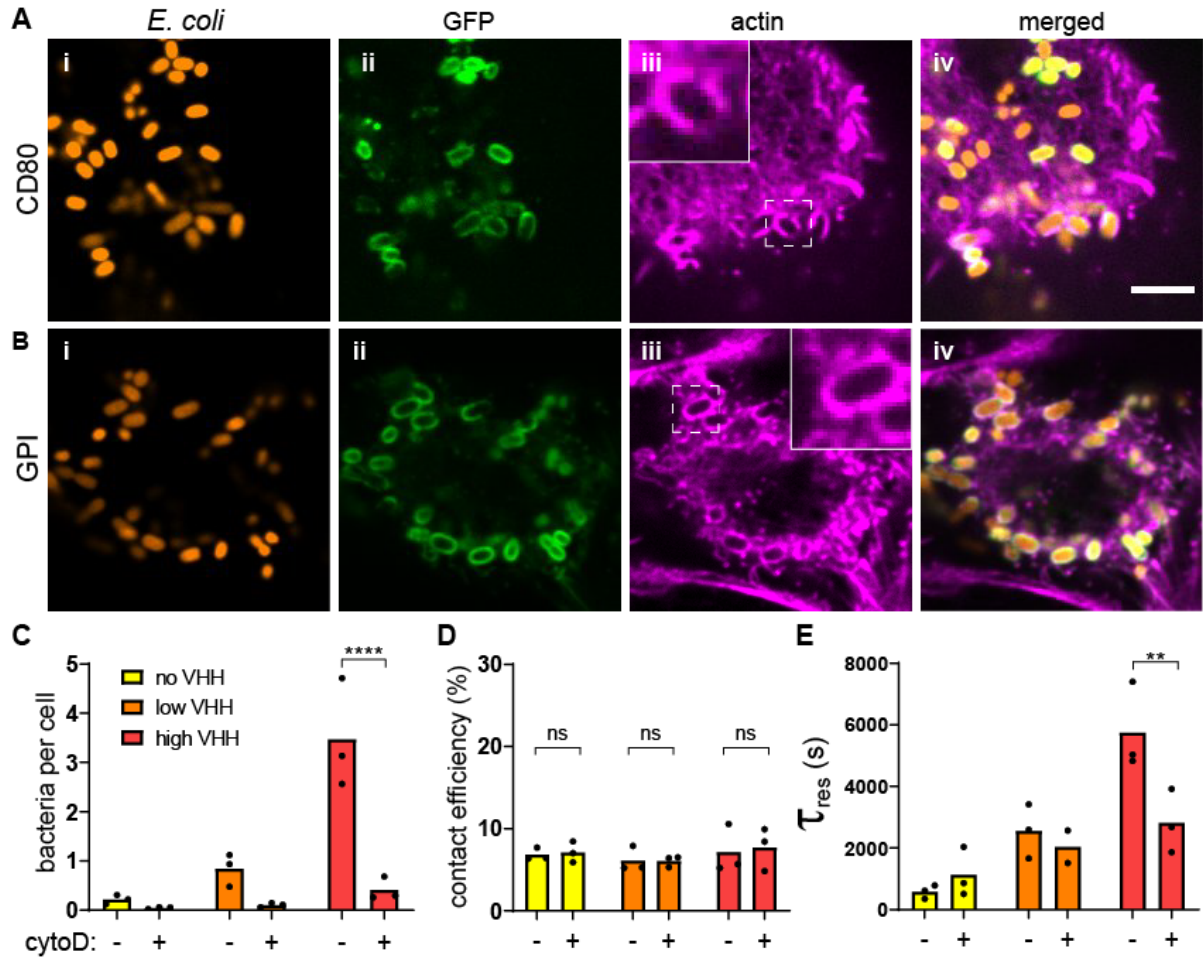


**Figure 13: Regulation of bacterial adhesion by host cytoskeleton.**

(A) Actin rearranges around attached bacteria. After static incubation with *E. coli* VHH (orange), HeLa cells displaying GFP with a CD80 anchor (green) were stained for actin (purple). Scale bar: 5  $\mu$ m. (B) Bacteria promote actin embeddings in the absence of any cytosolic component in the mammalian cell. After static co-culture with *E. coli* VHH (red), HeLa cells displaying GFP with a glycosylphosphatidylinositol (GPI), which does not harbor any cytosolic signaling domain, also shows strong actin remodeling around attached bacteria. (C) HeLa cells treatment with the actin polymerization inhibitor cytochalasin D (cytoD) reduces the bacterial count per HeLa cells. (D) Bacterial contact efficiency is independent of actin polymerization. (E) The characteristic residence time  $\tau_{res}$  decreases in the presence of cytochalasin D at high VHH density. Statistical tests: two-way ANOVA and Sidak post-hoc test (\*\*\*\*  $P < 10^{-4}$ , \*\*  $P < 0.01$ ).

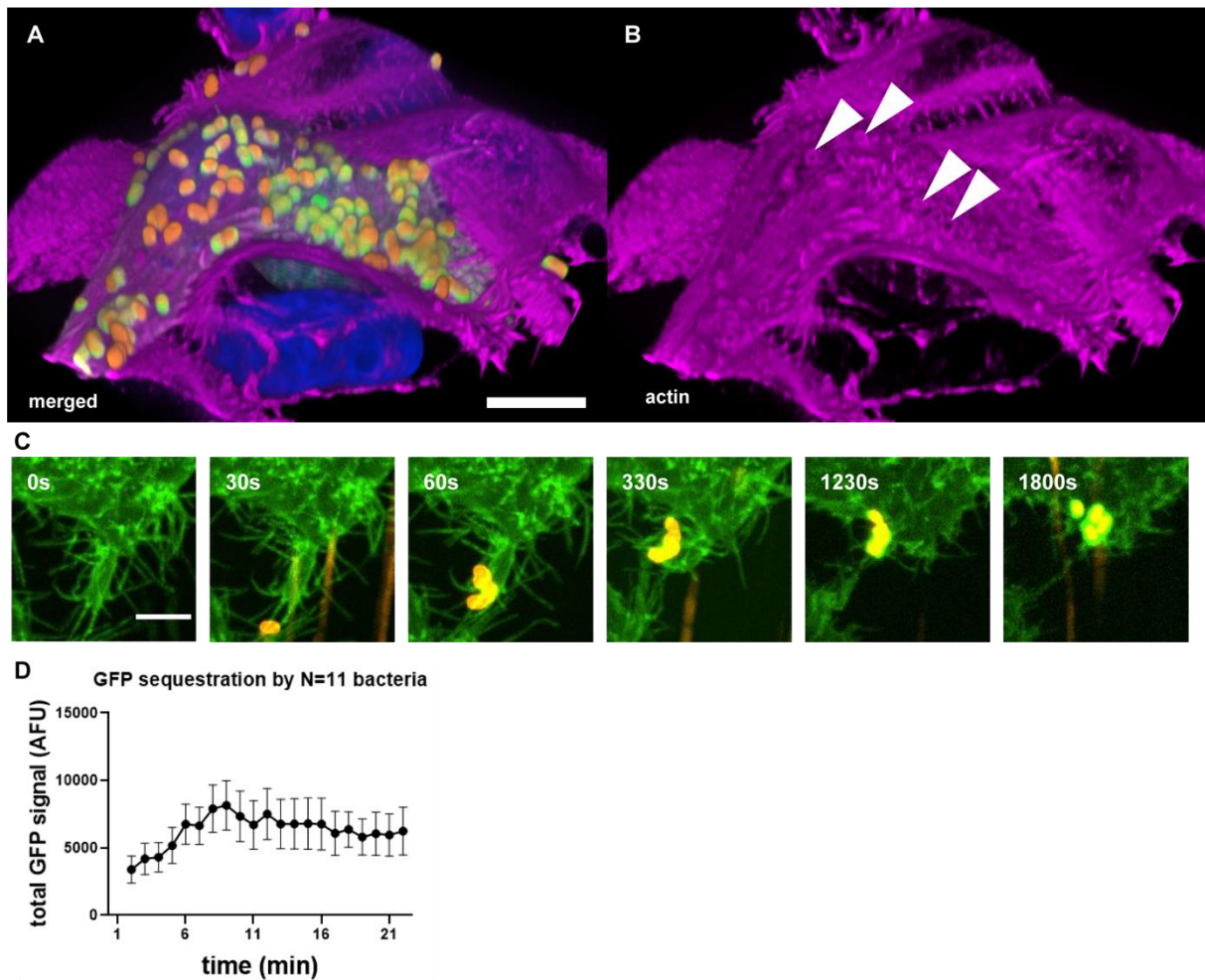


**Figure 14: HeLa cells actively remodel plasma membrane around bacteria.**

(A, B) Merged 3D visualization of a confocal Z-stack After 1h of *E. coli* VHH (red), HeLa cells displaying GFP with a GPI anchor (green) in static co-culture. Actin was stained with phalloidin (pink) and nuclei with DAPI (blue). Events of actin remodeling are indicated by white arrows in (B). Scale bar: 10  $\mu\text{m}$ . (C) HeLa GFP (CD80) cells actively pull bacteria towards their cell body. Maximum intensity projection of a confocal time-lapse experiment of *E. coli* VHH (red), HeLa GFP (green) and flow. Corresponds to supplementary movie S4. Scale bar: 5  $\mu\text{m}$ . (D) Bacteria sequester GFP within minutes in static conditions. Quantification of the mean fluorescence of N = 11 bacteria in supplementary movie S5. Error bars represent the standard error.

We further tested the role of membrane remodeling in bacterial attachment by employing cytochalasin D (cytoD), a drug inhibiting actin polymerization<sup>182</sup>. We measured an 8-fold reduction in *E. coli* VHH attachment on treated cells compared to the untreated control (Figure 13C). Inhibiting actin polymerization did not decrease the contact efficiency of bacteria at early timescales (Figure 13D). However, bacterial residence time was decreased in presence of the drug (Figure 13E). This difference was most dramatic for higher VHH densities. This suggests that membrane remodeling upon attachment takes place on the minute timescale, thereby stabilizing adhesin-receptor interactions.

## 2.7 THE GLYCOLALYX SHIELDS THE HOST FROM RECEPTOR-SPECIFIC BACTERIAL ADHESION

Membrane mechanics regulate how bacteria engage in specific adhesion to hosts cell on timescales of minutes. Still, membrane mechanical properties had little effect on the non-specific adhesion step, which differed so much between glass and cells, as the contact efficiencies upon membrane and cytoskeletal perturbations remained below 10% (Figure 13D). We thus still wondered why such a small proportion of bacteria could commit to specific adhesion upon encountering the host cell surface.

We reasoned that other mechanical components of the host cell surface could play a role in limiting bacterial adhesion. We thus hypothesized that the glycocalyx, a dense layer of glycoproteins and glycolipids that decorates the surface of most mammalian cells, could limit attachment. To test this, we investigated the role of the host glycocalyx in the dynamics of bacterial adhesion. We cultured HeLa GFP cells with a deglycosylating mix of enzymes, thereby promoting its degradation (Figure 15A)<sup>183,184</sup>. We confirmed specific enzymatic activity in mammalian medium by digesting fetuin, a N- and O-glycosylated control protein (Figure 16A). We also stained HeLa cells with rhodamine-labelled wheat germ agglutinin and observed a decrease in fluorescence in cells treated with the deglycosylating mix of enzymes (Figure 16B). We then tracked bacterial adhesion dynamics at the surface of deglycosylated HeLa cells, which showed a dramatic effect. First, there was six times more bacteria attached to deglycosylated cells compared to their native, untreated state (Figure 15B). The bacterial density on deglycosylated cells reached values close to the ones measured on glass (Figure 15B). We further examined the specific contributions of the glycocalyx in attachment dynamics by comparing contact efficiency and residence time distributions to the native state. Consistent with our hypothesis, we found that bacteria remained attached twice as efficiently to deglycosylated cells compared to untreated cells in a VHH-dependent manner (Figure 15C). Deglycosylation only slightly increased the characteristic residence time, both in the presence and absence of VHH (Figure 15D). Altogether, our data indicates that the mammalian glycocalyx shields the host cell membrane from direct engagement of bacterial adhesins to target receptors, thereby non-specifically limiting bacterial attachment.

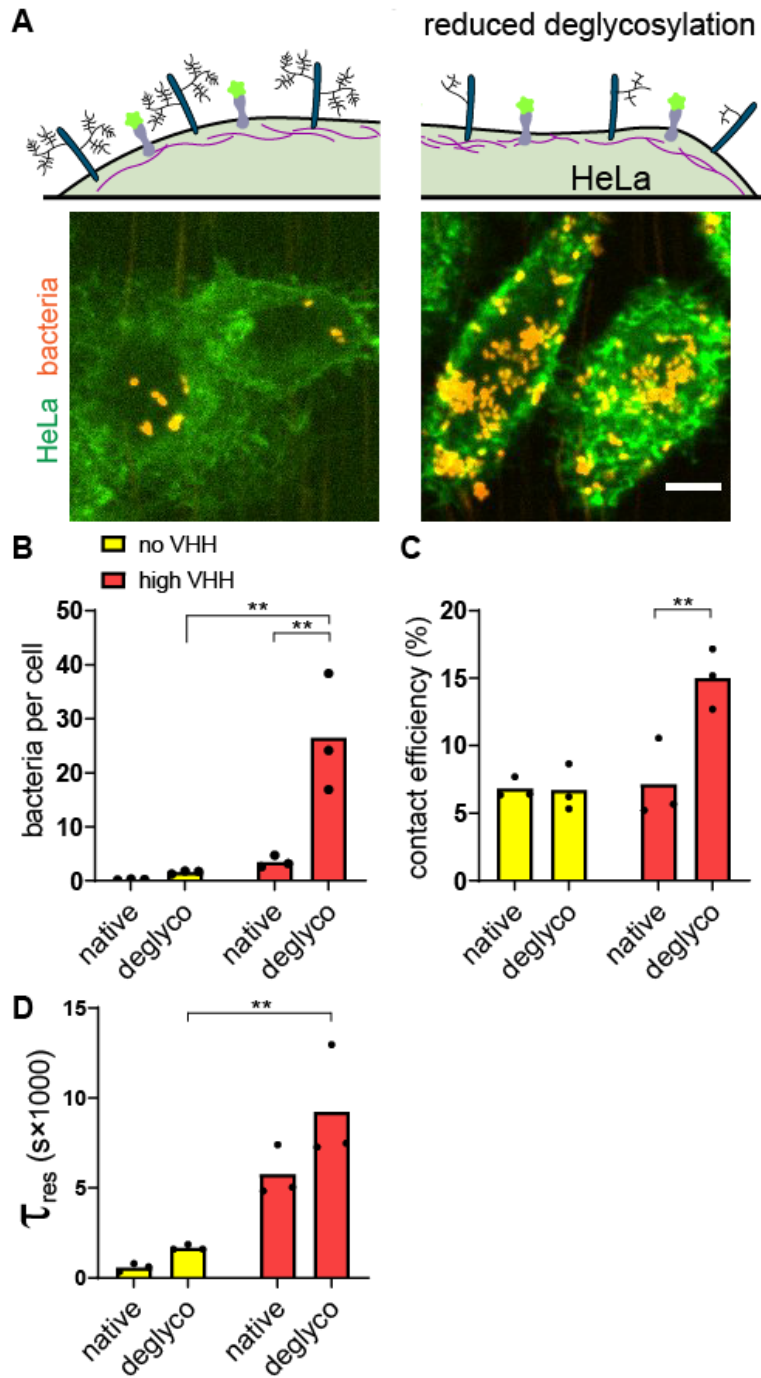


**Figure 15: The membrane glycocalyx inhibits bacterial attachment.**

(A) Enzymatic deglycosylation of HeLa cells surface proteins increases bacterial binding. The right image shows two deglycosylated HeLa cells covered by *E. coli* VHH while the negative control in otherwise identical conditions has low bacterial count. Scale bar: 10  $\mu$ m. (B-D) Comparison of bacterial adhesion dynamics between untreated cells (native) and deglycosylated cells (deglyco). (B) Final *E. coli* VHH count per HeLa cell is higher in deglycosylated cells. (C) Glycocalyx removal increases the contact efficiency of *E. coli* VHH. (D) Comparison of the characteristic residence time  $\tau_{res}$  with or without deglycosylation mix. Statistical tests: two-way ANOVA and Sidak post-hoc test. (\*\*  $P < 0.01$ ).

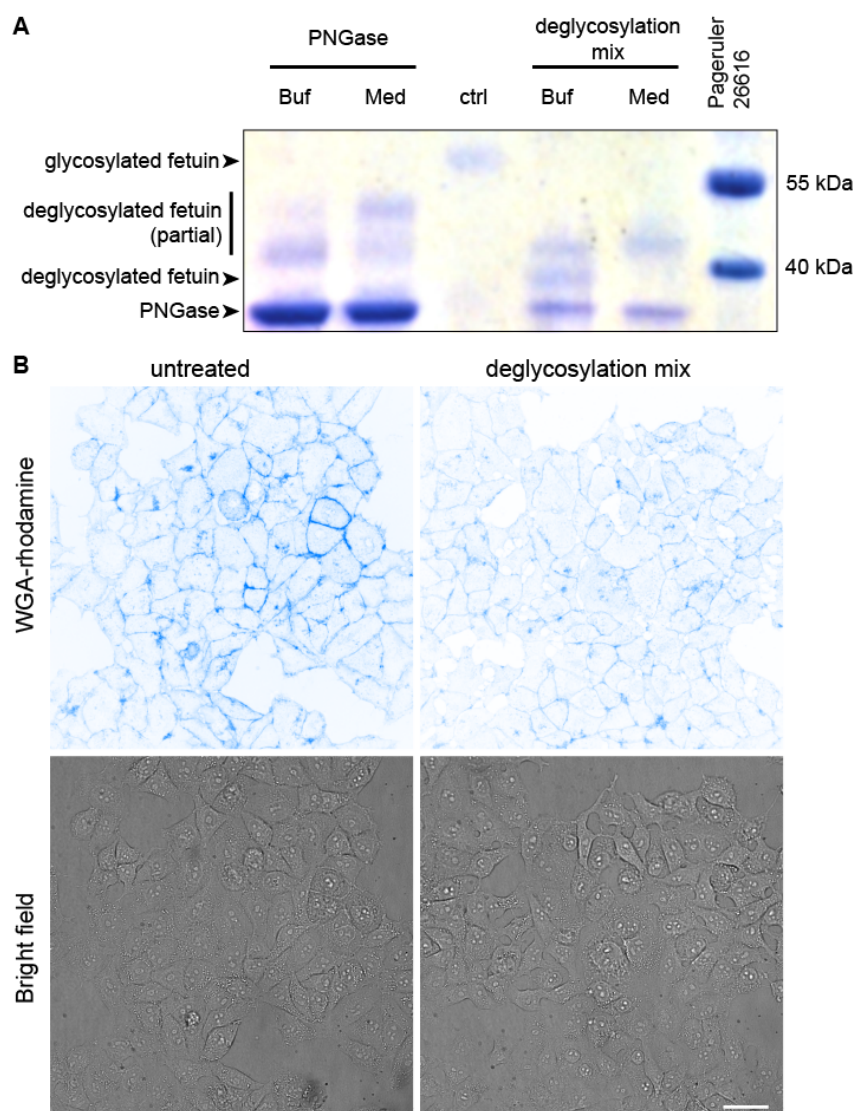


**Figure 16: Deglycosylation activity in mammalian cell culture medium.**

(A) SDS-PAGE gel showing 10  $\mu$ g of fetuin incubated overnight at 37°C in 20  $\mu$ L with either only PNGase or the deglycosylation mix of enzymes targeting N- and O-glycosylated proteins in either the non-denaturing buffer provided by the supplier (Buf) or Fluorobrite medium (Med) supplemented with glutamax. The gel indicates partial deglycosylation of fetuin in mammalian cell culture conditions compared to untreated fetuin (ctrl) and compared to ideal buffer conditions. (B) Live HeLa cells treated with the deglycosylation mix of enzymes show a reduction in N-acetyl glucosamine staining with wheat germ agglutinin (WGA). For WGA, we display inverted pictures of maximum intensity projection from confocal stacks. Scale bar: 40  $\mu$ m.

Since our system uses a truncated intimin, we generated a full-length fusion to test whether an extended scaffold could help overcome the glycocalyx. Bacterial load per cell decreased for the extended linker, as a result of a decrease in the characteristic residence time (Figure 17A, B), but had surprisingly no effect on contact efficiency (Figure 17C). One explanation for this would be that the longer linker would directly be responsible for the decrease in the characteristic residence. Alternatively, the fusion could be expressed to different levels,

causing a change in the second step (Figure 9H). Staining the extended intimin-VHH fusion with recombinant eGFP showed a 2.5-fold reduction in GFP signal compared to the truncated form, indicating that reduced expression participates in shortening residence time and weakening adhesion (Figure 17D, E). In summary, longer linkers as few nanometer-long do not help overcome the glycocalyx barrier.

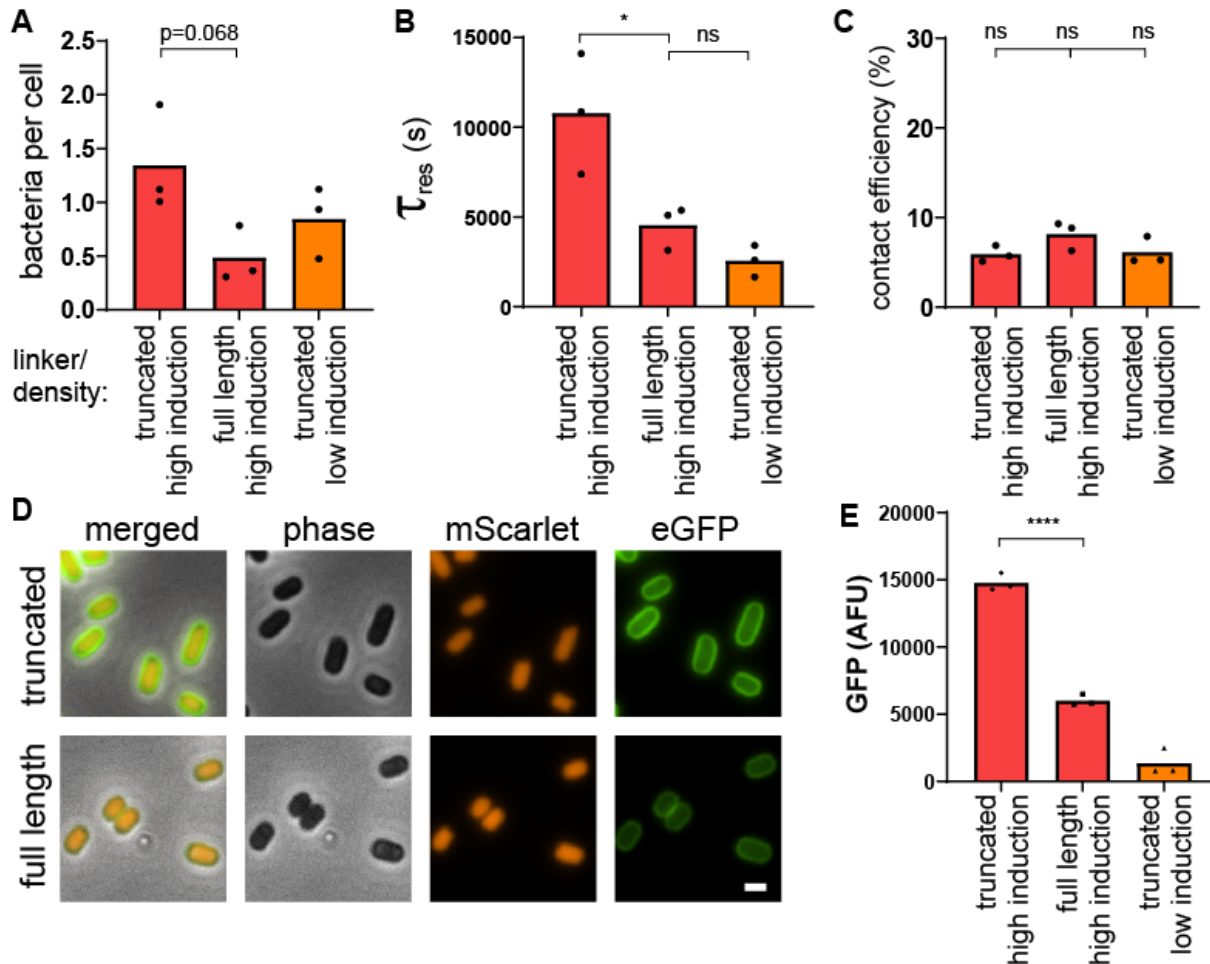


**Figure 17: Longer VHH linker does not improve binding in flow.**

(A) Final *E. coli* VHH count per HeLa cell is reduced with full-length intimin compared to truncated intimin at high and low level of induction. (B) The characteristic residence time is reduced with full-length intimin at high level of induction. (C) Linker size does not affect the contact efficiency. (D-E) Staining of “high VHH” bacteria using recombinant eGFP highlights a 2.5-fold decrease in the surface display efficiency. Statistical tests: one-way ANOVA and Tukey post hoc test (\*  $P < 0.05$ ; \*\*\*\*  $P < 10^{-4}$ ).

## 2.8 FLAGELLA AND FLOW COUNTERACT THE GLYCOCALYX SHIELD

Beyond simple short-range adhesins such as the ones belonging to the class of autotransporters, bacteria often display surface extensions such as flagella and fimbriae, sometimes capped with adhesins. These extended structures could help overcome the physical glycocalyx barrier by reaching through, thereby promoting the first step of adhesion.

We thus explored how surface filaments could play a role in the early adhesion step. We first compared the binding of flagellated and non-flagellated bacteria to HeLa GFP. We could not distinguish the bacterial numbers between flagellated and non-flagellated strains at the end of the experiments (Supplementary table 4). However, the details of attachment dynamics revealed that the flagellum mediates a tradeoff between non-specific and specific adhesion. On the one hand, we observed that flagellated *E. coli* have higher contact efficiency (Figure 18A). This shows that flagella promote short timescale non-specific attachment. On the other hand, the characteristic residence time of flagellated *E. coli* was more than twice shorter than its non-flagellated counterpart (Figure 18B). Consistent with this, the transient characteristic residence time was similar between conditions but the pre-exponent factor  $C_{res}$  had significantly decreased weight in our exponential fits, reflecting a high number of bacteria transiently binding and fewer bacteria strongly binding (Figure 18C and Movie S6). Altogether, flagella mediate a tradeoff in adhesion, increasing early commitment while decreasing subsequent specific attachment.

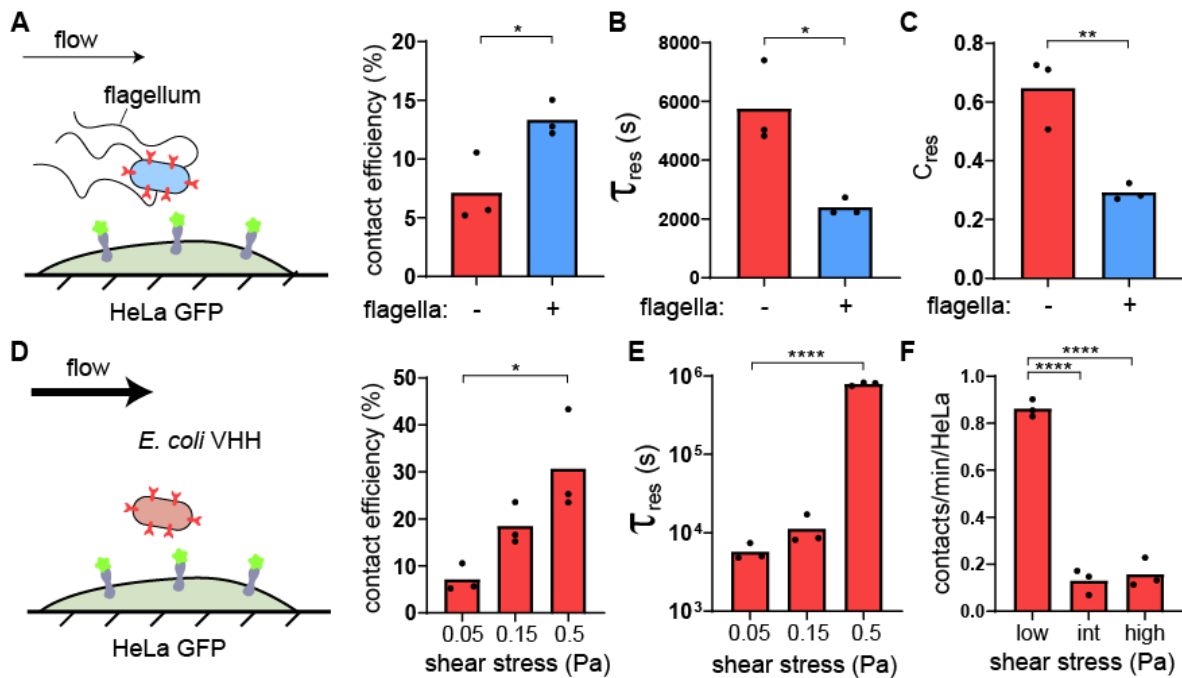


**Figure 18: Flagella and flow attenuate the glycocalyx shield.**

(A) Schematic of the experimental setup. Flagellated *E. coli* VHH (blue) were compared to non-flagellated *E. coli* VHH (“+” and “-”, respectively). *E. coli* VHH contact efficiency is increased in the presence of flagellum in flow. (B) The presence of flagella decreases the characteristic residence time in flow. (C) Comparison of the pre-exponential factor of the characteristic transient binding time  $\tau_{transient}$  in the presence or absence of flagella shows that the proportion of bacteria strongly binding to HeLa GFP is lower with flagella. (D) Schematic of the experimental setup. We measured the attachment dynamics of *E. coli* VHH in increasing shear stresses. Bacterial contact efficiency increases with flow intensity. (E) The characteristic residence time  $\tau_{res}$  increases with flow intensity. (F) Strong flows decrease the contact frequency despite a higher number of bacteria crossing the channel. Statistical tests for (A-C): two-tailed unpaired t-test (\*\*  $P < 0.01$ , \*  $P < 0.05$ ). Statistical tests for (D-F): one-way ANOVA and Tukey post hoc test (\*  $P < 0.05$ , \*\*\*\*  $P < 10^{-4}$ ).

Finally, we wondered whether fluid flow could balance the effect of the glycocalyx. Typically, hydrodynamic forces positively select for single bacteria whose adhesion force exceeds shear force. In the context of adhesion to host cells and based on molecular dynamic simulations, we suspected that flow could generate a shear force that deforms the ~100 nm thick glycoprotein layer, thereby reducing shielding<sup>13</sup>. Given these two flow-induced effects are antagonistic, we wondered how their combined contributions would ultimately affect bacterial attachment. We thus performed adhesion experiments of *E. coli* VHH to HeLa GFP at three different flow regimes. We applied flow rates that generated shear stress of 0.05, 0.15 and 0.5 Pa at the channel centerline. These stresses respectively generate 0.1, 0.3 and 1 pN hydrodynamic forces on single bacteria (assuming a bacterium is 2  $\mu\text{m}$  long, 1  $\mu\text{m}$  wide)<sup>185</sup>. We measured contact efficiency and residence times, which are normalized metrics, that is they do not depend on the influx of bacteria in the channel.

The contact efficiencies increased with shear stress, from 7% at low shear up to 31% at high shear (Figure 18D). This indicates that flow promotes the non-specific adhesion within the few seconds after contact. On the timescale of minutes where adhesins engage to their GFP receptors, the characteristic residence times of bacteria increased strongly with shear stress, up to two orders of magnitude (Figure 18E). Despite longer residence time and higher contact efficiency in strong flow, we could not measure clear changes in absolute bacterial load per HeLa cell compared to weaker flows (Supplementary table 4). We could attribute this to an unexpected decrease in the absolute number of bacterial contacts per mammalian cells with increasing flows, indicating that bacteria are less likely to encounter the host cells membrane under strong shear (Figure 18F). Altogether, our results suggest that higher flows improve bacterial attachment in two ways. First, stronger flow promotes early attachment by counteracting the glycocalyx. Second, increased flow further engages adhesins to their receptors.

## 2.9 DISCUSSION

### 2.9.1 Context

To infect or stably colonize their hosts, bacterial pathogens and commensals attach to the surface of biological tissues<sup>186</sup>. Adhesins are the major ingredient of bacterial adhesion *in vivo*. By binding to target receptor moieties at the surface of host cells, they confer strong attachment and specificity. We investigated how bacteria adhere to host cells by leveraging a tunable synthetic system comprising an adhesin (VHH) and a receptor (GFP). This system had been

engineered for therapeutic VHH library screening and has been applied to synthetic multicellular self-organization of bacterial populations<sup>47,158</sup>. We here repurposed it to investigate bacterial attachment to host cells while controlling adhesin expression and binding strength without affecting host viability.

## 2.9.2 Two steps adhesion to mammalian cells

We leveraged the versatility of the VHH-GFP system to perform a careful investigation of the dynamics adhesion. We first identified a temporal aspect of bacterial attachment to host cells, where a two-step sequence leads to specific attachment (Figure 19). After contact, bacteria attach non-specifically to host cells for not more than a minute. Bacteria subsequently engage adhesins to their receptors on a timescale consistent with adhesin-ligand rupture kinetics, in our case for minutes to hours. Sequential adhesion to host cells contrasts with the single specific step governing adhesion to abiotic surfaces (Figure 12). Bacterial adhesion has previously been characterized as a multi-step process, be it on abiotic surfaces (irreversible followed by reversible during biofilm formation) or on host cells (sequential deployment of adhesins). Our results distinguish themselves from these other multistep processes as they involve a single adhesin, and that host factors regulate each of these steps.

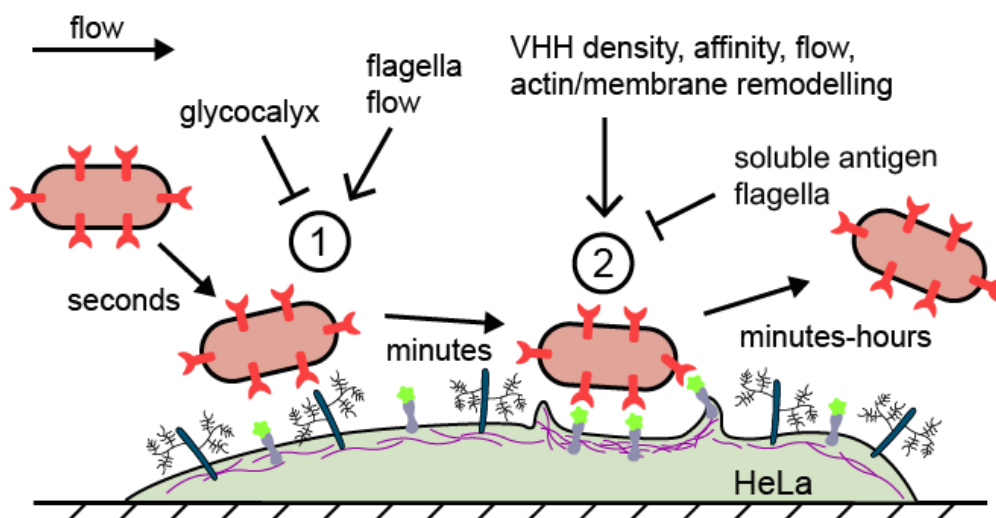


**Figure 19: A model for mechanically-regulated, two-step bacterial attachment to host cells.**

Upon contact of a bacterium with a host cell (1), the glycocalyx blocks attachment by sterically shielding the membrane. This short timescale interaction does not involve short-range adhesins nor mammalian membrane receptors. Strong shear forces and bacterial flagellum can increase the transient binding efficiency, in part by attenuating the glycocalyx shield. The bacterium subsequently binds engages adhesins onto host receptors to promote specific adhesion (2). This increased adhesin density, affinity to the receptor ligand, flow, and actin polymerization promote the specific adhesion step, while the flagella and soluble antigen repress it promoting bacterial detachment.

### 2.9.3 The mammalian surface has a significant impact on bacterial adhesion

The VHH display system allowed us to test the contributions of adhesin density and binding kinetics on attachment. While specific attachment increased with VHH density, the adhesin affinity and reaction rates ended up being a surprisingly weak regulator of attachment and detachment. This could be explained by the fact after engaging several adhesins of relatively high affinity, bacterial overall avidity rapidly predominates over the affinity of individual adhesins<sup>187</sup>. In contrast, we found that mechanical factors of the host environment strongly regulate each of the stages of adhesion. The host glycocalyx, a layer of glycans bound to glycolipids and surface glycoproteins, inhibits the first adhesion step by physically shielding the host membrane surface, in the case it is not the target itself<sup>186,188</sup>. Then, we found that the host cell actin cytoskeleton shapes the membrane around attached bacteria, thereby improving specific adhesion. Membrane embedded bacteria could thus engage VHH to additional GFP receptors, increasing overall adhesion strength. We propose that a passive ratchet mechanism triggers the actin-dependent membrane encapsulation of bacteria<sup>189,190</sup>.

### 2.9.4 Impacts of fluid flow on bacterial adhesion to cells

Surprisingly, we found that fluid flow improved attachment of *E. coli* VHH to HeLa GFP, both during non-specific and specific stages of adhesion. This was unexpected because fluid flow, by virtue of the shear force it generates, tends to remove bacteria from their attachment surface<sup>185</sup>. By shearing the glycocalyx, flow could improve the access of the bacterium to the cell membrane, thereby increasing non-specific contact efficiency<sup>13</sup>. Concerning the subsequent specific step, our observations are reminiscent of flow-enhanced adhesion as a result of the formation of catch bonds, as in *Streptococci* and uropathogenic *E. coli*<sup>191,192</sup>. However, VHH-GFP do not form catch bonds at the molecular level<sup>193</sup>. We hypothesize that flow improves specific adhesion via an indirect mechanism. For example, shearing of a bound bacterium generates tension onto the membrane, thereby stimulating actin recruitment<sup>194</sup>. This in turn engages more receptors, ultimately strengthening attachment. We finally note that as shear stress increases, more stringent selection for strongly attached cells could lead to the observed enhanced attachment. As a result, we cannot rule out that shear removes loosely attached bacteria at a rate that is faster than the temporal resolution of our imaging. All things considered, we demonstrated that the dependence of bacterial attachment on hydrodynamic forces cannot be simply extrapolated from a physically simplified behavior of a bacterium attached to a hard, inert surface.

### 2.9.5 Pathogens can target the mammalian glycocalyx

By engineering autotransporter-based adhesins, we could model a single type of adhesins. However, our results bring a new perspective on other adhesin types in the context of infection. We specifically highlighted the regulatory role of the glycocalyx in early attachment. Pathogens may overcome this first barrier using different strategies. For example, *Salmonella* uses reversible and irreversible sets of adhesin and actively degrades the glycocalyx during infection, strengthening attachment<sup>6,177</sup>. Another strategy consists of adhering to the glycocalyx directly rather than to membrane proteins, or to overcome the glycocalyx with adhesins that cap long pili or fimbriae. This in principle improves the efficiency of first step of attachment, but it usually needs to be combined with subsequent adhesive processes for tighter contact with the cell membrane<sup>166,177,188</sup>. Thus, adhesins targeting glycans and pili-associated adhesin could bind more efficiently in the first step, but cytoskeletal-dependent adhesion reinforcement would be limited in the second<sup>192,195,196</sup>.

### 2.9.6 Timely adhesin deployment

During the process of infection, bacteria use an arsenal of virulence factors. These are deployed in a timely fashion in response to relevant signals. Synchronizing expression of virulence factors with host cell contact could promote timely deployment<sup>185</sup>. For example, enteropathogenic *E. coli* transfer the intimin adhesin receptors Tir to gut epithelial cells upon contact<sup>159</sup>. The non-specific first step of adhesion thus offers a window of opportunity to deploy these systems within minutes.

### 2.9.7 Conclusion

Altogether, we have demonstrated that bacterial attachment to host cells differs from the expected behavior of simple adhesin-receptor interactions. Adhesin biochemistry and the physics of adhesion to inert materials only poorly predict adhesion to mammalian cells. This has therefore important implication in our view of infection. In the current context of the rise of multidrug resistant pathogens, our work provides new insights that could inform the development of anti-adhesive therapeutics<sup>164,188,197</sup>.

## 2.10 MATERIAL AND METHODS 1

### *Cloning*

Plasmids and primers were designed in silico using Benchling software and are described in supplementary table 2.

Bacterial genomic DNA was extracted using commercially available kits (Qiagen). Polymerase chain reaction was performed with Phusion polymerase (Thermo), restriction enzymes were purchased from NEB and primers from Microsynth (Switzerland). DNA fragments were separated on 1% agarose Tris acetic acid EDTA gel by electrophoresis. DNA fragments were purified with Monarch kits (NEB) and Gibson assembly was performed with the HiFi DNA assembly kit (NEB), in other cases, ligation was performed with T4 ligase (Thermo). Constructs were transformed by 30 seconds heat-shock in 60  $\mu$ L of chemically-competent XL10gold (Agilent). Bacteria were rescued in 600  $\mu$ L Super Optimal broth with Catabolite repression (SOC) medium for 45 to 60 min at 37°C with agitation prior to plating on their respective antibiotics-containing LB plates overnight at 37°C. Colonies were either screened by colony PCR with primers flanking the cloning sites with GoTaq G2 Green Master Mix (Promega) or after plasmid purification using GeneJET plasmid miniprep kit (Thermo). DNA was sent to Microsynth for Sanger sequencing.

### *Mammalian cell culture and induction*

HeLa cells were cultured in DMEM (Thermofisher) supplemented with 10% FBS (Life Technologies) at 37°C and 5% CO<sub>2</sub>. Prior to experiments, cells were trypsinized and resuspended in FluoroBrite (Life Technologies) supplemented with 10% FBS and 1% Glutamax (Life Technologies). Cells were seeded at 100,000 cells/mL in 96 well plates or 400,000 cells/mL microchannels (Ibidi  $\mu$ -Slide VI 0.4) one day prior to experiments. In microchannels, first 30  $\mu$ L of cell suspension were added. Cells were left to adhere for 5-6 hours, and then reservoirs were filled with additional 120  $\mu$ L of medium.

### *Mammalian cell engineering*

To generate a stable cell lines, we produced lentiviruses in HEK293T cells cultured in DMEM 10% FBS. Cells at 50% confluence were co-transfected with pMD2G (Addgene 12259), pCMVR8.74 (Addgene 22036) and a lentivector encoding the gene of interest (pXP340, see Supplementary Table 2) using Lipofectamine3000 (Life Technologies) and low-endotoxin purified plasmids. Medium was changed at day 1 and lentiviruses were collected at day 2 and

3, separated from cell debris by centrifugation, sterile filtered through 0.45 µm filter and added to HeLa cells. Cells were selected with G418 (Chemie Brunschwig) at 300 µg/mL. Resistant clones were obtained by limiting dilution in 96 well-plates. The resulting monoclonal cell line (HeLa GFP display) was induced overnight with doxycycline (HiMedia) at 500 ng/mL.

HeLa cells transiently expressing GPI-anchored were obtained by lipofection of the plasmid PeGFP\_GPI.

#### *Bacterial culture, engineering and induction*

*E. coli* K12 (BW25113) were cultured in LB at 37°C. Bacteria were stably engineered to express cytoplasmic mScarlet using pZA002 for Tn7 insertion<sup>198</sup>. pZA002 consists in a synthetic constitutive promoter upstream of mScarlet ligated into pGRG36 for chromosomal integration. Deletion of the flagellum was performed using the lambda red system and the PCR product using oXP851 oXP852 on *E. coli* genomic DNA to delete the *FliCDST* operon (Table S2)<sup>199</sup>. Flagellated and non-flagellated fluorescent *E. coli* were then electroporated with tetracycline-inducible intimin-based display constructs. pXP383 coding for the display of VHH of medium affinity was used in this study in non-flagellated *E. coli* unless stated otherwise. pXP384 and pXP388 display the VHH of lower and higher affinities, pDSG323 the empty scaffold and selected with kanamycin (Sigma) at 50 µg/mL<sup>158</sup>. To prepare adhesion experiments, early stationary pre-cultures were diluted 1:3000 and induced with sublethal doses of tetracycline (Sigma, 50 ng/mL for low VHH induction and 250 ng/mL for high VHH or for the empty intimin scaffold) overnight under shaking conditions.

#### *Cytoskeletal and glycocalyx perturbation*

Cytochalasin D (Sigma) at 1 µM was added 5 minutes prior to- and during the experiment. One microliter of Protein Deglycosylation Mix II (NEB) of was added per channel for overnight treatment (150 µL total).

#### *Attachment with soluble GFP*

Soluble recombinant GFP was added to the bacterial suspension at 10 µg/mL 5 minutes prior to the experiments.

### *Generation of a Ni-NTA functionalized glass surface for selective protein immobilization*

Addition of the Ni-NTA functionality to a glass surface was inspired by existing protocols<sup>200,201</sup>. Glass coverslips (#1.5) were placed in a holder and sonicated in acetone for 30 min. The coverslips were then rinsed with MilliQ water, dried with a stream of nitrogen gas and plasma treated for 10 minutes at maximal power (Zepto, Diener electronic). The plasma-treated coverslips were then transferred into 150 mL of 1% (v/v) (3-Aminopropyl)triethoxysilane (APTES) (Sigma-Aldrich) in toluene (Sigma-Aldrich) and stirred for 30 min. The cover slips were then rinsed in 150 mL of toluene for 10 minutes, dried by a stream of nitrogen gas, then baked at 80°C for 45 min. The coverslips were then cooled down with a stream of nitrogen gas and transferred into a 150 mL stirred solution of 2 mg/ mL p-Phenylene diisothiocyanate (PDITC) (Sigma-Aldrich) in 10% (v/v) anhydrous pyridine (Sigma-Aldrich) and 90% (v/v) N,N-dimethylformamide (DMF) (Sigma-Aldrich) for 2 h in darkness. The cover slips were then flushed with 1 volume of absolute ethanol, followed by a wash in acetone for 10 min and drying with a stream of nitrogen gas. Then half the cover slips were laid on a flat surface. We then prepared a solution of 457 mM N,N-Bis(carboxymethyl)-L-Lysine-hydrate (Sigma-Aldrich) in 1 M NaHCO<sub>3</sub> (Sigma-Aldrich). 90 µL of the N,N-Bis(carboxymethyl)-L-Lysine-hydrate solution were deposited onto the cover slips, then sandwiched with another coverslip on top. These were incubated overnight at room temperature. The unreacted PDITC was then blocked by immersing the coverslips into a solution of 5mg/ml BSA + 5% ethanolamine in PBS for 30 min. The slides were then washed in 1x PBS for 10 minutes under constant stirring, and transferred into a solution of 1% (w/v) solution of nickel sulfate (NiSO<sub>4</sub>) for 1 hour under stirring, then washed in 1x PBS for 10 min followed by a second wash in 0.1x PBS for 10 minutes and dried under a stream of nitrogen gas. 50 µL of recombinant GFP protein at 1 mg/mL were deposited onto each coverslip and incubated over 2 days in the dark at 4°C. The slides were again flushed in 1x PBS for 10 minutes followed by a second wash in 0.1x PBS for 10 minutes then dried with a stream of nitrogen.

### *Visualization*

For widefield visualizations, we used a Nikon TiE epifluorescence microscope equipped with a Hamamatsu ORCA Flash 4 camera and an oil immersion 100x Plan APO N.A. 1.45 objective. For all time-lapses and mammalian cell visualizations, we used a Nikon Eclipse Ti2-E inverted microscope coupled with a Yokogawa CSU W2 confocal spinning disk unit and equipped with a Prime 95B sCMOS camera (Photometrics). For time-lapses, we used a 40x objective with N.A. of 1.15 to acquire z-stacks with 2 µm intervals over 6 µm. Each plane was acquired at low laser power for 200 ms allowing to threshold out free bacteria in flow from bound bacteria. For

stained mammalian cell visualizations, we used a 100x oil immersion objective with N.A. of 1.45 to acquire z-stacks with 0.5  $\mu\text{m}$  intervals.

We used NIS Elements (Nikon) for three-dimensional rendering of z-stack pictures.

#### *Flow experiments and data acquisition*

Bacteria induced overnight were diluted 1:10 in Fluorobrite 10% FBS 1% Glutamax and loaded in syringes. We applied equivalent mean flow rates according to the different channel dimensions in Figure 12. Shear stress at the centerline was calculated using the formula:  $\text{shear stress} = 6 * \text{flow} * \text{kinematic viscosity} / (\text{channel width} * \text{channel height}^2)^9$ . Flow generating shear stress of 0.05 Pa at the channel centerline (unless stated otherwise) was applied using syringe pumps connected to microchannels seeded with induced HeLa cells at 50-80% confluency, or to channels functionalized with GFP. Z-stacks for bacterial contact efficiency was generated by confocal microscopy every second. Three different fields of view were sequentially imaged for 5 min per biological replicate.

Data to model residence time was generated by confocal microscopy of z-stacks every 10 s. Three different fields of view were simultaneously imaged for 60 min per biological replicate. Cell surface area was acquired once in the green channel at the start of the experiment. Number of HeLa cells was then approximated based on their average size as manually determined with 5 biological replicates of 3 frames each.

Illustrative confocal time-lapse with both channels for GFP and mScarlet were acquired at either 2 or 6 stacks per minute at 100x magnification.

#### *Bacteria tracking*

We use the maximum intensity projection of full stacks to detect attaching bacteria. We used the Fiji plugin Trackmate with LoG detector<sup>202</sup>. Threshold was set so that >95% of bacteria are detected on the final frame and <5% of the tracks were false positive (two different bacteria slowing down in the same area on consecutive frames). The LAP tracker was used with 5  $\mu\text{m}$  maximal inter-frame distance and gap closing, track splitting and closing with a maximal distance of 3  $\mu\text{m}$ . Final number of spots, tracks and spots statistics were exported for data analysis.

### *Data analysis and modeling*

Data generated by Trackmate was analyzed using Matlab. In brief, contact efficiency was defined as the number of tracks strictly longer than 2 frames, divided by the total number of contacts (bacterium appearing on one frame or more). Bacteria present from the first frame were removed from the analysis to exclude bacteria that attached during handling time.

Residence times of tracks strictly longer than two frames were considered and sorted in a histogram of 10 s bins. We further transformed this data into an “inverse” cumulative histogram to present results in a manner classical for adhesion events by defining:

$$\text{fraction remaining } (t = 20\text{s}) = \text{total number of tracks on three fields of view}$$

$$\text{fraction remaining } (t + 10) = \text{fraction remaining } (t) - \text{number of tracks of duration } t$$

Because many bacteria were bound at the end of the acquisition, we had to circumvent the artificial stop of tracks. To do so, we considered the binding events occurring within the first 30 minutes and followed them over 30 additional minutes for the fitting. We fitted the fraction remaining as a function of residence time with a dual exponential decay as follows:

$$\text{fraction remaining } (t) = C_{\text{transient}} * e^{-\frac{t}{T_{\text{transient}}}} + C_{\text{res}} * e^{-\frac{t}{T_{\text{res}}}}$$

The raw data for all experiments is summarized in table S4.

### *Static co-culture and mammalian cell staining*

Mammalian cells were co-incubated with bacteria for 5h 30min at a multiplicity of infection (MOI) of 50 (Figure 9C) or for 1h at a MOI of 200 (Figure 13A, B). Wells were washed once with PBS, fixed in 4% paraformaldehyde for 20 minutes, permeabilized with 0.1% Triton X-100 for 5 min and washed twice with PBS. Phalloidin-Atto 655 (Sigma) was used to stain actin at 500 nM for 15 min. DAPI was used for nuclei counterstain at 1  $\mu$ M for 5 min. Cells were washed twice with PBS and imaged by confocal microscope at 100x magnification.

### *Bacterial staining, titration and quantification*

Bacteria displaying VHH were washed with PBS and stained with recombinant GFP at 100  $\mu$ g/mL for 10 minutes prior to two PBS washes and imaging under a 1% agarose PBS pad. Wide field fluorescent pictures were taken at 100x and 1.5x lens magnification.

### *Production of recombinant proteins*

Plasmids SpyTag003-mKate2 and pET28a-eGFP (see Table S2) were retransformed into BL21 strain. Production was induced with 1 mM IPTG (Fisher bioreagents) at 20°C overnight. Bacteria were pelleted and lysed by sonication in lysis buffer (Tris 100mM, NaCl 0.5M, glycerol 5%) and SpyTag003-mKate2 was purified using fast flow His-affinity columns (GE Healthcare) and eluted with 500 mM imidazole. Buffer was exchanged to PBS using 30kDa ultracentrifugation spin columns (Merck) and aliquots at 1 mg/mL were snap frozen for further use.

### *$K_{D(\text{display})}$ measurements*

To measure VHH affinity when displayed at the bacterium surface, serial dilution of GFP were performed by increasing the volume to avoid antigen depletion. For each concentration, 100  $\mu$ L of bacteria induced with 250 ng/mL tetracycline overnight were washed with PBS and stained for two hours. For volumes below 50 mL, bacteria were pelleted and resuspended in 4% PFA in PBS. For volumes above 50 mL, bacteria were retrieved on 0.22  $\mu$ m filters using 4% PFA in PBS. Bacteria were then imaged under a 1% agarose PBS pad. Wide field fluorescent pictures were taken at 100x and 1.5x lens magnification.

Using Fiji software, bacteria were detected using the mScarlet channel and the corresponding regions of interests were used to quantify mean GFP intensity for each bacterium. Prism software (Graphpad) was used to perform a non-linear fit of the mean GFP signal among bacteria on the field of views using the formula “One site – specific binding”  $Y = \text{max} * [\text{GFP}] / (K_D + [\text{GFP}])$  and estimate  $K_{D(\text{display})}$ .

### *N-acetyl glucosamine staining of live HeLa cells*

HeLa cells were cultured in DMEM (Thermofisher) supplemented with 10% FBS (Life Technologies) at 37°C and 5% CO<sub>2</sub>. One microliter of Protein Deglycosylation Mix II (NEB) of was added per well of Ibidi 96-well plate for overnight treatment (150  $\mu$ L total). Cell supernatant was replaced with 100  $\mu$ L of 10  $\mu$ g/mL rhodamine-labelled wheat germ agglutinin (Vectorlabs) in PBS for 30 min at room temperature. Supernatant was replaced by 200  $\mu$ L PBS for confocal imaging.

### *HA tag staining*

Bacteria harboring a HA tag were washed with PBS and stained with anti-HA antibody conjugated with FITC (Abcam ab1208) at 10 µg/mL for 75 minutes in the dark, washed once with PBS and imaged under a 1% agarose PBS pad. Widefield fluorescent pictures were taken at 100x and 1.5x lens magnification.

### *GFP uptake rate*

*E. coli* VHH were added under static conditions at a MOI of 200 for a couple of minutes and washed 3 times before widefield epifluorescence imaging. HeLa GFP captured 11 bacteria. Image segmentation performed using the red channel (*E. coli*) to quantify the local total GFP signal around bacteria over time.

## 3 DEVELOPMENT OF AN ADHESIN DISPLAY SYSTEM AT THE SURFACE OF *A. TUMEFACIENS*

---

### 3.1 ABSTRACT

Despite *A. tumefaciens* being widely used for crop engineering, some plant species such as monocots remain somewhat refractory to *A. tumefaciens*-mediated transformation<sup>203</sup>. It is hypothesized that the limited attachment of the bacterium to non-natural hosts limits transfer efficiency by decreasing physical contact. Consistent with this, studies have shown a positive correlation in transformation efficiency and adhesion recalcitrant plant cells<sup>160,161</sup>. Altogether, it seems however that the scientific community has only a partial understanding of *A. tumefaciens* adhesion processes. In addition, we lack tools to fine-tune adhesion of the bacterium to target surfaces. To answer this, we investigated and repurposed a previously uncharacterized autotransporter in *A. tumefaciens*. Using its scaffold, we displayed at the surface of the bacterium adhesins of increasing complexity that highlighted the structural limitations of the passenger domain. Ultimately, we robustly displayed synthetic adhesins such as a nanobody anti-GFP at the surface of *A. tumefaciens*. Altogether, we anticipate the versatility of both nanobodies and our display scaffold will benefit the plant engineer community and beyond, by strengthening *A. tumefaciens* adhesion to recalcitrant cells, thus, increasing T-DNA transfer.

### 3.2 INTRODUCTION

#### 3.2.1 Synthetic multicellular assemblies

Multicellular assemblies allow mimicking of complex tissue organization. In addition, the addition of synthetic biology features to multicellular assemblies is an emerging field in all cell types<sup>204</sup>. In mammalian cells for instance, Ausländer *et al.* developed biocomputers made of up to nine cell lines assembled in a three-dimensional structure. Together, the cell mixture performed complex logical operations such as a three-input, two-output full adder<sup>205</sup>. Also, the addition of synthetic surface receptors allows researchers to connect different cells that would otherwise be indifferent to their neighbors. For example, Toda *et al.* engineered multilayered cellular structures that include sender and receiver cells communicating by using synthetic surface ligands fused to the Notch signaling pathway. By adding synthetic cell-cell contact

triggering intracellular signaling cascades, they mimicked embryonic development processes and even managed to regenerate three-layer tissues after injury<sup>206</sup>.

Similarly, in prokaryotes, Glass *et al.* expressed adhesins at the surface of gram-negative bacteria to pattern multicellular assemblies. They displayed three nanobody-antigen pairs that allowed them for instance to elegantly perform phase separation or sequential layering of bacterial strains<sup>158</sup>. The scaffold they used was initially developed by Salema *et al.* for the screening of nanobody libraries displayed at the surface of *E. coli* targeting live mammalian cells overexpressing cancer biomarkers<sup>47,157</sup>. This synthetic adhesion of bacteria to mammalian cells represents a robust and promising strategy to rewire bacterial machineries to host cells such as secretion systems.

### **3.2.2 *Agrobacterium tumefaciens***

*A. tumefaciens* is the gold standard bacterium for gene delivery to plant cells. In the wild, it casually transfers fragments of several tens of kilobases of pathogenic DNA to the target cell. In the lab, plant biotechnologists have repurposed this specie into a potent gene delivery tool for a broad range of plants, yeasts and fungi. As such, it is a promising candidate for the gene delivery to other eukaryotic cell types such as human cells. The availability of safe, efficient and precisely targeting gene delivery vectors is currently one of the main limiting factors for gene editing therapies *in vivo*. For instance, adeno-associated viruses (AAVs) currently used in humans are a bottleneck for the development of CRISPR-Cas9-mediated strategies for the treatment of genetic diseases, due to packaging capacity limitations. Could we envision using *A. tumefaciens* for therapeutic gene delivery? More generally, what are the limiting factors for rewiring *A. tumefaciens* to new cell types and how could we overcome them?

### **3.2.3 Motivation / aim**

Upon virulence gene activation, *A. tumefaciens* first binds target cells for T4SS-mediated T-DNA transfer<sup>207,208</sup>. Protocols advise to force cell-cell interaction, for instance by wounding the plant or by proceeding to syringe- or vacuum-driven agroinfiltration<sup>209</sup>. Reports show that the addition of extracellular cellulose correlates with T-DNA transfer efficiency to recalcitrant plant cells<sup>160</sup>. One plant extracellular glycoprotein was described in *Arabidopsis thaliana* as favoring agrobacterial T-DNA transfer<sup>161</sup>. VirB2 and VirB5 themselves might be involved in binding to target receptors, but their contribution as adhesin is difficult to decouple from the pilus formation<sup>210,211</sup>. Altogether, these studies suggest that increased bacterial adhesion favors T-DNA transfer. Still, the literature on *A. tumefaciens* adhesins only provides a partial

understanding of the adhesion process to plant surfaces<sup>208</sup>. Hence, could we engineer *A. tumefaciens* more systematically to increase its affinity to defined biomarkers? We still lack tools to fine-tune adhesion of the bacterium to biological surfaces. A modular system enabling *A. tumefaciens* to bind to surface proteins of interest could greatly broaden the target host range (Figure 20).

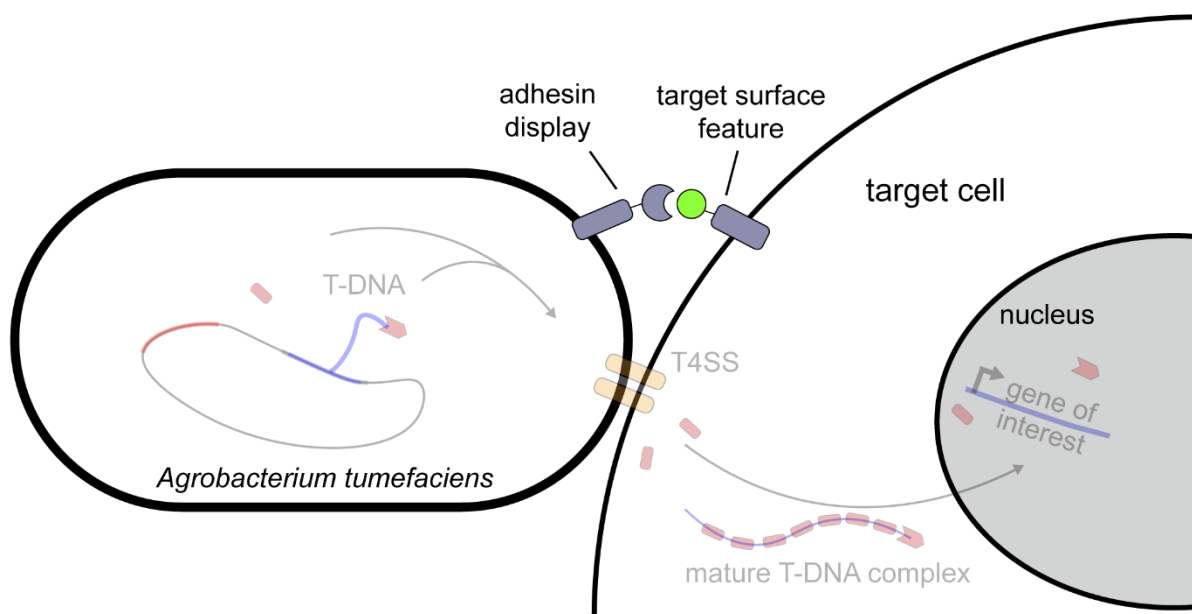


**Figure 20: Concept of a synthetic adhesin display to bind to surface features of target cells.**

### 3.2.4 Overview

Here, we developed the first of its kind modular synthetic adhesin display system for *A. tumefaciens*. To achieve this, we investigated a putative autotransporter located on the cryptic pAtC58 plasmid as candidate scaffold for adhesin display. We found a compatible tag to monitor successful display, with which we systematically investigated some of the passenger domain structural pre-requirements by using candidate passenger domains of increasing complexity. Altogether, we successfully repurposed the previously uncharacterized autotransporter for the display of multiple adhesins including lectins, nanobody and arginine-glycine-aspartic acid (RGD) peptide.

### 3.3 IDENTIFICATION OF A POTENTIAL SYNTHETIC ADHESIN SCAFFOLD IN *A. TUMEFACIENS*

In this chapter and the following one, we used the disarmed strain *A. tumefaciens* C58C1 pMP90 (GV3101, see Table S3), one of the most widely used strains to study *A. tumefaciens* biology and T-DNA transfer. We initially tried to transpose the *E. coli* intimin-based VHH display to *A. tumefaciens*, unsuccessfully. Genomic analysis revealed that *A. tumefaciens* C58 does not possess any annotated reverse autotransporter, and consequently likely does not express the right variants of the associated chaperones that enable proper insertion in the outer membrane and/or translocation of the passenger domain<sup>26,212</sup>. Nonetheless, two classical autotransporters genes are predicted, namely *atu5354* and nearby *atu5364*. We modeled the two putative autotransporters using RoseTTaFold to get a first impression of their three dimensional conformation and we used SignalP-5.0 to predict signal peptide for translocation from the cytosol to the periplasm (Figure 21)<sup>213,214</sup>.

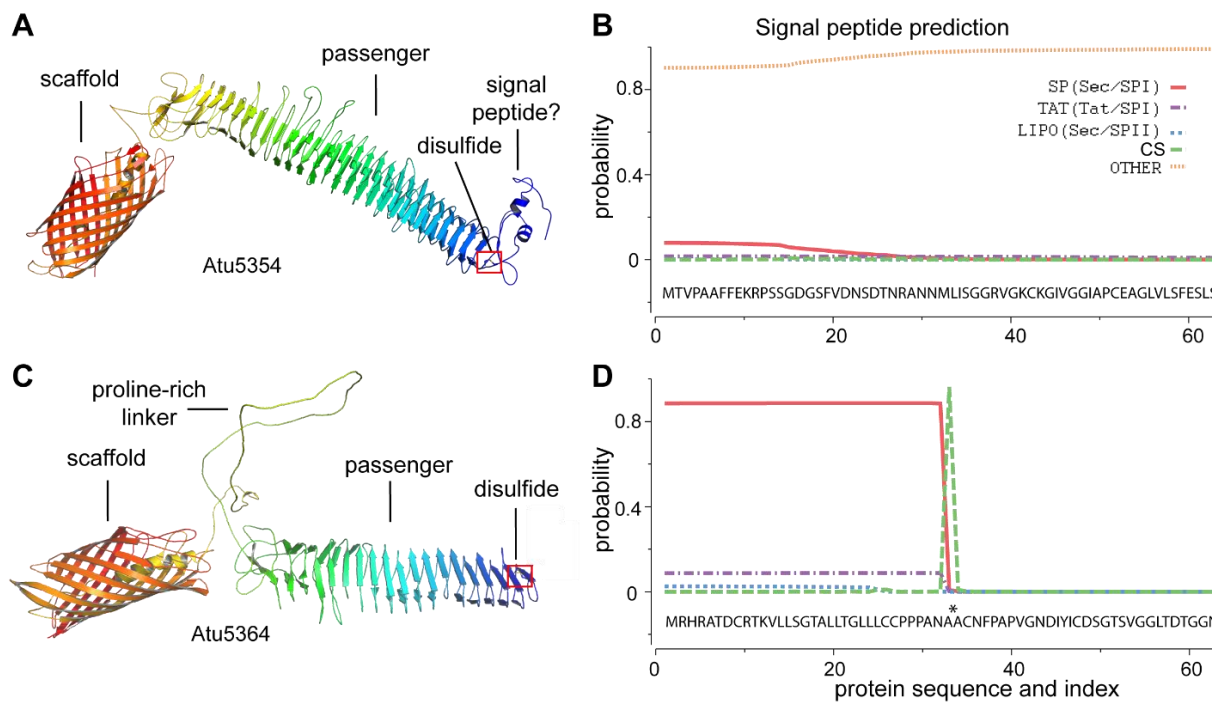


**Figure 21: *in silico* analysis of the two putative autotransporters in *A. tumefaciens*.**

(A,C) Model of Atu5354 and Atu5364, respectively, using RoseTTaFold. Both are T5aSS autotransporters with a C-terminal beta-barrel enclosing an alpha helix (scaffold) located in the outer membrane. They display a passenger domain of unknown function consisting of beta strands organized in a beta-solenoid and capped by a disulfide bond (framed in red). Atu5364 possesses an unfolded proline-rich linker between the scaffold and the passenger domain. (B,D) Signal peptide prediction using SignalP - 5.0 of Atu5354 (B) and Atu5364 (D). Atu5364 is the only protein for which a signal peptide is predicted, of a length of 33 amino acids. Sec/SPI: "standard" secretory signal peptides transported by the Sec translocon and cleaved by Signal Peptidase I (Lep). Sec/SPII: lipoprotein signal peptides transported by the Sec translocon and cleaved by Signal Peptidase II (Lsp). Tat/SPI: Tat signal peptides transported by the Tat translocon and cleaved by Signal Peptidase I (Lep). CS: putative cut site.

Both structures appear similar, with a C-terminal scaffold holding a passenger formed of repeated parallel beta-strand repeats organized in a beta-solenoid, a prevalent structure in T5aSS autotransporters<sup>215</sup>. *Atu5354* however does not have a signal peptide recognized by SignalP-5.0, which might be a consequence of the training set of the deep neural network-based method of SignalP-5.0, or *atu5354* could be a non-functional pseudogene. The main difference between the two passenger domains is that *Atu5364* harbors a long and unfolded proline-rich linker between the scaffold and the folded region of the passenger domain composed of 34 prolines out of 120 residues (28.3% vs. less than 4.7% on average). Prolines and glycines (8 here) are potent secondary structures breakers and help keeping the region unfolded<sup>216</sup>. In physiological conditions, this linker probably extends and helps the passenger domain reaching distant targets. Altogether, the predicted scaffold, signal peptide and long linker make *Atu5364* a promising candidate for the autotransporter-based display of synthetic passenger domains.

We also tried to better understand the function of *atu5364*. We submitted the folded domain of *Atu5364* passenger domain to SwissModel and I-Tasser, two protein structure homology-modelling servers<sup>217,218</sup>. Such algorithms rely on available protein structure homologous to the input sequence, and such templates can give an idea of its function. Table 1 summarizes the best matches from both methods. The functions of the different templates are however very diverse, and it is hard to infer any function for *Atu5364*. For instance, templates are involved in either actin-based motility, binding to host cells, binding to ice, production of S-layer or self association<sup>219–224</sup>.

**Table 1: Overview of the top templates used by SwissModel and I-Tasser homology-model modeling software with *Atu5364*(35-501) as input.**

Here, different fragments of 10 to 30% of the query sequence were aligned to templates. The “Local % identity” represents the identity percentage of these fragments with the templates used for modeling.

Protein template name	Host	Local % Identity	Function
<b>IcsA/VirG autotransporter</b>	<i>Shigella flexneri</i>	34	Intracellular, actin-based motility <sup>219</sup>
<b>P.69 pertactin autotransporter</b>	<i>Bordetella (para)pertussis</i>	30	Binding to host cells <sup>220</sup>
<b>Antifreeze protein</b>	<i>Marinomonas primoryensis</i>	27	Binding to ice crystal and ice growth prevention <sup>221</sup>
<b>RsaA</b>	<i>C. crescentus</i>	27	S-layer production for protection and/or pathogenicity <sup>222,223</sup>
<b>Ag43 autotransporter</b>	<i>E. coli</i>	24	Self-association <sup>224</sup>

After structure prediction by using templates locally, I-Tasser also re-aligns the whole predicted structure to the Protein Data Bank library. The top hits that are not the inputs themselves are plant hormonal or peptide receptor kinases (pdb 5HYX, 5GR8, 5GIJ, 2A0Z). It is possible yet highly hypothetical that Atu5364 is involved in binding to plant by dimerization to the homologous surface receptors at the plasma membrane. If that was the case, it would be a consequent of convergent evolution rather than gene acquisition from plants, since a BLAST alignment of Atu5364(35-501) to green plants did not give hits. Consistent with the involvement of the autotransporter with plant cells, transcriptomics analysis of *A. tumefaciens* in *Arabidopsis thaliana* tumors revealed an upregulation of *atu5364* transcription within plant tumors<sup>225</sup>.

Next, we determined if we could use the native promoter (Patu5364) for the display of synthetic passenger domains. We generated a GFP reporter of Patu5364, to determine its strength and/or inducibility. Based on the homology to the antifreeze protein, we tried induction in LB and compared it to LB in cold condition (Figure 22A, B). Because *atu5364* is located on the cryptic pAtC58 plasmid involved in facilitating metabolic activities in the plant root microenvironment and bulk soil, we tried to induce it in anaerobic condition (Figure 22C, E)<sup>103</sup>. We also verified whether it would be controlled by quorum sensing by culturing *A. tumefaciens* at maximal density as a puddle (Figure 22D). Finally, we also tried minimal medium, LB and acidic LB supplemented with acetosyringone (AS) (Figure 22F-H). None of the laboratory conditions tested gave GFP signal. As a consequence, we will need to use other endogenous or synthetic promoters to display proteins using Atu5364 scaffold.

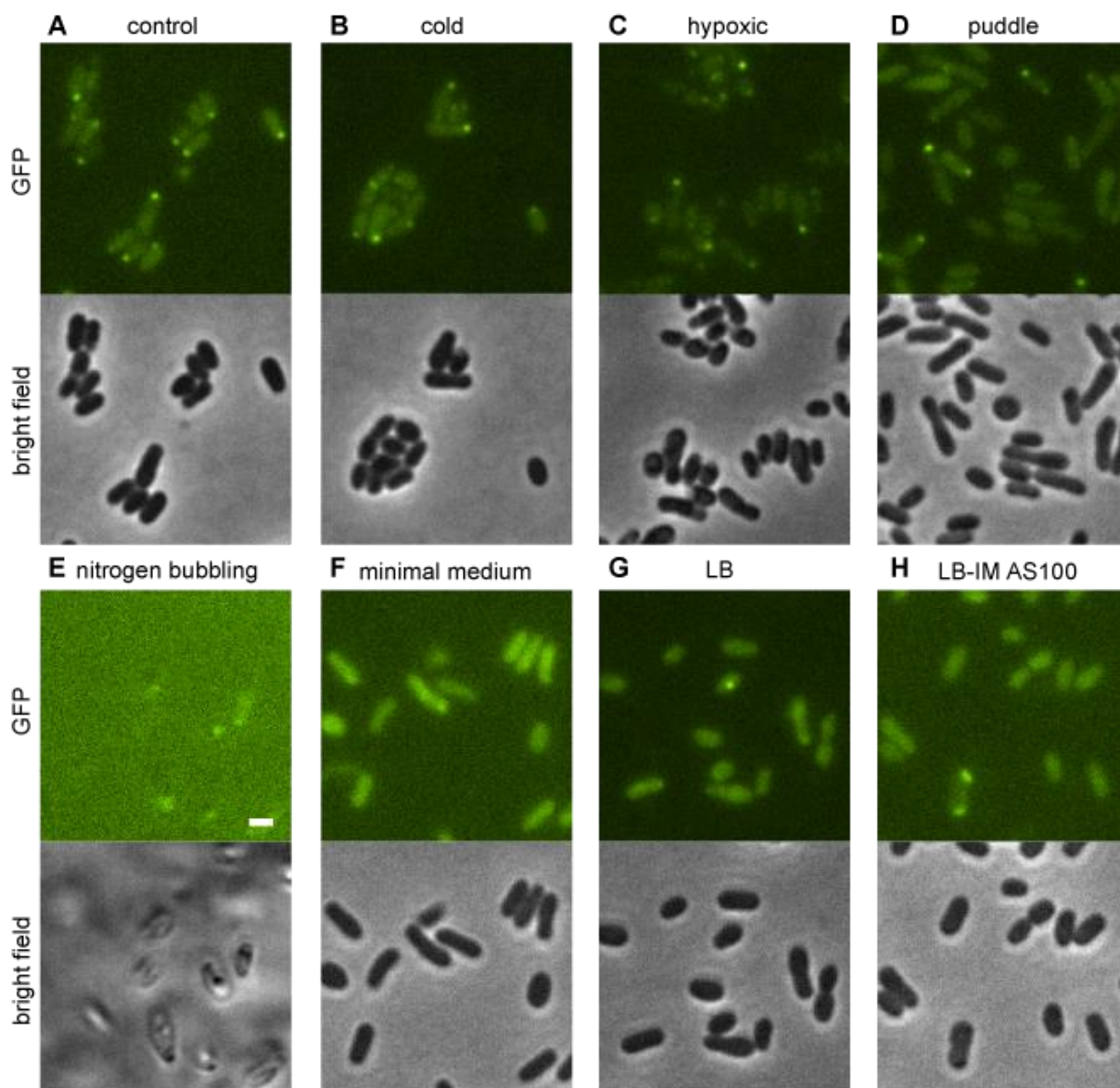


**Figure 22: Atu5364 is not induced in different lab conditions.**

A transcriptional reporter Patu5364 – eGFP was transformed in *A. tumefaciens* to monitor *atu5364* transcription level. Other than autofluorescent dots likely originating from LB medium in untransformed cells (A), no GFP signal was obtained after overnight culture in LB at 4°C (B), LB in a gas-tight tube (C), 100  $\mu$ L spotted on an LB plate (D), after 100 min nitrogen bubbling (E), in *Agrobacterium* minimal medium (F), LB (G) nor in LB-Induction Medium (LB-IM) supplemented with 100  $\mu$ M acetosyringone (H). Bar, 1  $\mu$ m.

### 3.4 INDUCTION SYSTEMS FOR *A. TUMEFACIENS* ENGINEERING

Because Patu5364 is not inducible under the laboratory conditions we tested, we need another promoter for controlling Atu5364 expression. The promoter driving *A. tumefaciens* *virE* operon (pVirE) is well characterized and commonly used for protein expression<sup>114,226,227</sup>. The VirA-VirG two-component system can be activated by addition of acetosyringone (AS) at low pH and further activates *vir* genes such as *virE* operon<sup>228</sup>. Using an mScarlet reporter, we investigated

different induction conditions for pVirE activation. We observed that physiological pH-buffered medium such as DMEM indeed downregulates pVirE (Figure 23), and confirmed that both low pH and AS are required for robust expression of the mScarlet reporter (Figure 23C, D).

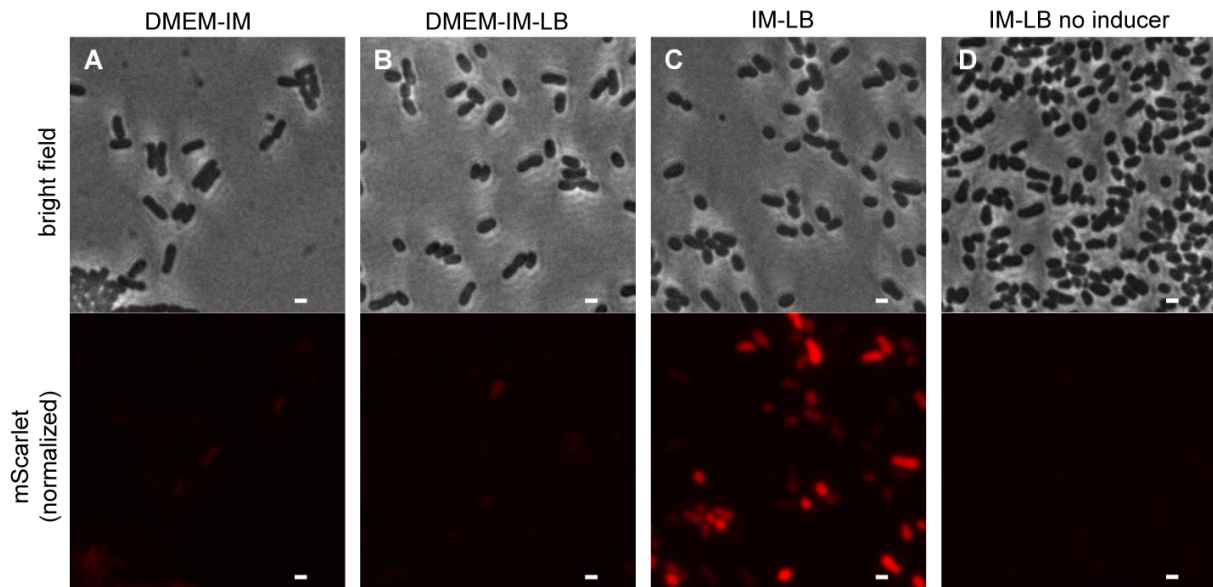


**Figure 23: The pVirE promoter requires low pH and acetosyringone.**

*A. tumefaciens* was retransformed with a pVirE – mScarlet reporter construct and induced in either DMEM and Induction medium (IM, pH=5.5) at a 1-1 ratio with 100  $\mu$ M acetosyringone (A), DMEM-IM-LB at a 1-1-1 ratio with 100  $\mu$ M acetosyringone (B), LB-IM at a 1-1 ratio with 100  $\mu$ M acetosyringone (C), or LB-IM at a 1-1 ratio without acetosyringone (D). mScarlet intensity scale is identical between samples. Bars, 1  $\mu$ m.

One key drawback of using the VirE promoter is that induction of virulence upregulates hundreds of other genes, some of which might be involved in adhesion<sup>225,229</sup>. To circumvent this, synthetic inducible promoters offer the option to decouple induction from endogenous transcription factors. In *A. tumefaciens*, a cumic acid-inducible system was developed by Denkovskiene *et al.* for VirE2 expression and assayed using T-DNA transient expression in tobacco leaves<sup>227</sup>. Here we re-cloned and assessed it using a cytosolic mScarlet reporter as an immediate readout (Figure 24). We confirmed that this system indeed offers a tight control of the gene expression and optimal induction at 10  $\mu$ M in LB at regular pH.

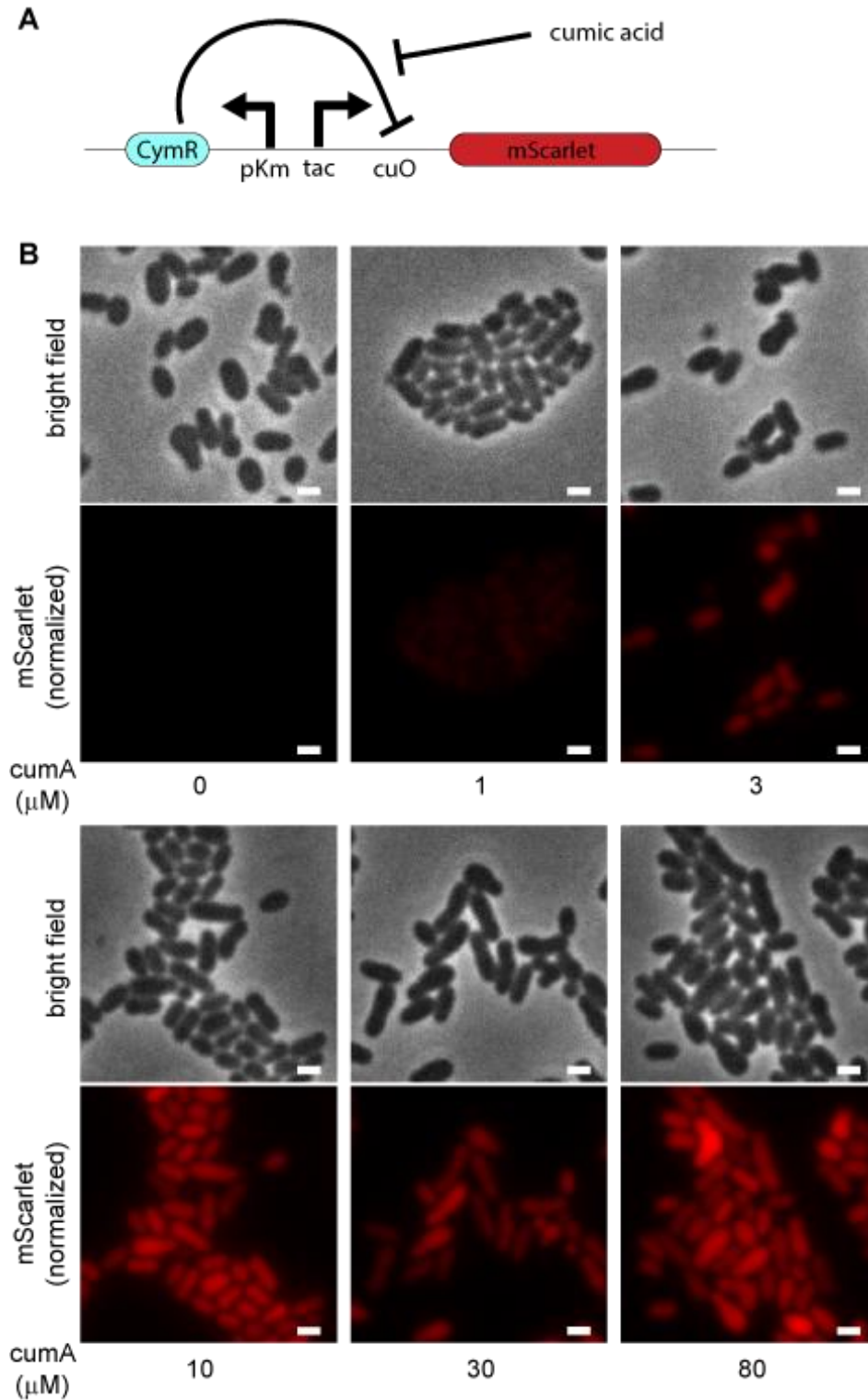


**Figure 24: The synthetic cumic acid-inducible promoter offers tight control of gene expression.**

(A) Schematic of the cumic acid (CumA)-inducible construct (tac\_cuO – mScarlet). A constitutive promoter (pKm) drives CymR expression, which binds to the cumic acid operator (cuO) and represses tac-driven mScarlet expression. Upon addition of cumic acid, CymR is released from cuO and mScarlet is produced. (B) Titration of a synthetic cumic acid-inducible promoter. Increasing concentrations of cumic acid were added to LB overnight. mScarlet intensity scale is identical between samples. Bar, 1  $\mu\text{m}$ .

### 3.5 MONITORING DISPLAY USING A TAG FUSION

We next looked for an approach to assess display efficiency. A number of studies have inferred the successful of bacterial display from biochemical methods such as Western blot from outer membrane fraction of bacteria<sup>230–232</sup>. We do not consider this as informative of the actual location of the passenger domain, which might be translocated or not: in the well-documented hairpin model, beta-barrel insertion in the outer membrane precedes passenger domain translocation<sup>30</sup>. To avoid false-positive results, we rather considered short protein tag fusions to the passenger domain to precisely monitor successful passenger display. Initially, we assessed two tags: hexahistidine (6xHis) tag and hemagglutinin tag (HA-tag), both of which can be stained with antibodies.

The WT passenger domain of Atu5364 has an N-terminal disulfide bond that could prevent display in aerobic conditions. Instead, as a first try, we opted for the display of two beta-stranded proteins devoid of disulfide bond: LecA and LecB, two lectins found in *P. aeruginosa*'s biofilms with affinity to galactose and fucose, respectively. These sugar residues are also found in other animal tissues and could be interesting targets for *A. tumefaciens*.

To investigate display efficiency, we generated fusions to Atu5364 scaffold by replacing the endogenous folded domain by LecA or LecB and one of the tags (Figure 25A). *A. tumefaciens* retransformed with the respective constructs were induced and the respective tags were stained with fluorescently-labeled antibodies. The 6xHis-tagged constructs failed to be displayed (Figure 25B), while we successfully stained the HA-tagged lectins with anti-HA antibody at the surface of bacteria (Figure 25C). One possible explanation is that 6 charged and ring-containing consecutive histidines electrostatically or sterically prevent translocation of the peptide chain through the beta-barrel scaffold. Furthermore, this is congruent with the low proportion of histidines within Atu5364: its passenger domain harbors 1 histidine in 578 residues (0.17% vs. 2.1% on average).

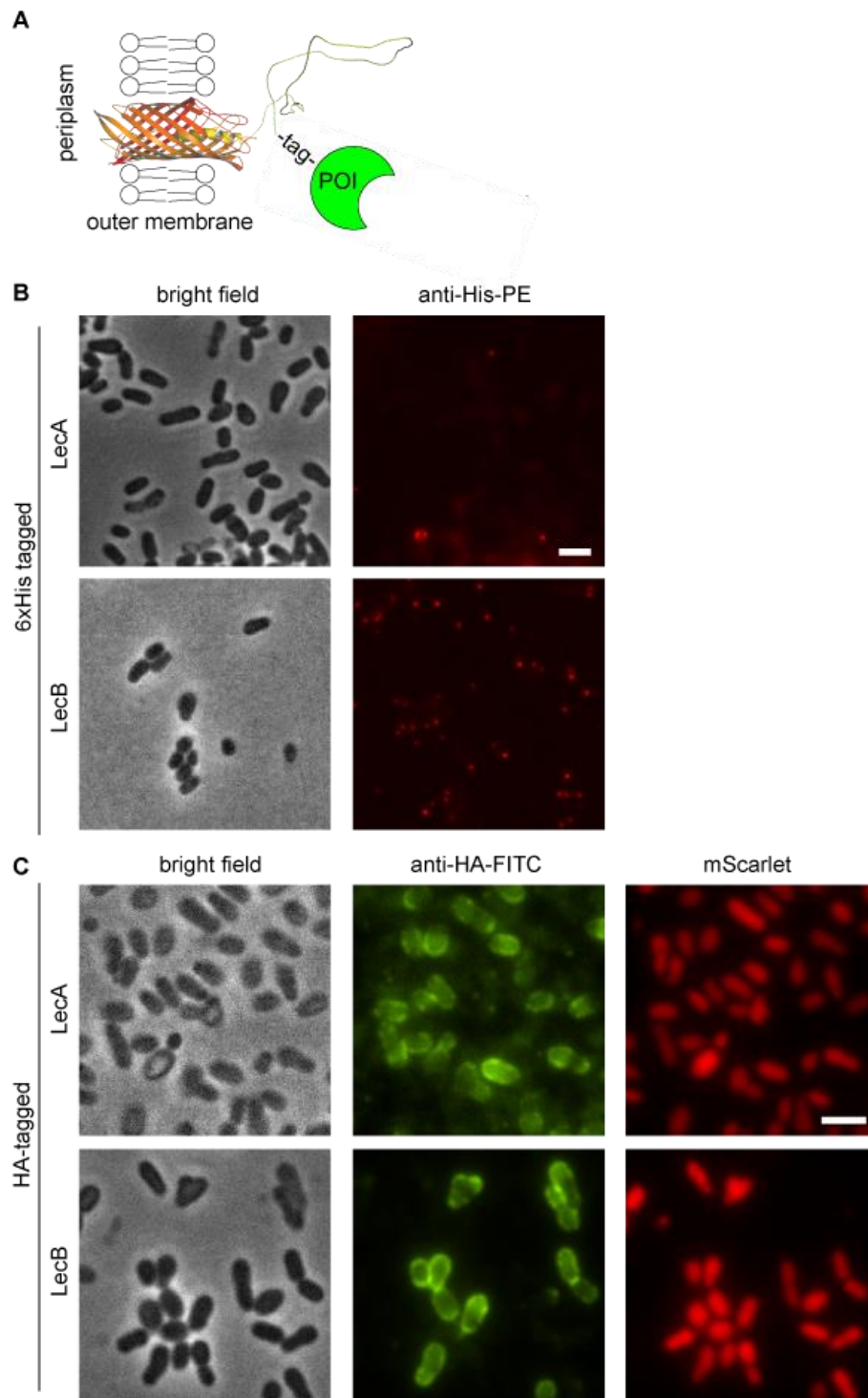


**Figure 25: 6xHis-tag prevents but HA tag enables PAO1 LecA and LecB display.**

(A) Schematic of the display approach: a protein of interest (POI) and a tag are replacing the passenger domain in Atu5364. (B) 6x-His tag prevents translocation. *A. tumefaciens* was retransformed with pVirE – 6xHis\_LecA or pVirE – 6xHis\_LecB, induced and unsuccessfully stained with anti-his phycoerythrin-conjugated antibody (anti-His-PE). (C) HA-tag allow lectin display. *A. tumefaciens* mScarlet was retransformed with tac\_cuO – LecA\_HA display tac\_cuO – LecB\_HA display, induced and successfully stained with FITC-conjugated anti-HA antibody (anti-HA-FITC). Bars, 2  $\mu$ m.

We next assessed the functionality of the displayed lectins. To measure the ability of *A. tumefaciens* displaying lectins to bind to the respective sugars, we coated streptavidin plates with biotinylated sugars and added bacteria. However, after washing, it occurs that none of the lectins improved bacterial binding to the respective sugars (Figure 26). One possible explanation is that bacterial LPS, pili or flagella might sterically hinder the lectins from reaching the surface and prevent binding. Alternatively, these lectins usually tetramerize, a process that might be sterically prevented by fusion of the C-termini of the lectins to the scaffold. LecA C-terminus is close to the adjacent monomer, while LecB C-terminus is close to the sugar binding pocket (Figure 26B, D).

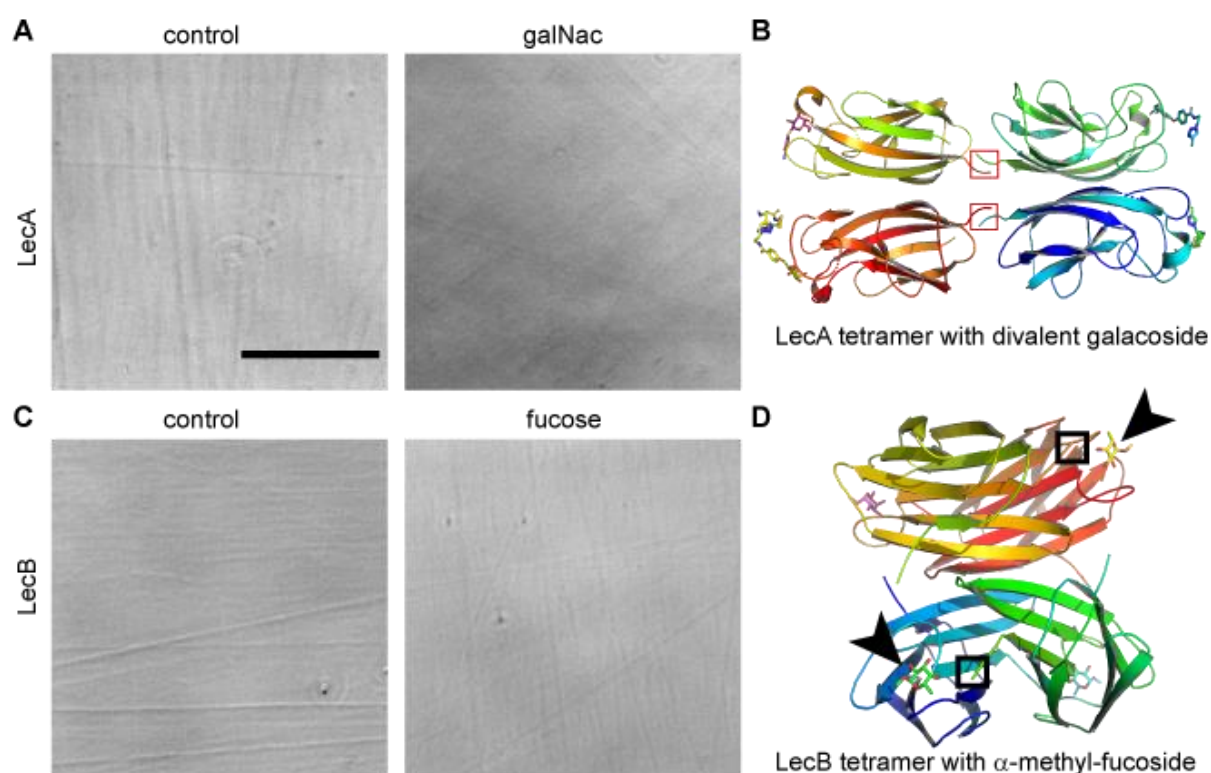


**Figure 26: LecA and LecB display does not enable *A. tumefaciens* to bind to plates coated with their respective sugar.**

(A,C) Bright field images of *A. tumefaciens* displaying LecA\_HA and LecB\_HA, respectively, added into polyacrylamide (PAA) – treated wells (control) or biotin-PAA-galNac (A) or fucose (C). Few bacteria (black dots) are visible and are out of focus (above the surface; not bound). (B) The Crystal structure of PAO1 LecA tetramer (pdb 4cp9 52). shows aThe tetrameric organization that might be prevented upon display due to the location of the. Red squares indicate C-termini of the monomers (red frames), that are linked to the autotransporter scaffold in the Atu5364-display system. (D) The Crystal structure of PA14 LecB tetramer (pdb 5a6x 53). The black frames showing the C-termini of two of the monomers (black frames), are relatively close to the fucose-binding site (black arrowheads).

### 3.6 FIMH DISPLAY IN *A. TUMEFACIENS*

To avoid potential multimerization issues, we next focused on a lectin that would be functional in its monomeric form. For instance, FimH(j96) has high affinity to mannose when displayed at the tip of uropathogenic *E. coli*'s type 1 fimbriae<sup>233,234</sup>. Using the same cloning strategy as for LecA and LecB, we displayed FimH on Atu5364 with an HA-tag. We retransformed *A. tumefaciens* constitutively expressing cytosolic mScarlet with a pVirE-inducible FimH\_HA display construct, induced and stained with FITC-conjugated anti-HA antibody. Only a few green spots were observed, mostly on mScarlet-negative cells (Figure 27A). This suggests that the display was prevented by the topology of FimH and induced cell toxicity.

We hypothesized that the presence of a disulfide bond in FimH between C3 and C44 creates a loop that prevents translocation through the beta-barrel. Leyton *et al.* indeed suggest that the maximal length between two cysteines should be no more than 18 amino acids, in agreement with disulfide bonds in known autotransporters<sup>33</sup>. Another study showed that mutations of one of FimH cysteines to a serine did not affect affinity to mannose at no- and low shear rates<sup>235</sup>. Hence, we generated a FimH(C3S) mutant that is deficient in forming disulfide bonds and displayed it as previously. We measured an increase in FITC signal around cells (Figure 27B), suggesting that disulfide bond removal indeed increases passenger translocation efficiency.

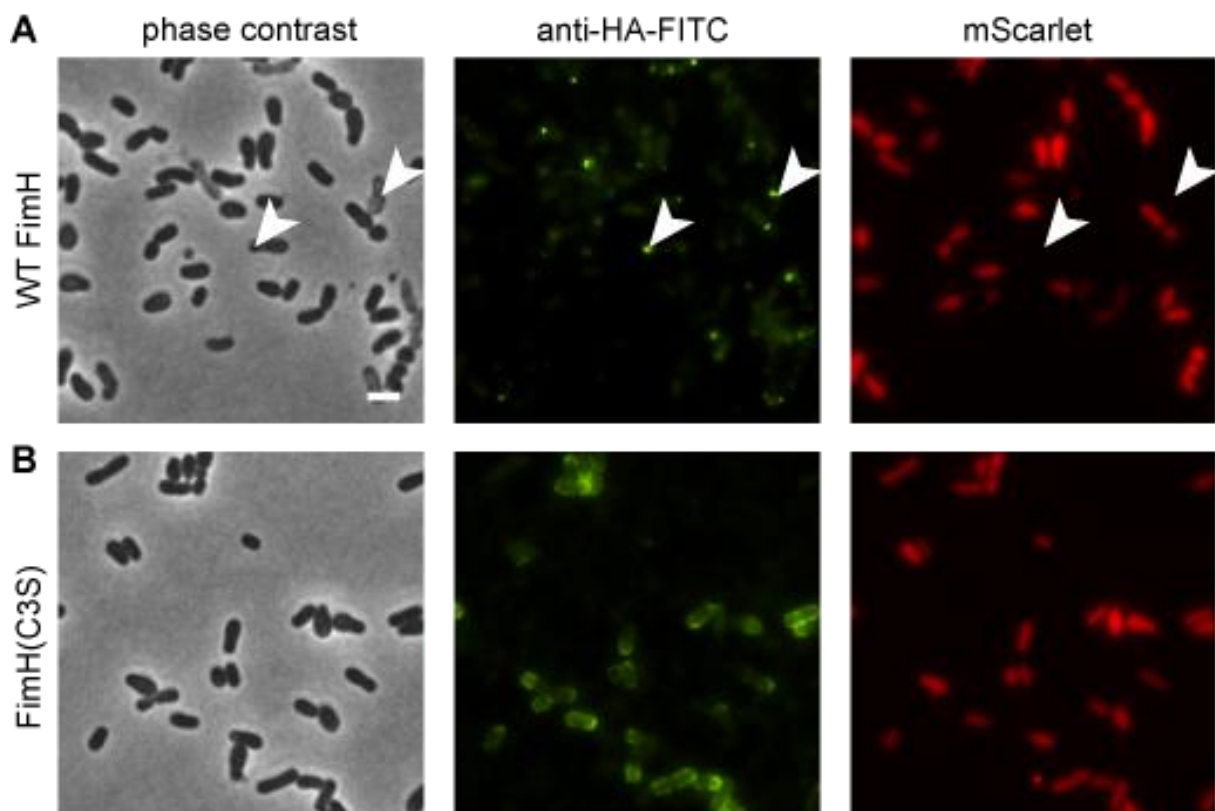


**Figure 27: FimH's disulfide bond removal increases display efficiency and bacterial viability.**

(A) FimH WT display induces cell death and patchy HA-staining. *A. tumefaciens* mScarlet was retransformed with pVirE – FimH\_HA tag display, induced and stained with FITC-conjugated anti-HA antibody (anti-HA-FITC). Low cell viability is visible in phase contrast (light grey cell bodies) and mScarlet (no signal). The anti-HA staining is uneven and mostly correlates with dead bacteria (white arrowheads). (B) FimH(C3S) display increases homogeneity of HA-staining and viability. *A. tumefaciens* mScarlet was retransformed with pVirE – FimH(C3S)-HA tag display, induced and stained with FITC-conjugated anti-HA antibody (anti-HA-FITC). Bacteria are healthy and the anti-HA staining is evenly distributed around the outer membrane. Bar, 2  $\mu$ m.

Next, we assessed the ability of *A. tumefaciens* displaying FimH(C3S) to bind to mannose-coated plates. Concomitantly, we generated *E. coli* control strains for FimH display at the tip of type 1 fimbriae<sup>167</sup>. FimH also mediates fimbriae polymerization initiation, which we verified under transmission electron microscopy. Both FimH and FimH(C3S) produced detectable fimbriae as opposed to *fimH*- control (Figure 28A). We then assayed *E. coli* and *A. tumefaciens* strains on mannose-coated plates, but only *E. coli* displaying FimH WT remained attached to the wells (Figure 28B, C). The inability of *A. tumefaciens* expressing FimH WT (Figure 28Cii) was expected according to the poor display efficiency (Figure 27A). However when displaying FimH(C3S), neither *A. tumefaciens* nor *E. coli* attached (Figure 28Biii and 28Ciii). We hypothesize that the shear forces during washing were too high for both strains expressing FimH(C3S)<sup>235</sup>.

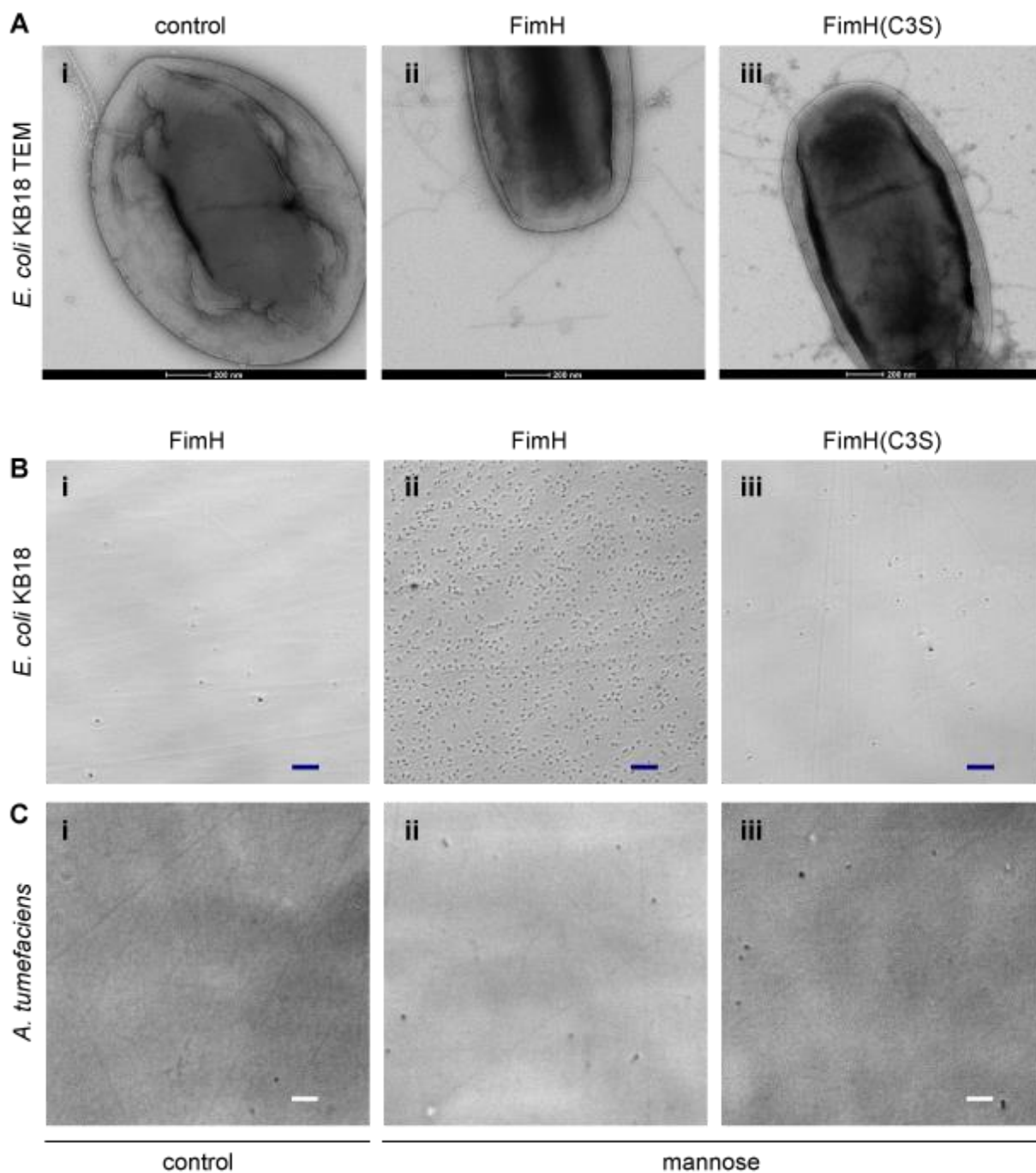


**Figure 28: FimH's disulfide bond removal impairs binding to mannose-coated surfaces.**

(A) *E. coli* expresses type I fimbriae in the presence of FimH with (ii) or without (iii) disulfide bonds. Transmission electron micrographs of negatively stained *E. coli* KB18 either untransformed (i), retransformed with pGB2-24 FimH j96 (ii) or FimH(C3S) j96 (iii). (B) FimH's disulfide bond is required for binding to mannose-coated plates. *E. coli* KB18 was retransformed with pGB2-24 FimH j96 (i-ii) or FimH(C3S) (iii). (C) Disulfide bond removal also impair affinity to mannose in *A. tumefaciens*. *A. tumefaciens* was retransformed with pVirE - FimH\_HA tag display (i-ii) or pVirE - FimH(C3S)\_HA tag display (iii) and induced.

Altogether, the three unsuccessful attempts in binding *A. tumefaciens* displaying lectins to sugar-coated plates do not exclude the possibility that lectins did not reach their target, due to

the microenvironment crowding of the bacterium. Alternatively, each lectin had at least one additional structural reason that could impede functionality (fusion of the scaffold leading to steric hindrance of tetramerization or hindrance of the sugar binding side, disulfide bonds preventing display). Hence, we searched for another passenger domain of interest that would be functional as a disulfide-free monomer, and decided to investigate the potential of *Bacillus subtilis* LipA.

### 3.7 ENZYMATIC DISPLAY IN *A. TUMEFACIENS*

Autotransporters are often used to display enzymes for biocatalysis<sup>35</sup>. Here we investigated whether Atu5364 scaffold was suitable for the display of functional *B. subtilis* LipA. Lipases hydrolyze ester bonds in triacylglycerides to form fatty acids and glycerol<sup>236</sup>. LipA is a cysteine-free, 281 amino-acid-long enzyme that has been displayed using the *P. aeruginosa* T5aSS autotransporter EstA in *E. coli*<sup>237</sup>. To assess display efficiency of lipases, tributyrin emulsion assays were developed<sup>237,238</sup>. They consist in agar plates supplemented with an emulsion of tributyrin that is hydrolyzed into soluble products by lipases such as LipA, leading to clear rings around bacteria expressing lipases (Figure 29A).

We cloned *B. subtilis* LipA onto the Atu5364 scaffold and expressed it in *A. tumefaciens* for tributyrin assays. The induction of the LipA display with cumic acid indeed increased the clearance rings compared to WT *A. tumefaciens* (Figure 29C, bottom and top spots, respectively), but to our surprise, cytosolic expression of LipA led to rings of similar diameter (left spots). LipA's structure includes several alpha helices (Figure 29B), structures that are absent in WT Atu5364 passenger domain and only present in the linker inside the beta-barrel scaffold (Figure 21). Once again, we included HA-tags to the LipA display constructs to monitor display efficiency. We observed aberrant bacterial shapes and no display upon induction and (Figure 29D).

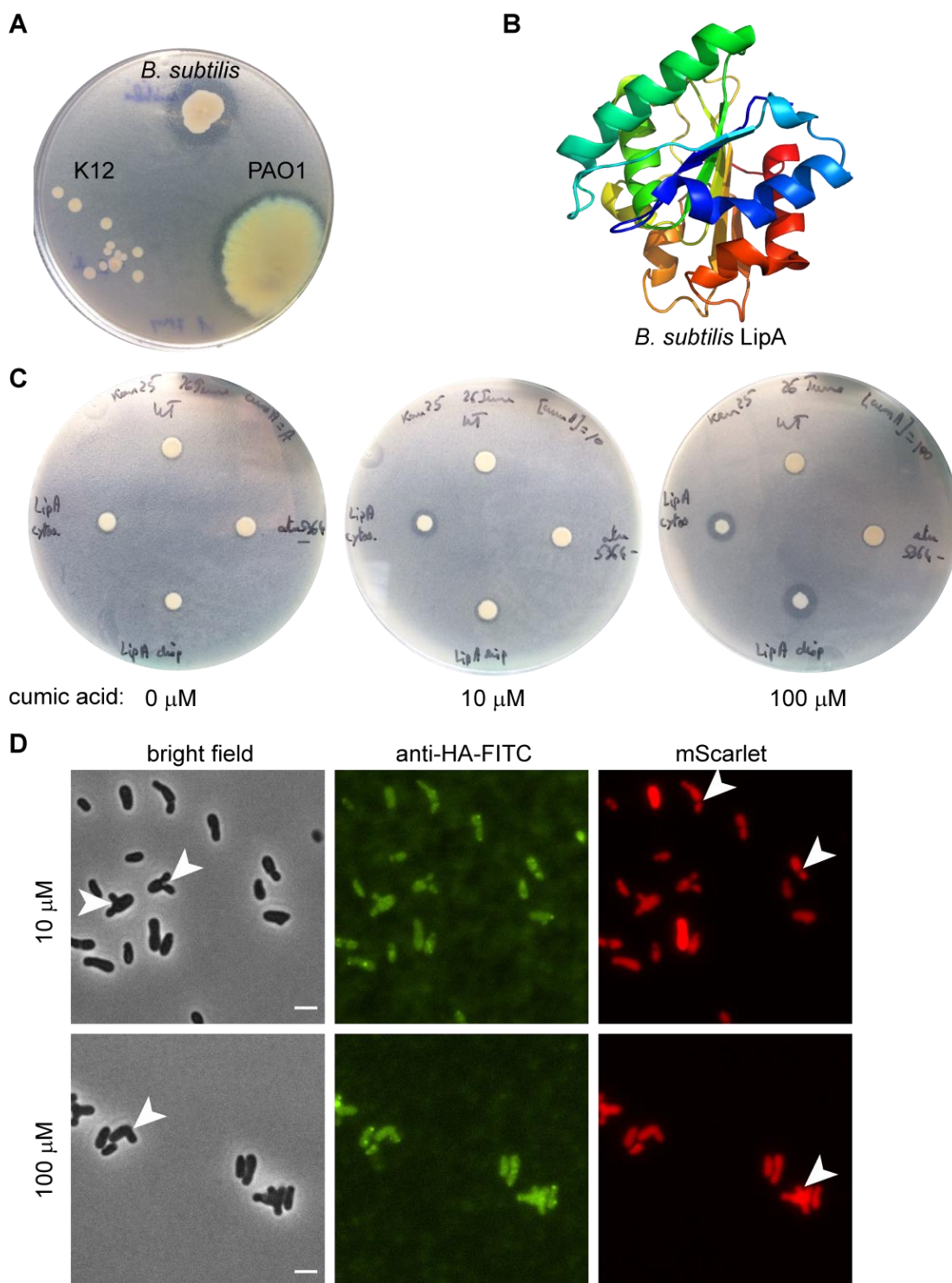


**Figure 29: *B. subtilis* LipA cannot be displayed using Atu5364.**

(A) Lipase activity was controlled in *B. subtilis*, along with *P. aeruginosa* (PAO1) and *E. coli* (K12). Clear rings around bacteria indicate tributyrin hydrolysis by endogenous lipases. (B) Crystal structure of *B. subtilis* LipA (pdb 5cri<sup>239</sup>) depicts several alpha helices that might hinder translocation. (C) In *A. tumefaciens*, LipA, displayed or cytosolic, induces tributyrin hydrolysis. *A. tumefaciens* was retransformed with tac<sub>cuO</sub> - LipA HA tag display or tac<sub>cuO</sub> - LipA HA tag (cytosolic) and assayed on tributyrin assay plates along with *A. tumefaciens* WT and *A. tumefaciens* atu5364-. The assay likely reports enzyme activity and diffusion upon bacterial lysis, rather than display efficiency, as reported in the literature. (D) LipA display induces aberrant bacterial shapes and inclusion bodies-looking spots (white arrowhead). *A. tumefaciens* was retransformed with tac<sub>cuO</sub> - LipA HA tag display, induced with either 10 or 100  $\mu$ M cumic acid and stained with anti-HA-FITC. Bar, 2  $\mu$ m.

Overall, we conclude that tributyrin emulsion plate rather report diffusion of active LipA from dead bacteria towards lipid droplets, rather than diffusion of lipid droplets towards displayed lipase, and probably have never been suitable for assaying lipase display efficiency. Beta-solenoids are a prevalent structure in T5aSS autotransporters<sup>215</sup>: here, the three-dimensional structure of LipA includes alpha helices that might be incompatible with the scaffold, the translocation mechanism or the associated chaperones.

### 3.8 NANOBODY DISPLAY IN *A. TUMEFACIENS*

In parallel to the display of lectins and enzymes that informed us on the nature of the structures that we can display on Atu5364, we tried to leverage our findings on synthetic VHH display-mediated adhesion to mammalian cells from the previous chapter. Hence, we mounted the VHH anti-GFP on the Atu5364 scaffold to monitor GFP binding efficiency. Figure 30A shows the initial VHH introduction strategy, which consisted in either replacing parts of the passenger domain (amino acids 35-160, 35-512 or 161-512) or in introducing VHH in front, within or after the folded domain of the passenger (in front of C35, D161 or A513). None of the 6 constructs performed satisfactorily, as GFP almost only stained dead *A. tumefaciens* also stained with propidium iodide (PI) (Two examples in Figure 30B, C). This indicates that VHH coupled to Atu5364 is functional, however, not displayed on the surface of *A. tumefaciens* cells.

The concomitant findings about FimH(C3S) led us to consider the removal of VHH's disulfide bond. For this construct, the removal of cysteines from the VHH anti-GFP has little effect on the affinity constant<sup>150</sup>. We hence cloned a disulfide-free VHH by site-directed mutagenesis of C24A and C98V and displayed it in *A. tumefaciens*. Figure 30D depicts the best performing display construct, where the disulfide-free VHH anti-GFP [VHH(cys-free)] display replaces the entire folded domain of the passenger and binds to recombinant eGFP without affecting viability.

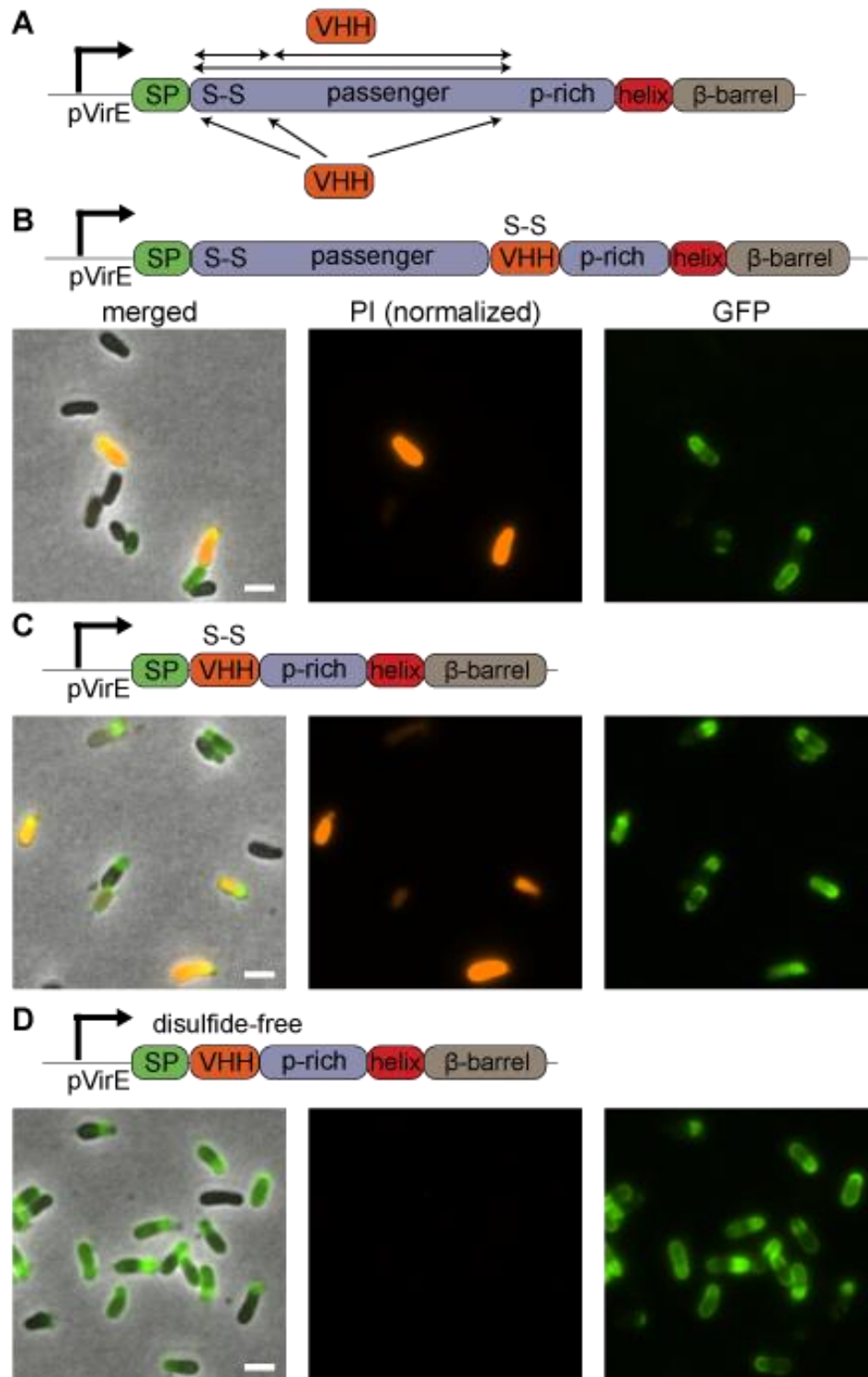


**Figure 30: VHH's disulfide bond removal improves display and viability and maintains affinity to GFP.**

(A) Schematic depicting the general VHH anti-GFP introduction approach: VHH either replaces the disulfide-bond (S-S) containing part of the passenger domain, the remaining part or the whole passenger domain, proline-rich (p-rich) linker excluded. VHH is also introduced after the SP, after the S-S of before the p-rich linker. (B-D) Upon removal of both disulfide bonds, bacteria efficiently display VHH. *A. tumefaciens* was retransformed with pVirE - internalVHH display (B), pVirE - VHH display (C) and pVirE - VHH(cys-free) display (D). Dead cells were stained with propidium iodide (PI) and VHH was stained with recombinant GFP. PI intensity scale is identical between samples. Bars, 2  $\mu$ m.

The previous experiment was performed using the commonly used pVirE promoter (with a view to coupling adhesion and virulence) on a binary vector for rapid screening. We also investigated whether other virulence promoters or a genomic integration of pVirE would be best suited for optimal induction. We introduced VHH(cys-free) display into the disarmed tumor-inducing plasmid under VirE or VirF promoters, by replacing either *virE2* or *virF* in their native locus. We also integrated the pVirE-driven construct into the tetracycline resistance locus (*tetRA*) located on the linear chromosome<sup>240</sup>. We titrated plasmid-based pVirE - VHH(cys-free) display and compared it to the maximum induction by genomically-integrated versions (Figure 31). The plasmid-based and Ti plasmid-integrated pVirE promoters displayed VHH(cys-free) at high and very high levels, a small difference probably likely due to plasmid copy number. Ti plasmid-integrated pVirF and chromosomally integrated pVirE, however, exhibited extremely weak expression of VHH(cys-free) at maximal induction.

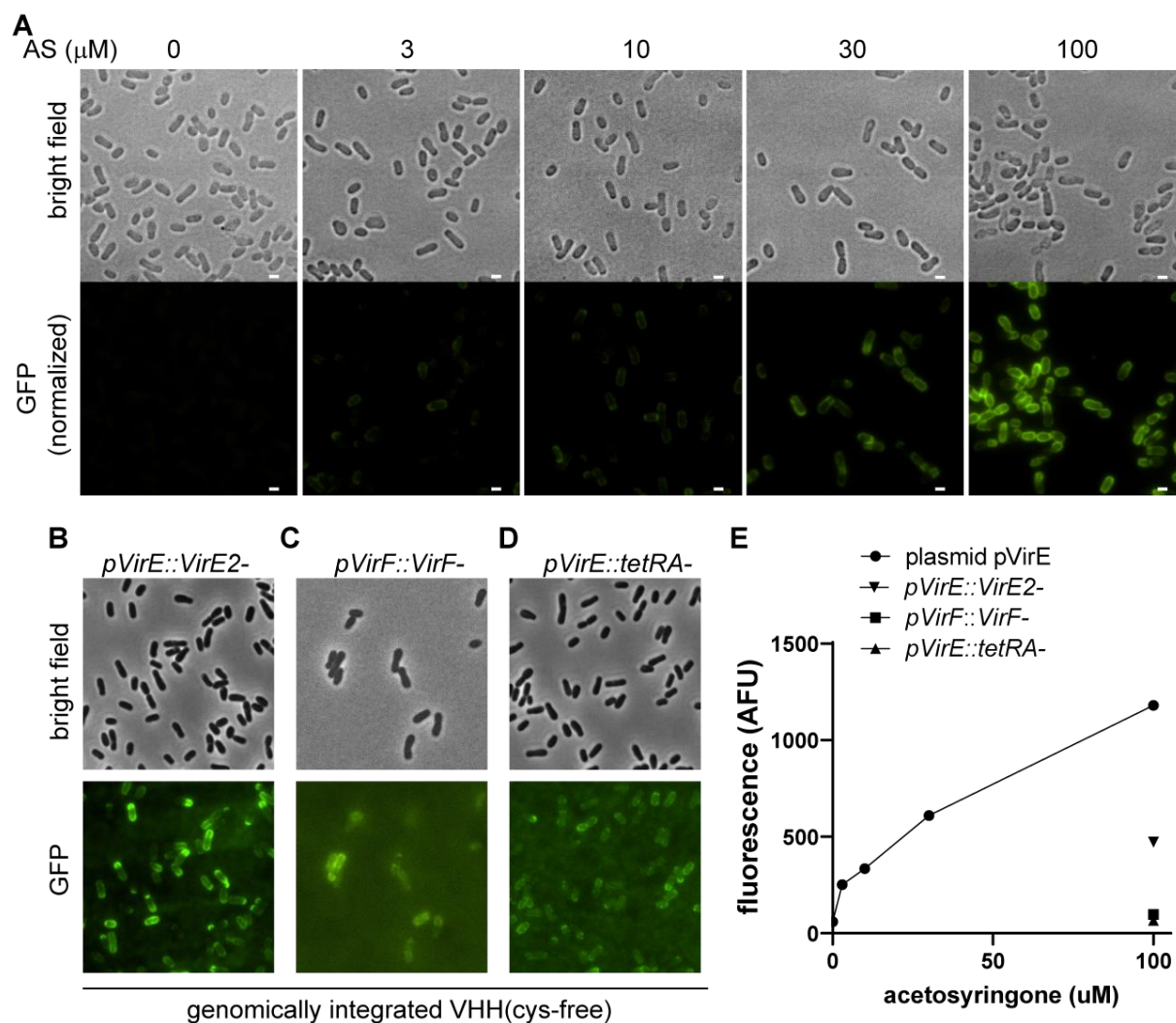


**Figure 31: pVirE is a potent inducible promoter for VHH display, both on binary vector and Tumor-inducing megaplasmid.**

(A) pVirE is a potent inducible promoter for VHH display on a binary vector. *A. tumefaciens* retransformed with pVirE – VHH(cys-free) display was induced with increasing concentrations of acetosyringone (AS) and stained with recombinant eGFP. GFP intensity scale is identical between samples. Bars, 1  $\mu$ m. (B) VHH(cys-free) substituting *VirE2* on the disarmed tumor inducing plasmid shows potent inducibility. (C) VHH(cys-free) substituting *VirF* on the disarmed tumor inducing plasmid shows low inducibility. (D) pVirE - VHH(cys-free) introduced into the *tetRA* locus, in the linear chromosome shows low inducibility. (E) Quantification of the mean bacterial GFP intensity of the data presented in (A-D).

In conclusion, the plasmid-based construct will be used in the following experiments. Note that for plasmid compatibility purposes, we subcloned this construct on a vector of the pRK2 ori / IncP $\alpha$  incompatibility family (pXP229, see Supplementary Table 2), while other binary vectors will belong to the pVS1 ori / pBR322 family<sup>241,242</sup>. This allowed us to retransform two different binary vectors in *A. tumefaciens*. Also, in future experiments involving *VirE2* variants (Chapter 4), we will leverage the VHH(cys-free) integrated in *virE2*- locus.

### 3.9 OTHER ADHESINS: DISPLAY OF RGD PEPTIDE AT THE SURFACE OF *A. TUMEFACIENS*

Finally, we wanted to not only target synthetic biomarkers such as GFP, but also endogenous ones. While VHH are extremely versatile to target any protein of interest, VHH targeting human biomarkers usually fall under intellectual property<sup>157,158</sup>. Instead, we investigated the ability to target eukaryotic cell surface integrins by displaying RGD tripeptides on the Atu5364 scaffold.

This approach emerged from the idea that VirB5, the tip protein of the T4SS pilus, could be homologous to *Helicobacter pylori* CagL, a pilus protein that functions as a specialized adhesin and bridges the T4SS to target cells<sup>210</sup>. However, VirB5 lacks the RGD-containing fragment of the protein, likely because *H. pylori* and other humans pathogens evolved human cells-specific adhesins<sup>210</sup>.

To compensate this absence *in trans*, here we fused the AGRGDSP sequence and HA-tag to the proline-rich linker and scaffold of Atu5364 as previously (Figure 32A). Upon induction and HA-tag staining, we observed robust expression of the RGD display at the surface of *A. tumefaciens* (Figure 32B).

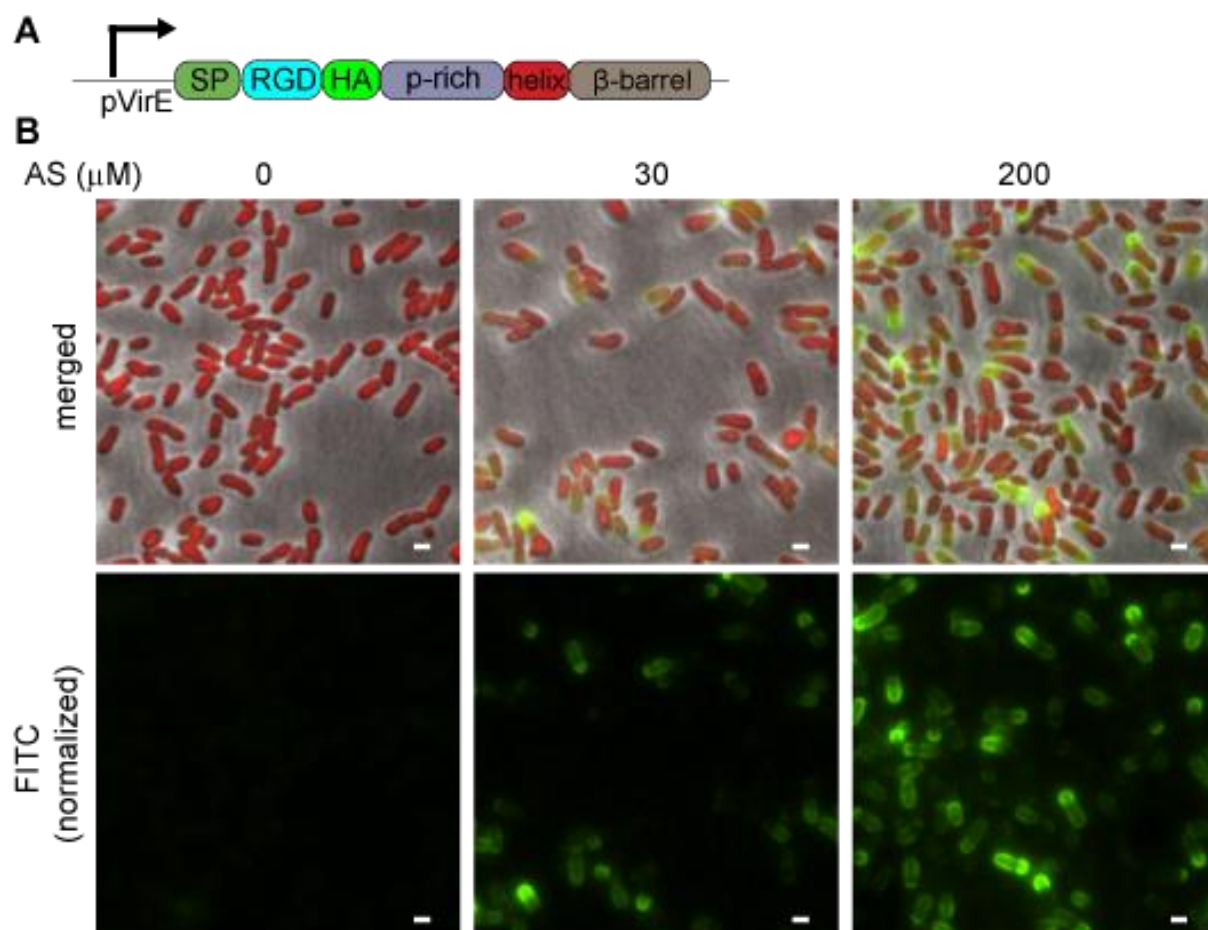


**Figure 32: Successful inducible RGD display at the surface of *A. tumefaciens***

(A) Schematic of the RGD display introduction. (B) *A. tumefaciens* mScarlet was retransformed with pVirE – RGD\_HA display and induced with AS for 8h prior to FITC-conjugated anti-HA staining (FITC). FITC intensity scale is identical between samples. Bars, 1  $\mu\text{m}$ .

## 3.10 DISCUSSION

### 3.10.1 Summary

The understanding of how *A. tumefaciens* adheres to target cells is only partial. Out of the five different bacterial exopolysaccharides characterized, only UPP mediates adhesion to biotic and abiotic surfaces upon contact<sup>105</sup>. It localizes unipolarly at the non-flagellated pole<sup>10</sup>. The structure of UPP is unknown except the fact it contains N-acetylglucosamine and N-acetylgalactosamine<sup>106</sup>. *A. tumefaciens* also harbors several flagella and ctp pili that mediate reversible attachment to surfaces<sup>107,108</sup>. Finally, a single adhesin has been described in *A. tumefaciens*: rhicadhesin, a  $\text{Ca}^{2+}$ -binding protein involved in pea root hairs binding<sup>110</sup>. Altogether, *A. tumefaciens*' limited capacity to deliver T-DNA to certain cell type such as monocots might be explained by limited or loose adhesion to target cells<sup>160,161</sup>.

Here we investigated *A. tumefaciens* Atu5364 autotransporter as a candidate scaffold for the display of synthetic passenger domains, aiming at designing a custom, target-specific adhesion system. *Atu5364* is localized on the cryptic pAt plasmid mostly involved in the soil and plant rhizosphere, and we found converging evidence that WT *Atu5364* has to be expressed under anaerobic conditions for efficient translocation (see Appendix 2). The N-terminal disulfide bond seems to prevent translocation in aerobic conditions: it is 13 amino-acids long, close to the upper limit of 18 amino acids reported by Leyton *et al.* in another autotransporter in *E. coli*<sup>33</sup>. Altogether, the actual function of *Atu5364* remains however to be thoroughly characterized.

In addition, we repurposed *Atu5364* in *A. tumefaciens*. We fused the scaffold to synthetic passenger domains of increasing structural complexity such as lectins and one enzyme. This highlighted some structural constraints about the passenger domains that can be translocated (see below). Finally, we managed to robustly display disulfide-free VHH anti-GFP and RGD peptide with the idea of targeting both synthetic and endogenous animal cell receptors. These insights will help designing synthetic adhesin display constructs enabling *A. tumefaciens* to bind to new target cells displaying the corresponding biomarker, e.g. synthetic or endogenous animal cell receptors. Synthetic adhesin displays could represent a key step towards rewiring *A. tumefaciens* for trans-kingdom gene delivery.

### 3.10.2 Limitations

By fusing the *Atu5364* scaffold to passenger domains of increasing structural complexity, we observed restrictions concerning the three-dimensional structure of synthetic passenger domains that can be displayed at the surface of *A. tumefaciens*.

First, we showed that disulfide bonds generating long loops such as FimH(C3-C44) or VHH(C24-C98) prevent display, in agreement with hairpin-based export of passenger model<sup>33,34</sup>. In this model, a linear translocation of the passenger domain is initiated by a hairpin formation close to the scaffold (Figure 3). Whether the translocation occurs through Bam (its closest homolog in *A. tumefaciens* is annotated Omp1, *atu1381*) or through the autotransporter itself, a loop would clog the transport process in both scenarios.

Second, we knocked out of the *dsbA* homolog *atu0800* to prevent disulfide bond formation (see Appendix 2, section 7.3). This resulted in mitigated results, as *atu0800* knockout greatly impacted bacterial shape and viability. We hypothesize that *atu0800* knockout has pleiotropic effects (including insensitivity to kanamycin), which explains the limited increase in passenger domain display efficiency.

Third, we uncovered that hexa-histidine tags dramatically prevent passenger display. We suggest that the succession of several bulky and charged histidine residues prevents passage through the beta-barrel. This might be specific to Atu5364 or more general: to our knowledge, hexahistidine tags have not been reported in other autotransporter systems.

Finally, the unfruitful display of *B. subtilis* lipase LipA, which does not contain disulfide bond, could indicate that the display of passenger domains is limited to proteins with secondary structures similar to the WT passenger domains, here, beta-strands. This could be explained by the absence of the alpha helix-specific chaperones that would keep LipA unfolded in the periplasm, preventing the linear translocation through the beta-barrel. LipA alpha-helices could also stall in the beta-barrel, as it is usually the secondary structure found within the beta barrel scaffold. Both hypotheses are in line with the preference of T5aSS for beta stranded passenger domain as reported by Rojas-Lopez *et al.*<sup>215</sup>.

In summary, under aerobic conditions, the Atu5364-based display is so far limited to short peptides and disulfide-free, beta-stranded proteins.

### 3.10.3 Conclusion

VHH are extremely versatile and can be engineered from naïve libraries towards almost any biomarker of interest<sup>154</sup>. Combined with our new VHH display system, these could be extremely useful to the plant engineer community as well as synthetic biologists trying to rewire *A. tumefaciens* DNA transfer to other cell types. The specific and tight binding to target cell surface biomarkers could represent a cornerstone towards broader *A. tumefaciens*-mediated trans-kingdom gene delivery.

### 3.11 MATERIAL AND METHODS 2

This section supplements Material and methods 1. Chemicals are purchased from Sigma, unless otherwise stated.

#### *Bacterial culture and induction*

*E. coli* were cultured at 37°C in LB containing either 100 µg/mL ampicillin (Huberlab), 50 µg/mL kanamycin, 25 µg/mL chloramphenicol, 50 µg/mL spectinomycin (Chemie Brunschwig). *A. tumefaciens* were culture at 28-30°C in LB containing 60 µg/mL gentamycin (Biochemica) or, when required, either 50 µg/mL kanamycin, 50 µg/mL spectinomycin or 100 µg/mL carbenicillin.

Unless otherwise stated, *A. tumefaciens* C58C1 pMP90 (GV3101, Accession number: GCA\_000092025.1)<sup>212</sup> was inoculated for 8h and early stationary cells were induced by addition of one volume of induction medium (IM) and 100 µM acetosyringone (AS) for virulence induction. Early stationary cells were induced overnight in LB by addition of cumic acid at 10 µM for cumic acid-inducible constructs.

#### *Composition of home-made media and agar plates:*

- 20x AB salts (per 200mL): 4 g NH<sub>4</sub>Cl, 1.2 g MgSO<sub>4</sub>·7H<sub>2</sub>O, 0.6 g KCl, 0.04 g CaCl<sub>2</sub>, 10 mg FeSO<sub>4</sub>·7H<sub>2</sub>O. Sterile filtered.
- 20x AB buffer (per 200mL): 12 g K<sub>2</sub>HPO<sub>4</sub>, 4 g NaH<sub>2</sub>PO<sub>4</sub>, pH to 7.0 using either KOH or H<sub>3</sub>PO<sub>4</sub>, as required, before autoclaving.
- IM: 1x AB salts, 0.5% glucose, 2 mM phosphate buffer pH 5.6, 50 mM 2-(4-morpholino)-ethane sulfonic acid (MES)
- Agrobacterium minimal medium: 1x AB salts, 1x AB buffer, 0.5% sucrose, antibiotics.
- ATGN plates: 1x AB salts, 1x AB buffer, 1% glucose, 1.5% noble agar, antibiotics
- ATSN plates: 1x AB salts, 1x AB buffer, 5% sucrose, 1.5% noble agar.

#### *Bacterial strain engineering*

For replicative plasmids, target bacteria were washed 3 times in bi-distilled water, concentrated 40 times and electroporated with 100 ng of plasmid, rescued for 60 min in SOC medium and

plated on the corresponding antibiotics plates. Electro-competent bacteria were snap-frozen in 15% glycerol solution.

For markerless genetic engineering of *A. tumefaciens*, we followed Morton and Fuqua, 2012<sup>240</sup>, using *E. coli* S17-1 for conjugation and pNPTS138 suicide vector (see supplementary Tables 2 and 3), with the following modifications: we added rifampicin (Axon Lab) at 25 µg/mL during selection and counterselection steps (ATGN and ATSN plates) to better kill donor *E. coli*. As kanamycin is inhibited by phosphate-buffered media, we increased the concentration to 1200 µg/mL during selection. LB plates containing rifampicin at 25 µg/mL and kanamycin at 300 µg/mL were sometimes more efficient than aforementioned ATGN plates. Mutants were screened by colony-PCR using primers flanking the knockin or knockout sites and validated by Sanger sequencing.

#### *Bacterial staining, titration and quantification*

Bacteria displaying VHH were washed with PBS and stained with recombinant GFP at 100 µg/mL for 10 minutes prior to two PBS washes. Bacteria harboring a HA tag or a 6x His tag were washed with PBS and stained with anti-HA antibody conjugated with FITC (Abcam ab1208) or anti-His antibody conjugated with phycoerythrin (Biolegend) at 10 µg/mL for 75 minutes in the dark on ice, washed once with PBS. For mScarlet-negative cells, viability was checked by concomitant addition of 10 µg/mL propidium iodide (PI) during staining. Wide field fluorescent pictures were taken under 1% agarose PBS pad at 100x and 1.5x lens magnification.

#### *Bioinformatics and modeling*

Protein sequences were submitted to the deep learning structure prediction online server RoseTTaFold, provided by the Baker lab: [robetta.bakerlab.org](https://robetta.bakerlab.org)<sup>213</sup>.

Protein sequences were submitted to the online deep neural network software SignalP-5.0 for signal peptide prediction ([services.healthtech.dtu.dk/service.php?SignalP-5.0](https://services.healthtech.dtu.dk/service.php?SignalP-5.0))<sup>214</sup>.

Average amino acid usage was extracted from [kazusa.or.jp/codon/cgi-bin/showcodon.cgi?species=260551](https://kazusa.or.jp/codon/cgi-bin/showcodon.cgi?species=260551).

#### *Tributyrin assay plates*

Tributyrin agar (Sigma 91015) emulsion plates were prepared according to the manufacturer's instruction with some modifications according to Kok *et al* 1993<sup>243</sup>. 10 g of neutral tributyrin

(Sigma 91010) was mixed 1:1 with a 10% gum Arabic solution and vortexed. This was added to 1 L of autoclaved the peptone/yeast extract/agar solution. The solution was vigorously mixed again and casted in petri dishes. Antibiotics and acetosyringone were added by diffusion 24h prior to the experiment.

2  $\mu$ L of bacterial culture were spotted on plates and let for three days at 30°C prior to imaging.

#### *Bacterial binding to sugar-coated plates*

Streptavidin-coated 96-well plates (Thermo) were coated with biotinylated multivalent sugars, linked by a polyacrylamide linker (PAA) (Glycotech) as follows: biotin-PAA-sugars were dissolved in 0.3 M sodium phosphate at 1 mg/mL. The negative control consists in biotin-PAA. Wells were pre-washed three times with solution 1: TBS, 0.1% BSA, 0.05% Tween20 (Fisher Bioreagent). Sugar stock was diluted 1 to 20 in the solution 1 and 100  $\mu$ L per well were used for the coating for 2 h at room temperature with shaking. Wells were washed twice with solution 1 prior to the addition of bacteria diluted 1 to 10 in HBSS for 30 min. Bacteria were washed twice with HBSS  $\text{Ca}^{2+}$   $\text{Mg}^{2+}$  prior to imaging at 20x magnification.

#### Transmission electron microscopy

Overnight cultures of bacteria were diluted 8 times in PBS prior to their transfer on electron microscope grids and negative stain. The samples were adsorbed on a glow-discharged carbon-coated copper grid 400mesh (EMS) washed with deionized water and stained with Uranyl Formate 0.75%.

Observation was made using a Tecnai Spirit electron microscope (Thermo) operated at 80 kV. Digital images were collected using a CCD camera Eagle (Thermo) 4098 X 4098 pixels, using a defocus range between -1.5 $\mu$ m and -2.5 $\mu$ m

#### *Binding to Arabidopsis thaliana roots*

Two-weeks old *A. thaliana* (columbia) were a gift from Prof Julia Santiago Cuellar, UNIL. Roots were immersed in 24-well plate in 1 mL of Murashige and Skoog medium supplemented with 2-(4-morpholino)-ethane sulfonic acid (MES) (Duchefa Biochemie) at 500 mg/mL or Induction medium [1 g/L  $\text{NH}_4\text{Cl}$ , 0.3 g/L  $\text{MgSO}_4$ , 0.15 g/L KCl, 0.01 g/L  $\text{CaCl}_2$ , 2.5 mg/L  $\text{FeSO}_4$ , 0.5% glucose, 2 mM MES] with slow shaking. Bacteria were added at a 1 to 1000 dilution with 40

$\mu$ M acetosyringone (AS) for 24h. Roots were washed twice in the same medium prior to imaging at 60x magnification on a coverslip and under a 1% PBS agarose pad.

## 4 *A. TUMEFACIENS* TARGETED ADHESION AND DELIVERY USING SYNTHETIC ADHESINS

---

Note: in this chapter, “VHH” alone implies cysteine-free VHH anti-GFP if not stated otherwise.

### 4.1 ABSTRACT

In the wild, *Agrobacterium tumefaciens* is a pathogen that delivers DNA using its type IV secretion system to wounded plants. It has been highly repurposed by plant engineers for gene delivery to a large scope of plant, yeast and fungal cells, and makes it an interesting candidate as a human gene delivery vector. However, some cell types such as plant monocots or animal cells show extremely low transformation efficiency. Interestingly, studies demonstrated a positive correlation between adhesion to recalcitrant plants and transformation efficiency. Hence, would an artificial binding of *A. tumefaciens* to non-natural target cells increase delivery?

Here we leveraged our synthetic adhesin display system at the surface of *A. tumefaciens*. On the host cell side, we displayed the target receptor at the surface of yeast and mammalian cells. In the presence of the adhesin pair, we observed a dramatic increase in bacterial adhesion to both cell types. In addition, we developed a highly sensitive split NanoLuc system that reported an increase in VirE2 transfer from the bacteria to mammalian cells when inducing the autotransporter display system. Both systems combined together represent a potent tool for *A. tumefaciens*’ T4SS biology, for plant biotechnologists seeking to target recalcitrant plant types and might be a cornerstone for bacterial-based gene editing therapies.

## 4.2 INTRODUCTION

### 4.2.1 *A. tumefaciens* T-DNA transfer

*A. tumefaciens* is a potent gene delivery vector for plants, yeasts and mushrooms<sup>244</sup>. Using its type IV secretion system, it delivers several ten of kilobases to target cells, and became the favorite bacterium for gene delivery in plant biotechnology<sup>245</sup>. To investigate and optimize T-DNA and helper protein uptake and translocation within the recipient cell, various genetic tools were developed such as T-DNA containing fluorescent reporter or resistance markers in addition to split fluorescent proteins fused to helper proteins<sup>246</sup>.

However, the molecular mechanisms of T-DNA transfer to the target cell is a disputed issue (Figure 6): either the T4SS creates a channel for direct cytosolic injection of T-DNA and helper proteins, or they target cells uptake them via a clathrin-mediated endocytosis mechanism<sup>129</sup>. Earlier in the infection process, the plant receptors targeted by the bacterium are also poorly characterized. For instance, there is no converging evidence of a target biomarker that would explain the large host range. In addition, some cell types such as plant monocots show extremely low transformation efficiency and require mechanical perturbation such as wounding, injection or sonication for efficient transformation<sup>203,207,209</sup>. This suggests that the bottleneck in the delivery process resides early on, potentially in the attachment phase. Consistent with this, Gaspar *et al.* characterized a plant extracellular glycoprotein, *Arabidopsis thaliana* AGP17, to be important for successful agrobacterial T-DNA delivery<sup>161</sup>. Also, Gürel *et al.* added cellulose to agrobacterial T-DNA transfer experiments and demonstrated a positive correlation between adhesion to recalcitrant plants and transformation efficiency<sup>160</sup>.

### 4.2.2 Motivation

*A. tumefaciens* delivered T-DNA to HeLa cells *in vitro* at an efficiency of about 1 cell in 50,000<sup>247</sup>. Later, *A. tumefaciens* stably transfected sea urchins embryos at 5% frequency<sup>248</sup>. Finally, scientists injected mice with *A. tumefaciens* carrying a mammalian T-DNA reporter. Bacteria survived and remained T4SS-competent for several days in the blood, but no gene transfer was detected in mice organs<sup>249</sup>. Did bacteria indeed bind to the target tissues? More generally would a synthetic binding of *A. tumefaciens* to non-natural target cells increase delivery?

Here, we leverage a synthetic nanobody (VHH) display in order to rewire the T4SS to new target cells (Figure 33). We managed to significantly increase *A. tumefaciens* binding to yeast and mammalian cells displaying the target surface receptor. In addition, we developed a sensitive split luciferase assay to quantify the transfer of helper proteins to target mammalian cell. This allowed us to optimize *A. tumefaciens*-mediated delivery to mammalian cells and to

refine hypotheses concerning the translocation mechanisms involved. Both systems combined together represent a potent tool for *A. tumefaciens*' T4SS biology, for plant biotechnologists seeking to target recalcitrant plant types and might be a cornerstone for bacterial-based gene editing therapies.

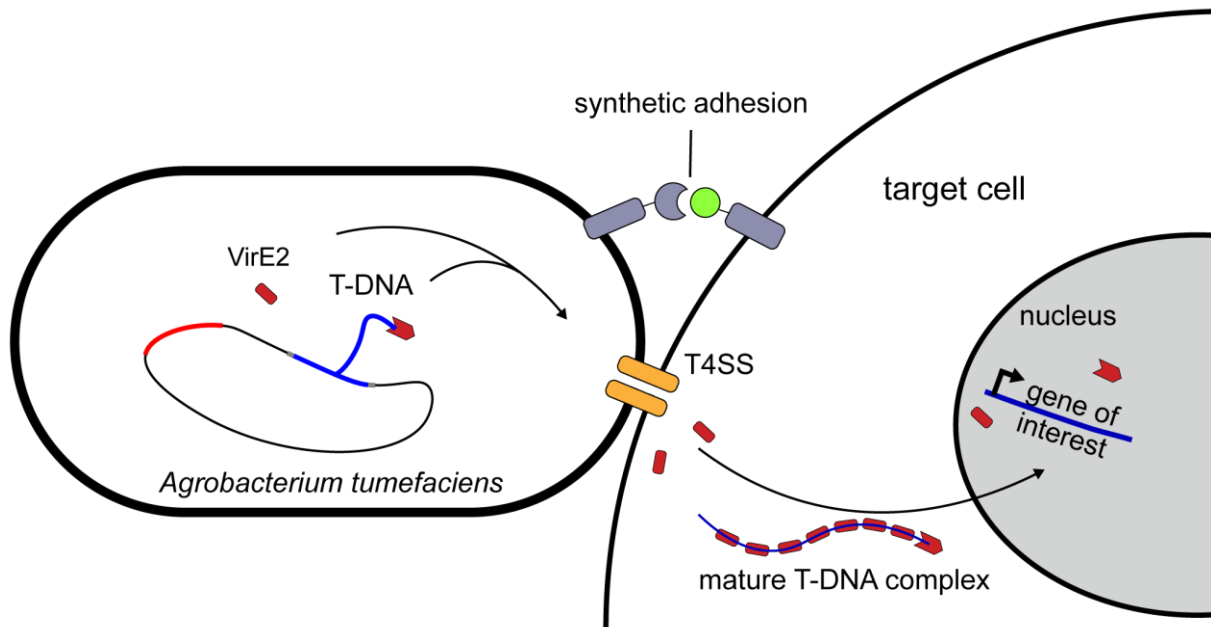


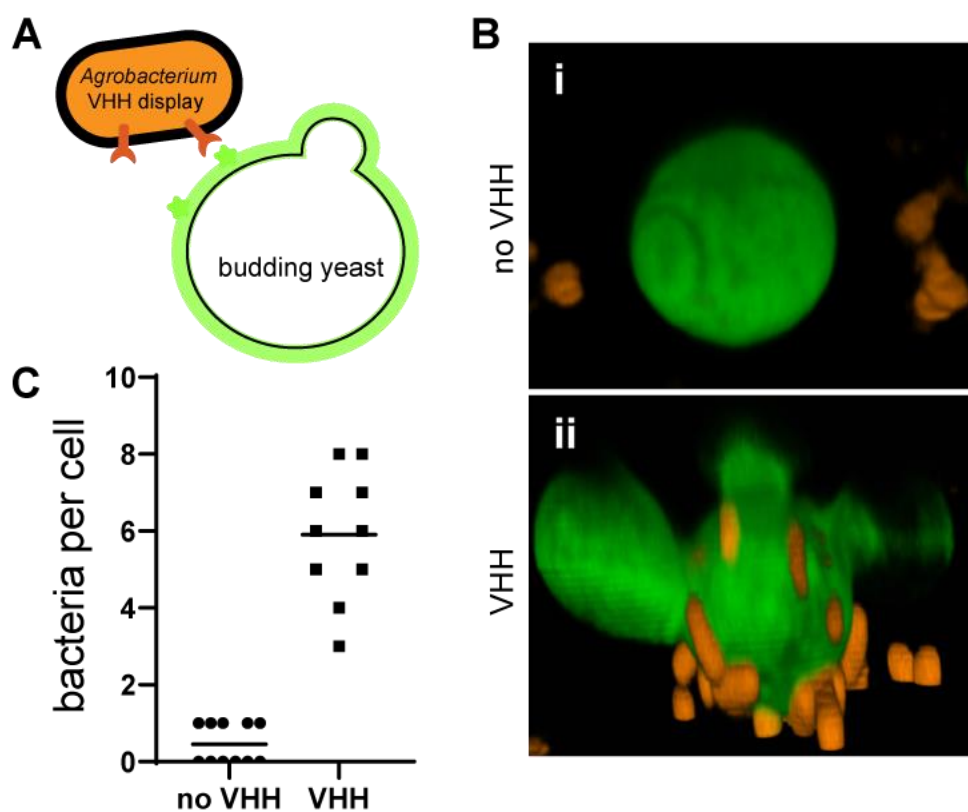
**Figure 33: Synthetic adhesion to rewire the T4SS of *A. tumefaciens* to new target cells.**

### 4.3 SYNTHETIC BINDING TO YEAST

Yeast cells have been used for several decades to study *A. tumefaciens*-mediated T-DNA transfer<sup>244,250</sup>. *Saccharomyces cerevisiae* helped for instance to decouple the role of *A. tumefaciens* helper proteins from target cells factors for T-DNA integration<sup>251</sup>. Large knockout libraries in yeast cells enabled rapid identification of host cell factors involved in the process, such as histone acetyltransferases and deacetylases<sup>252</sup>. In addition, split fluorescent protein enabled the localization of VirE2 translocated from bacteria to yeast<sup>253</sup>.

In this context, we constructed a GFP-displaying *S. cerevisiae*, as a target of *A. tumefaciens* VHH display (Figure 34A). We used *S. cerevisiae* eby100, a commonly used strain for yeast display libraries<sup>254</sup>. It overexpresses Aga1p that anchors into the cell wall and forms two disulfide bonds with Aga2p. Hence, we fused eGFP to Aga2p for displaying eGFP to the *S. cerevisiae* cell wall.

We induced both GFP-displaying yeast and *A. tumefaciens* with or without VHH display separately and mixed them prior to confocal microscopy imaging. A significant increase in the number of bacteria bound per yeast cells was observed in the presence of VHH vs. no VHH (Figure 34B, C). Confocal section further showed that bacteria displaying VHH strongly bound to the cell wall, to the extent of imprinting their shape into the yeast cell wall (Figure 34D, E).



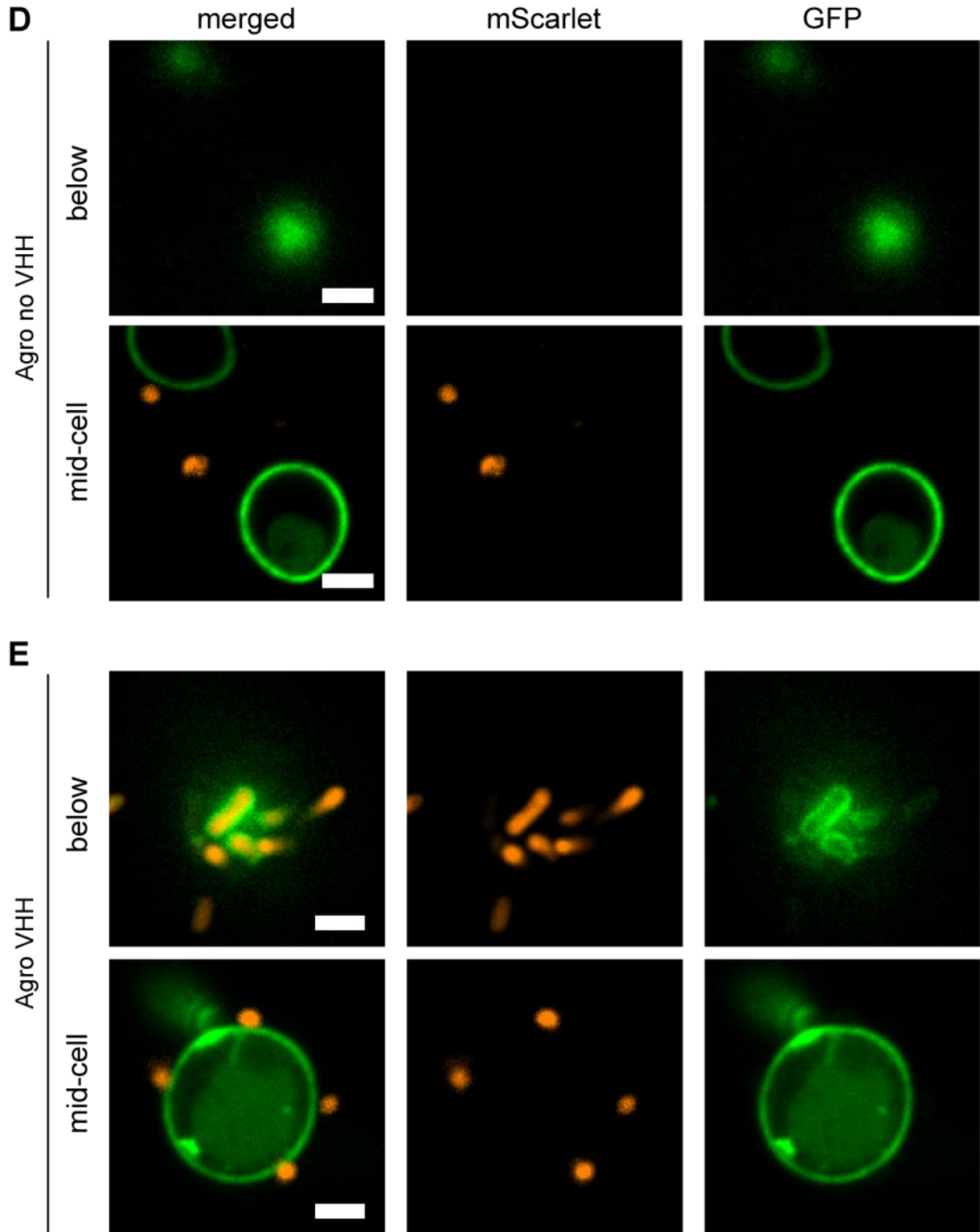


**Figure 34: Synthetic adhesion of *A. tumefaciens* VHH display to GFP-displaying yeast cells.**

(A) Schematic of the experimental setup. GFP is displayed in the yeast cell wall. (B) 3D visualization of *A. tumefaciens* (orange) binding to *S. cerevisiae* displaying GFP (green) in the absence (i) or presence (ii) of VHH display. (C) Quantification of the number of bound *A. tumefaciens* per yeast cell. Data from N=13 and N=10 yeast cells, respectively, from three independent fields of view. (D) Representative 2D confocal pictures of *A. tumefaciens* unable to bind to yeast cell. (E) Representative 2D confocal pictures of *A. tumefaciens* VHH display binding to GFP displaying yeast cell, both in the lower plane and to the side of *S. cerevisiae*. In the upper panels, bacterial shape imprint is visible. Bars, 2  $\mu$ m.

Usually, protocols for *A. tumefaciens*-mediated transformation in yeast suggest to force cell-cell contact by drying concentrated cell mixes on filters or directly agar plates (“puddle”)<sup>244,246</sup>. Here, we investigated whether the synthetic binding could increase *A. tumefaciens*-mediated T-DNA transfer. We retransformed the bacteria with T-DNA encoding for a kanamycin resistance cassette driven by a yeast promoter and followed by a terminator. We compared the puddle method to simply mixing both cell types in liquid, to leverage the synthetic binding. The state of the T-DNA (ssDNA and or dsDNA) required for integration is still disputed in yeast<sup>255</sup>. To promote dsDNA formation in yeast<sup>256</sup>, we included a co-infection condition: two bacteria expressing either the T-DNA cassette or its reverse complement were mixed and added to yeast. After cocultures, resistant yeasts were selected on plates containing a kanamycin analogue and cefotaxime to kill bacteria. Results presented in Figure 35 are representative of the outcomes obtained despite trying different infection media and conditions: we did not observe increase in transformation efficiency in the presence of synthetic cell-cell binding. This suggests that other predominant bottlenecks exist and prevent T-DNA transfer, one of them could be the cell wall mechanically blocking T-DNA transfer.

Also, on the long term, the concentration of free GFP in the yeast supernatant increases (not shown). While we systematically washed *S. cerevisiae* prior to co-culture, GFP leakage is something we cannot control during puddle infection for instance. Consequently, such leakage would have an auto-inhibitory effect on synthetic adhesion, which could explain the absence of effect of VHH on T-DNA resistance gene transfer.

For the infection in liquid condition, the GFP-containing supernatant could be regularly changed to prevent self-inhibition of the synthetic binding. The subnanomolar dissociation constant of VHH would however require thorough washing steps including centrifugations that could bias the results.

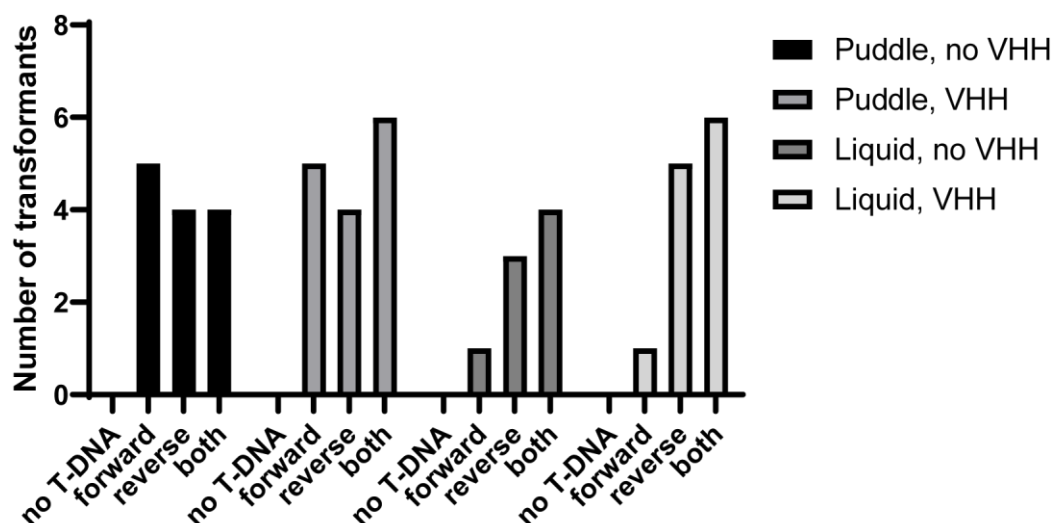


**Figure 35: Synthetic binding does not increase stable T-DNA integration.**

Quantification of the T-DNA resistance gene transfer efficiency into yeast. Yeast displaying GFP were infected by *A. tumefaciens* retransformed or not with pVirE – VHH(cys-free) display and a binary T-DNA vector encoding for a kanMX forward or reverse complement cassette. “Both” means yeast were co-infected by both bacterial strains to provide forward and reverse strains. Infections were either performed at high cell density by spotting on agar plates (puddle) or in liquid, where interactions are not forced. The graph represents one biological replicate among combinations of resistance cassette, cell numbers and media tested (see Material and methods 3). No significant increase was observed from no VHH to VHH-displaying *A. tumefaciens*.

#### 4.4 SYNTHETIC BINDING TO MAMMALIAN CELLS

Mammalian cells don’t have a cell wall and represent an attractive target for therapeutic gene delivery. In this context, we generated HEK293T constitutively displaying GFP cells and doxycycline-inducible GFP-display HeLa cells (see Material and methods 1 and 3). We first repeated the flow experiments on GFP-displaying HeLa cells using *A. tumefaciens* VHH display, but we did not observe significant binding compared to negative controls, as opposed to the findings with *E. coli* VHH display (chapter 2). We hypothesize that *A. tumefaciens*’ 4-6 flagella, its pili, or the bacterium’s microenvironment might be thicker than *E. coli*’s and the contact duration too short to enable VHH engagement. Consequently, we opted for static co-cultures.

We incubated HeLa cells with *A. tumefaciens* either retransformed with an empty vector, displaying cysteine-free VHH anti-mCherry or anti-GFP. After washing of unbound bacteria, we acquired confocal z-stacks and quantified the average number of bacteria per mammalian cell (Figure 36A-C). We observed a significant increase in the number of bound bacteria only when both adhesins were present. We prevented binding of bacteria to mammalian cells by pre-saturating VHH anti-GFP at the surface of bacteria by addition of soluble GFP.

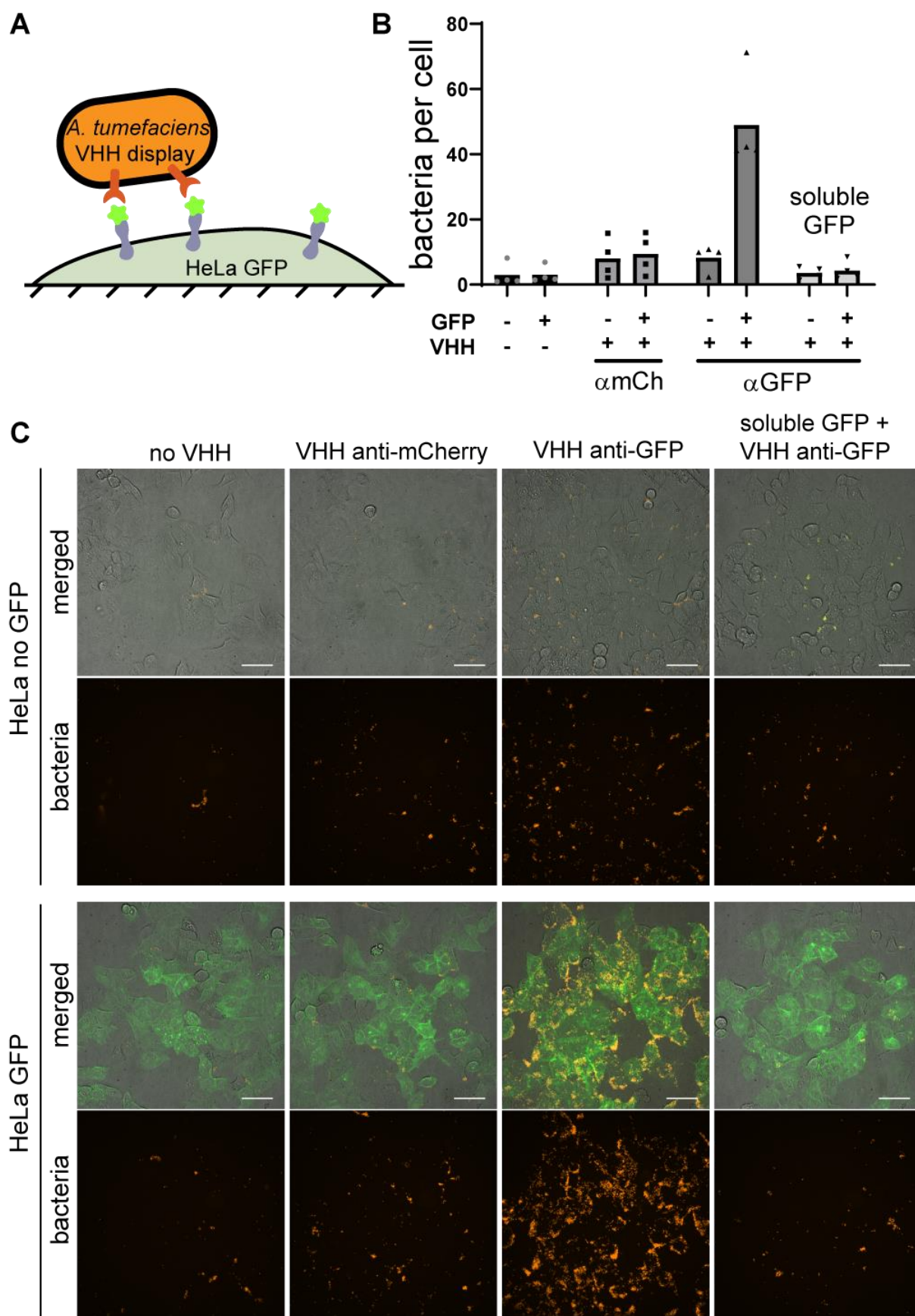
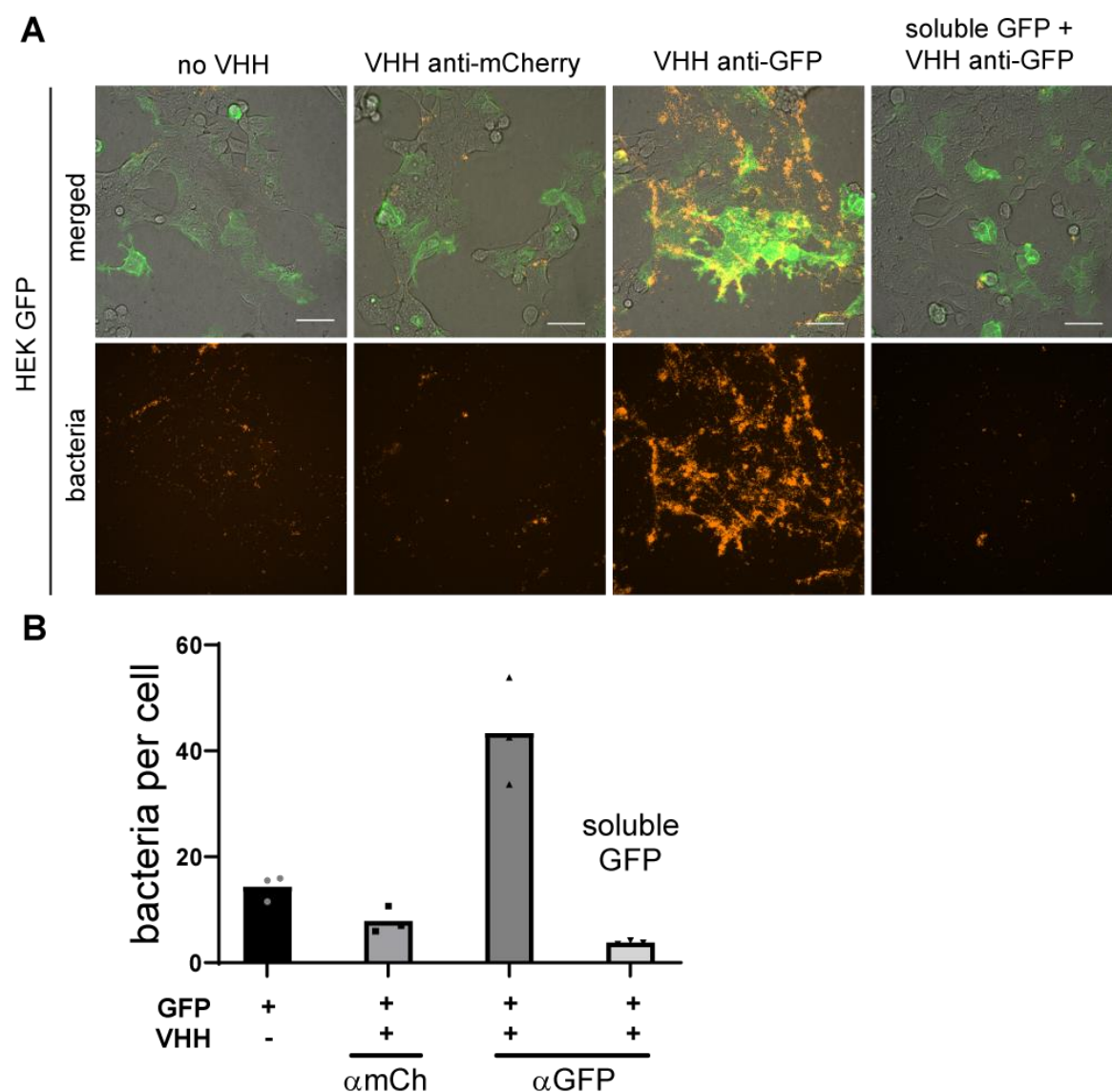


Figure 36: Synthetic adhesins increase binding of *A. tumefaciens* to HeLa cells.

(A) Schematic of the experimental setup. HeLa display GFP using a transmembrane anchor. (B) Quantification of the average number of bacteria per HeLa cells. HeLa were uninduced (GFP -) or induced for GFP display (GFP +), *A. tumefaciens* was retransformed with an empty vector (VHH -), pVirE – VHH anti-mCherry(cys-free) display (VHH +  $\alpha$ mCh) or pVirE – VHH anti-GFP(cys-free) display (VHH +  $\alpha$ GFP). In the last set of columns, soluble recombinant eGFP was added to prevent binding by saturating VHH receptors. Datapoints represent the means of four biological replicates. (C) Representative maximum intensity projections of *A. tumefaciens* binding to HeLa cells in the different conditions quantified in (B). Bars, 50  $\mu$ m.

We repeated the experiment with constitutively GFP displaying HEK cells and validated the fact that both adhesins are required for tight binding (Figure 37A, B).



**Figure 37: Synthetic adhesion of *A. tumefaciens* to HEK cells.**

(A) Representative maximum intensity projections of *A. tumefaciens* binding to GFP-displaying HEK cells in the different conditions quantified in (B). Bars, 50  $\mu$ m. (B) Quantification of the average number of bacteria per GFP-displaying HEK cells. *A. tumefaciens* was retransformed with an empty vector (VHH -), pVirE – VHHamCherry(cys-free) display (VHH +  $\alpha$ mCh) or pVirE – VHH(cys-free) display (VHH +  $\alpha$ GFP). In the last column, soluble recombinant eGFP was added to prevent binding by saturating VHH receptors. Datapoints represent the means of three biological replicates.

## 4.5 A. *TUMEFACIENS*-MEDIATED T-DNA TRANSFER IN MAMMALIAN CELLS

Since we obtained robust *A. tumefaciens* binding to mammalian cells, we proceeded towards the assessment of bacterial T-DNA delivery. We started by checking the ability of mammalian cells to process ssDNA into dsDNA prior to transcription and translation of reporter genes.

### 4.5.1 ssDNA can be processed and transcribed by mammalian cells

*A. tumefaciens*' T-DNA is a linear and single-stranded DNA (ssDNA). As such, transcription by eukaryotic cells is not expected to occur. In fact, transcription factors and DNA-dependent RNA polymerase operate on double-stranded DNA (dsDNA)<sup>257–259</sup>. Different models were proposed in plant cells to explain the transient expression of T-DNA (before genomic integration), such as the formation of T-circles or T-strand priming by short endogenous primers<sup>139,256</sup>.

In mammalian cells, Pelczar *et al.* chemically transfected synthetic T-DNA and reported stable integration in HeLa cells using a hygromycin resistance marker<sup>260</sup>. Random integration is however an event we would like to avoid on the long run to avoid carcinogenicity. Here instead, we wanted to assess if the ssDNA to dsDNA conversion could occur in mammalian cells for transient expression of T-DNA reporters. We produced synthetic T-DNA *in vitro* encoding the a constitutive GFP expression cassette surrounded by right and left borders (RB, LB) (Figure 38A, Material and Methods 3). Next, we transfected synthetic T-DNA forward and reverse complement separately in HeLa cells and detected GFP signal (Figure 38Bi, ii). When we co-transfected both forward and reverse complement strands, or when we transfected dsDNA from the PCR, we observed a higher signal intensity than with one ssDNA alone (Figure 38Biii, iv).

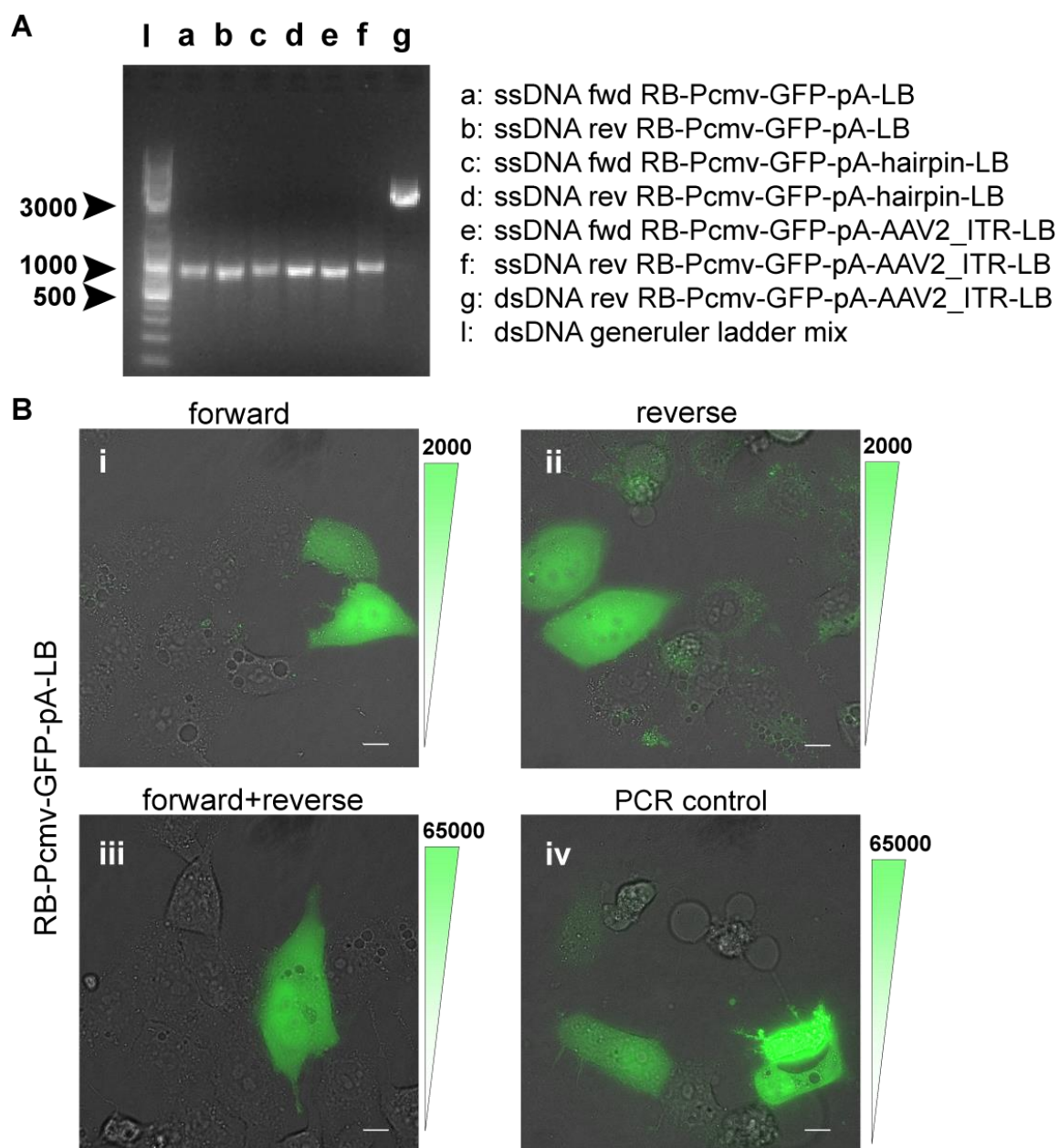


**Figure 38: ssDNA-transfected cells produce a GFP reporter.**

(A) Synthetic T-DNA forward and reverse complement were produced using Guide-it Long ssDNA Strandase kit and purified by gel extraction. They included a self-priming 10 base-pairs hairpin (hairpin) or an Adeno-associated virus 2 inverted terminal repeat (AAV2\_ITR). (B-E) Synthesized T-DNAs or dsDNA T-DNA control (PCR) were transfected by lipofection into HeLa cells and observed by fluorescence microscopy. Fluorescence intensity scale is displayed on the right-hand side. Bars, 10  $\mu$ m.

As ssDNA, T-DNA is subject to degradation by exonucleases. The 5' end is slightly better protected by covalently bound VirD2 than the 3' end<sup>139</sup>. Inspired by adeno-associated viruses (AAVs), we imagined a strategy to leverage such degradation in order trigger self-priming. In single-stranded AAV DNA, inverted terminal repeats (ITRs) generated a large T-shape structure that enables the 3' end to fold back on a palindromic sequence and initiates priming for replication (Figure 39A)<sup>261</sup>. To mimic this process, we introduced either a short hairpin

generated by 10 base-pair palindromes separated by a 5 base-pair loop (gggtatacgcAATAAgcgtataccc), or an AAV2 ITR in front of the right border. We produced ssDNAs, transfected them as previously and measured GFP signal (Figure 39B, C). We observed a slight increase in signal compared to no-hairpin ssDNA, but not to the same extent as dsDNA controls (Figure 38Biii, iv).

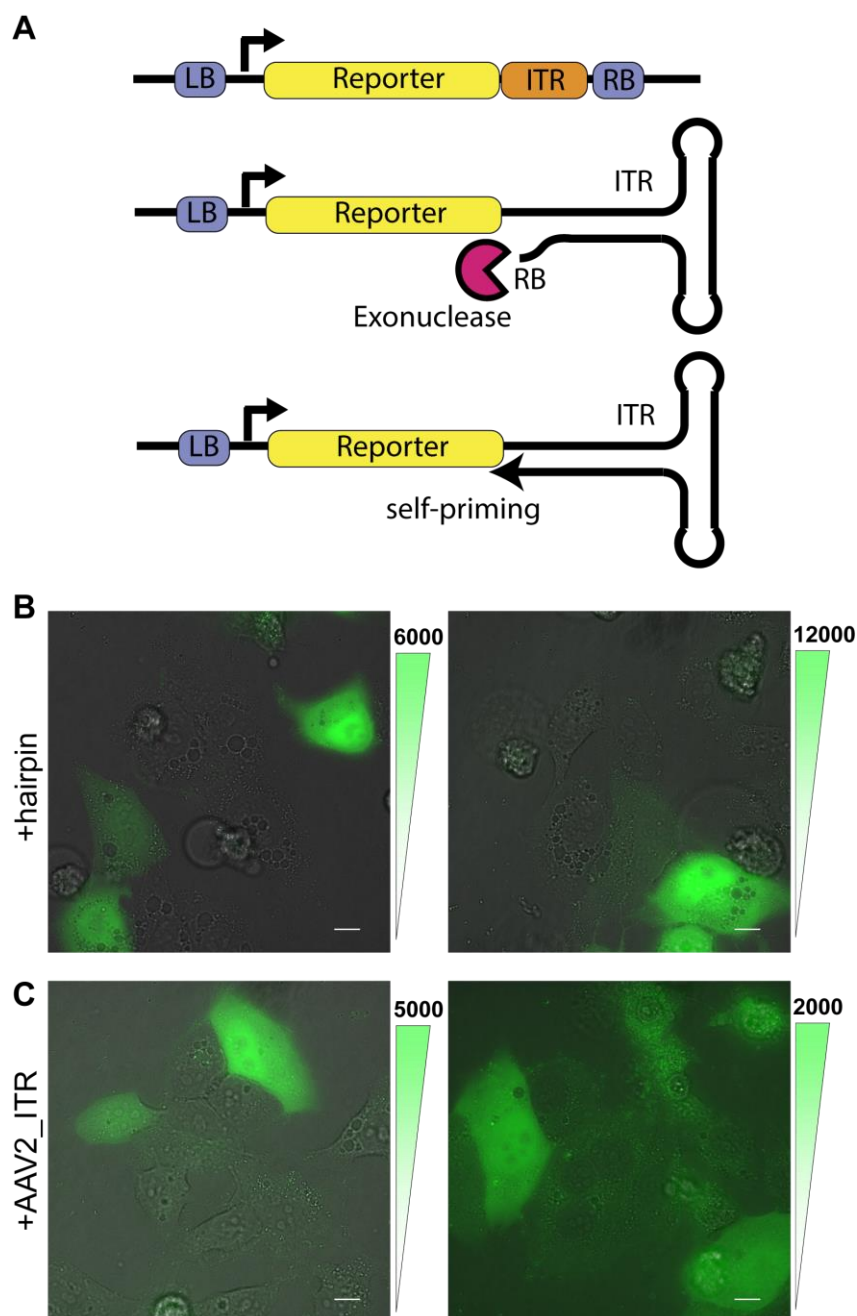


**Figure 39: Hairpins favoring self-priming of ssDNA in cells slightly increase signal**

(A) Schematic of the expected process. ssDNA contains a short hairpin or an AAV2 ITR (here) between the reporter gene and the right border (RB). ssDNA exonuclease digests the RB. The dsDNA ITR primes the remaining ssDNA to dsDNA. (B-C) Synthesized T-DNAs containing a short hairpin or a complete AAV2 ITR were transfected by lipofection into HeLa cells and observed by fluorescence microscopy. Fluorescence intensity scale is displayed on the right-hand side. Bars, 10  $\mu$ m.

#### 4.5.2 *A. tumefaciens* T-DNA transfer in HEK and HeLa cells

Since HeLa cells are able to process synthetic T-DNA to express their encoded reporter transgene, we moved on to try to deliver agrobacterial T-DNA. We generated two mammalian T-DNA reporters encoding turboRFP (forward and reverse complement) that we separately retransformed into *A. tumefaciens* with or without VHH display. We focused on monitoring transient transformation efficiency as this reports any incoming T-DNA, integrated or not in the genome.

We infected GFP-displaying mammalian cells with bacteria in different conditions (by screening medium composition, pH, duration and multiplicity of infection). Figure 40 depicts the “best” condition for which we could observe rare RFP-positive HEK cells. The synthetic binding did not significantly increased the efficiency, which remained close to the one reported by Kunik *et al.* in HeLa cells<sup>247</sup>. The cell overgrowth prevented the long-term follow-up in order to determine whether RFP resulted from transient expression or random integration in the genome. We did not observe any RFP-positive HeLa cell in any of the conditions.

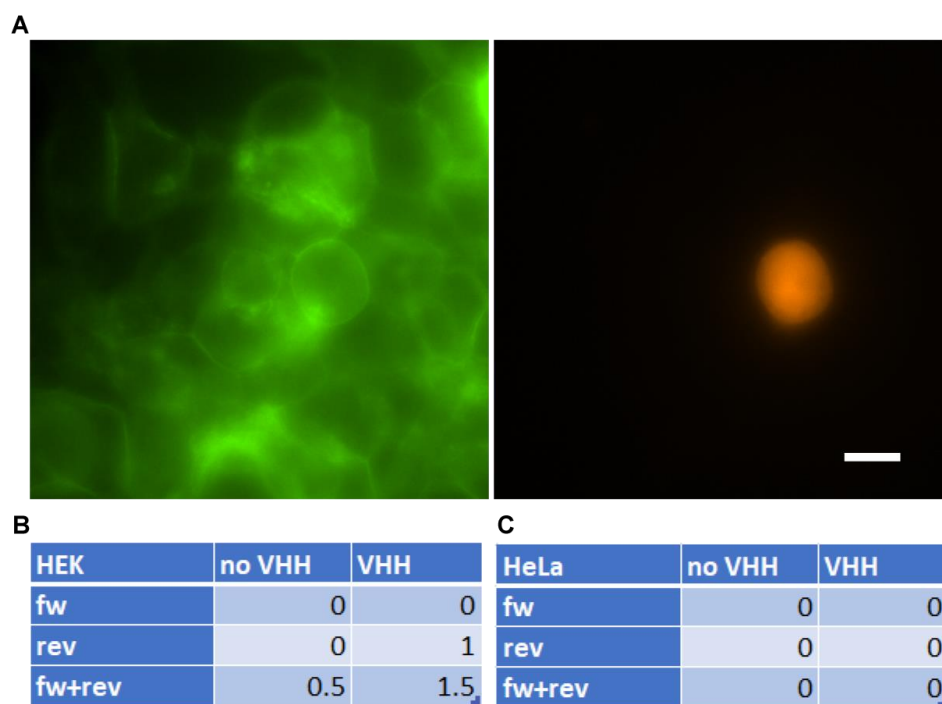


**Figure 40: Monitoring *A. tumefaciens*-mediated DNA transfer using a fluorescent reporter shows limited impact of VHH.**

(A) GFP-displaying HEK were infected with two *A. tumefaciens* strains containing pVirE – VHH(cys-free) display and a binary vector coding for either T-DNA = turboRFP forward (fw) or T-DNA = turboRFP reverse complement (rev). One red fluorescent cell can be seen in the right panel. Bar, 10  $\mu$ m. (B-C) Quantification of the *A. tumefaciens*-mediated gene transfer efficiency in GFP-displaying HEK cells (B) and GFP-displaying HeLa cells (C) from two representative experiments. Numbers report the average number of RFP-positive cells per well of 96-well plate (around 50,000 cells) for N=2 wells.

We also tried to add hairpins or AAV2 ITR to agrobacterial T-DNA transfer, which did not significantly increase transformation efficiency of GFP reporters (before the development of the VHH display, not shown). This could be tried again with the turboRFP reporter and the synthetic adhesins, but we cannot exclude that ss-DNA to ds-DNA conversion would occur before and interfere with the T4SS-secretion, or that AAV2 ITR T-shape would stall inside the T4SS machinery. Given the limited increase in transient expression from *in vitro*-produced T-DNA with hairpins or AAV2 ITR (Figure 39), we rather focused on the identification of other potential bottlenecks.

For instance, T-DNA might reach the mammalian cytosol but could stall due to the lack of proper transport or could be rapidly degraded. In order to identify if any T-DNA would reach the mammalian cytosol, we tried to adapt an RNA Fluorescent in situ hybridization (FISH) method for the detection of ssDNA (Figure 41).

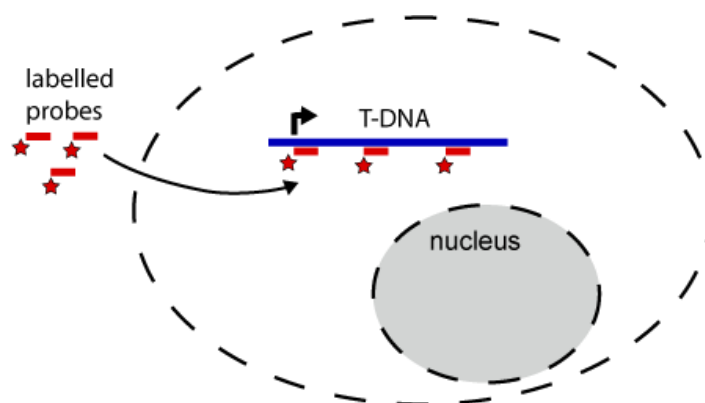


**Figure 41: ssDNA FISH concept.**

Cells are fixed and permeabilized, proteins are heat-denatured and fluorescently-labelled oligonucleotides complementary to the T-DNA are added.

Briefly, we designed fluorescently labeled oligonucleotide probes targeting ssDNA sequences. We transfected HeLa cells with *in vitro*-produced ssDNA or infected them with *A. tumefaciens* for agrobacterial T-DNA transfer. The RNA-FISH protocol was then performed with modifications (see Material and methods 3). Overall, we measured a signal of about twice the background in cells transfected with *in-vitro* synthesized ssDNA (Figure 42B). It was however impossible to distinguish signal stemming from bacteria, mammalian cells or unspecific staining (Figure 42A-C). Finally, the protocol includes harsh treatments that degrades membranes and proteins such as GFP, which would further reduce the precision of the readout (Figure 42D).

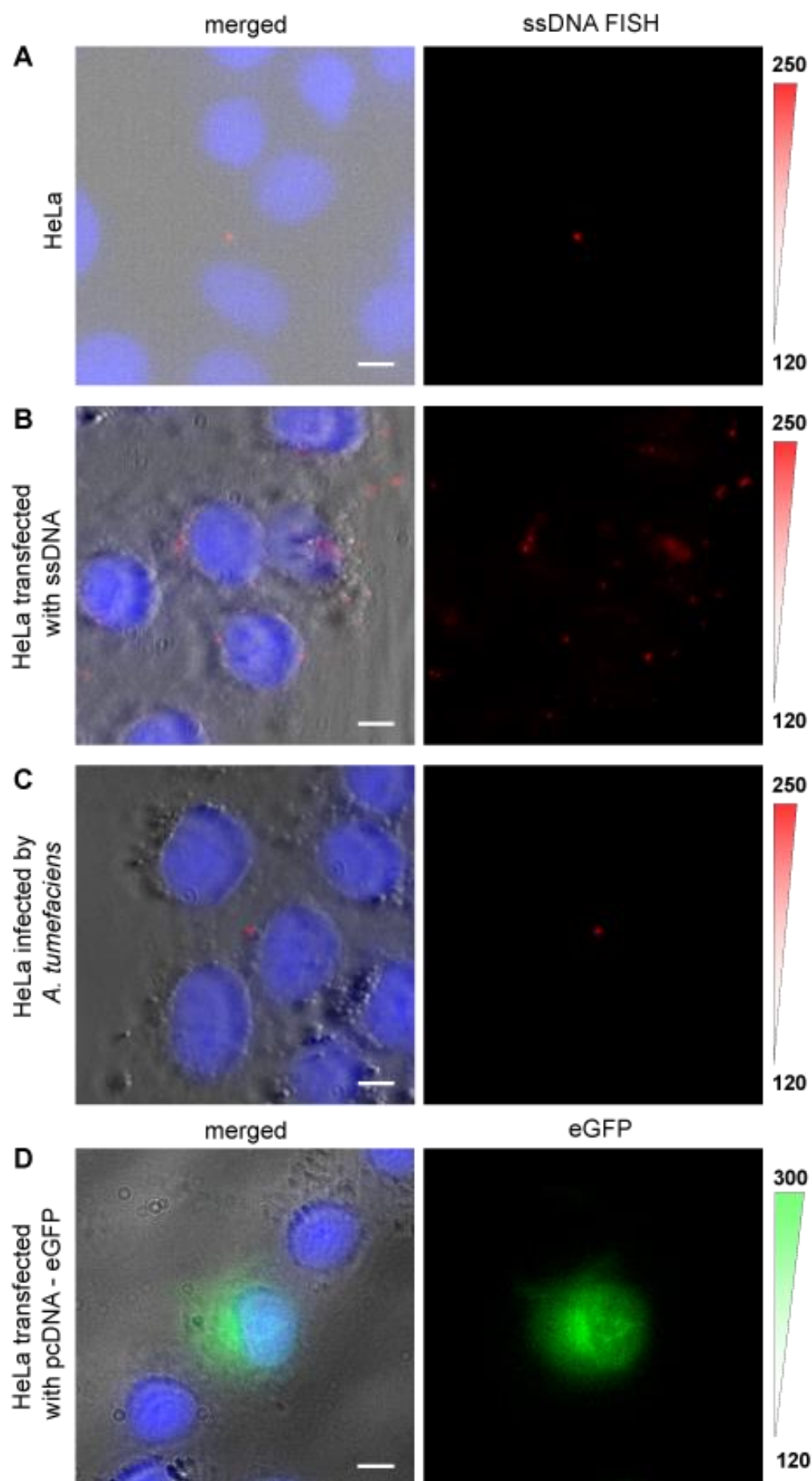


**Figure 42: ssDNA FISH gives low signal and does not allow precise T-DNA localization nor distinction from noise.**

(A-C) ssDNA FISH protocol was tried to detect ssDNA sequences coding for eGFP, in HeLa (A), HeLa transfected with in-vitro synthesized ssDNA (B) or HeLa infected by *A. tumefaciens* retransformed with T-DNA pCMV – eGFP (C). In all cases, low signal of about twice the background can be measured and cannot safely be attributed to specific signal. (D) HeLa cells transfected with pCMV – eGFP and treated with the same protocol (without FISH probes) show extremely low GFP signal at the end of the protocol, which would further impair clear 3D localization of any FISH signal. Bars, 10  $\mu$ m.

While some signal amplification methods exist, such as using secondary probes binding to overhang of sequence-specific probes, we judged the preliminary data to be insufficient to proceed further in this direction.

## **4.6 REPAIR TEMPLATE FOR CRISPR/Cas9 CUTS**

We looked for a more sensitive technique to report the presence of ssDNA in cells. Figure 38 showed a 30-fold increase in transient expression in the presence of both forward and reverse complement strand, compared to one strand only. This suggests that most ssDNA could be present but not transcribed when using fluorescent T-DNA reporters.

On the other hand, short ssDNA is a good repair template for CRISPR/Cas9 dsDNA breaks<sup>262</sup>. Consequently, we designed an experiment where the T-DNA consists in a 72 base pairs repair template for a frameshifted start codon of *NanoLuc* luciferase (Figure 43A). The frameshifted start codon is targeted by CRISPR/Cas9 to trigger a dsDNA break, which can be repaired using the short ssDNA harboring the correct sequence.

To probe this, we co-transfected GFP-displaying HeLa cells with the frameshifted *NanoLuc* and a second vector encoding Cas9 and guide RNA (gRNA) targeting the mutated start region (two gRNA tried). We then either infected cells with *A. tumefaciens* encoding the repair T-DNA, or chemically transfected them with the corresponding 72 bp-long oligonucleotides. The positive controls using the synthetic 72-bp template (last three conditions, compared to grey baseline, Figure 43B) show indeed an increase in the *NanoLuc* signal, suggesting that a successful repair of the *NanoLuc* gene. However, cells infected by *A. tumefaciens* showed a decrease in the luciferase activity, most likely due to cell toxicity and reduced cell growth (2<sup>nd</sup>, 3<sup>rd</sup> and 4<sup>th</sup> visible columns compared to the 1<sup>st</sup> column, Figure 43B). Finally, the baseline is high (“frameshifted reporter and Cas9+gRNA”), which can be explained by two different mechanisms. First, CRISPR/Cas9 cuts can result in random insertion and deletion by non-homologous end-joining<sup>263</sup>. Statistically, every fourth insertion would insert the missing thymine and restore *NanoLuc* start codon and frame. Second, leucine at position 4 is encoded by CUG,

a codon reported to be 19% efficient to initiate translation compared to AUG in HEK cells in a firefly luciferase assay<sup>264</sup>.

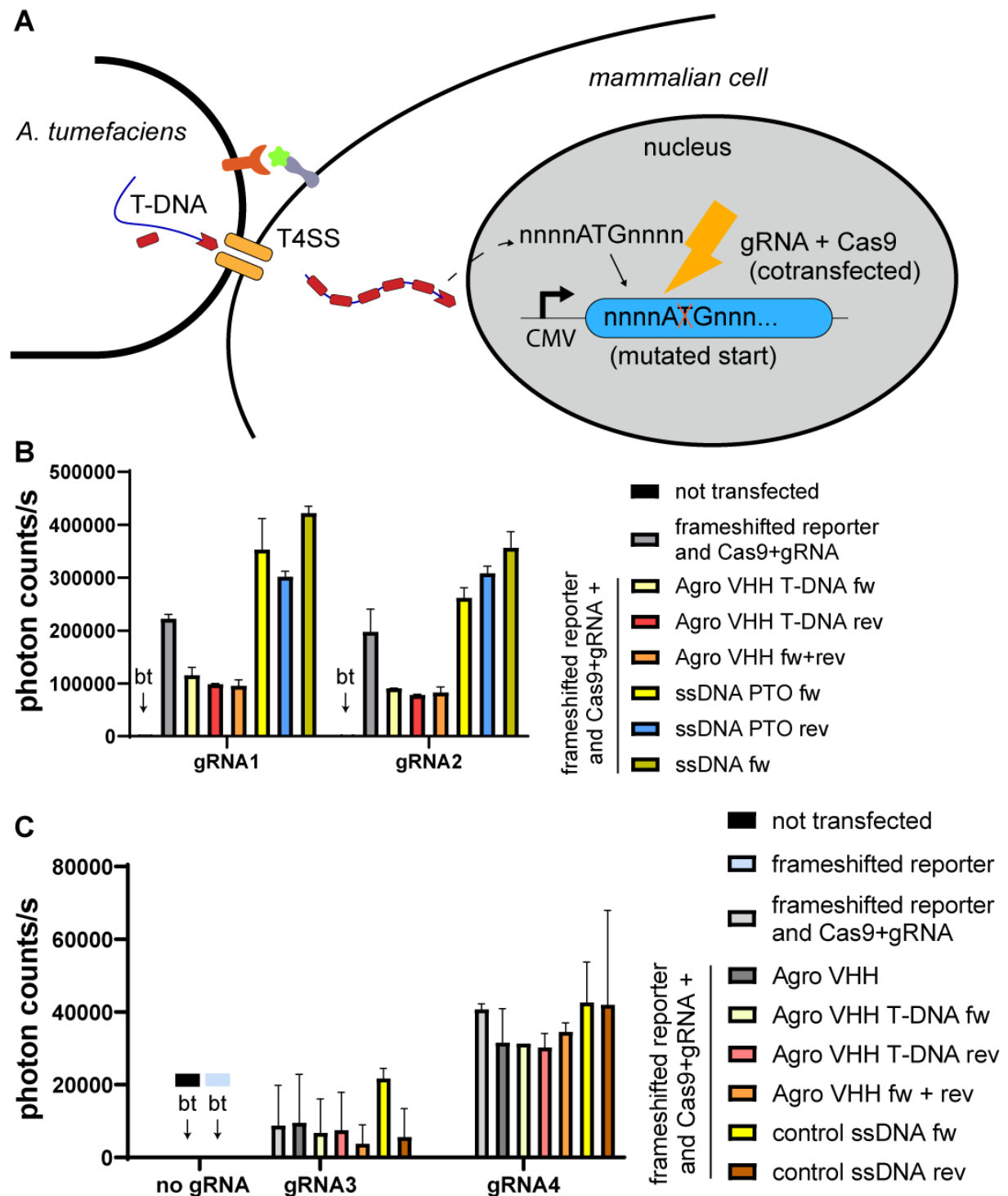


**Figure 43: Agrobacterial T-DNA is not used as ssDNA repair template for CRISPR-Cas9-induced cuts.**

(A) Schematic of the experiment. Mammalian cells are co-transfected with a NanoLuc reporter with a mutated start codon and a plasmid encoding Cas9 and a guide RNA (gRNA) targeting the mutated start site. T-DNA encodes a repair template that can be used by the cells to fix the mutated start codon. (B) NanoLuc activity in HeLa cells. “frameshifted reporter and gRNA+Cas9 only” consists in cells transiently co-transfected with pCMV – NanoLuc with a start codon ATG mutated into AG, and either gRNA1+Cas9

or gRNA2+Cas9 that targets the frameshifted start site. The next samples are co-transfected with the same set of plasmids and are additionally: infected by *A. tumefaciens* displaying VHH and harboring a 72 base-pairs repair T-DNA template matching the forward strand (Agro VHH T-DNA fw), the reverse complement strand (Agro VHH T-DNA rev) or both strains (Agro VHH fw+rev). Positive controls consist in co-transfection of ssDNA stabilized with Phosphorothioate modification (ssDNA PTO fw or rev) or non-stabilized (ssDNA fw). (C) NanoLuc activity in HeLa cells transfected with a NanoLuc containing a 2 bp frameshift after the 213<sup>th</sup> base pair. “gRNA3” and “gRNA4” target the surrounding of this frameshift. The additional control “frameshifted reporter” compared to the next datapoint shows that indels are stochastically fixing the gene. The additional sample “Agro VHH” that does not contain T-DNA sequence lead to similar expression levels as *A. tumefaciens* with T-DNA. Here the ssDNA controls do not restore NanoLuc production. (B-C). “bt”, below display resolution. Error bars represent the standard deviation of technical duplicates.

To avoid both the non-AUG start of transcription and the stochastic repair of the missing base, we two base pairs within the NanoLuc sequence after the 213<sup>th</sup> base pair. This generates a frameshift at about one third of the protein sequence in the middle of an alpha helix (pdb 5IBO<sup>265</sup>). We re-designed two new gRNA targeting the frameshifted sequence and repeated the experiment with this set of plasmid and *A. tumefaciens* VHH display encoding repair T-DNA for this frameshift. Overall, we measured a signal about 10-fold lower than previously (Figure 43C). We included two additional controls: “frameshifted reporter” and “Agro VHH” without T-DNA. The increase in signal from “frameshifted reporter” to “frameshifted reporter and Cas9+gRNA” (light blue, below threshold, and light grey bar, Figure 43) allowed us to conclude that the baseline in absence of repair ssDNA is due to stochastic repair of the gene by restoring the correct frame (e.g. insertion of 2 correct bases). Also, there was no visible difference between *A. tumefaciens* encoding for no T-DNA compared to the other ones, leading to the conclusion that T-DNA does not reach the nucleus or, if it did, remains too complexed by the helper proteins to be used as a repair template.

## 4.7 HELPER PROTEIN LOCALIZATION IN MAMMALIAN CELLS

Another potential bottleneck for successful T-DNA transfer within the mammalian cell could be the improper functioning and localization of key helper proteins. For instance, VirD2 gets imported in the plant nucleus, while according to the most recent literature, VirE2 remains cytosolic<sup>124,125,127</sup>. Similar localization would be required in mammalian cells for proper T-DNA protection and nuclear import.

To verify this we cloned WT VirE2 and a N-terminally tetra-cysteine-tagged VirD2 in mammalian expression vectors<sup>266,267</sup>. We transiently transfected HeLa cells and observed VirE2 by direct anti-VirE2 antibody staining and visualized it in HeLa cell’s cytosol (Figure 44A). We revealed VirD2 by staining of the tetra-cysteine-tag and showed nuclear localization (Figure 44B). Altogether, these results show that both helper proteins reside in the same cell

compartment as in plant cells, suggesting that their localization is not a bottleneck in mammalian cells. This also corroborates findings from Pelczar *et al.*, where both recombinant VirE2 and VirD2 increased the transfection efficiency of mammalian cells transfected with synthetic T-DNA<sup>260</sup>.

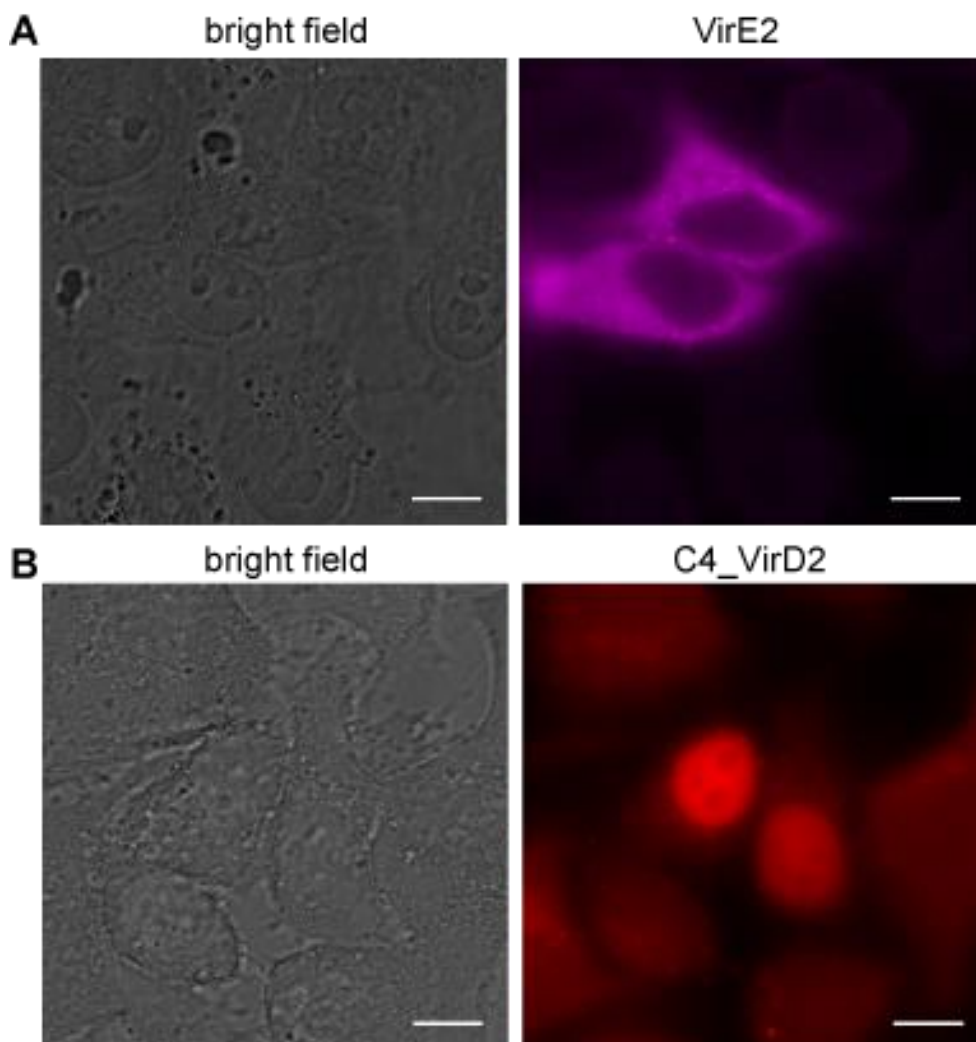


**Figure 44: VirE2 and VirD2 properly localize mammalian cell compartments.**

(A) VirE2 localizes in the mammalian cell cytosol. HeLa cells were transiently transfected with pCMV - VirE2 and stained with anti-VirE2 antibody. (B) VirD2 localizes in the mammalian cell nucleus. HeLa cells were transiently transfected with pCMV - C4\_VirD2 and the tetracysteine tag was stained. Bars, 10  $\mu$ m.

## 4.8 HELPER PROTEIN TRANSFER MONITORING

### 4.8.1 Split mCherry

So far, it is still unclear whether any T-DNA or helper proteins get translocated from the bacteria to the target mammalian cells. The DNA-based approaches for visualization of the incoming

One approach developed in plant and yeast cells for *A. tumefaciens*-mediated transfer is the use of split fluorescent proteins<sup>132,246</sup>. VirE2 is the most abundant Vir protein and is often fused to the short part of the split fluorescent proteins by insertion into an internal permissive site<sup>128,144</sup>. Li *et al.* used the VirE2 sequence derived from another tumor-inducing plasmid, pTiBo542 and fused at position P54. Here we work with VirE2 from pTiC58: from sequence alignment and structure prediction visualization, we mapped the permissive site to VirE2 from strain C58 to be proline 61 (Figure 45).



Since the GFP channel is already used for synthetic adhesion, we opted for the third generation of split superfolder mCherry (sfCherry3C) system<sup>123</sup>. We cloned pVirE – sfCherry11::VirE2, which contains the 11<sup>th</sup> beta strand of sfCherry internally fused to VirE2(P61). We retransformed the construct in *A. tumefaciens* VHH::VirE2-, which consists in pVirE-inducible VHH display genomically integrated into the *virE2* knockout locus (Figure 31). On the mammalian cell side, we generated GFP-displaying HeLa cells constitutively expressing sfCherry3C(1-10). That way, infection and sfCherry11::VirE2 transfer into the mammalian

reporter cells should lead to red fluorescent signal (Figure 46A, B). We first transiently transfected the HeLa reporter strain with a tagBFP\_sfCherry11 mammalian expression plasmid, which validated the proof of concept (Figure 46C). Indeed, we observed a red fluorescent signal (sfCherry panel) upon cell transfection (tagBFP panel).

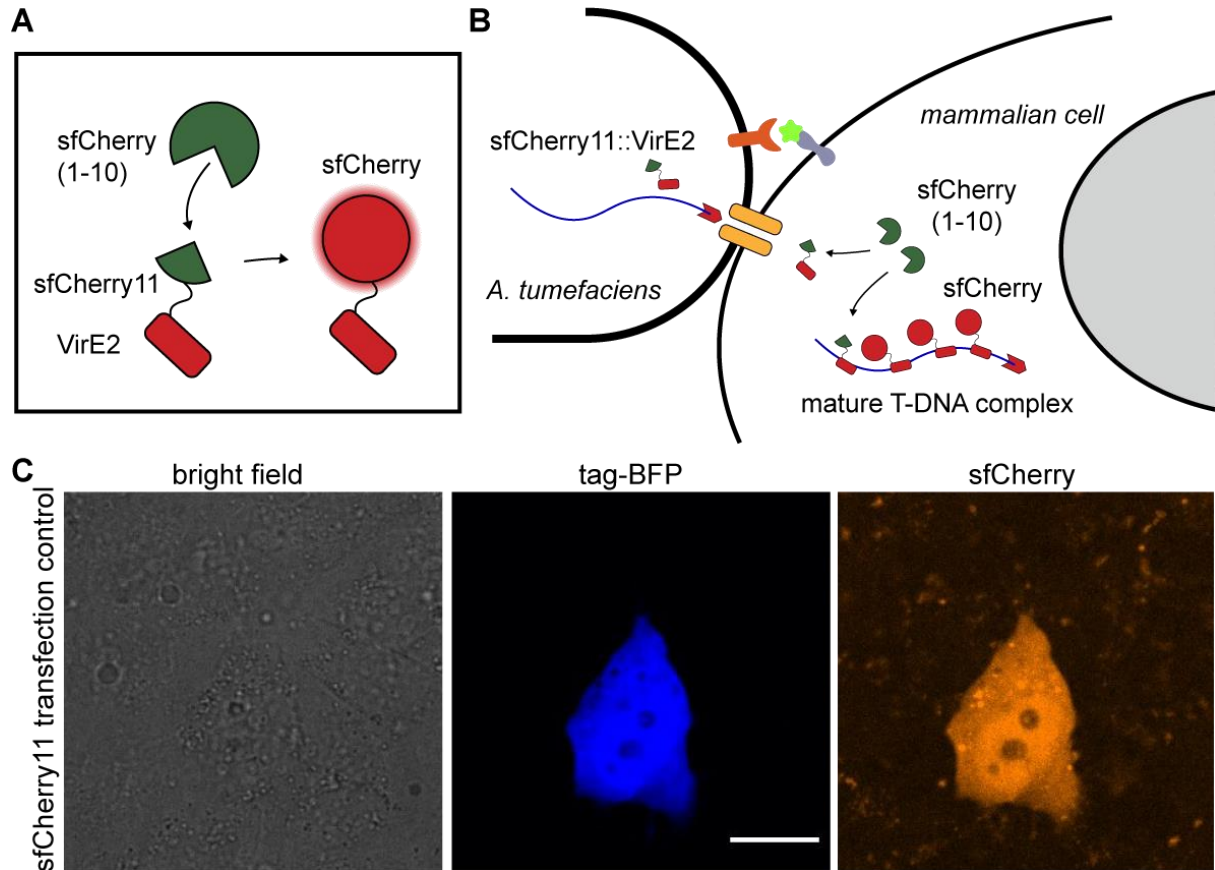


**Figure 46: Split sfCherry concept and control of the target cell line.**

(A) sfCherry is split into two parts, the large one contains the 10 first beta-strands of sfCherry (sfCherry(1-10)). The 11<sup>th</sup> remainder beta strand of the fluorescent protein can be fused to a protein of interest such as VirE2. Upon complementation of sfCherry(1-10) by sfCherry11, fluorescent signal is restored. (B) The mammalian target cell line constitutively expressing sfCherry(1-10) should report any incoming sfCherry11\_VirE2 translocated by bacteria. (C) HeLa cells constitutively expressing sfCherry(1-10) were transiently transfected with a tagBFP\_sfCherry11 reporter. Bar, 20  $\mu$ m.

Next, we infected GFP-displaying HeLa cells constitutively expressing sfCherry3C(1-10) with *A. tumefaciens* VHH::VirE2- pVirE – sfCherry11::VirE2 as schematized in Figure 46B. Despite optimization of bacterial pre-conditioning to mammalian culture medium, infection duration, pH or multiplicity of infection, we could not obtain clear red fluorescent signal differences between bacteria complemented with WT VirE2 (control) and sfCherry11::VirE2 strain. We concluded that either there is no VirE2 transferred, or the assay is not sensitive enough. Figure 47 is representative of one of the infection optimization assays, where red non-specific signal (A) cannot be distinguished from sfCherry signal (B).

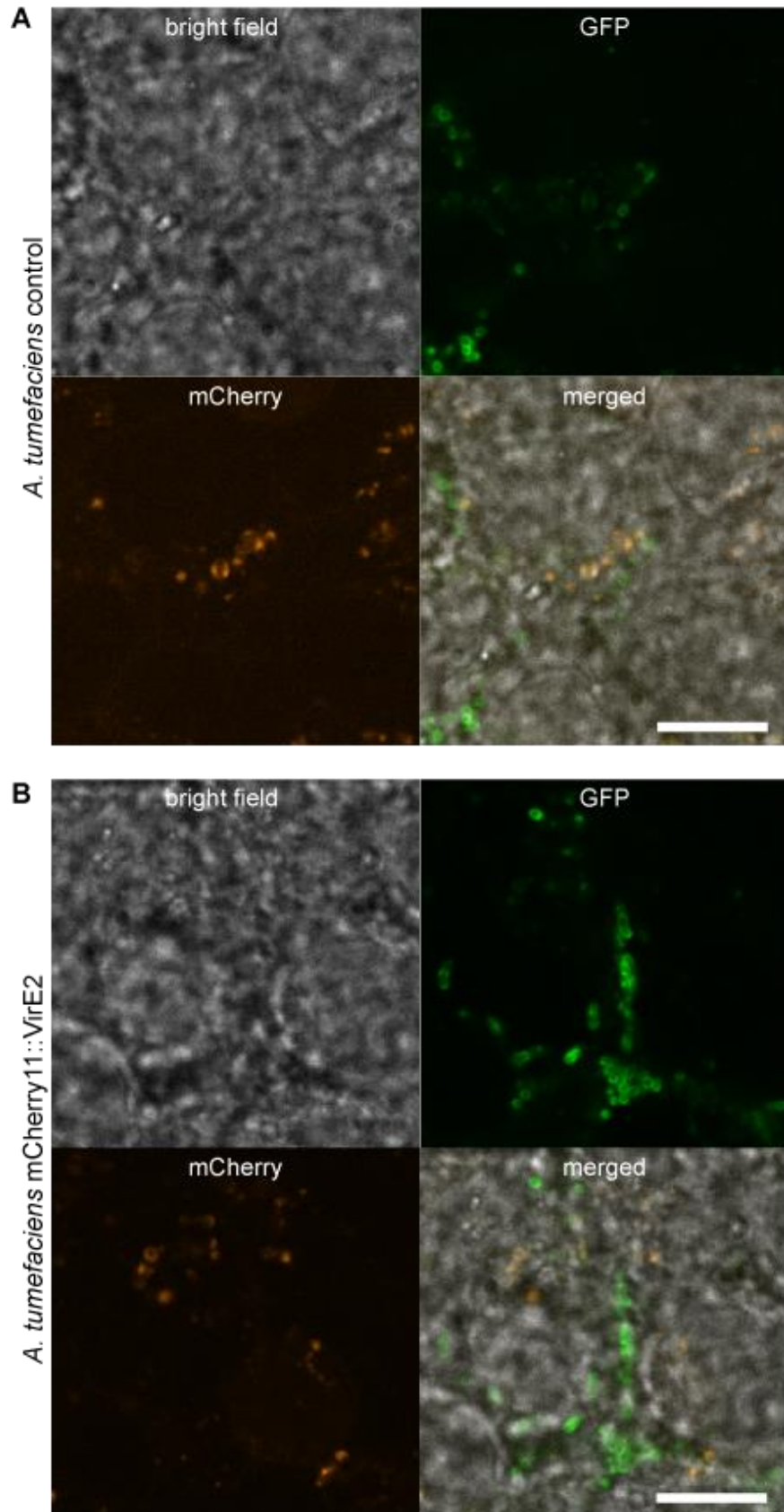


**Figure 47: Split sfCherry does not give a clear VirE2 transfer readout.**

GFP-displaying HeLa cells constitutively expressing sfCherry(1-10) were infected with *A. tumefaciens* VHH(cys-free)::VirE2- retransformed with pVirE-VirE2 WT (A) or pVirE-sfCherry11::VirE2 (B) for 30 h. Confocal microscopy slice. Bars, 10  $\mu$ m.

## 4.8.2 Split NanoLuc

The split fluorescent protein approach might not be sensitive enough to detect translocated VirE2 into mammalian cells. Some red unspecific fluorescent signal might result from autofluorescence or from spillage from GFP channel. Hence, we looked for other more orthogonal and more sensitive methods to report VirE2 transfer, such as split luciferase.

### 4.8.2.1 Experimental design

Split NanoLuc was used for protein translocation quantification for instance from *Salmonella*'s T3SS and recently in *H. pylori*'s T4SS to mammalian cells<sup>147,148</sup>. In these experiments, a long NanoLuc fragment (LgBit), expressed in the mammalian target cells, is complemented by fusion of a short high affinity fragment (HiBit) with a translocated protein. Here we cloned pVirE - HiBit::VirE2 (introduced at position P61) and retransformed it in *A. tumefaciens* VHH::VirE2- (Figure 48A). As reporter cell line, we generated a GFP-displaying HeLa stably and constitutively expressing LgBit.

First, we infected the reporter cell line with bacteria induced with an increasing concentration of inducer and noted an increase in luciferase activity (Figure 48B). Secondly, using the optimal inducer concentration, we titrated the multiplicity of infection. Again, we reported a positive correlation between the number of bacteria added to the reporter target cell line and the NanoLuc signal (Figure 48C). Both results indicate a successful transfer of VirE2 into the target cells in the presence of synthetic adhesion.

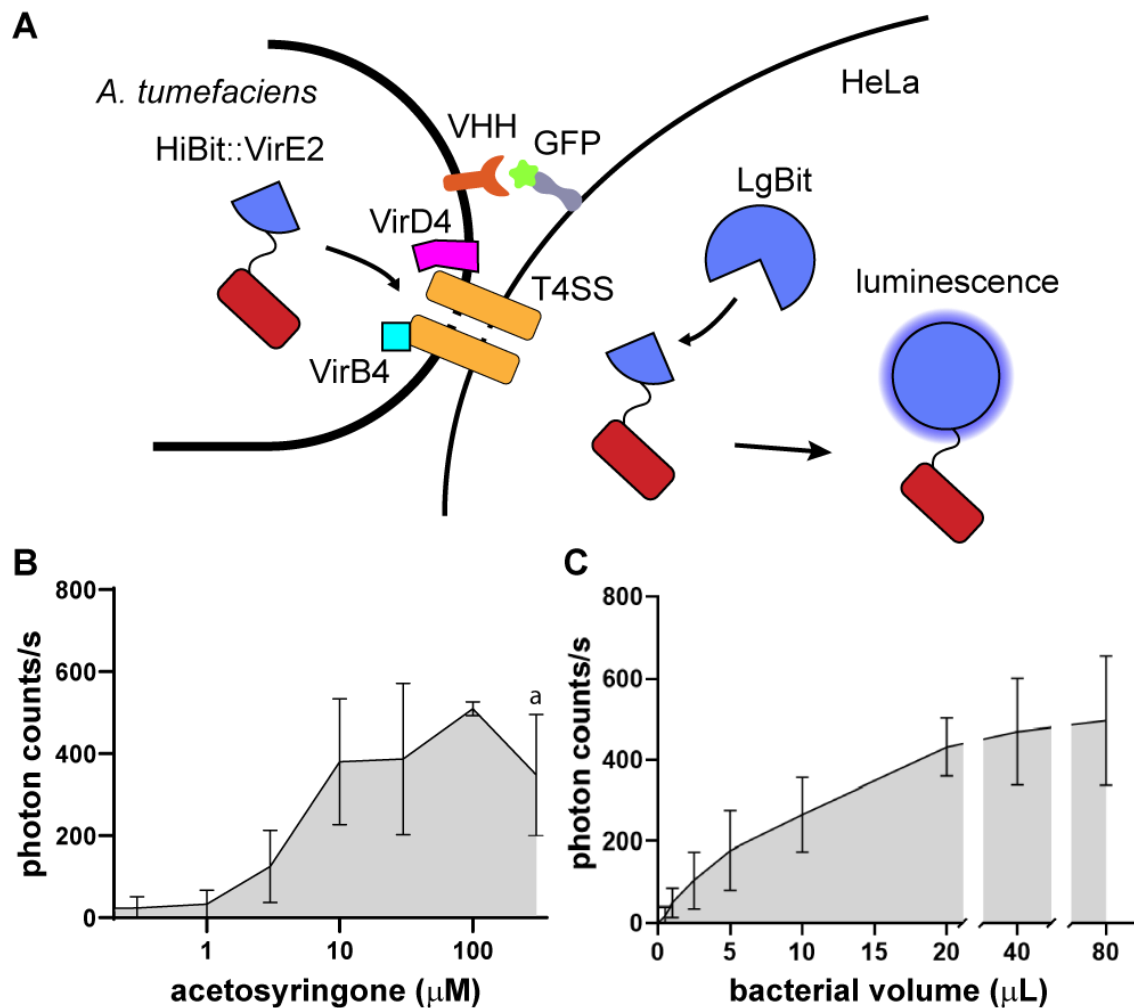


**Figure 48: Monitoring and optimizing VirE2 transfer using the split luciferase system.**

(A) Overview of the system: *A. tumefaciens* VirE2- is complemented with pVirE - HiBit::VirE2, which consists in an internal fusion into VirE2 of HiBit, a fragment that restores NanoLuc activity upon binding to LgBit, that is produced by HeLa cells. Both cell types can display the synthetic adhesin pair VHH-GFP. VirB4 (cyan square) is the motor ATPase that powers the T4SS and VirD4 is the coupling ATPase that brings the T4SS substrate to the T4SS. (B) The NanoLuc activity increases with the inducer concentration. *A. tumefaciens* VHH::VirE2- pVirE - HiBit::VirE2 was induced with increasing concentrations of AS and added to GFP-displaying HeLa cells expressing LgBit. (a) The bacterial optical density was lower than in other sample due to over-induction bacterial toxicity at 300  $\mu\text{M}$ . (C) The NanoLuc activity increases with the volume of bacteria added to the mammalian cells. *A. tumefaciens* VHH::VirE2- pVirE - HiBit::VirE2 was induced with 100  $\mu\text{M}$  AS and different volumes were added to GFP-displaying HeLa cells expressing LgBit. Error bars represent the standard deviation of biological triplicates.

#### 4.8.2.2 VirE2 transfer mostly depends on VHH display

Then, we assessed whether the synthetic binding increased VirE2 transfer. We mixed bacteria and mammalian cells with or without the respective adhesin display and we measured the complemented NanoLuc activity. In the presence of GFP, removal of VHH display decreased the signal back to baseline (Figure 49, first three columns). However, and to our surprise, in the absence of GFP and in the presence of VHH, the signal remained almost as high as with

both adhesins (4<sup>th</sup> column). This indicates that either the transfer of VirE2 is independent of GFP display, or the doxycycline-inducible promoter is leaky and produces sufficient amount of GFP.

To first check if this would be due to leaky expression of GFP from the doxycycline-inducible promoter, we included controls where we either pre-saturated bacteria with recombinant GFP, or displayed a VHH anti-mCherry instead of VHH anti-GFP (Figure 49, last two columns). VHH anti-mCherry gave again similar luciferase activity as VHH anti-GFP, while soluble recombinant GFP decreased the signal by 2.5-fold. We hypothesize that the reduction could be due to pH change during the addition of recombinant GFP, which is stored in phosphate buffered saline (PBS). In conclusion, the display of VHH has an intrinsic and GFP-independent impact that increases VirE2 transfer.

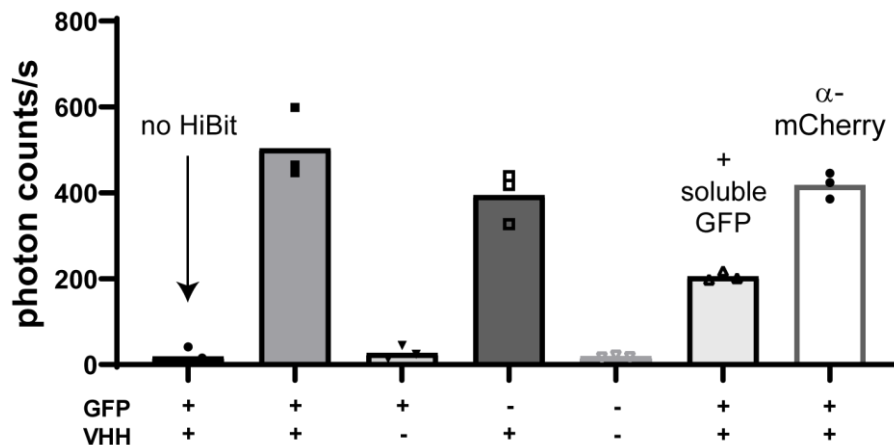


**Figure 49: VHH display causes some GFP-binding-independent VirE2 transfer.**

VirE2 transfer is the highest when both adhesins are present but a high NanoLuc signal remains in the presence of VHH without GFP display induction. *A. tumefaciens* VirE2- ("VHH-") or *A. tumefaciens* VHH::VirE2- ("VHH+") or were retransformed with pVirE - HiBit::VirE2 (except "no HiBit") and added to HeLa expressing LgBit and induced ("GFP+") or not ("GFP-"). Soluble GFP was added in the penultimate condition to prevent synthetic binding. *A. tumefaciens* VirE2- retransformed with pVirE - HiBit::VirE2 and pVirE - VHH(cys-free)anti-mCherry Spec<sup>R</sup> was used the last condition. Datapoints represent the means of biological triplicates.

#### 4.8.2.3 VirE2 transfer is cell-cell contact-dependent but T4SS-independent

To better understand the mechanism of contribution of VHH to VirE2 transfer, we performed additional experiments: first, we checked if mammalian cells could non-specifically uptake free VirE2 from the overnight supernatant. We spun down bacteria and applied the supernatant to reporter cells. We resuspended the pelleted bacteria and added them to separate wells. The signal predominately originated from resuspended bacteria, to a level similar as control bacteria (Figure 50A). This strongly suggests the transfer to be contact-dependent.

To investigate if the transfer is also T4SS-dependent, we knocked out the genes encoding the T4SS motor ATPase *virB4* and the ATP-dependent coupling factor *virD4*. Both *virB4* and *virD4* knockouts reduced the luciferase signal to some limited extent (Figure 50B). Hence, we infer that VirE2 uptake is mostly T4SS-independent.

Note that even so T-DNA is not reported to be required for VirE2 transfer<sup>135</sup>, here to fully recapitulate a pathogenic context, we included a binary vector encoding a synthetic T-DNA. We confirm that the addition of T-DNA did not change VirE2 translocation levels (left columns of Figure 50A and B).

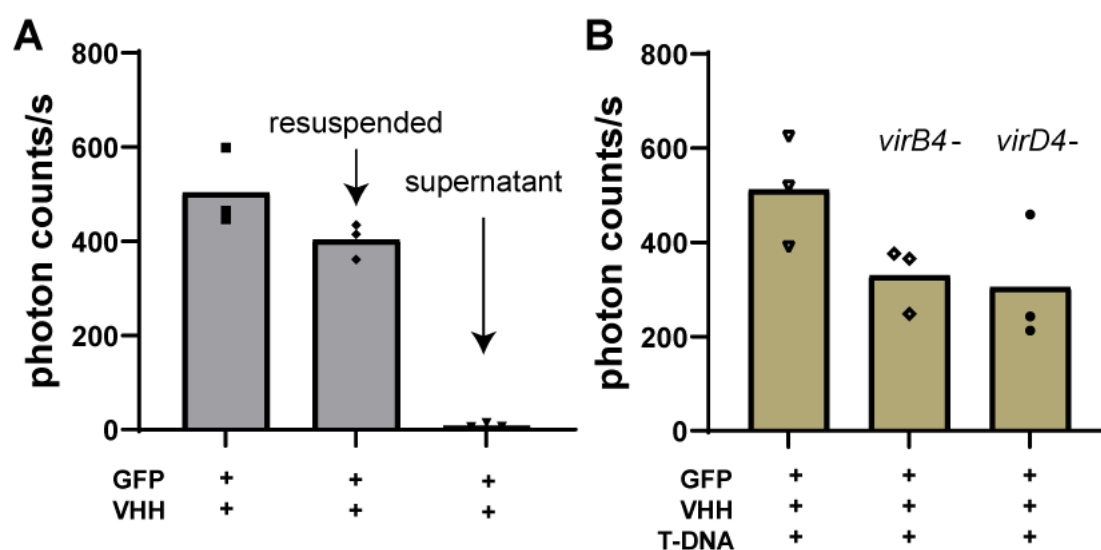


**Figure 50: VirE2 transfer is cell-cell contact dependent but mostly T4SS-independent.**

(A) NanoLuc signal comes from the bacteria and not their supernatant. *A. tumefaciens* VHH::VirE2-pVirE - HiBit::VirE2 were pelleted and resuspended in fresh medium, added to the GFP-displaying HeLa cells expressing LgBit. (B) VirE2 transfer is mostly T4SS-independent. Here bacteria were further retransformed with a binary plasmid encoding T-DNA = turboRFP fw, ("T-DNA+") to monitor the impact on T-DNA on VirE2 transfer. *virB4*- and *virD4*- denote *virB4* mutant and *virD4* mutant, respectively. Datapoints represent the means of biological triplicates.

#### 4.8.2.4 Mammalian cells can uptake VirE2 from fresh bacterial lysate

Altogether, the data suggest a VHH- and contact-dependent but mainly T4SS-independent VirE2 uptake by target reporter cells. VHH might decrease the bacterial viability and/or destabilize the surface stability, which could trigger VirE2 release upon contact to mammalian cells and unspecific uptake. To verify this, we sonicated bacteria and applied the supernatant to reporter cells. We measured an increase in VirE2 transfer from the supernatant of freshly sonicated bacteria (Figure 51), as opposed to the absence of VirE2 transfer from the supernatant of overnight culture (Figure 50A). These observations are consistent with the hypothesis of a contact-contact dependent lysis triggering VirE2 uptake, but future experiments should however include bacterial not displaying VHH, in case the synthetic display or the

scaffold synergizes with VirE2 uptake. Also, it will be important to characterize the VirE2 uptake mechanism, which might involve a clathrin-mediated endocytosis like in plants<sup>129</sup>.

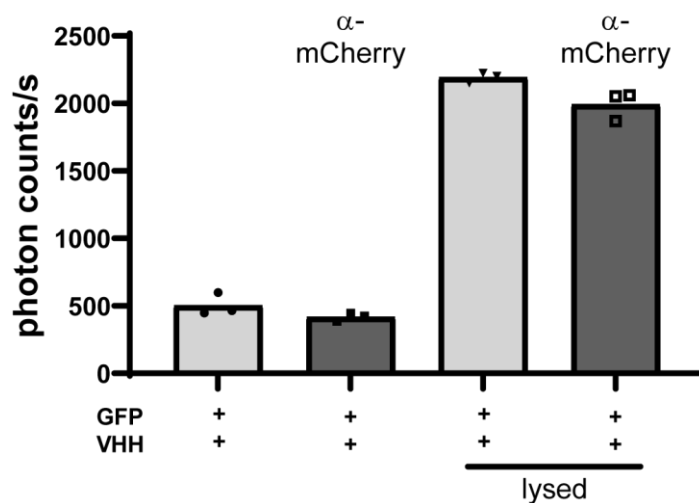


**Figure 51: Mammalian cells uptake VirE2 from bacterial lysate.**

VirE2 transfer was compared between VHH specific to GFP or unspecific (α-mCherry). Bacteria were lysed by sonication, spun down and the supernatant was applied to mammalian cells (lysed). *A. tumefaciens* VHH::VirE2- pVirE - HiBit::VirE2 (light grey) or *A. tumefaciens* VirE2- pVirE - HiBit::VirE2 and pVirE - VHH(cys-free)α-mCherry Spec<sup>R</sup> (dark grey) were compared on GFP-displaying HeLa cells expressing LgBit. Datapoints represent the means of biological triplicates.

#### 4.8.2.5 Split NanoLuc: outlook

Overall, the mode of action of VirE2 uptake by mammalian cell remains to be thoroughly characterized. It might be similar to clathrin-mediated uptake as reported in plants<sup>129</sup>, and clathrin inhibitors could be added to verify such hypothesis<sup>269</sup>. Also, additional experiments such as VirE2 or VHH production controlled by the cumic acid-inducible promoter could help decoupling them from other Vir proteins. For instance, VirE2 interacts with the cognate VirE3 at the plant cell entry site: does it promote uptake in mammalian cells<sup>270</sup>? Finally, does the Atu5364 scaffold or proline-rich linker have an intrinsic property that promotes VirE2 uptake?

## 4.9 SYNTHETIC BINDING OF *A. TUMEFACIENS* TO *CHLAMYDOMONAS REINHARDTII*

Despite trying to leverage a tight synthetic binding system, we only gained a partial understanding of T4SS-mediated transfer from *A. tumefaciens* to yeast and mammalian cells. A plant cell line that commonly accepts *A. tumefaciens* T-DNA would be better suited for measuring the impact of tight adhesion on transfer efficiency.

*Chlamydomonas reinhardtii* is a swimming, unicellular green algae that belongs to the green plants' lineage. *A. tumefaciens*-mediated transformation was successfully performed in this specie<sup>271</sup>. Furthermore, Molino *et al.* developed an mVenus display system in the cell wall of *C. reinhardtii*<sup>272</sup>. mVenus is a GFP derivative, hence, we first verified that VHH retained affinity to mVenus by adding recombinant mVenus to *A. tumefaciens* VHH display (Figure 52A).

Consequently, we tried to bind *A. tumefaciens* VHH display to mVenus-displaying *C. reinhardtii* (Figure 52B). We mixed bacteria and algae and observed them under agarose pad. In VHH anti-GFP-displaying bacteria, we observed an increase in bacterial number that laterally bound to mVenus-displaying algae (which maximizes surface contact), compared to VHH anti-mCherry control (Figure 52C, D). However, this data has to be considered with circumspection, as adding an agarose pad applies forces that could favor interaction by overcoming repulsive thresholds. Furthermore, we did not measure significant binding in free solution (data not shown), as opposed to the binding to GFP-displaying yeasts (Figure 34).

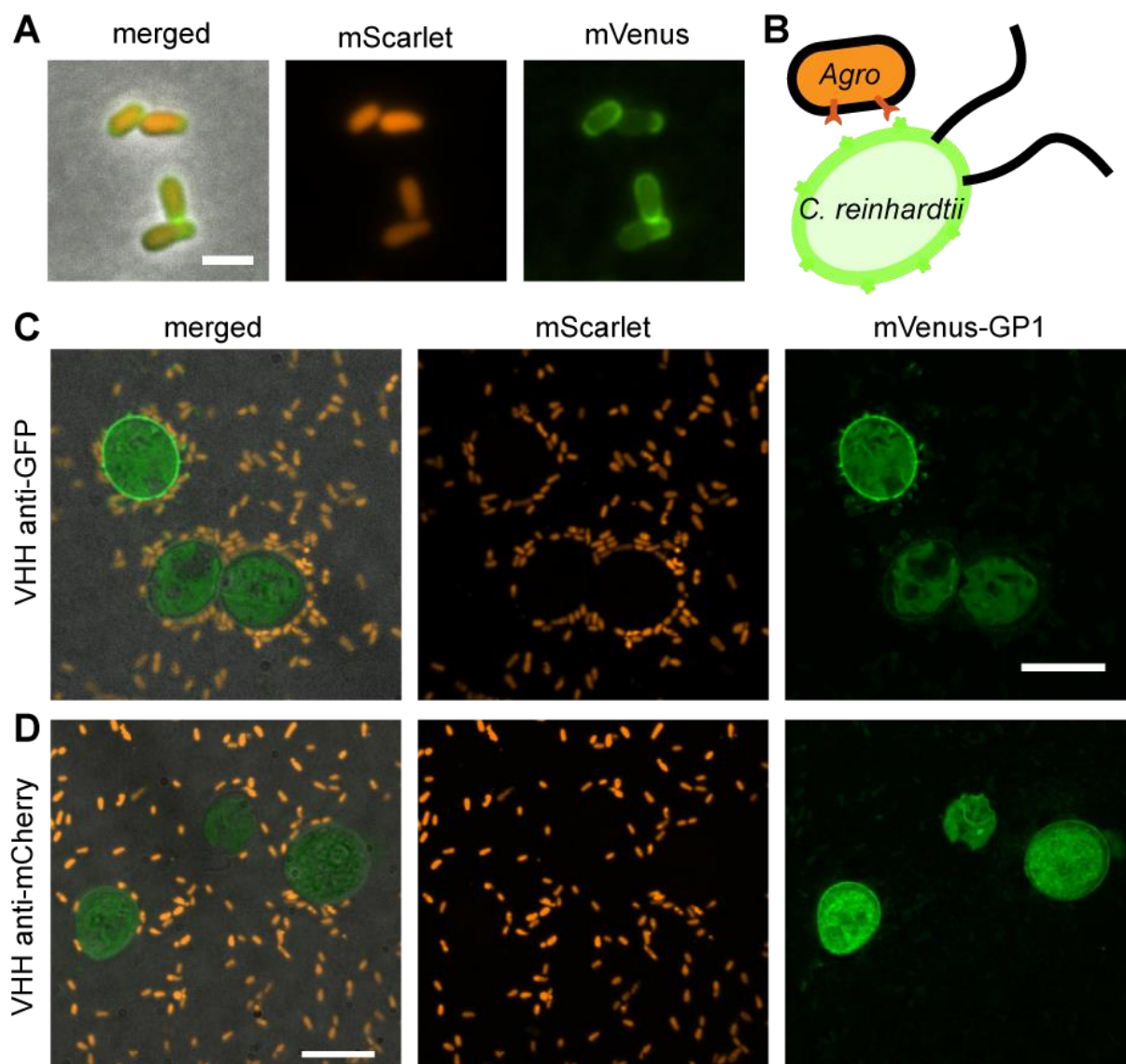


**Figure 52: *A. tumefaciens* VHH binds to recombinant mVenus and to some extent to mVenus-displaying *C. reinhardtii* under agarose pad.**

(A) *A. tumefaciens* mScarlet VHH display was stained with recombinant mVenus and imaged. Bar, 2  $\mu\text{m}$ . (B) Schematic of *A. tumefaciens* VHH display binding to *C. reinhardtii* mVenus display. (C-D) Synthetic adhesins increase the number of laterally-adhering *A. tumefaciens* to *C. reinhardtii*. *A. tumefaciens* mScarlet pVirE – VHH (B) and pVirE – VHH anti-mCherry(cys-free) (C) were mixed for 1h in TAP medium with *C. reinhardtii* displaying mVenus in its cell wall. Cells were transferred to coverslips and imaged by confocal microscopy under a 1% PBS agarose pad. Such observations cannot be made without addition of the agarose pad. Bars, 10  $\mu\text{m}$ .

Two hypotheses can explain such mitigated results. First, VHH affinity might be lower to mVenus compared to eGFP. Among the amino-acid variation between eGFP and mVenus, the mutation A206K might hinder the hydrophobic interaction with VHH(F98) (Figure 53).

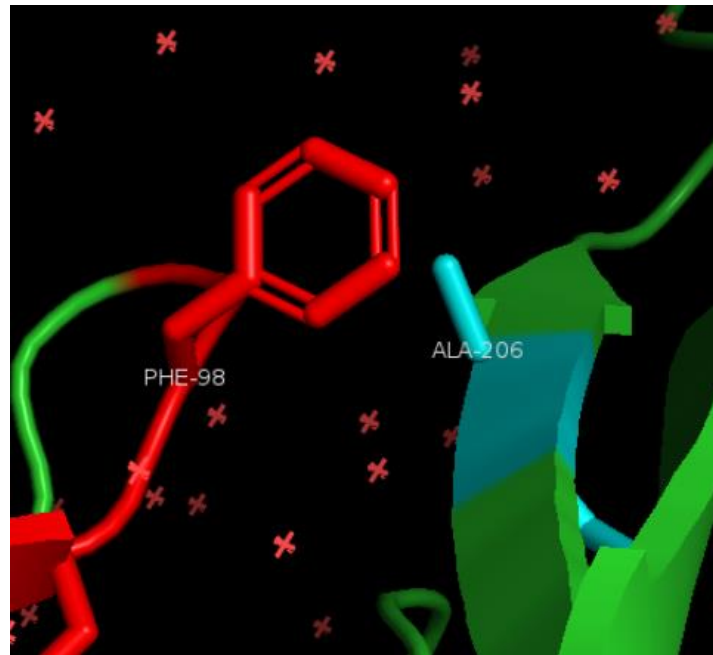


**Figure 53: VHH(F98) is in close proximity with GFP(A206).**

Cartoon representation of the crystal structure of the VHH:GFP complex (pdb: 3k1k). In mVenus, the mutation A206K might interfere with VHH(F98) and decrease affinity. Water molecules are depicted with red crosses.

The second hypothesis resides in the localization of the GP1 anchor used for mVenus fusion<sup>272</sup>. *C. reinhardtii*'s cell wall is composed of 7 layers, and GP1 is located in the penultimate w6 layer<sup>273</sup>. The outer layer w7 could consequently prevent direct mVenus-VHH interaction.

In future experiments, the impact of synthetic adhesion on T-DNA transfer efficiency could be measured using a binary vector harboring a T-DNA encoding a plant antibiotics resistance marker<sup>271</sup>. Cell-cell contact could be forced by doing co-culture puddle, such as for yeast cells<sup>244,246</sup>. Alternatively, Molino *et al.* also developed a plasma-membrane anchored mVenus display<sup>272</sup>. This could be introduced in cell wall-less *C. reinhardtii* to measure again synthetic binding and antibiotics resistance gene transfer<sup>274</sup>.

## 4.10 DISCUSSION

### 4.10.1 Summary

On a timescale of hours, *A. tumefaciens* has limited affinity to non-natural target cells such as yeast and mammalian cells. The synthetic adhesin display system we developed allowed us to rewire *A. tumefaciens* to target a synthetic cell surface receptor.

We quantified the binding to GFP-displaying yeast cells, in the presence or absence of VHH display on the bacterial side. We noted a significant increase in bacterial adhesion in the presence of the synthetic adhesin pair. We repeated the experiment with mammalian cells in depth. Key controls such as preventing adhesion using soluble GFP enabled us to validate the strong impact of the synthetic adhesin display on bacterial adhesion to mammalian cells.

We next developed a highly sensitive split luciferase assay that outperformed split fluorescent protein approach to monitor VirE2 delivery into target cells. This enabled us to conclude that VHH display increases VirE2 uptake by mammalian cells in a contact-dependent and mostly T4SS-independent process.

### 4.10.2 Yeast gene transfer limitations and outlook

The increased binding to yeast using the synthetic adhesin pair did not allow us to increase the T-DNA resistance gene transfer. It is possible that the yeast cell wall remains the major bottleneck, or GFP leakage leads to self-inhibition of the synthetic adhesins.

To improve T-DNA transfer, Piers *et al.* showed in 1996 that the addition of telomeric repeats improved the yeast transformation efficiency 500-fold<sup>250</sup>. Telomeres protect the terminal regions of linear chromosomal DNA from degradation. The repeats include a 50-to-500-base 3' ssDNA overhang and are coated with numerous host proteins. Telomeric repeats and associated proteins are organized in such a way that it prevents the cell to recognize the DNA end as double-strand break. In our system, we hypothesize that newly produced telomeric proteins in the cytosol might both drive T-DNA nuclear import and protection<sup>252</sup>.

Finally, *A. tumefaciens* was recently used to transfer Cas9 fused to helper proteins both in yeast and plant cells<sup>275</sup>. This allowed gene editing using transiently transferred Cas9, reducing risks of off-target mutations compared to constitutive expression, an approach that could be implemented in our system.

### 4.10.3 Transfer to mammalian cells: limitations and outlook

#### 4.10.3.1 Gene transfer

Using *A. tumefaciens* and a T-DNA encoding fluorescent proteins reporter, we reported a mammalian transformation efficiency close to the one reported 20 years ago by Kunik *et al.*<sup>247</sup>. Our synthetic adhesin display did not increase this number significantly, and to our knowledge, no other approach was reported in the literature to improve *A. tumefaciens* T-DNA transformation in mammalian cells. This suggests that other bottlenecks than adhesion prevent efficient T-DNA transfer, nuclear import or transcription in mammalian cells.

In the wild, *A. tumefaciens* triggers a variety of plant innate immune responses that can stop downstream steps of the transformation process<sup>276</sup>. Similarly, in mammalian cells, ssDNA might be detected by innate immune pathways in non-professional immune cells. Indeed, many DNA-based pathogens infect cells and release DNA in the cytosol. Outside mitosis, cytosolic DNA consequently represents a non-physiological or infected state that triggers the cGAS-STING pathway. Cyclic GMP-AMP synthase (cGAS) binds DNA and produces cyclic GMP-AMP, which activate stimulator of interferon genes (STING), leading to inflammatory response<sup>277</sup>. TREX1 is a 3' exonuclease present in the mammalian cytosol that degrades ssDNA<sup>278</sup>. In humans in the absence of TREX1, self-ssDNA accumulates in the cytosol, leading to the Aicardi Goutiere inflammatory syndrome due to cGAS-STING overactivation<sup>279</sup>. Here we could consider temporarily knocking down *in vitro* TREX1 using small interfering RNA (siRNA) to verify if ssDNA degradation by TREX1 is a limiting step for T-DNA transfer. Additionally, we could indirectly measure T-DNA transfer by measuring the production of cyclic GMP-AMP by ELISA assay<sup>280</sup>.

#### 4.10.3.2 Helper protein transfer

Both the inconclusive split fluorescent protein approach and the low absolute photon count of split NanoLuc suggest VirE2 to be transferred in low amount into mammalian cells. Nevertheless, the split NanoLuc occurs to be a sensitive tool for high-throughput optimization of VirE2 transfer. In plant cells, VirE2 is reported to be internalized via a clathrin-mediated endocytosis<sup>129</sup>. Here in mammalian cells, we could validate or invalidate this mechanism by screening clathrin inhibitors and measure HiBit::VirE2 uptake<sup>269</sup>.

Alternatively, one could leverage minute amount of proteins transferred to the target cells. For instance, Vergunst *et al.* fused VirE2 to the Cre recombinase. They monitored Cre-mediated recombination in plant cells by conferring resistance to cells undergoing recombination<sup>281</sup>. Furthermore, they demonstrated the transfer to be VirB- and VirD4-dependent. More recently, Cas9 fusions to the VirF peptide responsible for translocation allowed Schmitz *et al.* to target both yeast and plant reporter cells expressing gRNA<sup>275</sup>.

Consequently, such fusions could be tried in mammalian reporter cells to optimize helper proteins delivery at high throughput.

#### 4.10.4 Conclusion

Overall, the literature on *A. tumefaciens*' bottlenecks for T-DNA transfer is insufficient, even in plant cells. It remains for instance unclear which factors negatively impact the transformation of monocots compared to dicots<sup>203</sup>. More generally in eukaryotes: do limiting rates precede or succeed T-DNA transfer to the target cytosol? Is the T-DNA channeled or endocytosed? Do bacteria need to strongly bind to target cells and does the cell wall remain an issue? Does the innate immune system prevent T-DNA journey through the cytosol<sup>282</sup>? Does the transient transfection efficiency also rely on host DNA machinery factors like stable integration?

Here, we opted for an orthologous approach to better study the impact of adhesion on the T4SS. We targeted non-plant cells to decouple questions related to adhesion from intrinsic plant processes involved in T-DNA integration<sup>139</sup>. We developed a synthetic nanobody display strongly increasing bacterial affinity to target cell displaying the corresponding antigen. In our hands, the transformation efficiency of yeast did not increase with synthetic adhesion, which indicates that other bottlenecks remain. For instance, the cell wall itself might be the next main bottleneck in yeast cells.

In mammalian cells, we also robustly bound *A. tumefaciens* displaying VHH to GFP-displaying HeLa cells. To our surprise, this increased VirE2 transfer in a cell-cell contact-dependent but mostly GFP- and T4SS-independent manner. Preliminary data suggest that VHH display triggers bacterial lysis upon binding followed by VirE2 endocytosis, but further experiments are required to validate the underlying mechanisms.

Regarding the scarce data on *A. tumefaciens* in mammalian cells, we expect several bottlenecks that prevented any incremental progress for T-DNA transfer over the last 20 years. For instance, the innate cytosolic ssDNA sensing (cGAS-STING) and degradation (e.g. TREX1) might need to be overcome or bypassed. Here, we already showed that VirD2 retains nuclear localization activity in mammalian cells without further engineering. Down the road however, even in plants, the uncoating from VirE2, the ssDNA to dsDNA conversion are obscure processes. These still require in-depth characterization in plant cells in future experiments to facilitate translation to animal cells.

Altogether, we showed our synthetic nanobody display system enables the first step towards the development of bacterial-based gene delivery vectors, that is targeted binding to cells. The split NanoLuc will be a rapid, highly sensitive tool for high throughput delivery optimization

compared to split fluorescent protein reporters. More generally, we anticipate that the display scaffold combined with the modularity of nanobodies will profit the plant engineering community by easily providing *A. tumefaciens* with new affinities to any biomarker of interest.

## 4.11 MATERIAL AND METHODS 3

This section supplements Material and methods 1 and 2. Chemicals are purchased from Sigma unless otherwise stated.

*Composition of home-made media and agar plates:*

- SDCAA: 18.2% Sorbitol, 2% Glucose, 0.67% Yeast Nitrogen Base, 0.5% Casamino Acids, 0.54% Disodium Phosphate, 0.86% Monosodium Phosphate (Add 1.5% Agar for plates.
- SGCAA: 18.2% Sorbitol, 0.8% Glucose, 8% galactose, 0.67% Yeast Nitrogen Base, 0.5% Casamino Acids, 0.54% Disodium Phosphate, 0.86% Monosodium Phosphate
- Yeast-Agro cocultivation: 1x AB salts (cf. Material and methods 2), 2 mM phosphate buffer pH 5.6, 50mM MES, 2 g/L casamino acids (add 25 g/L agar for plates, as low pH decreases polymerization). Add 5mM sterile galactose after autoclaving. Diffuse 100  $\mu$ M AS for 24h in the plates before use.

*Engineering of S. cerevisiae*

*S. cerevisiae* eby100 was retransformed using 1  $\mu$ g of pGal1 – eGFP display and following the EZ yeast transformation kit II (Zymo). 100  $\mu$ L of cells were selected on SDCAA plates, which do not contain tryptophan. Colonies were directly selected by induction and visualization with fluorescent microscopy.

*A. tumefaciens binding to S. cerevisiae*

Yeast GFP display induced overnight in SGCAA were washed twice in PBS to remove GFP in suspension and concentrated 10 times. Induced *A. tumefaciens* were washed once in PBS and added to concentrated yeast at a 1 to 1 volume ratio for 60-90 min. Five  $\mu$ L of the cell mixture were transferred to and sandwiched between two coverslips,, the yeast cells were left to settle down and imaging was performed at 100x with a confocal microscope and 0.3  $\mu$ m step. We used NIS Elements (Nikon) for three-dimensional rendering of z-stack pictures.

#### *A. tumefaciens T-DNA transfer to S. cerevisiae*

*A. tumefaciens* were retransformed or not with pVirE – VHH(cys-free) display and a binary T-DNA vector encoding for a yeast kanamycin resistance cassette (kanMX) and/or a second T-DNA vector encoding a kanMX reverse complement cassette. Bacteria were induced in LB-IM AS 100  $\mu$ M. *S. cerevisiae* eby 100 pGal1 – eGFP display was induced in SGCAA overnight.

25  $\mu$ L of each cell type were mixed and spotted on Yeast-Agro cocultivation plates (referred as “puddle”). For liquid co-cultures, 25  $\mu$ L of each cell type were centrifuged and resuspended in 500  $\mu$ L Yeast-Agro cocultivation medium. After 3 days of infection, puddles were resuspended in 500  $\mu$ L PBS and 25  $\mu$ L were plated on YPD plates supplemented with 200  $\mu$ g/mL cefotaxime to kill bacteria and 200  $\mu$ g/mL G418 to selected yeasts that integrated the kanMX cassette. Similarly, 25  $\mu$ L of the liquid coculture were plated selection plates.

#### *Mammalian cell culture and engineering*

HEK293T cells were cultured in DMEM (Thermofisher) supplemented with 10% FBS (Life Technologies). A GFP-displaying monoclonal HEK cell line was generated by transfecting PvuI-linearized pXP145 and FACS sorting after 7 days of culture.

HeLa cells stably expressing the doxycycline-inducible GFP display (Material and methods 1) were further engineered to express the split mCherry part sfCherry3C(1-10) by transduction with a lentivector (pXP485). Lentivirus production is described in Material and methods 1. After removal of the lentivirus, a polyclonal cell line was obtained by selection with puromycin (Labforce) at 2  $\mu$ g/mL for one week.

HeLa cells stably expressing the doxycycline-inducible GFP display were further engineered to express LgBit by transduction (pXP499). A polyclonal cell line was obtained by selection with puromycin at 2  $\mu$ g/mL.

#### *Mammalian cell transient transfections and staining*

Mammalian cells were transfected with Lipofectamine 3000 (Life Technologies) overnight with 100 ng of purified plasmid per well of 96-well plates, following the manufacturer’s instructions.

VirE2 staining: Cells were washed twice with PBS, fixed with 4% paraformaldehyde for 10 min, permeabilized with 0.2% triton for 10 min, blocked with 1% BSA in PBS 0.1% Tween 20 and VirE2 was stained using a VirE2 antibody (Cusabio PA357288LA01AYS) at a 1:250 dilution

for 1 h. After 3x washes, secondary staining was performed using a Cy5-conjugated Goat Anti-Rabbit IgG (abcam 6564) at a 1:1000 dilution for 1 h. Cells were washed and imaged.

The tetracysteine (C4)-tagged constructs were detected following the TC-ReAsH kit II instructions (manual Invitrogen MP 34561). 2,3-dimercapto-1-propanol (BAL) (TCI) and ReAsH-EDT2 (Cayman) were purchased separately.

#### *A. tumefaciens binding to mammalian cells*

Cells were washed with medium twice prior to the addition of 10  $\mu$ L of induced bacteria per well of 96-well plates. Bacteria were homogenized by pipetting and left to adhere for 5 hours at 30°C and 5% CO<sub>2</sub> with 100  $\mu$ M AS. For the prevention of binding using soluble GFP, bacteria were incubated with 100  $\mu$ g/mL recombinant eGFP for 5 minutes prior to the addition to mammalian cells. Consequently, recombinant eGFP was also present during coculture at a concentration of 10  $\mu$ g/mL. After coculture, wells were washed 5 times with mammalian culture medium and imaging was performed in the region of the well the closest to the dispensing of the medium. Confocal microscope Z-stacks were acquired over 12  $\mu$ m and 2  $\mu$ m steps in three representative fields of view (one biological replicate). On each field of view, we estimated the number of HeLa cells and counted bacteria on maximum intensity projection using ImageJ and Trackmate<sup>202</sup>.

#### *A. tumefaciens-mediated gene transfer in mammalian cells*

Inducible GFP-displaying cells were induced overnight with doxycycline (HiMedia) at 1  $\mu$ g/mL overnight. Both constitutively expressing and inducible GFP-displaying cells were washed twice with medium prior to infection. 20  $\mu$ L of induced bacteria were added to the wells of 96-well plates for 4 h at 30°C with 5% CO<sub>2</sub> with 100  $\mu$ M AS. Wells were washed twice and medium was supplemented with cefotaxime at 200  $\mu$ g/mL to kill bacteria. After overnight incubation at 37°C 5% CO<sub>2</sub>, wells were screened by fluorescence microscopy with 10x magnification and images acquired at 40x magnification. Other trials of lower or equal efficiency not depicted in this thesis include: overnight infection, lower and higher multiplicity of infection, lower pH, higher AS concentrations, Fluorobrite medium, preconditioning and induction of *A. tumefaciens* in acidic culture medium (1:1 Induction medium and DMEM).

### *ssDNA FISH*

The Stellaris RNA FISH for adherent cells protocol (Biosearch technologies) was adapted to ssDNA FISH. Cy5-labelled oligonucleotides probes were designed using Stellaris website to avoid false positive in the human genome and purchased from Microsynth. Briefly, cells were washed once with PBS, fixed for 10 min in 4% PFA, washed twice with PBS, permeabilized with 70% ethanol for 1 h at 4°C, washed with PBS, treated with Proteinase K for 10 min at 20 µg/mL in PBS at room temperature, washed with PBS, washed with saline-sodium citrate (SSC) twice. Probes were applied in Stellaris hybridization buffer for 16h at 37°C at 25 µM total. Cells were washed with SSC twice, DAPI was used at 1 µg/mL for 5 min for nuclear staining and cells were washed with PBS twice before imaging.

### *Modeling of VirE2 and sequence alignment.*

VirE2 sequence from pTiBo542 (extracted from pCambia5105, Snapgene) was aligned to VirE2 (strain C58) using pairwise alignment Needle online server ([ebi.ac.uk/Tools/psa/emboss\\_needle](http://ebi.ac.uk/Tools/psa/emboss_needle) **Error! Hyperlink reference not valid.**)<sup>283</sup>.

VirE2 structure was modeled using I-Tasser online server ([zhanggroup.org/I-TASSER/](http://zhanggroup.org/I-TASSER/))<sup>218</sup>.

### *Split sfCherry assays*

HeLa GFP display stably expressing sfCherry3C(1-10) were washed and infected with 0.5 µL of *A. tumefaciens* in 96-well plates. AS was added to the medium at 200 µM. Wells were mixed by pipetting and observed by confocal microscopy at 100x magnification after 6 and 30 h of coculture at 30°C and 5% CO<sub>2</sub>. Other trials of lower or equal efficiency not depicted in this thesis include: higher multiplicity of infection for shorter time, Fluorobrite medium, preconditioning and induction of *A. tumefaciens* in acidic culture medium (1:1 Induction medium and DMEM).

### *Split luciferase assays*

A polyclonal cell line of HeLa cells stably expressing LgBit and doxycycline-inducible GFP display was used. Cells were seeded in 96-well plates (Costar 3603). 6 h later, they were induced when required with doxycycline at 1 µg/mL for overnight expression of GFP-display. Cells were washed twice with medium to remove shed GFP from the supernatant and 22 µL

of induced *A. tumefaciens* (LB-IM AS 100  $\mu$ M) were added to 100  $\mu$ L of culture medium for 5 h.

Wells were washed with OptiMEM (Thermo) twice and 20  $\mu$ L of a 1:19 mixture of substrate:buffer from the Nano-Glo Live Cell Assay (Promega) were added to 80  $\mu$ L of OptiMEM per well. After 3 min incubation with the reagent, luminescence activity was acquired using a multiwell plate reader (Tecan Spark) with 5 s integration time per well. Background from wells with only reagent and OptiMEM was subtracted from the values.

#### *Sonication of A. tumefaciens*

Induced cultures were sonicated in 1.5 mL Eppendorf on ice using a Branson 550 sonicator equipped with a microprobe at 30% power. 3 seconds pulse and 10 seconds rest cycles were applied for a total time of 45 seconds of sonication.

#### *CRISPR-Cas9 repair of mutated luciferase assays*

GFP-displaying HeLa cells were transiently transfected in 96-well plates with Lipofectamine 3000 and 50ng of pCMV – NanoLuc\_start\_mutated and either 50 ng of gRNA1+Cas9 or gRNA2+Cas9 that target the start site surrounding. When exogenous repair ssDNA was used, 50 additional ng of 72 base pairs oligonucleotides were added to the transfection mix. Both non-stabilized and phosphorothioate-stabilized primers (PTO) were purchased PAGE-purified from Microsynth.

Sequences for figure 43B:

ssDNA PTO fw (\* denotes PTO modification):

a\*g\*a\*aaagaagagtaagaagaaatataagagccaccATGgtattaccctggaggactttgtgggcgatt\*g\*g\*c

ssDNA PTO rev:

g\*c\*c\*aatcgccacaaagtctccagggtaaatacCATggtggctcttatatttcttctactctctt\*t\*c\*t

ssDNA fw:

agaaaagaagagtaagaagaaatataagagccaccATGgtattaccctggaggactttgtgggcgattggc

Sequences for figure 43C:

ssDNA fw:

taattattccatacgagggcctcagtggtgaccagATggggcaaattgagaagatttcaaagttgtatatc

ssDNA rev:

gatatacaactttgaaaatcttcaatttgccccATctggtcaccactgaggccctcgtatggaataatta

After overnight transfection, cells were washed and 22  $\mu$ L of induced bacteria were added to the wells for 5 h. Wells were washed twice and medium supplemented with cefotaxime at 200  $\mu$ g/mL to kill bacteria.

To monitor full-length NanoLuc activity in mammalian cells, the Nano-Glo luciferase assay (lytic) kit (Promega) was used according to the manufacturer's protocol and the readout otherwise was identical to the split NanoLuc assays.

### *Visualization*

For widefield visualizations, we used a Nikon TiE epifluorescence microscope equipped with a Hamamatsu ORCA Flash 4 camera and an oil immersion 100x Plan APO N.A. 1.45 objective.

For bacterial adhesion to yeast, roots and mammalian cells, we used a Nikon Eclipse Ti2-E inverted microscope coupled with a Yokogawa CSU W2 confocal spinning disk unit and equipped with a Prime 95B sCMOS camera (Photometrics). We used either a 40x air objective with N.A. of 1.15 to acquire z-stacks or a 100x oil immersion objective with N.A. of 1.45, depending on the resolution required.

We used NIS Elements (Nikon) for three-dimensional rendering of z-stack pictures.

### *Production of recombinant mVenus*

6xHis-tagged mVenus was produced like other florescent proteins, described in Material and methods 1.

### *C. reinhardtii culture and co-culture*

*C. reinhardtii* was grown in Tris-Acetate-Phosphate (TAP, Thermo) medium at room temperature 30-40 cm from a white light source (18W/840 Philips neon bulb). Liquid cultures were shaken at 140 rpm. When required, TAP 1.5% agar plates were supplemented with 5  $\mu$ g/mL Zeocin to select for the GP1-mVenus construct, 10  $\mu$ g/mL Hygromycin to select for T-DNA integration and 500  $\mu$ g/mL Cefotaxime to kill *A. tumefaciens*.

For adhesion experiments, *C. reinhardtii* were used at late exponential phase and washed twice to remove mVenus from the supernatant and concentrated 10 times. 50  $\mu$ L were mixed with 25  $\mu$ L of induced *A. tumefaciens* for 1 h. 1  $\mu$ L of the coculture was transferred to coverslip and a 1% agarose PBS pad was applied to it for immobilization and visualization.

For T-DNA transfer assay, *C. reinhardtii* were used at late exponential phase and washed twice to remove mVenus from the supernatant and concentrated 10 times in TAP containing 100  $\mu$ M AS. For solid (puddle) infection, 50  $\mu$ L were mixed with 50  $\mu$ L of induced bacteria (*A. tumefaciens* VHH(cys-free) anti-GFP or anti-mCherry + pCambia1301) and dispensed on TAP agar plate containing 100  $\mu$ M AS. Puddles were left to dry for 15 min in a sterile laminar flow hood and incubated overnight with illumination. For liquid infection, 100  $\mu$ L of concentrated algae and 100  $\mu$ L of induced bacteria were mixed in 24 well-plate in static condition overnight without illumination. Puddles were then resuspended in 150  $\mu$ L TAP medium and plated on antibiotics selection TAP agar plates. The totality of the liquid infection volume was plated on antibiotics selection TAP agar plates. Similar strategies were tried in IM instead of TAP with no increase in T-DNA transfer efficiency.

## 5 CONCLUSION AND PERSPECTIVES

---

### 5.1 THE MAMMALIAN MEMBRANE MICROENVIRONMENT REGULATES THE SEQUENTIAL ATTACHMENT OF BACTERIA TO HOST CELLS

#### 5.1.1 Results summary

In chapter 2, we repurposed a synthetic adhesion system to investigate the biophysical processes governing bacterial adhesion to host cells. The VHH-GFP pair in *E. coli* and HeLa cells enabled us to decouple adhesion from pathogenic processes. By visualizing attachment at high temporal resolution, we found that bacterial adhesion to host cell surface involves one additional step compared to inert surfaces. We hypothesized this extra step to be resulting from the host cell microenvironment. We found that bacteria first loosely attach to their host without engaging adhesins, assisted for instance by flagella. This step lasts about one minute during which bacteria can easily detach. We suggest that at this stage, the glycocalyx passively shields the host cell by keeping adhesins at a distance from their receptor ligand. Subsequently, adhesins engage with their target receptors to strengthen attachment for minutes to hours, an event favored by shear forces. Finally, actin cytoskeleton actively reshapes the host membrane around bacteria, which strengthen specific adhesion. Altogether, our results demonstrate that adhesin-ligand binding is not the only regulator of bacterial adhesion, due to the host mechanical microenvironment playing a critical role on the infection initiation.

#### 5.1.2 Future directions

##### 5.1.2.1 Plasma membrane mechanics

Here we extensively deciphered the respective contributions of the outer and inner membrane microenvironments. But what about the contribution of the mechanics of the plasma membrane itself to bacterial binding? For example, Ismaili *et al.* increased the host membrane fluidity using hexanol, benzyl alcohol or a fatty acid like-compound to prevent enteropathogenic *E. coli* binding<sup>173</sup>. Another study demonstrated that cholesterol content promoted *Neisseria meningitis* detachment from endothelial cells<sup>284</sup>. In our setup, we enriched or depleted cholesterol from membranes using methyl- $\beta$ -cyclodextrin (mBcd) prior to the addition of bacteria<sup>285</sup>. Preliminary experiments were however not correlating with cholesterol content (not shown). We suggest that changes in membrane cholesterol content can also perturb how the underlying cortical actin interacts with the plasma membrane. For instance mBcd can induce actin

depolymerization and promotes F-actin stress fibers, while cholesterol microdomains were shown to promote actin polymerization to the leading edge of moving cells<sup>286–289</sup>. In future experiments, we could imagine decoupling membrane fluidity from actin polymerization effects by combining cytoD and cholesterol/mBcd treatments.

#### **5.1.2.2 Applications for the development of other technologies**

Our synthetic system mimics a tight binding of a pathogen to target cells in a minimal biosafety environment. This is extremely handy for the experimental development of new technologies that usually initially lack biosafety requirements for studying pathogenic processes. We contributed to the study by Leitao *et al.* who tracked the dynamics of synthetic bacterial binding on deglycosylated HeLa cells using time-resolved scanning ion conductance microscopy<sup>290</sup>.

#### **5.1.2.3 Addition of pathogenic features**

We demonstrated that extracellular appendages such as flagella have a dramatic and dual role on bacterial adhesion. Future studies could for instance generate flagellar rotation mutants to decouple the flagellar mechanical forces from the adhesive forces. Alternatively, one could upgrade bacteria with other appendages such as pili to study their impact on bacterial binding kinetics. Would their predominant role be to promote transient binding or to prevent adhesin contact? What is the importance of pilus retraction?

Finally, the VHH display system and our methodology could be used in pathogenic species to fully recapitulate a pathogenic context. One could measure the impact of additional affinity to the target cell on T3SS-mediated toxicity. The intimin-based scaffold (reverse autotransporter) is however not always directly applicable to other bacteria. In this direction, we developed a new VHH display system in *P. aeruginosa* (see Appendix 1).

## **5.2 DEVELOPMENT OF AN ADHESIN DISPLAY SYSTEM AT THE SURFACE OF A. TUMEFACIENS**

### **5.2.1 Results summary**

In chapter 3, we repurposed a previous uncharacterized endogenous T5aSS autotransporter in *A. tumefaciens*. We replaced the passenger domain with adhesins of interest and placed the construct under acetosyringone or cumic acid-inducible promoter. We displayed a disulfide-free VHH anti-GFP and successfully stained the adhesin displayed at the surface of *A. tumefaciens* using soluble GFP. In a step towards targeting endogenous mammalian biomarkers, we also successfully displayed HA-tagged RGD tripeptide.

Along the way we observed that the three-dimensional structure of the passenger domain is so far restricted to beta-stranded proteins, in agreement with the putative structure of the WT passenger domain of Atu5364. Also, like for many other T5aSS autotransporters, we confirmed that disulfide bonds within WT and synthetic passenger domains prevent translocation in oxidative conditions, suggesting a role of Atu5364 in anaerobic environments.

### 5.2.2 Future directions

To broaden the synthetic display to various passenger domain structures, we suggest that other outer-membrane scaffold could compensate the limitations of Atu5364<sup>232</sup>. However, the only other putative *A. tumefaciens* C58 autotransporter scaffold, Atu5354, is 44% similar to Atu5364 at the sequence level and their predicted structures align closely (Figure 54). T5aSS autotransporters from others species, such as *P. aeruginosa* EstA, were successfully transposed to different species such as *E. coli*. Its passenger domain is a lipase that contains alpha-helices and one short disulfide bond (Figure 4). Hence, it would be interesting to see if EstA-based display broadens the structures we can mount on *A. tumefaciens*.

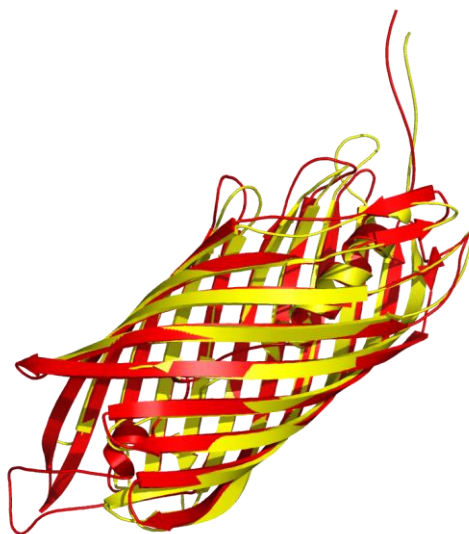


**Figure 54: The predicted structures of Atu5354 and Atu5364 scaffolds are highly similar.**

RoseTTaFold structure modeling of Atu5354 (red) and Atu5364 (yellow) scaffolds were aligned using Pymol software.

Alternatively, other autotransporter topologies such as reverse autotransporters are efficient in displaying disulfide-containing passenger domains, such as intimin from enteropathogenic *E. coli*. The latter was however unsuccessfully transposed to *A. tumefaciens* and *P. aeruginosa* (data not shown), which does not possess any reverse autotransporter, to our knowledge. To overcome this, it remains to be investigated whether pre-engineering of the

recipient strain with the corresponding periplasmic chaperones and outer-membrane beta-barrel assembly machinery (Bam) would help with non-endogenous autotransporter display<sup>291</sup>.

We were also unsuccessful at displaying LipA using Atu5364. Here as well, we suggest that missing periplasmic chaperones might explain the inability to display alpha helix-containing proteins. In addition, the melting temperature of LipA might be incompatible with Atu5364. In this context, Renn *et al.* showed an increase in display efficiency with destabilization of N-terminal globular domain of two passenger domains homologous to Hemoglobin Protease in *E. coli*<sup>292</sup>. On the other hand, they show that destabilization of the C-terminal part (green to red, Figure 55) reduced secretion efficiency. Hence it seems that the folding from the C- to the N-terminal end, in agreement with the hairpin model, could drive translocation of recalcitrant passenger domains. In future experiments, we could try keeping the endogenous beta-solenoid of Atu5364 and N-terminally fuse LipA to it, to mimic Hemoglobin Protease's structure.

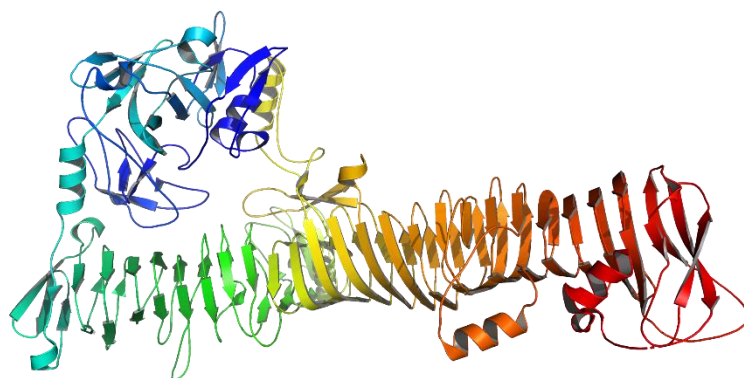


**Figure 55: Crystal structure of *E. coli* Hemoglobin Protease**

The Heme Binding protein is an autotransporter hemoglobin protease from pathogenic *E. coli* (pdb 1WXR<sup>293</sup>).

Additionally, we tried to bind to integrin-overexpressing MDA-MB-231 breast cancer cells using the RGD-display system, with limited success (data not shown)<sup>294</sup>. Additional experiments are required to determine whether the binding is limited by the RGD accessibility or conformation on the bacterial side, or by the accessibility or affinity of integrins for RGD in this cell line.

## 5.3 *A. tumefaciens* PROTEIN AND T-DNA TRANSFER TO YEAST AND MAMMALIAN CELLS

### 5.3.1 Results overview

In chapter 4, we robustly adhered *A. tumefaciens* to non-natural target cells using our synthetic nanobody display system: VHH-displaying bacteria accumulated on both GFP-displaying yeast and mammalian cells. We further validated the concept by preventing the adhesion to GFP-displaying HeLa and HEK cells by pre-saturating bacteria with soluble GFP.

However, the *A. tumefaciens*-mediated stable transformation of yeast cells and the transient transfection of HEK cells remained low and insensitive to the synthetic binding. ssDNA FISH, split sfCherry and CRISPR/Cas9 reporter for repair ssDNA approaches did not occur to be sensitive enough to report T-DNA or VirE2 transfer in mammalian cells. Instead, we developed a highly sensitive split NanoLuc assay that enable us to monitor HiBit::VirE2 transfer in reporter HeLa cells expressing LgBit.

Using the split NanoLuc, we found a positive correlation between the luminescence readout and the multiplicity of infection, the virulence or the presence of VHH. To our surprise, in the absence of GFP display, VHH display alone triggered VirE2 translocation. Further experiments showed that the transfer was cell-cell contact dependent but mostly T4SS-independent, and that mammalian cells can uptake VirE2 from bacterial lysates.

### 5.3.2 Summary of future directions

To this point, we cannot safely conclude where T-DNA transfer stalls, and several concomitant bottlenecks might explain the absence of incremental progress in the field over the last two decades.

First, hypervirulent *A. tumefaciens* strains could be tested to force translocation. For instance, hypervirulent *A. tumefaciens* strains such as AGL1, LBA4404, Chry5 or EHA105 were used to transform recalcitrant plant cells<sup>295–297</sup>. Similarly, constitutive VirG(N54D) expression triggered hypervirulence and increased plant transformation efficiency<sup>298</sup>. Such strains might prove more potent for infection at physiological pH.

Second, as discussed in section 4.10, several options are available to improve T-DNA delivery. Would the display of a cell wall-degrading enzyme synergize with the T4SS delivery? We could for instance adapt EstA autotransporter and associated chaperones to display cellulases to increase transformation efficiency in yeast or recalcitrant plant cells. The concept of including

telomeric repeats in T-DNA for improved delivery in yeasts could be extrapolated to mammalian cells too<sup>250</sup>. The knockdown of the host cytosolic DNase machinery TREX1 could also greatly improve transfer, as it degrades viral DNA in the cytosol<sup>299</sup>.

Third, at the protein delivery level, the fusion of Cas9 or Cre recombinase to T4SS secretion signals concepts could be applied in future experiments to our GFP-displaying cells. These would be highly sensitive approaches to assess the impact of tight synthetic binding to helper protein transfer<sup>275,281</sup>.

Fourth, one different approach would consist in favoring a T4SS-dependent transfer by engineering the T4SS pilus itself to increase affinity to mammalian cells. For instance, *H. pylori* CagL is homologous to *A. tumefaciens* VirB5, the pilus tip protein. CagL includes an RGD peptide with high affinity to human integrins to promote type IV secretion, which is absent in VirB5<sup>113,210</sup>. Hence, one approach would be to engineer VirB5 to include an RGD peptide on the pilus itself, without impairing the pilus assembly.

Finally, it might be easier at first to take a step back towards natural host of *A. tumefaciens*. To our knowledge, *C. reinhardtii* is the only green plant cell for which a fluorescent protein display was developed<sup>272</sup>. More efforts are however required to significantly bind *A. tumefaciens* to the algae. The outer cell wall layer w7 might contain biomarkers that could be targeted by *A. tumefaciens*. Alternatively, cell wall-deficient *C. reinhardtii* strains could be used for GFP display at the plasma membrane<sup>272,300</sup>.

### 5.3.3 Safety

Chapter 4 focused on the ability of *A. tumefaciens* to target and deliver T-DNA and helper proteins to non-natural hosts, including human cells *in vitro*. After further T4SS-delivery optimization *in vitro*, one should assess the safety of the approach in *in vivo* experiments.

As such, *A. tumefaciens* is likely to be too immunogenic and replicative for use *in vivo*. Like in plants, its pathogen-associated molecular pattern (PAMP) would likely trigger host immune response<sup>282</sup>. Two solutions can be envisioned: first, *A. tumefaciens* could be further engineered into an attenuated strain, for example by creating auxotrophic strains. For instance, *AroA* encodes an enzyme essential for the synthesis of aromatic amino acids. Its deletion in several species including *Salmonella* and *Pseudomonas* created attenuated auxotrophic strains that could be kept under control by animal models<sup>301,302</sup>. Second, the T4SS operon could be transferred to safer chassis already used in bacterial cancer clinical trials, such as attenuated *Salmonella* Typhimurium<sup>303</sup>.

Last yet importantly, the intrinsic feature of T-DNA random integration in plants would need to be avoided *in vivo*. As mentioned for retrovirus-mediated gene delivery, random integration in bone marrow cells led to leukemia in clinical trials. Consequently, strategies to detect random T-DNA integration will be required to optimize off-target-free solutions. For instance, to prevent random integration of linear ssDNA, one could think of forcing the formation of dsDNA T-circles<sup>304</sup>. Alternatively, T-DNA-free approaches might be safer, but it remains to be tried for example if *A. tumefaciens* is able to deliver gRNA along with Cas9 fusions. In any case, further studies are required for the development of safe *A. tumefaciens*-mediated gene editing therapies.

## 5.4 GENERAL CONCLUSION

Altogether, we used synthetic bacterial binding to mammalian cells, microfluidics and single cell tracking to demonstrate that adhesin-ligand binding is not the only regulator of bacterial adhesion. As opposed to abiotic surfaces, we highlighted that the mechanical microenvironments, namely bacterial surface appendages, the host glycocalyx and the underlying actin cytoskeleton, play a critical role on the onset of infection. In the current context of the rise of multidrug resistant pathogens, our work provides new insights that could inform the development of anti-adhesive therapeutics<sup>164,188,197</sup>.

Secondly, we developed a nanobody display system in *A. tumefaciens* using a fusion to a previously uncharacterized endogenous autotransporter. Our synthetic adhesin display system allowed us to rewire this plant DNA delivery vector to yeast and mammalian cells. We complemented our approach by developing a sensitive split NanoLuc system that enable us to monitor the delivery of a key helper protein in mammalian cells. We believe our tools will facilitate the identification of the remaining bottlenecks and could be a cornerstone towards the development of bacterial-based gene delivery vectors in humans. More broadly, we anticipate that the display scaffold combined with the modularity of nanobodies will profit the plant engineering community by easily providing *A. tumefaciens* with new affinities to any biomarker of interest.

## 6 APPENDIX 1: PSEUDOMONAS AERUGINOSA ESTA-BASED VHH DISPLAY

*P. aeruginosa* is a Gram-negative life-threatening opportunistic pathogen infecting immunocompromised and cystic fibrosis patients. It is a member of the ESKAPE pathogens, the leading causes of nosocomial infections and major concerns about multi-drug resistance<sup>305</sup>. *P. aeruginosa* efficiently kills mammalian cells using its toxin-injecting type III secretion machinery (T3SS)<sup>306</sup>. This requires initial binding to the target cell and reports suggest that LecA and LecB, yet soluble, or the minor pilin PilY1 from the type IV pilus are involved in binding to target cells<sup>307,308</sup>. A more systematic approach to direct pathogenic bacteria towards target cell membrane such as synthetic display of adhesin would help studying the cytotoxic effects at the cellular level.

Several studies have used *Pseudomonas* EstA autotransporter for lipase display in either *E. coli* or *P. aeruginosa/putida*, and more recently for the display of a nucleic acid polymerase at the surface of *E. coli*<sup>35,309</sup>. However, to our knowledge, none of the recombinant passenger domains mounted on EstA scaffold consisted in adhesins. In addition, the intimin-based VHH display was unsuccessful in *P. aeruginosa* too (data not shown), most likely for the same reasons as in *A. tumefaciens*: to our knowledge, PAO1 has only 3 autotransporters, all from the T5aSS family (EstA, [PA5112], arginine-specific autotransporter [PA0328] and “probable serine protease” [PA3535]). Hence *P. aeruginosa* likely lacks the associated chaperones for the display of reverse autotransporter such as intimin. Here, we leveraged our findings in *A. tumefaciens* to rationally design an engineering approach for EstA-based VHH display in *P. aeruginosa*.

### 6.1 ENGINEERING APPROACH

In order to prevent interference from the lipase activity, an inactivation mutation of EstA (EstA\*) was published by Beckert *et al.*<sup>237</sup>. Of note, EstA harbors a short disulfide bond close the scaffold (C282-C288), hence we both tried to display VHH with and without disulfide, either N-terminal of EstA\* passenger or replacing the entire passenger domain (Figure 56A). After induction using an arabinose-inducible promoter and staining using recombinant GFP, we noted the successful display of the disulfide-free VHH using the truncated EstA (Figure 56B-E).

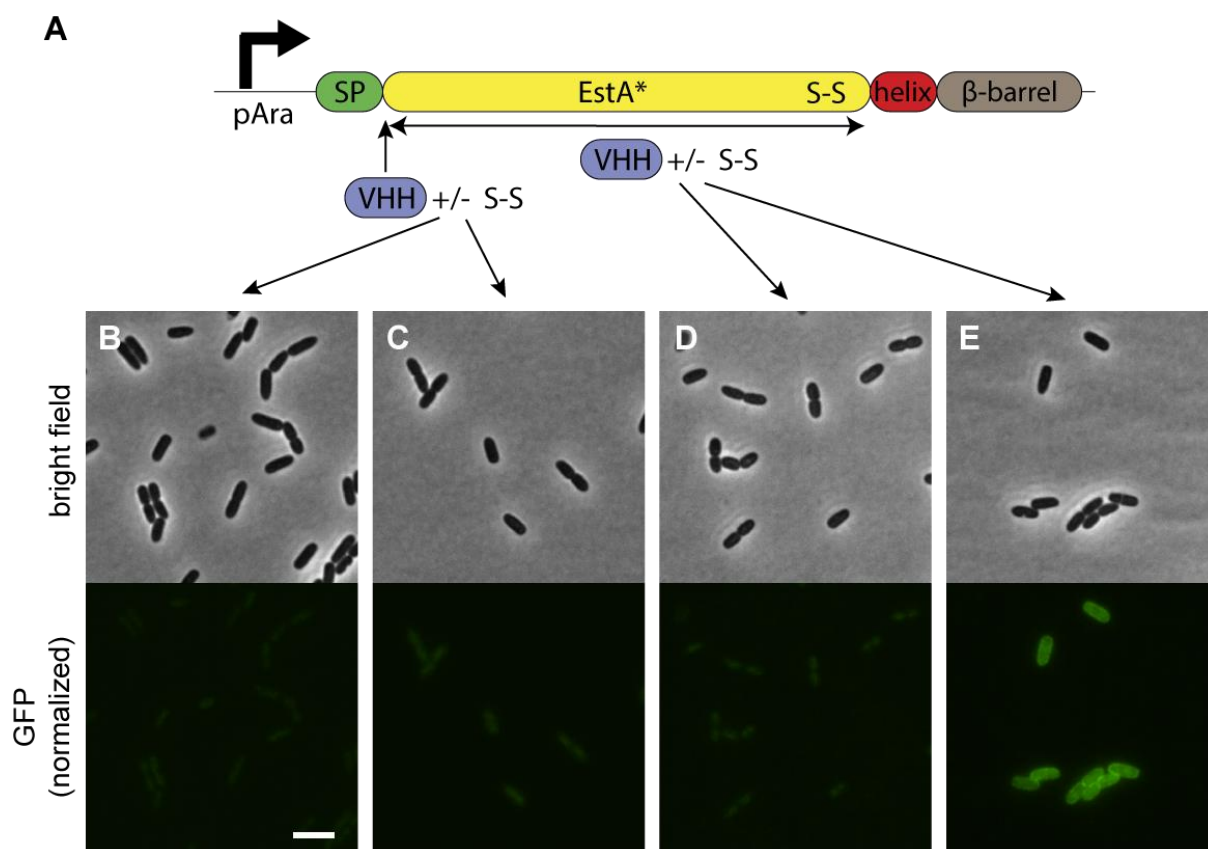


**Figure 56: Design of the VHH display in PAO1.**

(A) Schematic of the engineering approach. VHHαGFP with or without disulfide bond (S-S) was either introduced at the N-terminus of inactivated EstA (EstA\*) or instead of the whole enzyme. The secretion peptide (SP) and scaffold (helix and β-barrel) are kept for the display, and the construct is placed under an arabinose inducible promoter (pAra). (B-E) PAO1 retransformed with pAra – VHH display full-length EstA\* (A), VHH(cys-free) display full-length EstA\* (B), VHH display EstA scaffold (C) or VHH(cys-free) EstA scaffold (D). Bacteria were induced in LB and gentamycin at 60 μg/mL for 4h30 with 0.3% arabinose and stained with eGFP. eGFP intensity scale is identical between samples. Bar, 2 μm.

## 6.2 OPTIMIZATION

The signal of surface-bound GFP was rather low, we further improved the VHH display by optimizing the induction media and arabinose concentration. We found that cells induced for 8 hours in minimal medium (M9) resulted in around 4 times more signal than cells induced in LB (Figure 57A-C). Furthermore, M9 enabled induction of VHH display overnight, while cells induced in LB lost almost 100% of the signal (Figure 57D).

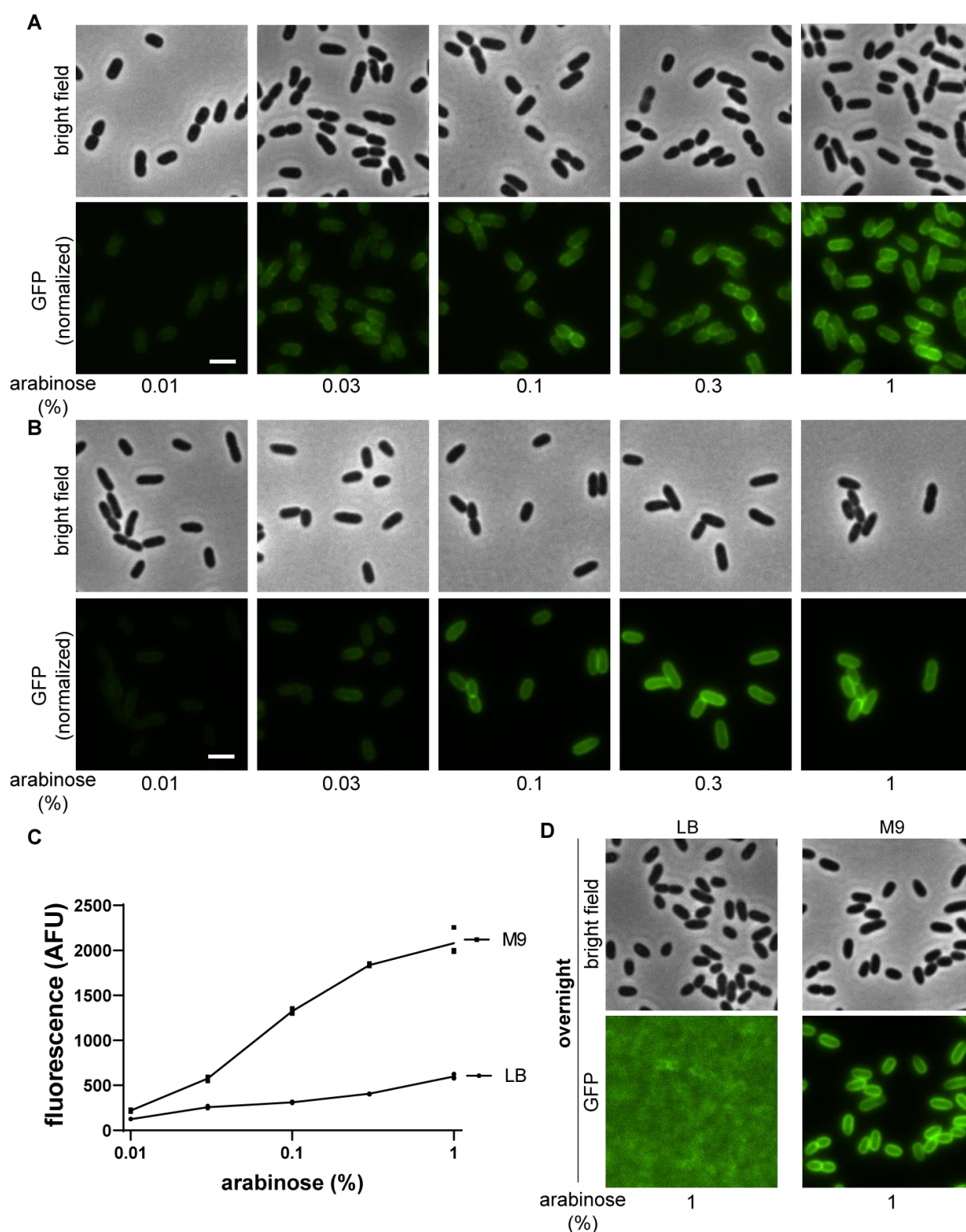


**Figure 57: Titration of the VHH display in PAO1 in different media.**

PAO1 retransformed with VHH(cys-free) EstA scaffold was induced with increasing concentrations of arabinose for 8h in LB (A) or M9 (B) and stained with eGFP. eGFP intensity scale is identical between samples. Bars, 1  $\mu$ m (C) Quantification of the mean GFP signal per bacterium in the different media as a function of arabinose concentration. (D) Comparison of the VHH display efficiency after overnight induction and eGFP staining shows a more sustainable induction in M9 compared to LB at 1% arabinose.

### 6.3 APPLICATION

We added *P. aeruginosa* displaying disulfide-free VHH to mammalian cells in static co-cultures and observed binding and cytotoxicity under confocal microscopy. We did not observe an increase in binding nor over-toxicity (propidium iodide staining) compared to WT *P. aeruginosa* (data not shown). The bacterium decorates itself with brush-like structures of lipopolysaccharides to protect itself against harsh chemicals (among other functions)<sup>310</sup>. It is particularly resistant to disinfection procedures in hospitals<sup>311</sup>. Consequently here, the bacterial own glycocalyx might be thicker than *E. coli*'s and sterically prevent membrane-membrane proximity and thus prevent VHH-GFP contact<sup>312</sup>. Alternatively, in a similar manner, extracellular appendages such as type IV pili might prevent VHH to reach GFP. To overcome this limitation, we could use longer linker such as the proline-rich linker of *A. tumefaciens* or pili-deficient *P. aeruginosa* mutants in future experiments.

## **7 APPENDIX 2: ATTEMPTED CHARACTERIZATION OF WT ATU5364 AND OXIDATION PREVENTION**

---

### **7.1 INVESTIGATING DISULFIDE BOND'S REMOVAL IN WT ATU5364**

In an effort to characterize the function of WT Atu5364, we incorporated a HA-tag in WT Atu5364 between the folded domain and the proline-rich domain, at the same place as with synthetic adhesins. To verify the display efficiency, we expressed it using the orthogonal cumic acid-inducible promoter (Figure 58A). Induction and staining with the FITC-conjugated anti HA antibody revealed a rare polar localization of Atu5364 (Figure 58B).

Since Atu5364 is located on the cryptic pAtC58 plasmid, which is involved in facilitating metabolic activities in the plant rhizosphere and bulk soil, we hypothesized that Atu5364 would be expressed in a reducing anaerobic environment. This would result in the prevention of disulfide bond formation between cysteines 35 and 48 of the passenger domain. To investigate this, we induced the construct overnight and bubbled nitrogen for 2 h prior to staining. A slight increase in FITC signal could be observed, yet still inhomogeneously distributed around the cell (Figure 58C). Finally, we genetically removed the disulfide by cloning a cysteine-free version of Atu5364 (C35M, C48S). Here, a more homogenous stain could be observed around bacteria (Figure 58D), suggesting that the disulfide bond prevented translocation in aerobic conditions.

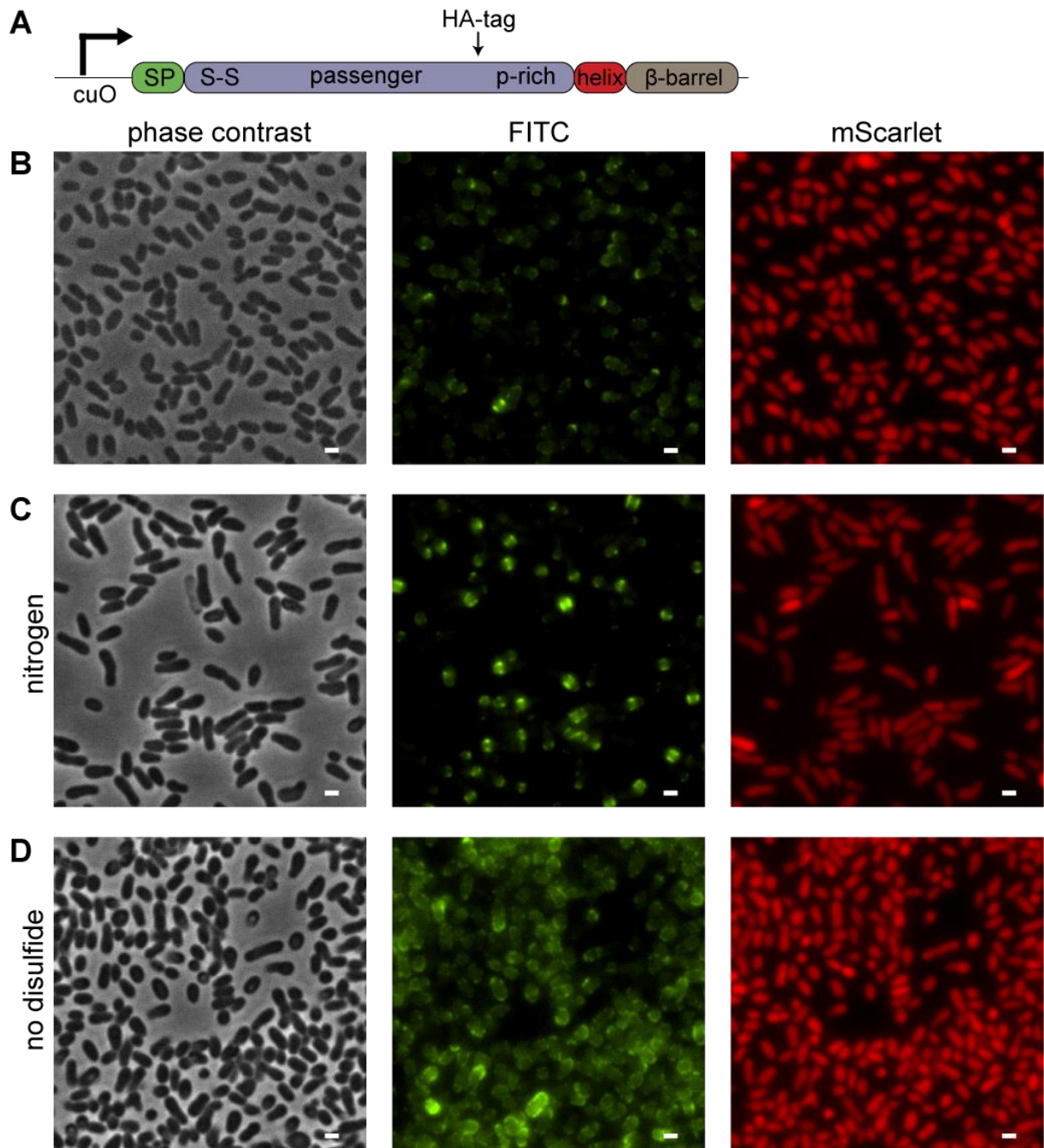


**Figure 58: Atu5364's disulfide bond removal promotes even surface distribution of the passenger domain.**

(A) Schematic of the genetic constructs used for assessing the impact of Atu5364's disulfide bond on display. (B-D) *A. tumefaciens mScarlet atu5364-* was retransformed with *tac\_cuO - atu5364\_HA* (B,C) or *tac\_cuO - atu5364\_cysteine\_free\_HA* (D) and stained with FITC-conjugated anti-HA antibody (anti-HA-FITC). (B) The staining is irregular and mostly unipolar. (C) Induced bacteria were cultured in reducing condition by bubbling nitrogen for 75 minutes prior to staining. The signal is slightly increased compared to (B) yet still uneven. (D) Disulfide-free Atu5364 is homogenously expressed at the surface of bacteria. Bars, 1  $\mu\text{m}$ .

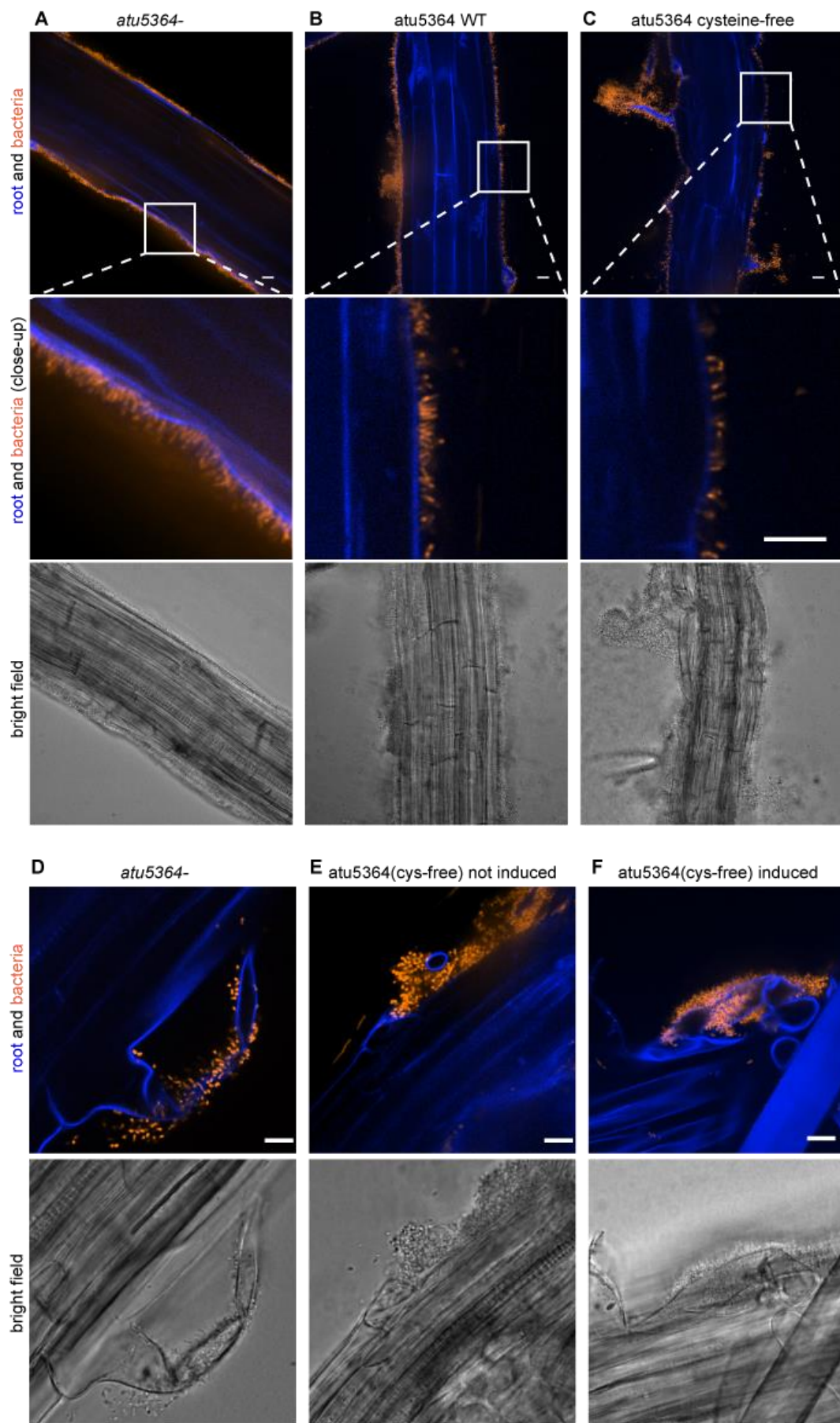
## 7.2 DOES WT ATU5364 MEDIATE BINDING TO ROOTS?

In the previous experiment, when overexpressing disulfide-free Atu5364, we did not observe increased sedimentation in culture tubes that would have suggested auto-aggregation of bacteria<sup>313</sup>. One possible function of Atu5364 could be adhesion to other cells types. As *atu5364* is located on the pAt plasmid involved in metabolism in the soil and rhizosphere, we designed an experiment to verify whether Atu5364 would improve binding to plant roots.

In this context, we immersed two-weeks old *A. thaliana* roots with *A. tumefaciens atu5364-*, or *A. tumefaciens atu5364-* complemented with inducible, plasmid-borne Atu5364 with or without cysteines. We performed the coculture experiments in different media. In acidified plant growth medium, *A. tumefaciens* bound to roots in a polar fashion (Figure 59A-C), reminiscent of unipolar polysaccharide (UPP)-mediated binding<sup>314</sup>. In *A. tumefaciens* induction medium, the bacteria preferentially bound to lateral root primordia (Figure 59D-F). We noted an increase in *A. tumefaciens* binding in the presence of the Atu5364 complementation construct, but we cannot explain the high binding in uninduced condition (E). The assay was highly variable, due to the buoyancy of the roots and their tendency to adhere to the side of the wells. In conclusion, further studies would be required in order to determine the actual function of WT Atu5364.

**Figure 59 (below): *A. tumefaciens* binding to *Arabidopsis thaliana* roots is independent of Atu5364.**

(A-C) *A. tumefaciens* (mScarlet, orange) uniformly binds to roots (blue autofluorescence) in a polar fashion in Murashige and Skoog + MES medium. (D-F) *A. tumefaciens* binds to lateral root primordia in Induction medium. (A,D) *A. tumefaciens atu5364-* pFGL815 (empty control). (B) *A. tumefaciens atu5364-* complemented with *tac\_cuo - atu5364\_HA*. (C,E,F) *A. tumefaciens atu5364-* complemented with *tac\_cuo - atu5364\_cysteine\_free\_HA*. The second line of panels are close-ups of the framed areas in the top panels. Bars, 10  $\mu$ m.



### 7.3 PREVENTION OF PERIPLASMIC OXIDATION BY KNOCKOUT OF THE *DSBA* HOMOLOG IN *A. TUMEFACIENS*

The prevention of disulfide bonds in WT Atu5364, FimH or VHH by substituting cysteine residues is a very effective way to improve cell surface display, but it might affect the functionality of the proteins. To circumvent this and avoid the need to systematically remove cysteines from the passenger domain, we looked for a solution to prevent oxidization of the passenger domain in the periplasm. One solution would be to interfere with the thiol disulfide oxidoreductase (DsbA), that initiates oxidation in the periplasm. For instance, in *E. coli*, Jose *et al.* showed an increase in *Vibrio cholerae* toxin B subunit translocation by the Iga $\beta$  autotransporter upon *dsbA* knockout<sup>34</sup>. An *A. tumefaciens* strain able to display any cysteine-containing passenger sequence would be strong upgrade for the flexibility of the display system, provided that reduced passenger domains keep their properties, or oxidize post-translocation.

We looked for the DsbA homolog in *A. tumefaciens*. A protein BLAST+ using *E. coli* K12 DsbA as input (ebi.ac.uk) gave as top homologue Atu0800 with an E value of 0.0019 and 23% of sequence identity. SignalP-5.0 expects a TAT signal peptide with 98% likelihood, confirming the periplasmic location of this DsbA homolog. Inversely, we used SwissModel with Atu0800 and found DsbA of different species (*Wolbachia pipientis*, *Chlamydia trachomatis*, *Salmonella enterica* serovar Typhimurium, *Staphylococcus aureus*, *P. aeruginosa* and *E. coli*) as the best templates.

Consequently, we generated *atu0800* knockout in *A. tumefaciens*. Surprisingly, the first observation was that the mutants became systematically kanamycin-insensitive. This might be either due to an improbable systematic insertion of the kanamycin resistance gene of the pNPTS138 suicide vector (see Table S2 and Material and Methods 2), or a deficit in kanamycin uptake by bacteria<sup>315</sup>.

We recloned the cumic acid-inducible Atu5364 and VHH anti-GFP display (with cysteines) into ampicillin/carbenicillin resistance vector and investigated the display efficiency in *atu0800*-background. In the case of the WT autotransporter, bacteria had aberrant, swollen and sometimes round shapes, but seemed to successfully display the construct (Figure 60).

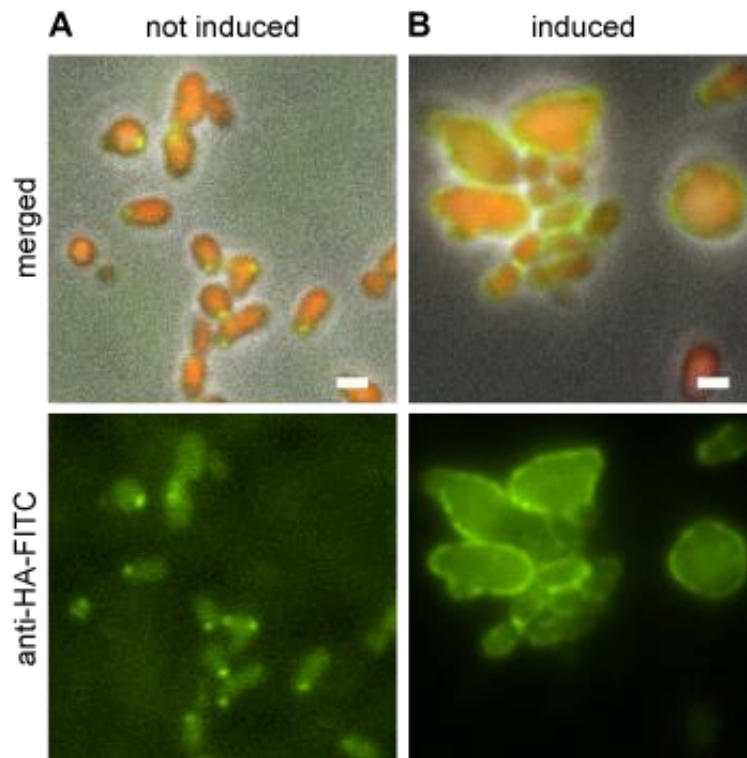


**Figure 60: *atu0800* knockout impairs bacterial shape and viability but enables Atu5364 display.**

*A. tumefaciens mScarlet atu0800-* was retransformed with *tac\_cuo - atu5364\_HA* in pPZPcarb, induced or not (B and A, respectively) and stained with FITC-conjugated anti-HA antibody (anti-HA-FITC). Bar, 1  $\mu$ m. Induced cells efficiently display Atu5364 but swell (B).

As for VHH display induction, we observed no significant increase in display efficiency compared to WT *A. tumefaciens* (Figure 61). One possible explanation would be that reduced cysteines, which contain each an additional hydrogen atom instead of forming a disulfide bond, sterically prevent VHH folding, as opposed to the precisely designed disulfide-free VHH (C24A, C98V)<sup>150</sup>. Alternatively, *dsbA* knockout, which has pleiotropic effects (e.g. shape, viability, kanamycin resistance), is also indirectly responsible for the failure at translocating VHH here.

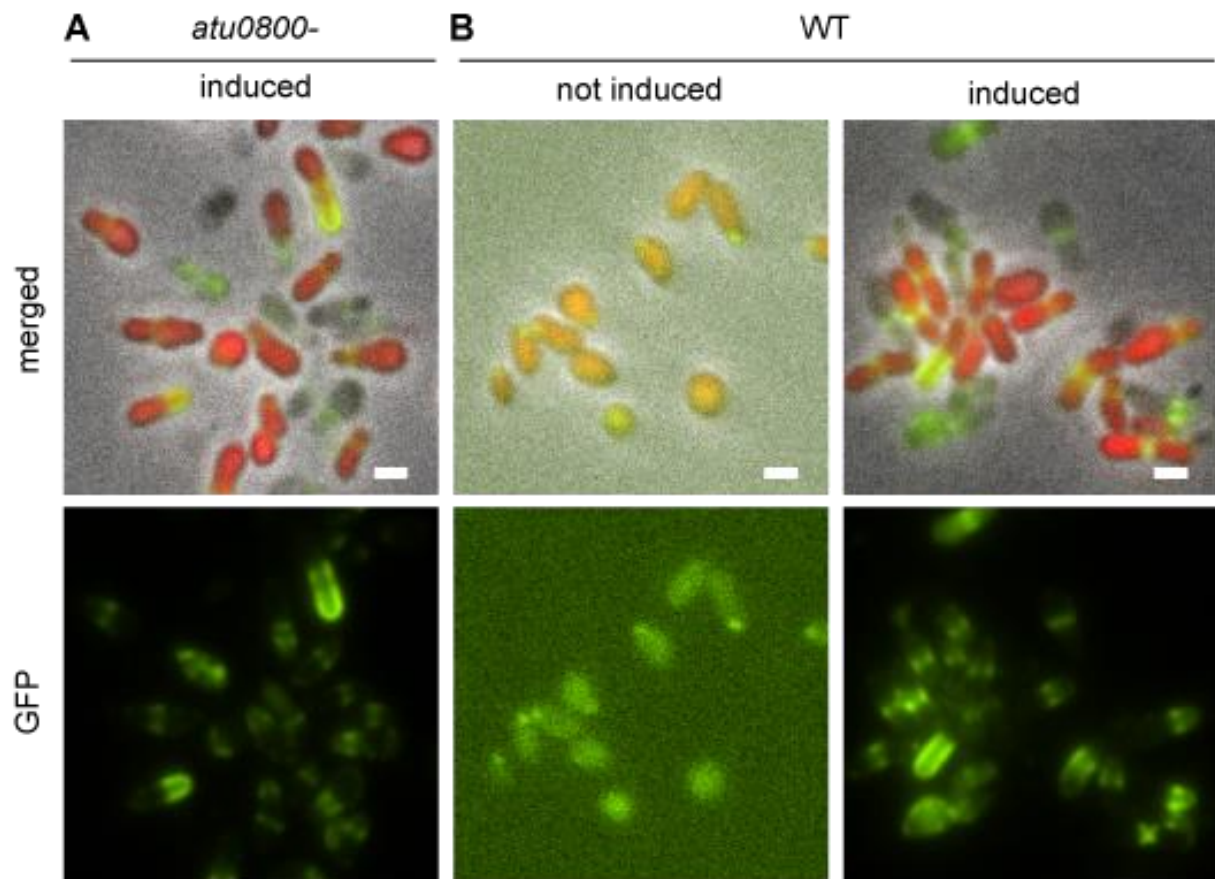


**Figure 61: *atu0800* knockout does not improve VHH display.**

*A. tumefaciens mScarlet atu0800-* (A) or *A. tumefaciens mScarlet* (B) were retransformed with tac\_cuo - VHH\_HA display in pZPcarb, induced or not and stained with recombinant eGFP. In both WT and *atu0800-*, a high cell death and unspecific staining are visible. Bar, 1  $\mu$ m.

## ADDITIONAL ACKNOWLEDGEMENTS

---

We thank:

- Dr. Bruno Correia, Stéphane Rosset and Dr. Leo Scheller at Ecole Polytechnique Fédérale de Lausanne (EPFL) for the production and purification of recombinant proteins, NanoLuc and split NanoLuc constructs
- Dr. Ingmar Riedel-Kruse (Stanford University) for the tetracycline-inducible nanobody display constructs
- Dr. Gisou Van der Goot (EPFL) for the GPI-anchored GFP construct
- Dr. Didier Trono and Sandra Offner (EPFL) for the HEK293T cells, lentivectors and tips for lentivirus production
- Dr. Joerg Huelsken (EPFL) for the CD80-GFP construct and HeLa cells
- Dr. Michael P. Rout (Rockefeller University) for the VHH anti-GFP of different affinities
- Dr. Simon Sieber (University of Zürich) for *C. reinhardtii* strains
- Dr. Csaba Koncz (Max Planck Institute for plant breeding research) for *A. tumefaciens* GV3101
- Dr. Julia Santiago (University of Lausanne) for *A. thaliana* roots
- Dr. Stanton B. Gelvin (Purdue University), Dr. Shen Q. Pan (University of Singapore), Dr. Reza Roushan (Leiden University) for fruitful discussion about *Agrobacterium*.
- Dr. Georgios Hatzopoulos (EPFL) for the help with *C. reinhardtii* work.
- Dr. Jessica Dessimoz for the trial with ssDNA-FISH.
- Many Addgene depositors of plasmids cited in Table S2.

We are grateful for the funding provided by the Gebert Rűf Foundation, project number GRS-057/16, the Novartis FreeNovation 2020 program and the EPFL School of Life Science interdisciplinary PhD program (Funding for Jeremy Wong).

## SUPPLEMENTARY INFORMATION

### Supplementary table 2: plasmids used in this study.

Construction by Gibson assembly unless stated otherwise.

Internal reference	Plasmid name(s)	Description Cloning approach: - Templates, primers used for PCR and/or enzymes for digestion - Followed by Gibson assembly (or ligation using T4 ligase when all DNA fragments are digested)	Reference
62	pJN105	Broad-host-range expression vectors that carry the L-arabinose-inducible <i>E. coli</i> araBAD promoter and the araC regulator. Works in PAO1, with leaky basal expression. Genta <sup>R</sup>	Newmann and Fuqua, 1999 <sup>316</sup>
290	pcDNA3.3 eGFP	Mammalian vector for pCMV-driven eGFP expression. Amp <sup>R</sup> , Neo <sup>R</sup>	Addgene 26822 <sup>317</sup>
291	pUCBB-eGFP	<i>E. coli</i> vector for constitutive expression of eGFP. Amp <sup>R</sup>	Addgene 32548 <sup>318</sup>
294	pX330-U6-Chimeric_BB-CBh-hSpCas9	A human codon-optimized SpCas9 and chimeric guide RNA expression plasmid. Amp <sup>R</sup>	Addgene 42230 <sup>319</sup>
296	pFGL815	Binary vector backbone for <i>Agrobacterium tumefaciens</i> with pVS1 ori. Kan <sup>R</sup>	Addgene 52322 <sup>320</sup>
298	pCW57-RFP-P2A-MCS (Neo)	All-in-one doxycycline-inducible lentiviral vector for expression of one gene in combination with turbo RFP using the P2A self-cleaving peptide. Amp <sup>R</sup> , Neo <sup>R</sup>	Addgene 89182 <sup>321</sup>
299	pEx18Ap	Suicide vector for two-step allelic exchange for S17- <i>Pseudomonas</i> mating. Amp <sup>R</sup>	Hoang <i>et al.</i> , 1998 <sup>322</sup>
302	pPZP200	<i>A. tumefaciens</i> binary vector with an MCS within T-DNA. pVS1 ori. Spec <sup>R</sup>	Hajdukiewicz <i>et al.</i> , 1994 <sup>323</sup>
303	pDSG323 pSB3K3 TetR pTet Neae2_v1	Tetracycline-inducible truncated intimin autotransporter scaffold ( <i>E. coli</i> ). Kan <sup>R</sup>	Glass <i>et. al.</i> , 2018 <sup>158</sup>
304	pDSG339 pSB3K3 TetR pTet Neae2_VHH	Tetracycline-inducible VHH anti-GFP display based on intimin autotransporter scaffold ( <i>E. coli</i> ). Kan <sup>R</sup>	Glass <i>et. al.</i> , 2018 <sup>158</sup>
368	pCB301 pJL-TRBO-G	We used the backbone of this binary vector in <i>A. tumefaciens</i> with IncPa1 ori. Kan <sup>R</sup>	Addgene 80083 <sup>324</sup>

<b>372</b>	pGEX6P1-mCherry-Nanobody	<i>E. coli</i> -optimized GST-tagged Nanobody anti mCherry	Addgene 70696 <sup>325</sup>
<b>433</b>	pGB2-24 FimH j96	<i>E. coli</i> vector for expression of FimH-j96 variant in KB18. Chloramph <sup>R</sup>	Sokurenko <i>et al</i> , 1994 <sup>326</sup>
<b>491</b>	pCTcon2	Yeast display expression vector with the yeast <i>trp1</i> selection marker. Kan <sup>R</sup> For in-frame insertion of C-terminal fusions to the cell-wall anchoring protein Aga2p, under the control of a galactose-inducible promoter.	Addgene 41843 <sup>327</sup>
<b>499</b>	pSP270	Yeast vector containing a kanMX marker pFA6_KanMX6	Unpublished , generous gift from Prof. Serge Pellet, UNIL
<b>517</b>	pSFFV_sfCherry2(11)_TagBFP	For expression of sfCherry2(11) fused to TagBFP in mammalian cells. Amp <sup>R</sup>	Addgene 82606 <sup>328</sup>
<b>522</b>	pET21a-CymR	<i>E. coli</i> expression vector for CymR production. Amp <sup>R</sup>	Addgene 51165 <sup>329</sup>
<b>523</b>	pKD227	Expresses <i>S. baltica</i> TtrS under the Ptac promoter. Used to PCR out the Pkm promoter . Spec <sup>R</sup>	Addgene 90954 <sup>330</sup>
<b>524</b>	pJM101	miniTn7 delivery plasmid with lacIq-Ptac inducible promoter. Amp <sup>R</sup> Genta <sup>R</sup>	Addgene 110558 <sup>331</sup>
<b>608</b>	PeGFP_GPI	pEGFP-N1 - preproinsulinSP eGFP linker DAF GPI eGFP display for mammalian cells , anchoring motif from CD55, preproinsulin secretion peptide	Ricci <i>et al</i> <sup>181</sup> , gift from Prof. Van der Goot, EPFL
<b>1053</b>	SpyTag003-mKate2	Expresses SpyTag003-mKate2 (a far-red fluorescent protein) in bacterial cytoplasm. Kan <sup>R</sup>	Addgene 133452 <sup>332</sup>
<b>1131</b>	pSFFV_sfCherry3C(1-10)	Lentiviral mammalian vector for constitutive expression of sfCherry3C(1-10). Amp <sup>R</sup>	Addgene 117482 <sup>328</sup>
<b>1159</b>	pRRL-PGK-LacZ-3HA-IRES-puro	Lentivector with constitutive hPGK promoter, LacZ HAtag, IRES. Amp <sup>R</sup> , Puro <sup>R</sup>	Trono lab, EPFL, unpublished
<b>1340</b>	pCambia1301	<i>A. tumefaciens</i> binary vector with T-DNA encoding plant-promoter-driven Hygromycin resistance gene and $\beta$ -glucuronidase. Kan <sup>R</sup>	Abcam ab275753
<b>EstA* pJN105</b>	EstA* pJN105	VHHαGFP_HA tag displayed at the N-terminus of inactivated PAO1 EstA under control of an arabinose-inducible promoter in pJN105. Genta <sup>R</sup>	This study, Jeremy

		<ul style="list-style-type: none"> <li>- pJN105, CGCTGAGCCTGGACTTCTGAACTAGTTCTAGAGCGGCCGC+TTGAGCGCCATTCTGATCATGAATTCGCTAGCCCAAAAAAAC</li> <li>- PAO1 gDNA, TTTTGGGCTAGCGAATTCATGATCAGAATGGCGCTCAAGC + GTTCGGCGACGCCCTCAGCGATGCCGGGCAGTTCCCCGAT</li> <li>- PAO1 gDNA, GCGACGCCCTCAGCGATGCCGGGCAGTTCCCCGATCCTG + CCTGGCGCTGAGCCTGGACTTCTGAACTAGTTCTAGAGCGGCCGC</li> </ul>	Wong, Persat lab
<b>pXP134</b>	T-DNA pCMV - eGFP	<p>T-DNA encoding a pCMV-driven eGFP expression in pPZP200. Spec<sup>R</sup></p> <ul style="list-style-type: none"> <li>- pPZP200, XmaI + PstI</li> <li>- pcDNA3.3 eGFP, aaacccggggacattgattattgactagtattataatagtaat + aaacccggggacattgattattgactagtattataatagtaat then XmaI + PstI</li> </ul>	This study
<b>pXP135</b>	pVirE-VirE0-1-2	<p>VirE0-1-2 gene in pFGL815 (resolvase excluded). Kan<sup>R</sup></p> <ul style="list-style-type: none"> <li>- pFGL815, agacggcggtacgttgccagccagccaacagct + ccgtaaacagtctgtagaaccgcaccaggacggc</li> <li>- <i>A. tumefaciens</i> gDNA, AGCTGTTGGCTGGCTGGCAACGTATCCGCCGTCT + gccgtcctggtgcgggttacagactgtttacggtg</li> </ul>	This study
<b>pXP136</b>	T-DNA pCMV – eGFP - hairpin	<p>T-DNA encoding a pCMV-driven eGFP expression in pPZP200. A 10 base-pairs hairpin is added compared to pXP134: gggtatacgcAATAAgcgtataccc after the poly(A). Spec<sup>R</sup></p> <p>Blunt ligation of pXP134 amplified with GCGTATACCCAAGCTTGCATGCCTGCAg + aataaGCGTATACCTGACAGGATATATTGGCGGG</p>	This study
<b>pXP137</b>	T-DNA pCMV – eGFP – AAV2_ITR	<p>T-DNA encoding for a pCMV-driven eGFP expression in pPZP200. AAV2_ITR is added compared to pXP134 after the poly(A). Spec<sup>R</sup></p> <ul style="list-style-type: none"> <li>- pXP134, atcactaggggtcctggaacaaacgacccaacacc + cgcagctgcctgcaggCGCCTTCAGTTTAACTATCAGTG</li> <li>- pX330-U6-Chimeric_BB-CBh-hSpCas90 , GCTTAGCTTGAGCTTGaggaacccctagtgtggag + GTCAAACACTGATAGTcctgcaggcagctgcg</li> </ul>	This study
<b>pXP145</b>	pCMV – GFP display	<p>Constitute eGFP (N105Y, E125V, Y146F) display based on C-terminal CD80 anchor, Amp<sup>R</sup>, Neo<sup>R</sup>.</p> <ul style="list-style-type: none"> <li>-</li> </ul>	Pierrat et. al, 2021 <sup>162</sup>
<b>pXP155</b>	pVirE - mScarlet	<p>mScarlet under control of VirE promoter in pFGL815. Kan<sup>R</sup></p> <ul style="list-style-type: none"> <li>- pXP135, CTCGCCCTTGCTCACCATcgtctaactccttttagccggc + GACGAGCTGTACAAGTGAAaccgcaccaggacggcc</li> <li>- mScarlet, ATGGTGAGCAAGGGCGAG + TCACTTGTACAGCTCGTCC</li> </ul>	This study
<b>pXP166</b>	pVirE - internalVHH display	<p>VHH-αGFP introduced between E512 and A513 into <i>atu5364</i> under control of VirE promoter in pFGL815. Kan<sup>R</sup></p> <ul style="list-style-type: none"> <li>- pXP182, cccaggtcaccgtctcctcagctgaggctcccgatat + accagctgcacctgagccatctccggggtgtatttg</li> <li>- pDSG339, atggctcaggtgcagct + taggagacgggtgacct</li> </ul>	This study

<b>pXP169</b>	pVirE – VHH display	VHH- $\alpha$ GFP replacing the passenger domain of atu5364 from C35 to E512 included, under control of VirE promoter in pFGL815. Kan <sup>R</sup> <ul style="list-style-type: none"> <li>- pXP182, cccaggtcaccgtctcctcagctgaggctcccgatat + accagctgcacctgagccatagctgcgttgcgggag</li> <li>- pDSG339, atggctcaggtgcagct + tggagagacggtgacct</li> </ul>	This study
<b>pXP174</b>	T-DNA = turboRFP fw	<i>A. tumefaciens</i> binary vector encoding a CMV-driven turboRFP as T-DNA. Spec <sup>R</sup> <ul style="list-style-type: none"> <li>- pXP134, tgatcagctcgctcatggtggctcttatattcttctact + caaactggggcacagataagctgccttctgcgg</li> <li>- pCW57-RFP-P2A-MCS RFP, aaatataagagccaccatgagcgagctgatcaagg + cgagaaggcagcttatctgtgccccagttgac</li> </ul>	This study
<b>pXP180carb</b>	T-DNA = turboRFP rev	<i>A. tumefaciens</i> binary vector encoding a reverse complement CMV-driven turboRFP as T-DNA. Carb <sup>R</sup> <ul style="list-style-type: none"> <li>- pXP217, ggggtgtgggtcggttggcCCGgggtaccgagctc + actagtcaataatcaatgtcCTGcaggcatgcaagct</li> <li>- pXP174, gaacaaacgaccaacac + gacattgattattgactagtattaatagt</li> </ul>	This study
<b>pXP182</b>	pVirE - atu5364 WT	Atu5364 WT under control of VirE promoter in pCB301. Kan <sup>R</sup> <ul style="list-style-type: none"> <li>- pXP135, aaccgcaccaggagcggc + cgtctaactccttttagccggc</li> <li>- <i>A. tumefaciens</i> gDNA, cggctaaaaggagtttagacgatcgccatcgagctac + ctggccgtcctggtgcggttctaccacttgatgttgagaccg</li> </ul>	This study
<b>pXP213</b>	pVirE – VHH(cys-free) display (for plasmid compatibility reasons with T-DNA vectors, we used the subclone pXP229)	VHH- $\alpha$ GFP cysteine-free (C24A, C98V) display under control of VirE promoter in pFGL815. VHH replaces the passenger domain of atu5364 from C35 to E512 included. Kan <sup>R</sup> <ul style="list-style-type: none"> <li>- pXP169, gccgtgtattacGTGaatgtcaatgtggccttga + tccagaggctgcCGCggagagtctcagagacc</li> <li>- pXP169, ctgagactctccGCGgcagcctctggattccc + cacattgacattCACgtaatacacggccgtgtc</li> </ul>	This study
<b>pXP217</b>	pPZPcarb empty vector	<i>A. tumefaciens</i> binary vector encoding a MCS as T-DNA. Amp/Carb <sup>R</sup> <ul style="list-style-type: none"> <li>- pPZP200, ggaaatgtgaataactcatGATGTTTAACTTTGTTTTAGGGCG + actgattaagcattggttaaTGCTAGCTAGAAATTCGTTCAAG</li> <li>- pEx18Ap, ttaccaatgcttaacagtgagg + atgagtattcaacattccgtgt</li> </ul>	This study
<b>pXP226</b>	pET28 - eGFP	6xHis-tagged eGFP in pET28a for recombinant expression. Kan <sup>R</sup>	Pierrat et. al, 2021 <sup>162</sup>
<b>pXP228</b>	pVirE – VirE2 WT	Plasmid complementation of VirE2 under control of VirE promoter in pCB301. Kan <sup>R</sup> <ul style="list-style-type: none"> <li>- pCB301, caaccgtaaacagctctgtagctaagagaaaagagcgtttattaga + agacggcgggatacgttgccagccagccaacagct</li> <li>- pXP135, caacgtatccgcccgtc + ctacagactgtttacgggttg</li> </ul>	This study
<b>pXP229</b>	pVirE – VHH(cys-free) $\alpha$ GFP display (used in this study)	VHH- $\alpha$ GFP cysteine-free (C24A, C98V) display under control of VirE promoter in pCB301. VHH replaces the passenger domain of atu5364 from C35 to E512 included. Kan <sup>R</sup> <ul style="list-style-type: none"> <li>- pCB301, gtctcaacatcaagtggtagctaagagaaaagagcgtttattaga + agacggcgggatacgttgccagccagccaacagct</li> </ul>	This study

		- pXP213, caacgtatccgccgtc + ctaccactgatgttgagacc	
<b>pXP233_ pNPTS138</b>	<i>virE2</i> knockout in pNPTS138	<p>Suicide vector for the knockout of <i>virE2</i> in <i>A. tumefaciens</i>. pNPTS138, two-step allelic exchange protocol. Kan<sup>R</sup> Sucrose<sup>S</sup></p> <ul style="list-style-type: none"> <li>- pNPTS138, EcoRI + XbaI</li> <li>- Overlap extension PCR of the following two PCR products followed by EcoRI + XbaI digestion: <ul style="list-style-type: none"> <li>o pXP229, atgaccatgattacgaattcagtcaggtgacctggcg + catcgtctaactccttttagcc</li> <li>o <i>A. tumefaciens</i> gDNA, ctaaaaggagtagacgatgtagatttctgataccgcgtc + gcctgcaggtcgactctagatattcacatgcttcgcgc</li> </ul> </li> </ul>	This study
<b>pXP234_ pNPTS138</b>	VHH(cys-free) display knockin instead of VirE2	<p>Suicide vector for the knockin of cysteine-free VHH-αGFP instead of <i>virE2</i> in <i>A. tumefaciens</i>. pNPTS138, two-step allelic exchange protocol. Kan<sup>R</sup> Sucrose<sup>S</sup></p> <ul style="list-style-type: none"> <li>- pNPTS138, EcoRI + XbaI</li> <li>- Overlap extension PCR of the following two PCR products followed by EcoRI + XbaI digestion: <ul style="list-style-type: none"> <li>o pXP229, atgaccatgattacgaattcagtcaggtgacctggcg + ctaccactgatgttgagacc</li> <li>o <i>A. tumefaciens</i> gDNA, gtctcaacatcaagtggttagatttctgataccgcgtcag + gcctgcaggtcgactctagatattcacatgcttcgcgc</li> </ul> </li> </ul>	This study
<b>pXP250</b>	pSynth - mScarlet knock-in in <i>tetR</i>	<p>Suicide vector for the introduction of <i>mScarlet</i> under control of a consensus synthetic promoter originally optimized for <i>E. coli</i>: <a href="http://parts.igem.org/Part:BBa_J23119">http://parts.igem.org/Part:BBa_J23119</a>, introduced into the <i>tetR</i> locus. pNPTS138, two-step allelic exchange protocol. Kan<sup>R</sup> Sucrose<sup>S</sup></p> <ul style="list-style-type: none"> <li>- pNPTS138, EcoRI + HindIII</li> <li>- <i>A. tumefaciens</i> gDNA, cggccgaagctagcgaattcccttcatttcggctgttcac + AGGACTGAGCTAGCTGTCAAcggtatgaaggagaagctgc</li> <li>- pZA002, TTGACAGCTAGCTCAGTCC + TTACTTATACAGTTCATCCATACCAC</li> <li>- <i>A. tumefaciens</i> gDNA, TGGATGAAGTGTATAAGTAAgcactttatctctgccttg + agccggctggcgccaagcttggtattggcggcggtattatc</li> </ul>	This study
<b>pXP255</b>	pVirE – VHHamCherry(cys-free) display	<p>VHH-anti-mCherry cysteine-free (C24A, C98V) display under control of VirE promoter in pCB301</p> <ul style="list-style-type: none"> <li>- pXP229, tatattagcagcaatcagcgccgtgtatggttactggggccagggg + gctttctgcaaaacgtccagaggctgcCGC</li> <li>- pGEX6P1-mCherry-Nanobody, GCGgcagcctctggacgttttcagaaagcagc + ctgattgtgctaataatagttaccagattggctgcCACataatacac</li> </ul>	This study
<b>pXP257</b>	pCMV - VirE2	<p>Constitutive mammalian expression of VirE2 driven by a CMV promoter. Amp<sup>R</sup></p> <ul style="list-style-type: none"> <li>- pcDNA3.3 eGFP, gctgccttctgcgggg + ggtggctcttatatttcttactcttct</li> <li>- <i>A. tumefaciens</i> gDNA, gaagaaatataagagccaccatggatccgaaggccga + caagccccgcagaaggcagcctacagactgtttacggttggg</li> </ul>	This study
<b>pXP265</b>	pVirE – FimH display	<p>FimH(j96) display under control of VirE promoter in pCB301. Kan<sup>R</sup></p> <ul style="list-style-type: none"> <li>- pXP229, gctgaggtcccgatc + agctgcgtttgcggg</li> </ul>	This study

		<ul style="list-style-type: none"> <li>- pGB2-24 FimH j96, ctctcccgcacaaacgcagctttcgctgtaaaaccgcc + gtgatatcgaggcctcagcgcgcagtaggcac</li> </ul>	
<b>pXP267</b>	pGal1 – eGFP display	Galactose-inducible Aga2p-eGFP yeast display in pCTcon2, Kan <sup>R</sup> , <i>trp1</i> Ligation of the following: <ul style="list-style-type: none"> <li>- pCTcon2, NheI + XhoI</li> <li>- pcDNA3.3 egfp, tcggctagcatggtgagcaagggcgag + gatctcgagtcactgtacagctcgctcc then NheI + XhoI</li> </ul>	This study
<b>pXP269</b>	pVirE – RGD display	RGD display under control of VirE promoter in pCB301. AGRGDSP replaces the passenger domain of <i>atu5364</i> from C35 to E512 included. Kan <sup>R</sup> <ul style="list-style-type: none"> <li>- pXP182, CGCGGCGACAGCCCCGgctgaggctcccgatcac + GCCGGCagctgcgtttgcggg</li> </ul>	This study
<b>pXP272</b>	pCMV – C4_VirD2	Constitutive mammalian expression of N-terminally tetracysteine (CCPGCC) tagged VirD2 driven by a CMV promoter. Amp <sup>R</sup> <ul style="list-style-type: none"> <li>- pcDNA3.3 eGFP, gctgccttctgcggg + ACAACATCCCCGGGCAGCAcatgggtgctcttatatttctttac</li> <li>- <i>A. tumefaciens</i> gDNA, TGCTGCCCCGGGATGTTGTcccgatcgagctcaagtt + caagccccgcagaaggcagcctatctctatttccccacg</li> </ul>	This study
<b>pXP273</b>	<i>atu5364</i> knockout	Suicide vector for the markerless deletion of <i>atu5364</i> . pNPTS138, two-step allelic exchange protocol. Kan <sup>R</sup> Sucrose <sup>S</sup> <ul style="list-style-type: none"> <li>- pNPTS138, EcoRI + HindIII</li> <li>- <i>A. tumefaciens</i> gDNA, cggccgaagctagcgaattcaatccgagcggttgcag + gcggcgacggctacatcgctcctcggaaccg</li> <li>- <i>A. tumefaciens</i> gDNA, ttccgaaggacgatgtagccgtgccgccg + agccggctggcgccaagcttcatctgggtgcggc</li> </ul>	This study
<b>pXP277</b>	pVirE - FimH_6xHis display	FimH and 6xHis tag display under control of VirE promoter in pCB301. Kan <sup>R</sup> <ul style="list-style-type: none"> <li>- pXP229, gctgaggctcccgatc + agctgcgtttgcggg</li> <li>- pGB2-24 FimH j96, ctctcccgcacaaacgcagctttcgctgtaaaaccgcc + atcgggagcctcagcatgatgatgatggtggccgagtaggcaccac</li> </ul>	This study
<b>pXP282</b>	kanMX cassette T-DNA in pPZP200	<i>A. tumefaciens</i> binary vector encoding a yeast kanamycin/G418 resistance cassette as T-DNA. Spec <sup>R</sup> <ul style="list-style-type: none"> <li>- pPZP200, cttgggtttgtgccatctgTGACAGGATATATTGGCGGG + cgatcttctagggcgagacGTTTACACCACAATATATCCTGCC</li> <li>- pSP270, gtctgcccctaagaagatcgctgtttgccaggtgaccacgttggtcaagtagctgcctcgctcccc + cagatggcaacaaacccaaggaacctgggataacggaggcttcacggaggcggttagtatcgaatcg</li> </ul>	This study
<b>pXP283</b>	kanMX reverse complement cassette T-DNA in pPZPcarb	<i>A. tumefaciens</i> binary vector encoding a yeast kanamycin/G418 resistance cassette as T-DNA. Carb <sup>R</sup> <ul style="list-style-type: none"> <li>- pPZPcarb, cgatcttctagggcgagacTGACAGGATATATTGGCGGG + cttgggtttgtgccatctgGTTTACACCACAATATATCCTGCC</li> </ul>	This study

		<ul style="list-style-type: none"> <li>- pSP270, gtctgccctaagaagatcgctgtttgccagggtgaccacgttggtcaagtagcttgccctgtcccc + cagatggcaacaaacccaaggaacctgggataacggaggctcatcgaggcggttagtatcgaatcg</li> </ul>	
<b>pXP288</b>	pVirE sfCherry2_11::VirE2 (pFGL815)	<p>sfCherry2_11 peptide introduced at position P61 in VirE2 under control of VirE promoter in pFGL815. Kan<sup>R</sup></p> <ul style="list-style-type: none"> <li>- pXP135, tagaaccgcaccaggac + ctgggtctctcgactgctccacgatggtgtacgggcttccgtgcatg</li> <li>- pXP135, cagtacgagagagccgaggccagacacagcaccactcacacggatgatctcg + gccgtcctggtgcggttctacagactgtttacggttg</li> </ul>	This study
<b>pXP293</b>	FimH(C3S) in pGB2-24	<p>Disulfide-free FimH(C3S) for expression in <i>E. coli</i> KB18. Amp<sup>R</sup></p> <ul style="list-style-type: none"> <li>- pGB2-24 FimH j96, ggcggctgcgatgtt + tgaccaggcatttaccgac</li> <li>- pGB2-24 FimH j96, gtaaatgcctggtcattcgccAGCaaaaccgccaatg + cgagcagaaacatcgag</li> </ul>	This study
<b>pXP294</b>	pVirE – FimH(C3S) 6xHis display	<p>FimH(C3S) and 6xHis tag display under control of VirE promoter in pCB301. Kan<sup>R</sup></p> <ul style="list-style-type: none"> <li>- pXP277, ctctcccgcacaaacgcagctttgccAGCaaaaccgcc + agacggcggatacgttgccagccagccaacagct</li> <li>- pXP277, AGCTGTTGGCTGGCTGGCAACGTATCCGCCGTCT + agctgcgtttgcggg</li> </ul>	This study
<b>pXP299</b>	pVirE - His_LecA	<p>LecA 6xHis display under control of VirE promoter in pCB301. Kan<sup>R</sup></p> <ul style="list-style-type: none"> <li>- pXP277, ggcggccaccatcat + agctgcgtttgcggg</li> <li>- PAO1 gDNA, ctctcccgcacaaacgcagctATGGCTTGGAAGGTGAGG + tgatgatgatggtggccgccGGACTGATCCTTTCCAATATTGA</li> </ul>	This study
<b>pXP300</b>	pVirE - His_LecB	<p>LecB 6xHis display under control of VirE promoter pCB301. Kan<sup>R</sup></p> <ul style="list-style-type: none"> <li>- pXP277, ggcggccaccatcat + agctgcgtttgcggg</li> <li>- PAO1 gDNA, ctctcccgcacaaacgcagctATGGCAACACAAGGAGTGTTC + tgatgatgatggtggccgccGCCGAGCGGCCAGTT</li> </ul>	This study
<b>pXP302</b>	VHH(cys-free) display knock-in instead of <i>virF</i>	<p>Suicide vector for the replacement of <i>virF</i> by VHH-αGFP cysteine-free (C24A, C98V) in <i>A. tumefaciens</i> chromosome. pNPTS138, two-step allelic exchange protocol. Kan<sup>R</sup> Sucrose<sup>S</sup></p> <ul style="list-style-type: none"> <li>- pNPTS138, EcoRI + HindIII</li> <li>- <i>A. tumefaciens</i> gDNA, acggccgaagctagcgaattcggttcggatcgcca + cgtgcatgctcctctttc</li> <li>- pXP229, agaaagaaggagcatgcagatgcggcatcgagctac + ctaccattgatgttgagacc</li> <li>- <i>A. tumefaciens</i> gDNA, gtctcaacatcaagtggtagtttcttgatccaccgc + aagccggctggcgccaagcttccgcatggacaag</li> </ul>	This study
<b>pXP304</b>	pVirE - atu5364_HA	<p>Atu5364-HA-tag display under control of VirE promoter in pCB301. Kan<sup>R</sup></p> <ul style="list-style-type: none"> <li>- pXP229, TACCGTATGATGTTCCCGACTATGCCgctgaggctcccgatc + ccagccagccaacagc</li> <li>- pXP182, AGCTGTTGGCTGGCTGGCAACGTATCCGCCGTCT + AACATCATACGGGTactccgggggtggtattgg</li> </ul>	This study
<b>pXP305</b>	pVirE - atu5364_cysteine_free_HA	<p>Cysteine-free atu5364(C35M, C48S)-HA-tag display under control of VirE promoter in pCB301. Kan<sup>R</sup></p>	This study

		<ul style="list-style-type: none"> <li>- pXP229, TACCCGTATGATGTTCCCGACTATGCCgctgaggctcccgatc + ccagccagccaacagc</li> <li>- pXP182, AACATCATACGGGTActccggggtggtattgg + cccgcaaacgcagctATGaatttccagccccggttgaaatgacatttatattCcgacagcgga</li> <li>- pXP182, AGCTGTTGGCTGGCTGGCAACGTATCCGCCGTCT + agctgcgttgcggg</li> </ul>	
<b>pXP306</b>	pVirE – FimH_HA tag display	<p>FimH(j96)_HA-tag display under control of VirE promoter in pCB301. Kan<sup>R</sup></p> <ul style="list-style-type: none"> <li>- pXP229, TACCCGTATGATGTTCCCGACTATGCCgctgaggctcccgatc + ccagccagccaacagc</li> <li>- pXP265, AGCTGTTGGCTGGCTGGCAACGTATCCGCCGTCT + AACATCATACGGGTAgccgccagtaggcac</li> </ul>	This study
<b>pXP307</b>	pVirE – FimH(C3S)_HA tag display	<p>FimH(C3S)(j96)_HA-tag display under control of VirE promoter in pCB301. Kan<sup>R</sup></p> <ul style="list-style-type: none"> <li>- pXP229, TACCCGTATGATGTTCCCGACTATGCCgctgaggctcccgatc + ccagccagccaacagc</li> <li>- pXP294, AGCTGTTGGCTGGCTGGCAACGTATCCGCCGTCT + AACATCATACGGGTAgccgccagtaggcac</li> </ul>	This study
<b>pXP308</b>	pVirE – VHH(cys-free)_HA tag display	<p>VHH-αGFP cysteine-free (C24A, C98V) HA tag display under control of VirE promoter in pCB301</p> <ul style="list-style-type: none"> <li>- pXP229, TACCCGTATGATGTTCCCGACTATGCCgctgaggctcccgatc + agacggcggatacgttgccagccagccaacagct</li> <li>- pXP229, AGCTGTTGGCTGGCTGGCAACGTATCCGCCGTCT + AACATCATACGGGTAgccgccagtaggcac</li> </ul>	This study
<b>pXP313</b>	tac_cuo - mScarlet	<p>Cumic-acid inducible mScarlet in pFGL815. Kan<sup>R</sup></p> <ul style="list-style-type: none"> <li>- pXP155, ccagccagccaacagc + cagcacactggcggccgttactagaaataattttgttaactttaagaaggagatataccATGGTGAGCAAGG GCG</li> <li>- pET21_CymR, gggagctgttgctggctgggtaacgttgaatttgcataacgt + atgagcccgaacgtcg</li> <li>- pKD227, cgacgttcgggctcatcttgcgaaacgatcctcatcct + gcatgcatttaaatacgcgtccggaattgccagctg</li> <li>- pJM101, acgcgtatttaaatacgtgctgcagtcgacggtgcac + taacggccgccagtgctggaattcataatacaaacagaccagattgtctgtttgttccacacattatacagagccgat</li> </ul>	This study
<b>pXP316</b>	atu0800 knockout	<p>Suicide vector for the knockout of <i>atu0800</i> in <i>A. tumefaciens</i>. pNPTS138, two-step allelic exchange protocol. Kan<sup>R</sup> Sucrose<sup>S</sup></p> <ul style="list-style-type: none"> <li>- pNPTS138, EcoRI + HindIII</li> <li>- <i>A. tumefaciens</i> gDNA, cggccgaagctagcgaattcgattgcacccggccg + aggcttcggtgatcacatgaaagcacctgttgtaaatg</li> </ul>	This study

		<ul style="list-style-type: none"> <li>- <i>A. tumefaciens</i> gDNA, acaggtgcttcatgtgatcaccgaagccttcag + agccggctggcgccaagcttgcttgccattgatgagc</li> </ul>	
<b>pXP319</b>	tac_cuO – LecA_HA display	<p>Cumic-acid inducible PAO1 LecA display with HA tag in pFGL815. Kan<sup>R</sup></p> <ul style="list-style-type: none"> <li>- pXP313, NcoI + BsrGI</li> <li>- pXP313, tagaaccgcaccaggac + gtatatctccttctaaagttaaacaaaattatttc</li> <li>- pXP299, actttaagaaggagatatacatgcggcatcgagctac + GAACATCATACGGGTAgccgccGGACTGATCCTTTCCAATATTGAC</li> <li>- pXP304, ggcggcTACCCGTATG + ctggccgtcctggtgcggttctaccacttgatgttgagaccg</li> </ul>	This study
<b>pXP320</b>	tac_cuO – LecB_HA display	<p>Cumic-acid inducible PAO1 LecB display with HA tag in pFGL815. Kan<sup>R</sup></p> <ul style="list-style-type: none"> <li>- pXP313, NcoI + BsrGI</li> <li>- pXP313, tagaaccgcaccaggac + gtatatctccttctaaagttaaacaaaattatttc</li> <li>- pXP300, actttaagaaggagatatacatgcggcatcgagctac + AACATCATACGGGTAgccgccGCCGAGCGGCCAGT</li> <li>- pXP304, ggcggcTACCCGTATG + ctggccgtcctggtgcggttctaccacttgatgttgagaccg</li> </ul>	This study
<b>pXP321</b>	Patu5364 - mScarlet	<p>mScarlet transcriptional reporter for the promoter of <i>atu5364</i> in pFGL815. Kan<sup>R</sup></p> <ul style="list-style-type: none"> <li>- pXP155, ccagccagccaacagc + ATGGTGAGCAAGGGCGAG</li> <li>- <i>A. tumefaciens</i> gDNA, gggagctgttggtggtggaacttttgacggctcc + GCCTCGCCCTTGCTCACCATcgtccttcggaaccgg</li> </ul>	This study
<b>pXP323</b>	tac_cuO - <i>atu5364</i> _HA	<p>Cumic-acid inducible <i>atu5364</i> display with HA tag in pFGL815. Kan<sup>R</sup></p> <ul style="list-style-type: none"> <li>- pXP313, NcoI + BsrGI</li> <li>- pXP313, tagaaccgcaccaggac + gtatatctccttctaaagttaaacaaaattatttc</li> <li>- pXP304, actttaagaaggagatatacatgcggcatcgagctac + ctggccgtcctggtgcggttctaccacttgatgttgagaccg</li> </ul>	This study
<b>pXP324</b>	tac_cuO - <i>atu5364_cysteine_free</i> _HA	<p>Cumic-acid inducible cysteine-free <i>Atu5364</i> (C35M, C48S) display with HA tag in pFGL815. Kan<sup>R</sup></p> <ul style="list-style-type: none"> <li>- pXP313, NcoI + BsrGI</li> <li>- pXP313, tagaaccgcaccaggac + gtatatctccttctaaagttaaacaaaattatttc</li> <li>- pXP305, actttaagaaggagatatacatgcggcatcgagctac + ctggccgtcctggtgcggttctaccacttgatgttgagaccg</li> </ul>	This study
<b>pXP328</b>	Patu5364 - eGFP	<p>eGFP transcriptional reporter for the promoter of <i>atu5364</i> in pFGL815. Kan<sup>R</sup></p> <ul style="list-style-type: none"> <li>- pXP321, GACGAGCTGTACAAGTGAaaccgcaccaggacggcc + GCCTCGCCCTTGCTCACCATcgtccttcggaaccgg</li> <li>- pUCBB-eGFP, ATGGTGAGCAAGGGCGAG + TCACTTGTACAGCTCGTCC</li> </ul>	This study
<b>pXP340</b>	tetON – GFP-display	<p>Mammalian lentivector containing a tetracycline-inducible GFP(N105Y, E125V,Y146F) - display anchored with a truncated CD80 transmembrane domain in pRRLSIN.cPPT.insert.WPRE</p>	Pierrat et. al, 2021 <sup>162</sup>
<b>pXP342</b>	tac_cuO - <i>atu5364</i> _HA in pPZPcarb	<p>Cumic-acid inducible <i>atu5364</i> display with HA tag in pPZPcarb. Amp<sup>R</sup></p> <ul style="list-style-type: none"> <li>- pXP217, AACCGCACCAAGGACGG + ccagccagccaacagc</li> </ul>	This study

		<ul style="list-style-type: none"> <li>- pXP323, gggagctgttgctggctgggtaacgtttgaatttgcataacgt + gccgtcctggcggttctaccacttgatgttgagaccg</li> </ul>	
<b>pXP343</b>	tac_cuo - VHH_HA display in pPZPcarb	<p>Cumic-acid inducible VHH-αGFP HA-tag display in pPZPcarb. Amp<sup>R</sup></p> <ul style="list-style-type: none"> <li>- pXP217, AACCGCACCAGGACGG + ccagccagccaacagc</li> <li>- pXP313, gggagctgttgctggctgggtaacgtttgaatttgcataacgt + gtatatctccttctaaagttaacaaaattatttc</li> <li>- pXP169, actttaagaaggagatatacatgcggcatcgagctac + gccgtcctggcggttctaccacttgatgttgagaccg</li> </ul>	This study
<b>pXP344 bis</b>	tac_cuo - LipA HA tag display	<p>Cumic-acid inducible LipA (<i>Bacillus subtilis</i>) display with HA tag in pFGL815. Kan<sup>R</sup></p> <ul style="list-style-type: none"> <li>- pXP323, TACCCGTATGATGTTCCCGAC + agctgcgttgcggg</li> <li>- B. subtilis gDNA, cccgcaaacgcagctgaacacaatccagtcg + TCGGGAACATCATACGGGTAattcgatttctggccccc</li> </ul>	This study
<b>pXP349</b>	tac_cuo - LipA HA tag (cytosolic)	<p>Cumic-acid inducible LipA (<i>Bacillus subtilis</i>) without signal peptide with HA tag in pFGL815. Kan<sup>R</sup></p> <ul style="list-style-type: none"> <li>- pXP323, TACCCGTATGATGTTCCCGAC + gtatatctccttctaaagttaacaaaattatttc</li> <li>- B. subtilis gDNA, AAGAAGGAGATATACATGGCTGAACACAATCCAGTCG + TCGGGAACATCATACGGGTAattcgatttctggccccc</li> </ul>	This study
<b>pXP383</b>	pTet – intimin_VHH K <sub>D</sub> = 0.59 nM	VHH anti GFP display. Kan <sup>R</sup> , K <sub>D</sub> = 0.59 nM Tet-inducible VHH display based on truncated intimin + HA tag.	Pierrat et. al, 2021 <sup>162</sup>
<b>pXP384</b>	pTet – intimin_VHH K <sub>D</sub> = 16 nM	Low affinity VHH anti GFP display. Kan <sup>R</sup> , K <sub>D</sub> = 16 nM Tet-inducible VHH display based on truncated intimin + HA tag.	Pierrat et. al, 2021 <sup>162</sup>
<b>pXP388</b>	pTet – intimin_VHH K <sub>D</sub> = 20 pM	High affinity VHH anti GFP display. Kan <sup>R</sup> , K <sub>D</sub> = 20 pM Tet-inducible VHH display based on truncated intimin + HA tag.	Pierrat et. al, 2021 <sup>162</sup>
<b>pXP457</b>	pVirE - sfCherry2_11::VirE2 (pCB301)	<p>sfCherry2_11 peptide introduced at position P61 in VirE2 under control of VirE promoter in pCB301. Kan<sup>R</sup></p> <ul style="list-style-type: none"> <li>- pCB301, ctaagagaaaagagcggttattagaataatcg + ccagccagccaacagc</li> <li>- pXP288, gggagctgttgctggctggcaacgtatccgccgtctc + taaacgctcttcttagctacagactgtttacggttggg</li> </ul>	This study
<b>pXP462</b>	pVirE – VHH(cys-free)::TetR	<p>Suicide vector for introducing VHH-αGFP cysteine-free (C24A, C98V) display under control of VirE promoter into <i>A. tumefaciens tetR</i> locus. pNPTS138, two-step allelic exchange protocol. Kan<sup>R</sup> Sucrose<sup>S</sup></p> <ul style="list-style-type: none"> <li>- pXP250, gcactttatcttctcgcttg + cggtatgaaggagaagctgc</li> <li>- pXP229, gcagcttctccttcataccgcaacgtatccgccgtctc + aaggcgagaagataaagtcctaccacttgatgttgagaccg</li> </ul>	This study

<b>pXP466</b>	virE knockout	<p>Suicide vector for deletion of the <i>virE</i> operon. pNPTS138, two-step allelic exchange protocol. Kan<sup>R</sup> Sucrose<sup>S</sup></p> <ul style="list-style-type: none"> <li>- pNPTS138, EcoRI + HindIII</li> <li>- <i>A. tumefaciens</i> gDNA, cggccgaagctagcgaattcggcctgcagaacaccg + cttgaatcggtaatttcatttcattgccccgaatggc</li> <li>- <i>A. tumefaciens</i> gDNA, aatgaaattaccgattcaagtgtcc + agccggctggcgccaagctttccgaaacgatctgcg</li> </ul>	This study
<b>pXP479</b>	pVirE – RGD-HA display	<p>RGD + HA tag display under control of VirE promoter in pCB301. AGRGDSP replaces the passenger domain of atu5364 from C35 to E512 included. Kan<sup>R</sup></p> <ul style="list-style-type: none"> <li>- pXP269, tagaaccgcaccaggac + AACATCATACGGGTACGGGCTGTGCGCCG</li> <li>- pXP269, TACCCGTATGATGTTCCCGACTATGCCgctgaggctcccgatatca + gccgtcctggtgcggttctaccactgatgttgagaccg</li> </ul>	This study
<b>pXP485</b>	sfCherry3C(1_10) in lentivector	<p>Second generation lentivector containing a constitutive hPGK promoter driving sfCherry3C(1-10) (split mCherry) expression. Amp<sup>R</sup>, Puro<sup>R</sup></p> <p>Ligation of the following:</p> <ul style="list-style-type: none"> <li>- pRRL-PGK lacZ-3HA-IRES-puro, BamHI + NheI</li> <li>- pSFFV_sfCherry3C(1-10), aaaGGATCCaccatggaggaggacaacatg + aaaGCTAGCtcagtcctcgttggtggt followed by BamHI + NheI</li> </ul>	This study
<b>pXP496</b>	pVirE - HiBit::VirE2	<p>HiBit peptide introduced at position P61 in <i>VirE2</i> under control of VirE promoter in pCB301. Kan<sup>R</sup></p> <ul style="list-style-type: none"> <li>- pXP457, ctaagagaaaagagcgtttattagaataatcg + TTCTTGAACAGGCGCCAGCCGAGACcgggcttcggtgcatg</li> <li>- pXP457, GGCTGGCGCCTGTTCAAGAAGATCTCGactcacacggatgatctcgg + taaacgctcttttcttagctacagactgtttacggttggg</li> </ul>	This study
<b>pXP499</b>	hPGK – LgBit in lentivector	<p>Second generation lentivector containing a constitutive hPGK promoter driving LgBit (split NanoLuc) expression. Amp<sup>R</sup>, Puro<sup>R</sup></p> <p>Ligation of the following:</p> <ul style="list-style-type: none"> <li>- pRRL-PGK lacZ-3HA-IRES-puro, BamHI + NheI</li> <li>- LgBit (synthesized), tctctccccAGGGGGATCCACCatgGTCTTCACACTCGAAGATTTTCG + CGGCCGCGTTTCGCTAGCttaGTTGATGGTTACTCGGAACAG, then BamHI + NheI</li> </ul>	Dixon et. al, 2016 <sup>146</sup> . This study.
<b>pXP504</b>	<i>virB4</i> knockout	<p>Suicide vector for the knockout of <i>virB4</i> in <i>A. tumefaciens</i>. pNPTS138, two-step allelic exchange protocol. Kan<sup>R</sup> Sucrose<sup>S</sup></p> <ul style="list-style-type: none"> <li>- pNPTS138, EcoRI + HindIII</li> <li>- <i>A. tumefaciens</i> gDNA, cggccgaagctagcgaattccgatgctttgaaagataaccgtg + ccttgatcatgctccgagcattacgc</li> </ul>	This study

		<ul style="list-style-type: none"> <li>- <i>A. tumefaciens</i> gDNA, gctcggagcatgatcaaaggtggggaactatg + agccggctggcgccaagcttcgaataagtcgccagctctc</li> </ul>	
<b>pXP505</b>	<i>virD4</i> knockout	<p>Suicide vector for the knockout of <i>virD4</i> in <i>A. tumefaciens</i>. pNPTS138, two-step allelic exchange protocol. Kan<sup>R</sup> Sucrose<sup>S</sup></p> <ul style="list-style-type: none"> <li>- pNPTS138, EcoRI + HindIII</li> <li>- <i>A. tumefaciens</i> gDNA, cggccgaagctagcgaattcgagaagatgccgatcgatagtg + ctgaagtcacatcacttcaccgagattcttcg</li> <li>- <i>A. tumefaciens</i> gDNA, tgaagtgatgtgacttcaagctgcctttcac + agccggctggcgccaagcttcgcatagtaaacgatgtaggag</li> </ul>	This study
<b>pXP513</b>	pAra – VHH display full-length EstA*	<p>VHHαGFP_HA tag displayed at the N-terminus of inactivated PAO1 EstA under control of an arabinose-inducible promoter in pJN105. Genta<sup>R</sup></p> <ul style="list-style-type: none"> <li>- EstA* pJN105, ATGATGTTCCCGACTATGCCCCCTTCGCCCTATTCGACG + ctgcacctgagccatAGCAGCCTGCGGGGCG</li> <li>- pDSG339, atggctcaggtgcagct + AGTCGGGAACATCATACGGGTAtgaggagacggtgacctg</li> </ul>	This study
<b>pXP514</b>	pAra – VHH(cys-free) display full-length EstA*	<p>VHHαGFP cysteine-free (C24A, C98V)_HA tag displayed at the N-terminus of inactivated PAO1 EstA under control of an arabinose-inducible promoter in pJN105. Genta<sup>R</sup></p> <ul style="list-style-type: none"> <li>- EstA* pJN105, ATGATGTTCCCGACTATGCCCCCTTCGCCCTATTCGACG + ctgcacctgagccatAGCAGCCTGCGGGGCG</li> <li>- pXP308, atggctcaggtgcagct + GGCATAGTCGGGAACATCATAC</li> </ul>	This study
<b>pXP515</b>	pAra – VHH display EstA scaffold	<p>VHHαGFP_HA tag displayed by replacing EstA passenger domain under control of an arabinose-inducible promoter in pJN105. Genta<sup>R</sup></p> <ul style="list-style-type: none"> <li>- EstA* pJN105, ATGATGTTCCCGACTATGCCCCGACCTACGGGATCAACG + ctgcacctgagccatAGCAGCCTGCGGGGCG</li> <li>- pDSG339, atggctcaggtgcagct + AGTCGGGAACATCATACGGGTAtgaggagacggtgacctg</li> </ul>	This study
<b>pXP516</b>	pAra – VHH(cys-free) EstA scaffold	<p>VHHαGFP cysteine-free (C24A, C98V)_HA tag displayed by replacing EstA passenger domain under control of an arabinose-inducible promoter in pJN105. Genta<sup>R</sup></p> <ul style="list-style-type: none"> <li>- EstA* pJN105, ATGATGTTCCCGACTATGCCCCGACCTACGGGATCAACG + ctgcacctgagccatAGCAGCCTGCGGGGCG</li> <li>- pXP308, atggctcaggtgcagct + GGCATAGTCGGGAACATCATAC</li> </ul>	This study
<b>pXP524</b>	pCMV – NanoLuc WT	<p>CMV-driven NanoLuc WT in pCDNA3.3. Amp<sup>R</sup></p> <ul style="list-style-type: none"> <li>- pCDNA3.3 eGFP, gctgccttctgcgggg + ggtggctcttatattcttcttactcttct</li> <li>- pLS169 (unpublished, encodes NanoLuc [Promega]), aatataagagccaccATGGTATTTACCCTGGAGGACT + gcagaaggcagctcaAGCTAAGATACGCTCACAAAGAC</li> </ul>	This study

<b>pXP525</b>	pCMV – NanoLuc start mutated	CMV-driven NanoLuc with a mutated start codon : <i>atg</i> mutated to <i>ag</i> in pCDNA3.3. Amp <sup>R</sup> <ul style="list-style-type: none"> <li>- pcDNA3.3 eGFP, gctgccttctgcgggg + ggtggctcttatatttcttacttct</li> <li>- pLS169 (unpublished, encodes NanoLuc [Promega]), aaatataagagccaccAGGTATTTACCCTGGAGGACTTTG + gcagaaggcagctcaAGCTAAGATACGCTCACAAAGAC</li> </ul>	This study
<b>pXP526</b>	gRNA1+Cas9	U6-driven gRNA1 gaagaaatataagagccacc and CpMV-driven Cas9 expression Amp <sup>R</sup> <ul style="list-style-type: none"> <li>- pX330-U6-Chimeric_BB-CBh-hSpCas9, Bpil</li> <li>- CACCGgaagaaatataagagccacc and AAACggtggctcttatatttcttcC annealed and ligated into the Bpil-digested backbone</li> </ul>	This study
<b>pXP527</b>	gRNA2+Cas9	U6-driven gRNA1 agtctccagggtaaatacc and pCMV-driven Cas9 expression. Amp <sup>R</sup> <ul style="list-style-type: none"> <li>- pX330-U6-Chimeric_BB-CBh-hSpCas9, Bpil</li> <li>- caccgAGTCCTCCAGGGTAAATACC and aaacGGTATTTACCCTGGAGGACTc annealed and ligated into the Bpil-digested backbone</li> </ul>	This study
<b>pXP531</b>	pET28a – 6xHis_mVenus	6xHis-tagged eGFP in pET28a for recombinant expression. Kan <sup>R</sup> <ul style="list-style-type: none"> <li>- pET28a, ATGGACGAGCTGTACAAGTGAGATCCGGCTGCT + CTCGCCCTTGCTCACCATGCTGCTGTGATGATGATG</li> <li>- mVenus, ATGGTGAGCAAGGGCGAG + TCACTTGTACAGCTCGTCC</li> </ul>	This study
<b>pXP533</b>	pCMV – NanoLuc mutated in the middle	CMV-driven NanoLuc with two bases removed after base number 212 ( <i>at</i> removed) in pCDNA3.3. Amp <sup>R</sup> <ul style="list-style-type: none"> <li>- pXP524, gctgccttctgcgggg + CTGGTCACCACTGAGGCC</li> <li>- pXP524, CTCAGTGGTGACCAGGGGGCAAATTGAGAAGA + gcagaaggcagctcaAGCTAAGATACGCTCACAAAGAC</li> </ul>	This study
<b>pXP534</b>	gRNA3+Cas9	U6-driven gRNA3 gggcctcagtggtgaccagg and CpMV-driven Cas9 expression Amp <sup>R</sup> <ul style="list-style-type: none"> <li>- pX330-U6-Chimeric_BB-CBh-hSpCas9, Bpil</li> <li>- caccGGGCCTCAGTGGTGACCAGG and aaacCCTGGTCACCACTGAGGCCC annealed and ligated into the Bpil-digested backbone</li> </ul>	This study
<b>pXP535</b>	gRNA4+Cas9	U6-driven gRNA4 aatcttctcaatttgccccc and pCMV-driven Cas9 expression. Amp <sup>R</sup> <ul style="list-style-type: none"> <li>- pX330-U6-Chimeric_BB-CBh-hSpCas9, Bpil</li> <li>- caccgAATCTTCTCAATTTGCCCCC and aaacGGGGCAAATTGAGAAGATTc annealed and ligated into the Bpil-digested backbone</li> </ul>	This study
<b>pXP540</b>	pVirE - VHH(cys-free) $\alpha$ -mCherry Spec <sup>R</sup>	VHH anti mCherry display (cysteine free) in pPZP200 Spec <sup>R</sup> <ul style="list-style-type: none"> <li>- pPZP200, AACCGCACCAGGACGG + ccagccagccaacagc</li> <li>- pXP255, AGCTGTTGGCTGGCTGGCAACGTATCCGCCGTCT + ctggccgctcgtggtgcggttctaccactgtatgttgagaccg</li> </ul>	This study
<b>pZA002</b>	pSynth - mScarlet	pGRG36 j23119_mScarlet Constitutive synthetic promoter driving the expression of mScarlet in Tn7 vector.	Pierrat et. al, 2021 <sup>162</sup>

### Abbreviations:

Amp = ampicillin

Chloramph = chloramphenicol

gDNA = genomic DNA

Genta = gentamycin

HA tag = YPYDVPDYA = Human influenza hemagglutinin position 98-106

Kan = kanamycin

Neo = neomycin

pCMV = cytomegalovirus promoter

Puro = puromycin

<sup>R</sup> = resistance marker

Rif = rifampicin

Spec = Spectinomycin

*Trp1* = phosphoribosylanthranilate isomerase, an enzyme that catalyzes the third step in tryptophan biosynthesis, for auxotrophic selection

**Supplementary table 3: strains used in this study**

Internal name	Strain name	Description	Reference
2	S17-1	<i>E. coli</i> donor vector for conjugation pro, res <sup>-</sup> hsdR17 (rK <sup>-</sup> mK <sup>+</sup> ) recA <sup>-</sup> with an integrated RP4-2-Tc::Mu-Km::Tn7, Tpr	Simon <i>et al.</i> , 1983 <sup>333</sup>
8	<i>E. coli</i> K12	WT <i>E. coli</i> from the keio collection BW25113	Baba <i>et al.</i> , 2006 <sup>334</sup>
336	<i>E. coli</i> mScarlet	<i>E. coli</i> constitutively expressing mScarlet, introduced using pZA002 in <i>E. coli</i> K12	Pierrat <i>et al.</i> , 2021 <sup>162</sup>
380	GV3101	<i>Agrobacterium tumefaciens</i> C58C1 + pMP90, Rif <sup>R</sup> , Genta <sup>R</sup> , Chloramph <sup>R</sup> The virulence plasmid pC58 was removed from the C58 background and replaced by a disarmed version, pMP90 (Genta <sup>R</sup> ) that does not contain a T-DNA sequence. This strain is the starting point for all derivatives.	Koncz <i>et al.</i> , 1986 <sup>102</sup>
429	<i>E. coli</i> KB18	<i>E. coli</i> K12 AAEC191A <i>fim</i> <sup>-</sup> partially complemented with pPKL114, a plasmid containing <i>Fim</i> operon except <i>FimH</i> (stop codon). This strain can be retransformed with plasmids coding for different FimH variants.	Sokurenko <i>et al.</i> 1995 <sup>326</sup> Gift from Jens Möller
464	<i>A. tumefaciens</i> VirE2-	Markerless <i>VirE2</i> knockout generated with pXP233_pNPTS138 in GV3101	This study
466	<i>A. tumefaciens</i> VHH display (cys-free)::VirE2-	VHH-αGFP cysteine-free display was knocked in instead of <i>VirE2</i> using pXP234_pNPTS138 in GV3101	This study
468	<i>A. tumefaciens</i> mScarlet	Constitutive synthetic promoter driving <i>mScarlet</i> expression introduced in the <i>tetR</i> locus using pXP250 in GV3101	This study
492	<i>S. cerevisiae</i> eby100	<i>Saccharomyces cerevisiae</i> for yeast display. It produces Aga1 under control of the gal1 promoter and it is trp auxotroph. Parent strain: BJ5465. Full genomic characteristics: MATa AGA1::GAL1-AGA1::URA3 ura3-52 trp1 leu2-delta200 his3-delta200 pep4::HIS3 prbd1.6R can1 GAL	ATCC mya-4941, gift from Bruno Correia.

<b>502</b>	<i>A. tumefaciens</i> mScarlet atu5364-	Markerless knockout of <i>atu5364</i> in strain 468 using pXP273	This study
<b>535</b>	<i>A. tumefaciens</i> VHH:: <i>VirF</i> - cysteine-free display	VHH- $\alpha$ GFP cysteine-free display was knocked in instead of <i>VirF</i> using pXP302 in strain GV3101	This study
<b>544</b>	<i>A. tumefaciens</i> mScarlet atu0800-	Markerless knockout of <i>atu0800</i> , a DsbA analog, generated with pXP316 in strain 468	This study
<b>1154</b>	<i>Agrobacterium tumefaciens</i> <i>virE</i> -	Markerless knockout of the <i>virE</i> operon, using pXP466	This study
<b>1190</b>	<i>A. tumefaciens virE</i> - <i>pVirE</i> VHH(cys-free):: <i>tetR</i>	Introduction of VHH(cysteine free) display under control of pVir in the <i>tetR</i> locus in strain 1154 using pXP462	This study
<b>1237</b>	<i>A. tumefaciens</i> VHH:: <i>VirE2</i> - cysteine-free display and <i>VirB4</i> -	Markerless knockout of <i>VirB4</i> , the motor ATPase of the T4SS generated with pXP504 in <i>A. tumefaciens</i> VHH:: <i>VirE2</i> - cysteine-free display	This study
<b>1239</b>	<i>A. tumefaciens</i> VHH:: <i>VirE2</i> - cysteine-free display and <i>VirD4</i> -	Markerless knockout of <i>VirD4</i> , the T-DNA coupling ATPase of the T4SS generated with pXP505 in <i>A. tumefaciens</i> VHH:: <i>VirE2</i> - cysteine-free display	This study
<b>AP196</b>	<i>S. cerevisiae</i> eby100 eGFP display	<i>S. cerevisiae</i> eby100 containing pXP267 for Aga2p-eGFP display. Selection with the <i>trp1</i> auxotrophic marker.	This study
<b>HeLa tetON GFP disp v4.2 clone 1</b>	HeLa inducible GFP display	Monoclonal cell line of HeLa transduced with lentivectors packaging pXP340, a mammalian lentivector containing a tetracycline-inducible GFP(N105Y, E125V,Y146F) - display anchored with a truncated CD80 transmembrane	Pierrat et. al, 2021 <sup>162</sup>
<b>HeLa tetON GFP + lenti pXP499 pool puro selected</b>	HeLa GFP inducible display + LgBit	Polyclonal cell line of HeLa inducible GFP transduced with lentivectors packaging pXP499 - constitutive hPGK promoter driving LgBit (split NanoLuc) expression	This study
<b>HEK293T GFPdisp</b>	HEK GFP constitutive	Monoclonal cell line of HEK293T cells containing pXP145 - pCMV-driven GFP(N105Y, E125V,Y146F) -display anchored with a truncated CD80 transmembrane	This study
<b>WT Chlamydomonas reinhardtii</b>	<i>C. reinhardtii</i> WT	Chlamydomonas reinhardtii CC-1690 wild type mt+ [Sager 21 gr]	Simon Sieber, Uni Zürich
<b>mVenus_GP1 Chlamydomonas reinhardtii</b>	<i>C. reinhardtii</i> mVenus display	Chlamydomonas reinhardtii CC-1690 stably engineered with mVenus-GP1, which anchors mVenus in the cell wall.	Molino et al. 2021 <sup>272</sup>

# Supplementary table 4: Raw data of the mathematical models for characteristic residence times.

Non-flagellated bacteria binding to HeLa GFP (GFP display induced with doxycycline 300ng/uL, no other treatment) with 0.05 Pa flow unless precised otherwise.

\* The data show raw bacterial/cell count and is not normalized to the incoming flux of bacteria at different flow.

Condition:	no VHH			low VHH			high VHH			high VHH 0.15 Pascal*			high VHH 0.5 Pascal*		
Parameter:	1	2	3	1	2	3	1	2	3	1	2	3	1	2	3
biological replicate number	1	2	3	1	2	3	1	2	3	1	2	3	1	2	3
bacteria/cell	0.12	0.22	0.31	0.48	1.12	0.93	3.14	2.56	4.71	2.86	0.83	0.72	5.73	4.77	7.35
contact efficiency (%)	7.69	6.35	6.41	5.22	7.90	5.28	5.66	5.21	10.56	23.58	15.21	16.61	43.33	25.31	23.50
contact/HeLa/min	na	na	na	na	na	na	0.90	0.83	0.86	0.07	0.17	0.15	0.13	0.11	0.23
Tau transient	42.81	115.23	64.21	45.27	79.51	168.49	83.58	111.29	150.93	76.13	104.12	250.16	410.72	368.01	403.52
C(transient) (pre-exponential factor)	0.60	0.55	0.71	0.42	0.46	0.59	0.29	0.50	0.26	0.14	0.18	0.25	0.18	0.26	0.26
Tau residence	349.89	787.35	614.69	1660.81	3418.10	2599.66	5035.13	7404.10	4829.25	8121.70	8552.34	17142.11	811265.52	823606.66	751465.61
C(res) (pre-exponential factor)	0.54	0.33	0.30	0.63	0.55	0.43	0.72	0.52	0.68	0.89	0.79	0.69	0.82	0.77	0.73
r <sup>2</sup>	0.99	0.99	0.99	0.99	0.99	0.99	0.99	0.97	0.99	0.98	0.95	0.99	0.99	0.97	0.96
average number of tracks used from technical replicates for fitting technical replicates	25.33	27.33	27.00	42.33	32.00	18.00	51.33	24.67	59.33	51.67	24.00	25.33	154.67	98.67	191.33
	3	3	3	3	3	3	3	3	3	3	3	3	3	3	3
Mean and standard deviation:	Mean		SD	Mean		SD	Mean		SD	Mean		SD	Mean		SD
bacteria/cell	0.22		0.09	0.84		0.33	3.47		1.11	1.47		1.20	5.95		1.30
contact efficiency (%)	6.82		0.76	6.13		1.53	7.14		2.97	18.47		4.48	30.71		10.96
contact/HeLa/min	na		na	na		na	0.86		0.04	0.13		0.05	0.16		0.06
Tau transient	74.08		37.21	97.76		63.61	115.27		33.85	143.47		93.45	394.09		22.86
C(transient) (pre-exponential factor)	0.62		0.08	0.49		0.09	0.35		0.13	0.19		0.06	0.23		0.05
Tau residence	583.98		220.34	2559.52		879.33	5756.16		1430.87	11272.05		5088.18	795445.93		38584.68
C(res) (pre-exponential factor)	0.39		0.13	0.54		0.10	0.64		0.11	0.79		0.10	0.77		0.05

Condition:	high Lag02			high Lag94-10					high VHH + flagella			no VHH on coverslip		
Parameter:	1	2	3	1(excluded)	2	3	4	5	1	2	3	1	2	3
biological replicate number	1	2	3	1(excluded)	2	3	4	5	1	2	3	1	2	3
bacteria/cell	1.09	0.34	0.35	5.86	6.10	2.49	7.21	7.35	1.74	0.88	2.40	0.07	0.23	0.02
contact efficiency (%)	5.46	7.72	10.16	4.52	11.44	7.51			12.77	12.20	15.03	4.48	1.18	18.00
contact/HeLa/min	na	na	na	na	na	na	na	na	na	na	na	na	na	na
Tau transient	84.24	98.31	129.71	142.47	75.33	113.09	109.94	115.27	97.83	99.37	102.81	54.93	81.02	49.87
C(transient) (pre-exponential factor)	0.42	0.77	0.50	0.48	0.22	0.21	0.42	0.26	0.70	0.64	0.66	0.43	0.69	0.74
Tau residence	5691.90	3752.25	10379.55	775491.25	15019.45	10447.47	7458.48	12225.10	2222.34	2226.74	2728.50	704.32	2816.59	705.52
C(res) (pre-exponential factor)	0.46	0.29	0.45	0.57	0.76	0.82	0.56	0.73	0.27	0.31	0.24	0.68	0.35	0.45
r <sup>2</sup>	0.99	0.99	0.97	0.99	0.98	0.99	0.98	0.97	1.00	0.99	0.99	0.98	0.99	0.96
average number of tracks used from technical replicates for fitting technical replicates	19.00	11.67	14.33	61.00	69.67	28.67	27.33	41.67	90.33	93.67	164.00	19.67	49.33	6.67
	3	3	3	3	3	3	3	3	3	3	3	3	3	3
Mean and standard deviation:	Mean		SD						Mean		SD	Mean		SD
bacteria/cell	0.59		0.43	5.79		2.27			1.67		0.76	0.11		0.11
contact efficiency (%)	7.78		2.35	9.48		2.78			13.33		1.50	7.89		8.91
contact/HeLa/min	na		na	na		na			na		na	na		na
Tau transient	104.09		23.28	103.41		18.85			100.00		2.55	61.94		16.72
C(transient) (pre-exponential factor)	0.56		0.18	0.28		0.10			0.67		0.03	0.62		0.16
Tau residence	6607.90		3407.28	11287.63		3171.41			2392.53		290.97	1408.81		1219.17
C(res) (pre-exponential factor)	0.40		0.10	0.72		0.11			0.27		0.03	0.49		0.17

(continued)

Condition:	high VHH on coverslip			no VHH deglycosylated HeLa			high VHH deglycosylated HeLa			no VHH + cytoD			low VHH + cytoD		
Parameter:	1	2	3	1	2	3	1	2	3	1	2	3	1	2	3 (excluded)
biological replicate number	1	2	3	1	2	3	1	2	3	1	2	3	1	2	3
bacteria/cell	34.23	33.91	33.04	1.78	1.21	1.69	38.39	24.14	16.87	0.06	0.02	0.06	0.06	0.11	0.14
contact efficiency (%)	58.35	44.08	51.59	5.32	6.22	8.66	12.70	15.19	17.17	7.01	8.44	5.90	6.41	5.30	6.49
contact/HeLa/min	na	na	na	na	na	na	na	na	na	na	na	na	na	na	na
Tau transient	52.90	187.27	55.46	66.54	92.09	87.58	245.92	172.69	165.94	87.51	22.81	122.35	66.46	84.05	289.54
C(transient) (pre-exponential factor)	0.01	0.12	0.02	0.87	0.74	0.51	0.26	0.34	0.31	0.87	0.34	0.27	0.44	0.41	0.79
Tau residence	40212.18	34273.82	68787.27	1594.37	1588.92	1850.64	12955.29	7479.94	7263.22	859.99	509.55	2036.69	1513.69	2572.95	463341.00
C(res) (pre-exponential factor)	0.99	0.88	0.99	0.24	0.26	0.51	0.74	0.66	0.70	0.19	0.76	0.10	0.59	0.36	0.17
r <sup>2</sup>	0.98	0.99	0.98	0.99	0.97	0.98	1.00	1.00	1.00	0.97	0.97	0.96	0.96	0.94	0.94
average number of tracks used from technical replicates for fitting	668.67	192.33	1399.67	30.00	24.33	29.67	125.67	137.67	163.00	4.67	4.00	7.00	6.67	6.33	6.00
technical replicates	3	3	3	3	3	3	3	3	3	3	3	3	3	3	3
Mean and standard deviation:	Mean		SD	Mean		SD	Mean		SD	Mean		SD	Mean		SD
bacteria/cell	33.73		0.61	1.56		0.31	26.46		10.95	0.05		0.02	0.11		0.04
contact efficiency (%)	51.34		7.14	6.73		1.73	15.02		2.24	7.12		1.27	6.07		0.67
contact/HeLa/min	na		na	na		na	na		na	na		na	na		na
Tau transient	98.54		76.85	82.07		13.64	194.85		44.36	77.55		50.51	146.68		124.03
C(transient) (pre-exponential factor)	0.05		0.06	0.71		0.18	0.30		0.04	0.50		0.33	0.55		0.21
Tau residence	47757.76		18452.54	1677.97		149.56	9232.82		3225.58	1135.41		799.96	155809.22		266330.87
C(res) (pre-exponential factor)	0.95		0.06	0.33		0.15	0.70		0.04	0.35		0.36	0.37		0.21

Condition:	high VHH + cytoD			high VHH + intimin full length linker			high VHH noGFP			high VHH prevention with soluble GFP		
Parameter:	1	2	3	1	2	3	1	2	3	1	2	3
biological replicate number	1	2	3	1	2	3	1	2	3	1	2	3
bacteria/cell	0.26	0.30	0.68	0.78	0.37	0.31	0.48	0.31	0.44	0.40	0.41	0.80
contact efficiency (%)	9.94	4.82	8.42	8.83	9.31	6.32	3.57	6.20	4.39	na	na	na
contact/HeLa/min	na	na	na	na	na	na	na	na	na	na	na	na
Tau transient	180.30	53.86	52.19	171.78	192.98	92.58	81.67	75.44	40.46	90.87	81.43	112.61
C(transient) (pre-exponential factor)	0.49	0.48	0.13	0.45	0.42	0.48	0.66	0.95	0.61	0.64	0.52	0.50
Tau residence	3920.20	2681.01	1864.03	3146.97	5101.07	5381.80	1165.53	2149.20	1527.26	1145.01	1168.40	1175.51
C(res) (pre-exponential factor)	0.44	0.44	0.79	0.53	0.53	0.56	0.26	0.20	0.48	0.36	0.47	0.50
r <sup>2</sup>	0.99	0.96	0.96	0.97	0.97	0.97	0.97	0.99	0.96	0.99	0.99	0.99
average number of tracks used from technical replicates for fitting	24.00	10.33	11.67	19.00	14.50	11.83	15.67	13.67	15.67	22.67	31.33	33.67
technical replicates	3	3	3	6	6	6	3	3	3	3	3	3
Mean and standard deviation:	Mean		SD	Mean		SD	Mean		SD	Mean		SD
bacteria/cell	0.41		0.23	0.49		0.26	0.41		0.09	0.54		0.23
contact efficiency (%)	7.73		2.63	8.15		1.60	4.72		1.35	0.00		0.00
contact/HeLa/min	na		na	na		na	na		na	na		na
Tau transient	95.45		73.49	152.45		52.92	65.86		22.21	94.97		15.99
C(transient) (pre-exponential factor)	0.36		0.20	0.45		0.03	0.74		0.19	0.55		0.08
Tau residence	2821.75		1035.29	4543.28		1217.36	1614.00		497.54	1162.97		15.96
C(res) (pre-exponential factor)	0.56		0.20	0.54		0.02	0.31		0.15	0.44		0.07

## REFERENCES

1. Van Epps JS, Younger JG. Implantable device-related infection. *Shock*. 2016;46(6):597-608. doi:10.1097/SHK.0000000000000692
2. Singhai M, Malik A, Shahid M, Malik MA, Goyal R. A Study on Device-Related Infections with Special Reference to Biofilm Production and Antibiotic Resistance. *J Glob Infect Dis*. 2012;4(4):193. doi:10.4103/0974-777X.103896
3. Spengler C, Maikranz E, Santen L, Jacobs K. Modeling Bacterial Adhesion to Unconditioned Abiotic Surfaces. *Front Mech Eng*. 2021;7(May):1-7. doi:10.3389/fmech.2021.661370
4. Straub H, Bigger CM, Valentin J, et al. Bacterial Adhesion on Soft Materials: Passive Physicochemical Interactions or Active Bacterial Mechanosensing? *Adv Healthc Mater*. 2019;8(8). doi:10.1002/adhm.201801323
5. Kuo JCH, Paszek MJ. Glycocalyx Curving the Membrane: Forces Emerging from the Cell Exterior. *Annu Rev Cell Dev Biol*. 2021;37:257-283. doi:10.1146/annurev-cellbio-120219-054401
6. Arabyan N, Park D, Foutouhi S, et al. Salmonella Degrades the Host Glycocalyx Leading to Altered Infection and Glycan Remodeling. *Sci Rep*. 2016;6:1-11. doi:10.1038/srep29525
7. Kosmalska AJ, Casares L, Elosegui-Artola A, et al. Physical principles of membrane remodelling during cell mechanoadaptation. *Nat Commun*. 2015;6. doi:10.1038/ncomms8292
8. Prystopiuk V, Feuillie C, Herman-Bausier P, et al. Mechanical Forces Guiding Staphylococcus aureus Cellular Invasion. *ACS Nano*. 2018;12(4):3609-3622. doi:10.1021/acsnano.8b00716
9. Persat A, Nadell CD, Kim MK, et al. The mechanical world of bacteria. *Cell*. 2015;161(5):988-997. doi:10.1016/j.cell.2015.05.005
10. Li G, Brown PJB, Tang JX, et al. Surface contact stimulates the just-in-time deployment of bacterial adhesins. *Mol Microbiol*. 2012;83(1):41-51. doi:10.1111/J.1365-2958.2011.07909.X
11. Rossy T, Nadell CD, Persat A. Cellular advective-diffusion drives the emergence of bacterial surface colonization patterns and heterogeneity. *Nat Commun*. 2019;1-9. doi:10.1038/s41467-019-10469-6
12. Ruhel R, Kataria R. Biofilm patterns in gram-positive and gram-negative bacteria. *Microbiol Res*. 2021;251(March):126829. doi:10.1016/j.micres.2021.126829
13. Cruz-Chu ER, Malafeev A, Pajarskas T, Pivkin I V., Koumoutsakos P. Structure and response to flow of the glycocalyx layer. *Biophys J*. 2014;106(1):232-243. doi:10.1016/j.bpj.2013.09.060
14. Lauga E. Bacterial Hydrodynamics. *Annu Rev Fluid Mech*. 2016;48:105-130. doi:10.1146/ANNUREV-FLUID-122414-034606
15. Haiko J, Westerlund-Wikström B. The role of the bacterial flagellum in adhesion and virulence. *Biology (Basel)*. 2013;2(4):1242-1267. doi:10.3390/biology2041242
16. Scharfman A, Arora SK, Delmotte P, et al. Recognition of lewis x derivatives present on

- mucins by flagellar components of *Pseudomonas aeruginosa*. *Infect Immun*. 2001;69(9):5243-5248. doi:10.1128/IAI.69.9.5243-5248.2001
17. Lukaszczyk M, Pradhan B, Remaut H. *The Biosynthesis and Structures of Bacterial Pili*. Vol 92. Springer International Publishing; 2019. doi:10.1007/978-3-030-18768-2\_12
  18. Sauer MM, Jakob RP, Luber T, et al. Binding of the Bacterial Adhesin FimH to Its Natural, Multivalent High-Mannose Type Glycan Targets. *J Am Chem Soc*. 2019;141(2):936-944. doi:10.1021/jacs.8b10736
  19. Nilsson LM, Thomas WE, Trintchina E, Vogel V, Sokurenko E V. Catch bond-mediated adhesion without a shear threshold: Trimannose versus monomannose interactions with the FimH adhesin of *Escherichia coli*. *J Biol Chem*. 2006;281(24):16656-16663. doi:10.1074/jbc.M511496200
  20. Sauer MM, Jakob RP, Eras J, et al. Catch-bond mechanism of the bacterial adhesin FimH. *Nat Commun*. 2016;7(10738):1-13. doi:10.1038/ncomms10738
  21. Ellison CK, Kan J, Dillard RS, et al. Obstruction of pilus retraction stimulates bacterial surface sensing. *Science*. 2017;358(6362):535-538. doi:10.1126/science.aan5706
  22. Domenech A, Brochado AR, Sender V, et al. Proton Motive Force Disruptors Block Bacterial Competence and Horizontal Gene Transfer. *Cell Host Microbe*. 2020;27(4):544-555.e3. doi:10.1016/j.chom.2020.02.002
  23. Veening JW, Blokesch M. Interbacterial predation as a strategy for DNA acquisition in naturally competent bacteria. *Nat Rev Microbiol*. 2017;15(10):621-629. doi:10.1038/nrmicro.2017.66
  24. Charles-Orszag A, Tsai FC, Bonazzi D, et al. Adhesion to nanofibers drives cell membrane remodeling through one-dimensional wetting. *Nat Commun*. 2018;9(1). doi:10.1038/s41467-018-06948-x
  25. Meuskens I, Saragliadis A, Leo JC, Linke D. Type V secretion systems: An overview of passenger domain functions. *Front Microbiol*. 2019;10(MAY):1-19. doi:10.3389/fmicb.2019.01163
  26. Grijpstra J, Arenas J, Rutten L, Tommassen J. Autotransporter secretion: Varying on a theme. *Res Microbiol*. 2013;164(6):562-582. doi:10.1016/j.resmic.2013.03.010
  27. Sjölander M, Altenbacher G, Hagner M, Sun W, Schedin-Weiss S, Sjölander H. Meningococcal outer membrane protein nhha triggers apoptosis in macrophages. *PLoS One*. 2012;7(1). doi:10.1371/journal.pone.0029586
  28. Coppens F, Castaldo G, Debraekeleer A, et al. Hop-family *Helicobacter* outer membrane adhesins form a novel class of Type 5-like secretion proteins with an interrupted  $\beta$ -barrel domain. *Mol Microbiol*. 2018;110(1):33-46. doi:10.1111/MMI.14075
  29. Leo JC, Grin I, Linke D. Type V secretion: Mechanism(S) of autotransport through the bacterial outer membrane. *Philos Trans R Soc B Biol Sci*. 2012;367(1592):1088-1101. doi:10.1098/rstb.2011.0208
  30. Oberhettinger P, Leo JC, Linke D, Autenrieth IB, Schütz MS. The inverse autotransporter intimin exports its passenger domain via a hairpin intermediate. *J Biol Chem*. 2015;290(3):1837-1849. doi:10.1074/jbc.M114.604769
  31. Chauhan N, Hatlem D, Orwick-Rydmark M, et al. Insights into the autotransport process of a trimeric autotransporter, *Yersinia* Adhesin A (YadA). *Mol Microbiol*. 2019;111(3):844-862. doi:10.1111/MMI.14195
  32. Manta B, Boyd D, Berkmen M. Disulfide Bond Formation in the Periplasm of *Escherichia*

coli. *EcoSal Plus*. 2019;8(2). doi:10.1128/ECOSALPLUS.ESP-0012-2018

33. Leyton DL, Sevastsyonovich YR, Browning DF, et al. Size and conformation limits to secretion of disulfide-bonded loops in autotransporter proteins. *J Biol Chem*. 2011;286(49):42283-42291. doi:10.1074/jbc.M111.306118
34. Jose J, Krämer J, Klauser T, Pohlner J, Meyer TF. Absence of periplasmic DsbA oxidoreductase facilitates export of cysteine-containing passenger proteins to the Escherichia coli cell surface via the Iga( $\beta$ ) autotransporter pathway. *Gene*. 1996;178(1-2):107-110. doi:10.1016/0378-1119(96)00343-5
35. Nicolay T, Vanderleyden J, Spaepen S. Autotransporter-based cell surface display in Gram-negative bacteria. *Crit Rev Microbiol*. 2015;41(1):109-123. doi:10.3109/1040841X.2013.804032
36. van den Berg B. Crystal Structure of a Full-Length Autotransporter. *J Mol Biol*. 2010;396(3):627-633. doi:10.1016/j.jmb.2009.12.061
37. Wilhelm S, Gdynia A, Tielen P, Rosenau F, Jaeger KE. The autotransporter esterase EstA of Pseudomonas aeruginosa is required for rhamnolipid production, cell motility, and biofilm formation. *J Bacteriol*. 2007;189(18):6695-6703. doi:10.1128/JB.00023-07
38. Fairman JW, Dautin N, Wojtowicz D, et al. Crystal structures of the outer membrane domain of intimin and invasin from enterohemorrhagic E. coli and enteropathogenic Y. pseudotuberculosis. *Structure*. 2012;20(7):1233-1243. doi:10.1016/j.str.2012.04.011
39. Weikum J, Kulakova A, Tesei G, et al. The Extracellular Juncture Domains in the Intimin Passenger Adopt a Constitutively Extended Conformation Inducing Restraints to Its Sphere of Action. *SSRN Electron J*. 2020:1-18. doi:10.2139/ssrn.3635798
40. Luo Y, Frey EA, Pfuetzner RA, et al. Crystal structure of enteropathogenic Escherichia coli intimin-receptor complex. *Nature*. 2000;405(6790):1073-1077. doi:10.1038/35016618
41. Finlay BB, Cossart P. Exploitation of mammalian host cell functions by bacterial pathogens. *Science*. 1997;276(5313):718-725. doi:10.1126/science.276.5313.718
42. Leo JC, Oberhettinger P, Schütz M, Linke D. The inverse autotransporter family: Intimin, invasin and related proteins. *Int J Med Microbiol*. 2015;305(2):276-282. doi:10.1016/j.ijmm.2014.12.011
43. Kenny B, DeVinney R, Stein M, Reinscheid DJ, Frey EA, Finlay BB. Enteropathogenic E. coli (EPEC) transfers its receptor for intimate adherence into mammalian cells. *Cell*. 1997;91(4):511-520. doi:10.1016/S0092-8674(00)80437-7
44. Isberg RR, Leong JM. Multiple  $\beta$ 1 chain integrins are receptors for invasin, a protein that promotes bacterial penetration into mammalian cells. *Cell*. 1990;60(5):861-871. doi:10.1016/0092-8674(90)90099-Z
45. Schulte R, Kerneis S, Klinke S, et al. Translocation of Yersinia enterocolitica across reconstituted intestinal epithelial monolayers is triggered by Yersinia invasin binding to  $\beta$ 1 integrins apically expressed on M-like cells. *Cell Microbiol*. 2000;2(2):173-185. doi:10.1046/j.1462-5822.2000.00047.x
46. Nägele V, Heesemann J, Schielke S, Jiménez-Soto LF, Kurzai O, Ackermann N. Neisseria meningitidis adhesin NadA targets  $\beta$ 1 integrins: Functional similarity to Yersinia invasin. *J Biol Chem*. 2011;286(23):20536-20546. doi:10.1074/jbc.M110.188326
47. Salema V, Marín E, Martínez-Arteaga R, et al. Selection of Single Domain Antibodies

- from Immune Libraries Displayed on the Surface of *E. coli* Cells with Two  $\beta$ -Domains of Opposite Topologies. *PLoS One*. 2013;8(9):1-18. doi:10.1371/journal.pone.0075126
48. Diggle SP, Stacey RE, Dodd C, Cámara M, Williams P, Winzer K. The galactophilic lectin, LecA, contributes to biofilm development in *Pseudomonas aeruginosa*. *Environ Microbiol*. 2006;8(6):1095-1104. doi:10.1111/j.1462-2920.2006.001001.x
  49. Tielker D, Hacker S, Loris R, et al. *Pseudomonas aeruginosa* lectin LecB is located in the outer membrane and is involved in biofilm formation. *Microbiology*. 2005;151(5):1313-1323. doi:10.1099/mic.0.27701-0
  50. Chemani C, Imberty A, De Bentzmann S, et al. Role of LecA and LecB lectins in *Pseudomonas aeruginosa*-induced lung injury and effect of carbohydrate ligands. *Infect Immun*. 2009;77(5):2065-2075. doi:10.1128/IAI.01204-08
  51. Novoa A, Eierhoff T, Topin J, et al. A LecA Ligand Identified from a Galactoside-Conjugate Array Inhibits Host Cell Invasion by *Pseudomonas aeruginosa*. *Angew Chemie*. 2014;126(34):9031-9035. doi:10.1002/ANGE.201402831
  52. Sommer R, Wagner S, Varrot A, et al. The virulence factor LecB varies in clinical isolates: consequences for ligand binding and drug discovery. *Chem Sci*. 2016;7(8):4990-5001. doi:10.1039/C6SC00696E
  53. Yi Y, Ma Y, Gao F, et al. Crystal structure of EHEC intimin: Insights into the complementarity between EPEC and EHEC. *PLoS One*. 2010;5(12):1-8. doi:10.1371/journal.pone.0015285
  54. Tram G, Poole J, Adams FG, Jennings MP, Eijkelkamp BA, Attack JM. The *Acinetobacter baumannii* Autotransporter Adhesin Ata Recognizes Host Glycans as High-Affinity Receptors. *ACS Infect Dis*. 2021;7(8):2352-2361. doi:10.1021/acsinfecdis.1c00021
  55. Kumar H, Kawai T, Akira S. Pathogen recognition by the innate immune system. *Int Rev Immunol*. 2011;30(1):16-34. doi:10.3109/08830185.2010.529976
  56. Pruitt RN, Gust AA, Nürnberger T. Plant immunity unified. *Nat Plants*. 2021;7(4):382-383. doi:10.1038/s41477-021-00903-3
  57. Boudarel H, Mathias JD, Blaysat B, Grédiac M. Towards standardized mechanical characterization of microbial biofilms: analysis and critical review. *npj Biofilms Microbiomes*. 2018;4(1). doi:10.1038/s41522-018-0062-5
  58. Greathouse KL, Stone JK, Harris CC. Cancer-Type-Specific Bacteria: Free-loaders or Partners? *Cancer Cell*. 2020;38(2):158-160. doi:10.1016/j.ccell.2020.06.017
  59. Felgner S, Kocijancic D, Frahm M, Weiss S. Bacteria in cancer therapy: Renaissance of an old concept. *Int J Microbiol*. 2016;2016. doi:10.1155/2016/8451728
  60. Forbes NS. Engineering the perfect (bacterial) cancer therapy. *Nat Rev Cancer*. 2010;10(11):785-794. doi:10.1038/nrc2934
  61. June CH, O'Connor RS, Kawalekar OU, Ghassemi S, Milone MC. CAR-T cell immunotherapy for human cancer. *Science*. 2018;359(6382):1361-1365. doi:10.1126/science.aar6711
  62. Chien T, Doshi A, Danino T. Advances in bacterial cancer therapies using synthetic biology. *Curr Opin Syst Biol*. 2017;5:1-8. doi:10.1016/j.coisb.2017.05.009
  63. Low KB, Ittensohn M, Le T, et al. Lipid A mutant *Salmonella* with suppressed virulence and TNF $\alpha$  induction retain tumor-targeting in vivo. *Nat Biotechnol*. 1999;17(1):37-41. doi:10.1038/5205

64. Stirling F, Bitzan L, O'Keefe S, et al. Rational Design of Evolutionarily Stable Microbial Kill Switches. *Mol Cell*. 2017;68(4):686-697.e3. doi:10.1016/j.molcel.2017.10.033
65. Koh M, Yao A, Gleason PR, Mills JH, Schultz PG. A General Strategy for Engineering Noncanonical Amino Acid Dependent Bacterial Growth. *J Am Chem Soc*. 2019;141(41):16213-16216. doi:10.1021/jacs.9b08491
66. Wagner S, Galan JE. *Bacterial Type III Protein Secretion Systems*. Vol 427.; 2020.
67. Ittig SJ, Schmutz C, Kasper CA, et al. A bacterial type III secretion-based protein delivery tool for broad applications in cell biology. *J Cell Biol*. 2015;211(4):913-931. doi:10.1083/jcb.201502074
68. González-Prieto C, Lesser CF. Rationale redesign of type III secretion systems: toward the development of non-pathogenic E. coli for in vivo delivery of therapeutic payloads. *Curr Opin Microbiol*. 2018;41:1-7. doi:10.1016/j.mib.2017.10.011
69. Alvarez-Martinez CE, Christie PJ. Biological Diversity of Prokaryotic Type IV Secretion Systems. *Microbiol Mol Biol Rev*. 2009;73(4):775-808. doi:10.1128/MMBR.00023-09
70. Guzmán-Herrador DL, Steiner S, Alperi A, González-Prieto C, Roy CR, Llosa M. DNA delivery and genomic integration into mammalian target cells through Type IV A and B secretion systems of human pathogens. *Front Microbiol*. 2017;8(AUG):1503. doi:10.3389/fmicb.2017.01503
71. Dominguez AA, Lim WA, Qi LS. Beyond editing: Repurposing CRISPR-Cas9 for precision genome regulation and interrogation. *Nat Rev Mol Cell Biol*. 2016;17(1):5-15. doi:10.1038/nrm.2015.2
72. Kuzmin DA, Shutova M V., Johnston NR, et al. The clinical landscape for AAV gene therapies. *Nat Rev Drug Discov*. 2021;20(3):173-174. doi:10.1038/d41573-021-00017-7
73. Ma CC, Wang ZL, Xu T, He ZY, Wei YQ. The approved gene therapy drugs worldwide: from 1998 to 2019. *Biotechnol Adv*. 2020;40(December 2019):107502. doi:10.1016/j.biotechadv.2019.107502
74. Ou X, Ma Q, Yin W, Ma X, He Z. CRISPR/Cas9 Gene-Editing in Cancer Immunotherapy: Promoting the Present Revolution in Cancer Therapy and Exploring More. *Front Cell Dev Biol*. 2021;9:1179. doi:10.3389/FCCELL.2021.674467
75. Hope Henderson. CRISPR Clinical Trials: A 2021 update. *Innovative Genomics Institute*. <https://innovativegenomics.org/news/crispr-clinical-trials-2021/>. Published March 3, 2021. Accessed December 2, 2021.
76. Bulcha JT, Wang Y, Ma H, Tai PWL, Gao G. Viral vector platforms within the gene therapy landscape. *Signal Transduct Target Ther*. 2021;6(1). doi:10.1038/s41392-021-00487-6
77. Jinek M, Chylinski K, Fonfara I, Hauer M, Doudna JA, Charpentier E. A Programmable Dual-RNA-Guided DNA Endonuclease in Adaptive Bacterial Immunity. 2012;337(August):816-822.
78. Gillmore JD, Gane E, Taubel J, et al. CRISPR-Cas9 In Vivo Gene Editing for Transthyretin Amyloidosis. *N Engl J Med*. 2021;385(6):493-502. doi:10.1056/NEJMOA2107454
79. Mancuso P, Chen C, Kaminski R, et al. CRISPR based editing of SIV proviral DNA in ART treated non-human primates. *Nat Commun* 2020 111. 2020;11(1):1-11. doi:10.1038/s41467-020-19821-7

80. Biasco L, Baricordi C, Aiuti A. Retroviral Integrations in Gene Therapy Trials. *Mol Ther*. 2012;20(4):709-716. doi:10.1038/MT.2011.289
81. Marshall E. Gene Therapy Death Prompts Review of Adenovirus Vector. *Science*. 1999;286(5448):2244-2245. doi:10.1126/SCIENCE.286.5448.2244
82. Weitzman MD, Linden RM. Adeno-Associated Virus Biology. *Methods Mol Biol*. 2011;Adeno-Asso(Chapter 1). doi:10.1007/978-1-61779-370-7
83. Davidsson M, Wang G, Aldrin-Kirk P, et al. A systematic capsid evolution approach performed in vivo for the design of AAV vectors with tailored properties and tropism. *Proc Natl Acad Sci U S A*. 2019;116(52):27053-27062. doi:10.1073/pnas.1910061116
84. Schmit PF, Pacouret S, Zinn E, et al. Cross-Packaging and Capsid Mosaic Formation in Multiplexed AAV Libraries. *Mol Ther - Methods Clin Dev*. 2020;17(June):107-121. doi:10.1016/j.omtm.2019.11.014
85. Keeler AM, Flotte TR. Recombinant Adeno-Associated Virus Gene Therapy in Light of Luxturna (and Zolgensma and Glybera): Where Are We, and How Did We Get Here? *Annu Rev Virol*. 2019;6:601-621. doi:10.1146/annurev-virology-092818-015530
86. Uddin F, Rudin CM, Sen T. CRISPR Gene Therapy: Applications, Limitations, and Implications for the Future. *Front Oncol*. 2020;10:1387. doi:10.3389/FONC.2020.01387
87. Kim E, Koo T, Park SW, et al. In vivo genome editing with a small Cas9 orthologue derived from *Campylobacter jejuni*. *Nat Commun*. 2017;8. doi:10.1038/ncomms14500
88. Yang Y, Wang L, Bell P, et al. A dual AAV system enables the Cas9-mediated correction of a metabolic liver disease in newborn mice. *Nat Biotechnol* 2016 343. 2016;34(3):334-338. doi:10.1038/nbt.3469
89. Muhuri M, Maeda Y, Ma H, et al. Overcoming innate immune barriers that impede AAV gene therapy vectors. *J Clin Invest*. 2021;131(1). doi:10.1172/JCI143780
90. Colella P, Ronzitti G, Mingozzi F. Emerging issues in AAV-mediated in vivo gene therapy. *Mol Ther - Methods Clin Dev*. 2017. doi:10.1016/j.omtm.2017.11.007
91. Gao X, Tao Y, Lamas V, et al. Treatment of autosomal dominant hearing loss by in vivo delivery of genome editing agents. *Nature*. 2018;553(7687):217-221. doi:10.1038/nature25164
92. Fajrial AK, He QQ, Wirusanti NI, Slansky JE, Ding X. A review of emerging physical transfection methods for CRISPR/Cas9-mediated gene editing. *Theranostics*. 2020;10(12):5532-5549. doi:10.7150/thno.43465
93. Lassalle F, Campillo T, Vial L, et al. Genomic species are ecological species as revealed by comparative genomics in *Agrobacterium tumefaciens*. *Genome Biol Evol*. 2011;3(1):762-781. doi:10.1093/GBE/EVR070
94. Zupan J, Muth TR, Draper O, Zambryski P. The transfer of DNA from *Agrobacterium tumefaciens* into plants: a feast of fundamental insights. *Plant J*. 2000;23(1):11-28. doi:10.1046/J.1365-313X.2000.00808.X
95. Britton MT, Escobar MA, Dandekar AM. The oncogenes of *agrobacterium tumefaciens* and *agrobacterium rhizogenes*. *Agrobacterium From Biol to Biotechnol*. 2008;Chapter 14:523-563. doi:10.1007/978-0-387-72290-0\_14
96. Sardesai N, Subramanyam S. *Agrobacterium*: A Genome-Editing Tool-Delivery System. *Curr Top Microbiol Immunol*. 2018;418:463-488. doi:10.1007/82\_2018\_101
97. Singer K. *The Mechanism of T-DNA Integration: Some Major Unresolved Questions*.

Springer International Publishing; 2018. doi:10.1007/82\_2018\_98

98. Ooms G, Hooykaas PJJ, Van Veen RJM, Van Beelen P, Regensburg-Tuïnk TJG, Schilperoort RA. Octopine Ti-plasmid deletion mutants of *Agrobacterium tumefaciens* with emphasis on the right side of the T-region. *Plasmid*. 1982;7(1):15-29. doi:10.1016/0147-619X(82)90023-3
99. Hood EE, Gelvin SB, Melchers LS, Hoekema A. New *Agrobacterium* helper plasmids for gene transfer to plants. *Transgenic Res*. 1993;2(4):208-218. doi:10.1007/BF01977351
100. Lazo GR, Stein PA, Ludwig RA. A DNA Transformation–Competent *Arabidopsis* Genomic Library in *Agrobacterium*. *Bio/Technology* 1991 910. 1991;9(10):963-967. doi:10.1038/nbt1091-963
101. Palanichelvam K, Oger P, Clough SJ, Cha C, Bent AF, Farrand SK. A Second T-Region of the Soybean-Supervirulent Chrysopine-Type Ti Plasmid pTiChry5, and Construction of a Fully Disarmed vir Helper Plasmid. <http://dx.doi.org/10.1094/MPMI200013101081>. 2007;13(10):1081-1091. doi:10.1094/MPMI.2000.13.10.1081
102. Koncz C, Schell J. The promoter of TL-DNA gene 5 controls the tissue-specific expression of chimaeric genes carried by a novel type of *Agrobacterium* binary vector. *Mol Gen Genet MGG* 1986 2043. 1986;204(3):383-396. doi:10.1007/BF00331014
103. Platt TG, Morton ER, Barton IS, Bever JD, Fuqua C. Ecological dynamics and complex interactions of *Agrobacterium* megaplasmids. *Front Plant Sci*. 2014;5(November):1-15. doi:10.3389/fpls.2014.00635
104. Gordon JE, Christie PJ. The *Agrobacterium* Ti Plasmids. *Microbiol Spectr*. 2014;2(6):295-313. doi:10.1128/9781555818982.ch17
105. Matthyse AG. Exopolysaccharides of *Agrobacterium tumefaciens*. *Curr Top Microbiol Immunol*. 2018;418:111-141. doi:10.1007/82\_2018\_100
106. Heindl JE, Wang Y, Heckel BC, Mohari B, Feirer N, Fuqua C. Mechanisms and regulation of surface interactions and biofilm formation in *Agrobacterium*. 2014;5(May):1-21. doi:10.3389/fpls.2014.00176
107. Tomlinson AD, Ramey-hartung B, Day TW, Merritt PM, Fuqua C, Fuqua C. *Agrobacterium tumefaciens* ExoR represses succinoglycan biosynthesis and is required for biofilm formation and motility. 2018;(2010):2670-2681. doi:10.1099/mic.0.039032-0
108. Wang Y, Haitjema CH, Fuqua C. The Ctp Type IVb Pilus Locus of *Agrobacterium tumefaciens* Directs Formation of the Common Pili and Contributes to Reversible Surface Attachment. 2014;196(16):2979-2988. doi:10.1128/JB.01670-14
109. Aguilar J, Zupan J, Cameron TA, Zambryski PC. *Agrobacterium* type IV secretion system and its substrates form helical arrays around the circumference of virulence-induced cells. *Proc Natl Acad Sci*. 2010;107(8):3758-3763. doi:10.1073/pnas.0914940107
110. Dardanelli M, Angelini J, Fabra A. A calcium-dependent bacterial surface protein is involved in the attachment of rhizobia to peanut roots. <https://doi.org/10.1139/w03-054>. 2011;49(6):399-405. doi:10.1139/W03-054
111. Aly KA, Baron C. The VirB5 protein localizes to the T-pilus tips in *Agrobacterium tumefaciens*. 2007;(153):3766-3775. doi:10.1099/mic.0.2007/010462-0
112. Zupan J, Hackworth CA, Aguilar J, Ward D, Zambryski P. VirB1\* promotes T-pilus formation in the vir-type IV secretion system of *Agrobacterium tumefaciens*. *J Bacteriol*.

- 2007;189(18):6551-6563. doi:10.1128/JB.00480-07
113. Buß M, Tegtmeyer N, Schnieder J, et al. Specific high affinity interaction of *Helicobacter pylori* CagL with integrin  $\alpha$ V $\beta$ 6 promotes type IV secretion of CagA into human cells. *FEBS J.* 2019;286(20):3980-3997. doi:10.1111/FEBS.14962
  114. Lacroix B, Citovsky V. Extracellular VirB5 Enhances T-DNA Transfer from *Agrobacterium* to the Host Plant. *PLoS One.* 2011;6(10):e25578. doi:10.1371/JOURNAL.PONE.0025578
  115. Cascales E, Atmakuri K, Sarkar MK, Christie PJ. DNA Substrate-Induced Activation of the *Agrobacterium* VirB/VirD4 Type IV Secretion System. *J Bacteriol.* 2013;195(11):2691-2704. doi:10.1128/JB.00114-13
  116. Banta LM, Kerr JE, Cascales E, et al. An *Agrobacterium* VirB10 mutation conferring a type IV secretion system gating defect. *J Bacteriol.* 2011;193(10):2566-2574. doi:10.1128/JB.00038-11
  117. Jakubowski SJ, Kerr JE, Garza I, et al. *Agrobacterium* VirB10 domain requirements for type IV secretion and T pilus biogenesis. *Mol Microbiol.* 2009;71(3):779-794. doi:10.1111/J.1365-2958.2008.06565.X
  118. Li YG, Christie PJ. The *Agrobacterium* VirB/VirD4 T4SS: Mechanism and Architecture Defined Through In Vivo Mutagenesis and Chimeric Systems. *Curr Top Microbiol Immunol.* 2018;418:233-260. doi:10.1007/82\_2018\_94
  119. Vergunst AC, Van Lier MCM, Den Dulk-Ras A, Grosse Stüve TA, Ouwehand A, Hooykaas PJJ. Positive charge is an important feature of the C-terminal transport signal of the VirB/D4-translocated proteins of *Agrobacterium*. *Proc Natl Acad Sci.* 2005;102(3):832-837. doi:10.1073/PNAS.0406241102
  120. Zhang X, Van Heusden GPH, Hooykaas PJJ. Virulence protein VirD5 of *Agrobacterium tumefaciens* binds to kinetochores in host cells via an interaction with Spt4. *Proc Natl Acad Sci U S A.* 2017;114(38):10238-10243. doi:10.1073/PNAS.1706166114
  121. Bundock P, Dulk-ras A Den, Beijersbergen A, Hooykaas PJJ. Trans-kingdom T-DNA transfer from *Agrobacterium tumefaciens* to *Saccharomyces cerevisiae*. *EMBO J.* 1995;14(13):3206-3214. doi:10.1002/j.1460-2075.1995.tb07323.x
  122. Niu X, Zhou M, Henkel C V., Van Heusden GPH, Hooykaas PJJ. The *Agrobacterium tumefaciens* virulence protein VirE3 is a transcriptional activator of the F-box gene VBF. *Plant J.* 2015;84(5):914-924. doi:10.1111/TPJ.13048
  123. Li X, Zhu T, Tu H, Pan SQ. *Agrobacterium* VirE3 Uses Its Two Tandem Domains at the C-Terminus to Retain Its Companion VirE2 on the Cytoplasmic Side of the Host Plasma Membrane. *Front Plant Sci.* 2020;11:464. doi:10.3389/FPLS.2020.00464/BIBTEX
  124. Howard EA, Zupan JR, Citovsky V, Zambryski PC. The VirD2 protein of *A. tumefaciens* contains a C-terminal bipartite nuclear localization signal: Implications for nuclear uptake of DNA in plant cells. *Cell.* 1992;68(1):109-118. doi:10.1016/0092-8674(92)90210-4
  125. Gelvin SB. Finding a way to the nucleus. *Curr Opin Microbiol.* 2010;13(1):53-58. doi:10.1016/j.mib.2009.11.003
  126. Tzfira T, Citovsky V. Comparison between nuclear localization of nopaline- and octopine-specific *Agrobacterium* VirE2 proteins in plant, yeast and mammalian cells. *Mol Plant Pathol.* 2001;2(3):171-176. doi:10.1046/j.1364-3703.2001.00065.x
  127. Lapham RA, Lee LY, Xhako E, Gómez EG, Nivya VM, Gelvin SB. *Agrobacterium* VirE2

- Protein Modulates Plant Gene Expression and Mediates Transformation From Its Location Outside the Nucleus. *Front Plant Sci.* 2021;12:1051. doi:10.3389/FPLS.2021.684192
128. Li X, Yang Q, Peng L, et al. Agrobacterium-delivered VirE2 interacts with host nucleoporin CG1 to facilitate the nuclear import of VirE2-coated T complex. *Proc Natl Acad Sci U S A.* 2020;117(42):26389-26397. doi:10.1073/pnas.2009645117
  129. Li X, Pan SQ. Agrobacterium delivers VirE2 protein into host cells via clathrin-mediated endocytosis. *Sci Adv.* 2017;3(3):1-12. doi:10.1126/sciadv.1601528
  130. Dumas F, Duckely M, Pelczar P, Van Gelder P, Hohn B. An Agrobacterium VirE2 channel for transferred-DNA transport into plant cells. *Proc Natl Acad Sci U S A.* 2001;98(2):485-490. doi:10.1073/pnas.98.2.485
  131. Li YG, Hu B, Christie PJ. Biological and Structural Diversity of Type IV Secretion Systems. *Protein Secret Bact.* 2019:277-289. doi:10.1128/microbiolspec.psib-0012-2018
  132. Tu H, Li X, Yang Q, Ling P, Pan SQ. Real-Time Trafficking of Agrobacterium Virulence Protein VirE2 Inside Host Cells. *Curr Top Microbiol Immunol.* 2018. doi:10.1007/82\_2018\_131
  133. Yang Q, Li X, Tu H, Pan SQ. *Agrobacterium* -delivered virulence protein VirE2 is trafficked inside host cells via a myosin XI-K-powered ER/actin network. *Proc Natl Acad Sci.* 2017;114(11):2982-2987. doi:10.1073/pnas.1612098114
  134. Lacroix B, Citovsky V. Pathways of DNA transfer to plants from *Agrobacterium tumefaciens* and related bacterial species. *Annu Rev Phytopathol.* 2019;57:231-251. doi:10.1146/annurev-phyto-082718-100101
  135. Citovsky V, Zupan J, Warnick D, Zambryski P. Nuclear Localization of Agrobacterium VirE2 Protein in Plant Cells. *Science.* 1992;256(5065):1802-1805. doi:10.1126/SCIENCE.1615325
  136. Van Kregten M, De Pater S, Romeijn R, Van Schendel R, Hooykaas PJJ, Tijsterman M. T-DNA integration in plants results from polymerase- $\theta$ -mediated DNA repair. *Nat Plants* 2016 211. 2016;2(11):1-6. doi:10.1038/nplants.2016.164
  137. Chilton MDM, Que Q. Targeted Integration of T-DNA into the Tobacco Genome at Double-Stranded Breaks: New Insights on the Mechanism of T-DNA Integration. *Plant Physiol.* 2003;133(3):956-965. doi:10.1104/pp.103.026104
  138. Tzfira T, Frankman LR, Vaidya M, Citovsky V. Site-Specific Integration of *Agrobacterium tumefaciens* T-DNA via Double-Stranded Intermediates. *Plant Physiol.* 2003;133(3):1011-1023. doi:10.1104/pp.103.032128
  139. Gelvin SB. Plant DNA repair and Agrobacterium T-DNA integration. *Int J Mol Sci.* 2021;22(16). doi:10.3390/ijms22168458
  140. Dawson JE, Nicholson LK. Folding kinetics and thermodynamics of *Pseudomonas syringae* effector protein AvrPto provide insight into translocation via the type III secretion system . *Protein Sci.* 2008;17(7):1109-1119. doi:10.1110/ps.034223.107
  141. Sorg JA, Miller NC, Marketon MM, Schneewind O. Rejection of impassable substrates by *Yersinia* type III secretion machines. *J Bacteriol.* 2005;187(20):7090-7102. doi:10.1128/JB.187.20.7090-7102.2005
  142. Cabantous S, Terwilliger TC, Waldo GS. Protein tagging and detection with engineered self-assembling fragments of green fluorescent protein. *Nat Biotechnol.* 2005;23(1):102-

107. doi:10.1038/nbt1044
143. Li X, Yang Q, Tu H, Lim Z, Pan SQ. Direct visualization of Agrobacterium -delivered VirE2 in recipient cells. 2014;487-495. doi:10.1111/tpj.12397
  144. Zhou X, Christie PJ. Mutagenesis of the Agrobacterium VirE2 Single-Stranded DNA-Binding Protein Identifies Regions Required for Self-Association and Interaction with VirE1 and a Permissive Site for Hybrid Protein Construction. 1999;181(14):4342-4352.
  145. Remy I, Michnick SW. A highly sensitive protein-protein interaction assay based on Gaussia luciferase. *Nat Methods*. 2006;3(12):977-979. doi:10.1038/nmeth979
  146. Dixon AS, Schwinn MK, Hall MP, et al. NanoLuc Complementation Reporter Optimized for Accurate Measurement of Protein Interactions in Cells. *ACS Chem Biol*. 2016;11(2):400-408. doi:10.1021/acscchembio.5b00753
  147. Westerhausen S, Nowak M, Torres-Vargas CE, et al. A NanoLuc luciferase-based assay enabling the real-time analysis of protein secretion and injection by bacterial type III secretion systems. *Mol Microbiol*. 2020;113(6):1240-1254. doi:10.1111/mmi.14490
  148. Lettl C, Haas R, Fischer W. Kinetics of CagA type IV secretion by Helicobacter pylori and the requirement for substrate unfolding. *Mol Microbiol*. 2021;116(3):794-807. doi:10.1111/mmi.14772
  149. Muyldermans S. Nanobodies: Natural single-domain antibodies. *Annu Rev Biochem*. 2013;82:775-797. doi:10.1146/annurev-biochem-063011-092449
  150. Saerens D, Conrath K, Govaert J, Muyldermans S. Disulfide Bond Introduction for General Stabilization of Immunoglobulin Heavy-Chain Variable Domains. *J Mol Biol*. 2008;377(2):478-488. doi:10.1016/j.jmb.2008.01.022
  151. Liu H, Schittny V, Nash MA. Removal of a Conserved Disulfide Bond Does Not Compromise Mechanical Stability of a VHH Antibody Complex. *Nano Lett*. 2019;19(8):5524-5529. doi:10.1021/acs.nanolett.9b02062
  152. Kirchhofer A, Helma J, Schmidthals K, et al. Modulation of protein properties in living cells using nanobodies. *Nat Struct Mol Biol*. 2010;17(1):133-139. doi:10.1038/nsmb.1727
  153. Olichon A, De Marco A. Preparation of a naïve library of camelid single domain antibodies. *Methods Mol Biol*. 2012;911:65-78. doi:10.1007/978-1-61779-968-6\_5
  154. Muyldermans S. Applications of Nanobodies. *Annu Rev Anim Biosci*. 2021;9:401-421. doi:10.1146/annurev-animal-021419-083831
  155. Rothbauer U, Zolghadr K, Tillib S, et al. Targeting and tracing antigens in live cells with fluorescent nanobodies. *Nat Methods*. 2006;3(11):887-889. doi:10.1038/nmeth953
  156. Scully M, Cataland SR, Peyvandi F, et al. Caplacizumab Treatment for Acquired Thrombotic Thrombocytopenic Purpura. *N Engl J Med*. 2019;380(4):335-346. doi:10.1056/nejmoa1806311
  157. Salema V, Mañas C, Cerdán L, et al. High affinity nanobodies against human epidermal growth factor receptor selected on cells by E. coli display. *MAbs*. 2016;8(7):1286-1301. doi:10.1080/19420862.2016.1216742
  158. Glass DS, Riedel-Kruse IH. A Synthetic Bacterial Cell-Cell Adhesion Toolbox for Programming Multicellular Morphologies and Patterns. *Cell*. 2018;174(3):649-658.e16. doi:10.1016/j.cell.2018.06.041
  159. Pizarro-Cerdá J, Cossart P. Bacterial adhesion and entry into host cells. *Cell*.

2006;124(4):715-727. doi:10.1016/j.cell.2006.02.012

160. Gürel F, Uçarlı C, Tufan F, Kalaskar DM. Enhancing T-DNA Transfer Efficiency in Barley (*Hordeum vulgare* L.) Cells Using Extracellular Cellulose and Lectin. *Appl Biochem Biotechnol*. 2015;176(4):1203-1216. doi:10.1007/s12010-015-1640-0
161. Gaspar YM, Nam J, Schultz CJ, et al. Characterization of the Arabidopsis Lysine-Rich That Results in a Decreased Efficiency of Agrobacterium Transformation 1. 2004;135(August):2162-2171. doi:10.1104/pp.104.045542.2162
162. Pierrat X, Wong J, Al-Mayyah Z, Persat A. The Mammalian Membrane Microenvironment Regulates the Sequential Attachment of Bacteria to Host Cells. *MBio*. 2021;12(4).
163. Nadell CD, Drescher K, Foster KR. Spatial structure, cooperation and competition in biofilms. *Nat Rev Microbiol*. 2016;14(9):589-600. doi:10.1038/nrmicro.2016.84
164. Viela F, Mathelié-Guinlet M, Viljoen A, Dufrêne YF. What makes bacterial pathogens so sticky? *Mol Microbiol*. 2020;113(4):683-690. doi:10.1111/mmi.14448
165. Petrova OE, Sauer K. Sticky situations: Key components that control bacterial surface attachment. *J Bacteriol*. 2012;194(10):2413-2425. doi:10.1128/JB.00003-12
166. Berne C, Ellison CK, Ducret A, Brun Y V. Bacterial adhesion at the single-cell level. *Nat Rev Microbiol*. 2018;16(10):616-627. doi:10.1038/s41579-018-0057-5
167. Thomas WE, Trintchina E, Forero M, Vogel V, Sokurenko E V. Bacterial Adhesion to Target Cells Enhanced by Shear Force. *Cell*. 2002;109(7):913-923.
168. Kolewe KW, Zhu J, Mako NR, Nonnenmann SS, Schiffman JD. Bacterial Adhesion Is Affected by the Thickness and Stiffness of Poly(ethylene glycol) Hydrogels. *ACS Appl Mater Interfaces*. 2018;10(3):2275-2281. doi:10.1021/acsami.7b12145
169. Lecuyer S, Rusconi R, Shen Y, et al. Shear stress increases the residence time of adhesion of *Pseudomonas aeruginosa*. *Biophys J*. 2011;100(2):341-350. doi:10.1016/j.bpj.2010.11.078
170. de la Serna JB, Schütz GJ, Eggeling C, Cebecauer M. There is no simple model of the plasma membrane organization. *Front Cell Dev Biol*. 2016;4:1-17. doi:10.3389/fcell.2016.00106
171. Ribet D, Cossart P. How bacterial pathogens colonize their hosts and invade deeper tissues. *Microbes Infect*. 2015;17(3):173-183. doi:10.1016/j.micinf.2015.01.004
172. Girard V, Mourez M. Adhesion mediated by autotransporters of Gram-negative bacteria: Structural and functional features. *Res Microbiol*. 2006;157(5):407-416. doi:10.1016/j.resmic.2006.02.001
173. Ismaili A, Meddings JB, Ratnam S, Sherman PM. Modulation of host cell membrane fluidity: A novel mechanism for preventing bacterial adhesion. *Am J Physiol - Gastrointest Liver Physiol*. 1999;277(1 40-1):201-208. doi:10.1152/ajpgi.1999.277.1.g201
174. Dufrêne YF. Sticky microbes: Forces in microbial cell adhesion. *Trends Microbiol*. 2015;23(6):376-382. doi:10.1016/j.tim.2015.01.011
175. Bell GI. Models for the specific adhesion of cells to cells. *Science*. 1978;200(4342):618-627. doi:10.1126/science.347575
176. Patel S, Mathivanan N, Goyal A. Bacterial adhesins, the pathogenic weapons to trick host defense arsenal. *Biomed Pharmacother*. 2017;93:763-771.

doi:10.1016/j.biopha.2017.06.102

177. Misselwitz B, Kreibich SK, Rout S, Stecher B, Periaswamy B, Hardt WD. Salmonella enterica serovar typhimurium binds to hela cells via fim-mediated reversible adhesion and irreversible type three secretion system 1-mediated docking. *Infect Immun*. 2011;79(1):330-341. doi:10.1128/IAI.00581-10
178. Sabzevari H, Kantor J, Jaigirdar A, et al. Acquisition of CD80 (B7-1) by T Cells. *J Immunol*. 2001;166:2505-2513. doi:10.4049/jimmunol.166.4.2505
179. Kubala MH, Kovtun O, Alexandrov K, Collins BM. Structural and thermodynamic analysis of the GFP:GFP-nanobody complex. *Protein Sci*. 2010;19(12):2389-2401. doi:10.1002/pro.519
180. Fridy PC, Li Y, Keegan S, et al. A robust pipeline for rapid production of versatile nanobody repertoires. *Nat Methods*. 2014;11(12):1253-1260. doi:10.1038/nmeth.3170
181. Ricci V, Galmiche A, Doye A, Necchi V, Solcia E, Boquet P. High cell sensitivity to Helicobacter pylori VacA toxin depends on a GPI-anchored protein and is not blocked by inhibition of the clathrin-mediated pathway of endocytosis. *Mol Biol Cell*. 2000;11(11):3897-3909. doi:10.1091/mbc.11.11.3897
182. D W Goddette and C Frieden. Actin polymerization. The mechanism of action of cytochalasin D. *J Biol Chem*. 1986;261(34):15974-15980. doi:.
183. Nishida-Aoki N, Tominaga N, Kosaka N, Ochiya T. Altered biodistribution of deglycosylated extracellular vesicles through enhanced cellular uptake. *J Extracell Vesicles*. 2020;9(1). doi:10.1080/20013078.2020.1713527
184. Howlader MA, Li C, Zou C, Chakraborty R, Ebesoh N, Cairo CW. Neuraminidase-3 Is a Negative Regulator of LFA-1 Adhesion. *Front Chem*. 2019;7:1-15. doi:10.3389/fchem.2019.00791
185. Dufrêne YF, Persat A. Mechanomicrobiology: how bacteria sense and respond to forces. *Nat Rev Microbiol*. 2020;18(4):227-240. doi:10.1038/s41579-019-0314-2
186. Tripathi P, Beaussart A, Alsteens D, et al. Adhesion and nanomechanics of pili from the probiotic lactobacillus rhamnosus GG. *ACS Nano*. 2013;7(4):3685-3697. doi:10.1021/nn400705u
187. McKenzie M, Ha SM, Rammohan A, Radhakrishnan R, Ramakrishnan N. Multivalent Binding of a Ligand-Coated Particle: Role of Shape, Size, and Ligand Heterogeneity. *Biophys J*. 2018;114(8):1830-1846. doi:10.1016/j.bpj.2018.03.007
188. Spaulding CN, Klein RD, Ruer S, et al. Selective depletion of uropathogenic E. coli from the gut by a FimH antagonist. *Nature*. 2017. doi:10.1038/nature22972
189. Tollis S, Dart AE, Tzircotis G, Endres RG. The zipper mechanism in phagocytosis: Energetic requirements and variability in phagocytic cup shape. *BMC Syst Biol*. 2010;4. doi:10.1186/1752-0509-4-149
190. Romero S, Le Clainche C, Gautreau AM. Actin polymerization downstream of integrins: Signaling pathways and mechanotransduction. *Biochem J*. 2020;477(1):1-21. doi:10.1042/BCJ20170719
191. González C, Chames P, Kerfelec B, Baty D, Robert P, Limozin L. Nanobody-CD16 Catch Bond Reveals NK Cell Mechanosensitivity. *Biophys J*. 2019;116(8):1516-1526. doi:10.1016/j.bpj.2019.03.012
192. Yakovenko O, Nunez J, Bensing B, et al. Serine-Rich Repeat Adhesins Mediate Shear-Enhanced Streptococcal Binding to Platelets. *Infect Immun*. 2018;86(6).

doi:<https://doi.org/10.1128/IAI.00160-18>. Editor

193. Klamecka K, Severin PM, Milles LF, Gaub HE, Leonhardt H. Energy profile of nanobody-GFP complex under force. *Phys Biol*. 2015;12(5):56009. doi:10.1088/1478-3975/12/5/056009
194. Kurdi R Al, Vallade M, Riveline D. Membrane and acto-myosin tension promote clustering of adhesion proteins. *Pnas*. 2004;101(8):2229-2234.
195. Johansson MM, Bélurier E, Papageorgiou AC, et al. The binding mechanism of the virulence factor streptococcus suis adhesin P subtype to globotetraosylceramide is associated with systemic disease. *J Biol Chem*. 2020;295(42):14305-14324. doi:10.1074/jbc.RA120.014818
196. Mühlenkamp M, Oberhettinger P, Leo JC, Linke D, Schütz MS. Yersinia adhesin A (YadA) - Beauty & beast. *Int J Med Microbiol*. 2015;305(2):252-258. doi:10.1016/j.ijmm.2014.12.008
197. Krachler AM, Orth K. Targeting the bacteria-host interface strategies in anti-adhesion therapy. *Virulence*. 2013;4(4):284-294. doi:10.4161/viru.24606
198. Mckenzie GJ, Craig NL. Fast , easy and efficient : site-specific insertion of transgenes into Enterobacterial chromosomes using Tn 7 without need for selection of the insertion event. 2006;7:1-7. doi:10.1186/1471-2180-6-39
199. Datsenko KA, Wanner BL. One-step inactivation of chromosomal genes in Escherichia coli K-12 using PCR products. *Proc Natl Acad Sci U S A*. 2000;97(12):6640-6645. doi:10.1073/pnas.120163297
200. Chevalier S, Cuestas-Ayllon C, Grazu V, Luna M, Feracci H, De La Fuente JM. Creating biomimetic surfaces through covalent and oriented binding of proteins. *Langmuir*. 2010;26(18):14707-14715. doi:10.1021/la103086b
201. Bañuls MJ, Puchades R, Maquieira Á. Chemical surface modifications for the development of silicon-based label-free integrated optical (IO) biosensors: A review. *Anal Chim Acta*. 2013;777:1-16. doi:10.1016/j.aca.2013.01.025
202. Tinevez JY, Perry N, Schindelin J, et al. TrackMate: An open and extensible platform for single-particle tracking. *Methods*. 2017;115:80-90. doi:10.1016/j.ymeth.2016.09.016
203. Sood P, Bhattacharya A, Sood A. Problems and possibilities of monocot transformation. *Biol Plant*. 2011;55(1):1-15. doi:10.1007/s10535-011-0001-2
204. Kim H, Jin X, Glass DS, Riedel-Kruse IH. Engineering and modeling of multicellular morphologies and patterns. *Curr Opin Genet Dev*. 2020;63:95-102. doi:10.1016/j.gde.2020.05.039
205. Ausländer D, Ausländer S, Pierrat X, Hellmann L, Rachid L, Fussenegger M. Programmable full-adder computations in communicating three-dimensional cell cultures. *Nat Methods*. 2018;15(1):57-60. doi:10.1038/nmeth.4505
206. Toda S, Blauch LR, Tang SKY, Morsut L, Lim WA. Programming self-organizing multicellular structures with synthetic cell-cell signaling. *Science*. 2018;361(6398):156-162. doi:10.1126/science.aat0271
207. Krenek P, Samajova O, Luptovciak I, Dorskocilova A, Komis G, Samaj J. Transient plant transformation mediated by Agrobacterium tumefaciens: Principles, methods and applications. *Biotechnol Adv*. 2015;33(6):1024-1042. doi:10.1016/j.biotechadv.2015.03.012
208. Thompson MA, Onyeziri MC, Fuqua C. Function and Regulation of Agrobacterium

- tumefaciens Cell Surface Structures that Promote Attachment. *Curr Top Microbiol Immunol*. 2018. doi:10.1007/82
209. Leuzinger K, Dent M, Hurtado J, et al. Efficient agroinfiltration of plants for high-level transient expression of recombinant proteins. *J Vis Exp*. 2013;(77):1-9. doi:10.3791/50521
  210. Backert S, Fronzes R, Waksman G. VirB2 and VirB5 proteins : specialized adhesins in bacterial type-IV secretion systems ? 2008;(August):409-413. doi:10.1016/j.tim.2008.07.001
  211. Chumakov MI. Protein apparatus for horizontal transfer of agrobacterial T-DNA to eukaryotic cells. *Biochem*. 2013;78(12):1321-1332. doi:10.1134/S000629791312002X
  212. Wood DW, Setubal JC, Kaul R, et al. The genome of the natural genetic engineer *Agrobacterium tumefaciens* C58. *Science*. 2001;294(5550):2317-2323. doi:10.1126/science.1066804
  213. Baek M, DiMaio F, Anishchenko I, et al. Accurate prediction of protein structures and interactions using a three-track neural network. *Science*. 2021;373(6557):871-876. doi:10.1126/SCIENCE.ABJ8754
  214. Almagro Armenteros JJ, Tsirigos KD, Sønderby CK, et al. SignalP 5.0 improves signal peptide predictions using deep neural networks. *Nat Biotechnol* 2019 374. 2019;37(4):420-423. doi:10.1038/s41587-019-0036-z
  215. Rojas-lopez M, Zorgani MA, Kelley LA, Bailly X, Rosini R, Desvaux M. Identification of the Autochaperone Domain in the Type Va Secretion System ( T5aSS ): Prevalent Feature of Autotransporters with a  $\beta$  -Helical Passenger. 2018;8(January):1-10. doi:10.3389/fmicb.2017.02607
  216. Imai K, Mitaku S. Mechanisms of secondary structure breakers in soluble proteins. *Biophysics (Oxf)*. 2005;1:55-65. doi:10.2142/BIOPHYSICS.1.55
  217. Waterhouse A, Bertoni M, Bienert S, et al. SWISS-MODEL: homology modelling of protein structures and complexes. *Nucleic Acids Res*. 2018;46(W1):W296-W303. doi:10.1093/NAR/GKY427
  218. Yang J, Yan R, Roy A, Xu D, Poisson J, Zhang Y. The I-TASSER Suite: protein structure and function prediction. *Nat Methods* 2015 121. 2014;12(1):7-8. doi:10.1038/nmeth.3213
  219. Brotcke Zumsteg A, Goosmann C, Brinkmann V, Morona R, Zychlinsky A. IcsA is a *Shigella flexneri* adhesin regulated by the type III secretion system and required for pathogenesis. *Cell Host Microbe*. 2014;15(4):435-445. doi:10.1016/J.CHOM.2014.03.001
  220. Leininger E, Roberts M, Kenimer JG, et al. Pertactin , an Arg-Gly-Asp-containing *Bordetella pertussis* surface protein that promotes adherence of mammalian cells. *Proc Natl Acad Sci*. 1991;88(2):345-349. doi:10.1073/PNAS.88.2.345
  221. Garnham CP, Campbell RL, Davies PL. Anchored clathrate waters bind antifreeze proteins to ice. *Proc Natl Acad Sci U S A*. 2011;108(18):7363-7367. doi:10.1073/PNAS.1100429108/
  222. Herrmann J, Jabbarpour F, Bargar PG, et al. Environmental Calcium Controls Alternate Physical States of the *Caulobacter* Surface Layer. *Biophys J*. 2017;112(9):1841-1851. doi:10.1016/J.BPJ.2017.04.003
  223. Lau JHY, Nomellini JF, Smit J. Analysis of high-level S-layer protein secretion in

- Caulobacter crescentus. *Can J Microbiol.* 2010;56(6):501-514. doi:10.1139/W10-036
224. Heras B, Totsika M, Peters KM, et al. The antigen 43 structure reveals a molecular Velcro-like mechanism of autotransporter-mediated bacterial clumping. *Proc Natl Acad Sci U S A.* 2014;111(1):457-462. doi:10.1073/PNAS.1311592111
  225. González-Mula A, Lang J, Grandclément C, et al. Lifestyle of the biotroph *Agrobacterium tumefaciens* in the ecological niche constructed on its host plant. *New Phytol.* 2018;219(1):350-362. doi:10.1111/nph.15164
  226. Hirooka T, Rogowsky PM, Kado CI. Characterization of the virE locus of *Agrobacterium tumefaciens* plasmid pTiC58. *J Bacteriol.* 1987;169(4):1529-1536. doi:10.1128/jb.169.4.1529-1536.1987
  227. Denkovskiene E, Paskevicius S, Werner S, Gleba Y, Razanskiene A. Inducible Expression of *Agrobacterium* Virulence Gene VirE2 for Stringent Regulation of T-DNA Transfer in Plant Transient Expression Systems. 2015;28(11):1247-1255.
  228. Rogowsky PM, Close TJ, Chimera JA, Shaw JJ, Kado CI. Regulation of the vir genes of *Agrobacterium tumefaciens* plasmid pTiC58. *J Bacteriol.* 1987;169(11):5101-5112. doi:10.1128/jb.169.11.5101-5112.1987
  229. Haryono M, Cho ST, Fang MJ, et al. Differentiations in gene content and expression response to virulence induction between two *agrobacterium* strains. *Front Microbiol.* 2019;10(JULY):1-10. doi:10.3389/fmicb.2019.01554
  230. Nicolay T, Lemoine L, Lievens E, Balzarini S, Vanderleyden J, Spaepen S. Probing the applicability of autotransporter based surface display with the EstA autotransporter of *Pseudomonas stutzeri* A15. 2012:1-11.
  231. Xiao L, Zhou L, Sun C, et al. Apa is a trimeric autotransporter adhesin of *Actinobacillus pleuropneumoniae* responsible for autoagglutination and host cell adherence. *J Basic Microbiol.* 2012;52(5):598-607. doi:10.1002/jobm.201100365
  232. Jong WSP, Schillemans M, ten Hagen-Jongman CM, Luirink J, van Ulsen P. Comparing autotransporter  $\beta$ -domain configurations for their capacity to secrete heterologous proteins to the cell surface. *PLoS One.* 2018;13(2):1-23. doi:10.1371/journal.pone.0191622
  233. Lund B, Marklund B -I, Strömberg N, Lindberg F, Karlsson K -A, Normark S. Uropathogenic, *Escherichia coli* can express serologically identical pili of different receptor binding specificities. *Mol Microbiol.* 1988;2(2):255-263. doi:10.1111/j.1365-2958.1988.tb00027.x
  234. Sokurenko E V, Chesnokova V, Dykhuizen DE, et al. Pathogenic adaptation of *Escherichia coli* by natural variation of the FimH adhesin. *Proc Natl Acad Sci U S A.* 1998;95(15):8922-8926. doi:10.1073/pnas.95.15.8922
  235. Nilsson LM, Yakovenko O, Tchesnokova V, et al. The cysteine bond in the *Escherichia coli* FimH adhesin is critical for adhesion under flow conditions. *Mol Microbiol.* 2007;65(5):1158-1169. doi:10.1111/j.1365-2958.2007.05858.x
  236. Gupta R, Gupta N, Rath P. Bacterial lipases: An overview of production, purification and biochemical properties. *Appl Microbiol Biotechnol.* 2004;64(6):763-781. doi:10.1007/s00253-004-1568-8
  237. Becker S, Theile S, Heppeler N, et al. A generic system for the *Escherichia coli* cell-surface display of lipolytic enzymes. *FEBS Lett.* 2005;579(5):1177-1182. doi:10.1016/j.febslet.2004.12.087

238. Wilhelm S, Tommassen JAN, Al WET. A Novel Lipolytic Enzyme Located in the Outer Membrane of *Pseudomonas aeruginosa*. 1999;181(22):6977-6986.
239. Nordwald EM, Plaks JG, Snell JR, Sousa MC, Kaar JL. Crystallographic Investigation of Imidazolium Ionic Liquid Effects on Enzyme Structure. *ChemBioChem*. 2015;16(17):2456-2459. doi:10.1002/CBIC.201500398
240. Morton ER, Fuqua C. Unit 3D.2 Genetic manipulation of *Agrobacterium*. *Curr Protoc Microbiol*. 2012;(SUPPL.25):1-17. doi:10.1002/9780471729259.mc03d02s25
241. Lee L-Y, Gelvin SB. T-DNA Binary Vectors and Systems. *Plant Physiol*. 2007;146(2):325-332. doi:10.1104/pp.107.113001
242. Murai N. Review: Plant Binary Vectors of Ti Plasmid in *Agrobacterium tumefaciens* with a Broad Host-Range Replicon of pRK2, pRi, pSa or pVS1. *Am J Plant Sci*. 2013;4(April):932-939. doi:10.4236/ajps.2013.44115
243. Kok RG, Christoffels VM, Vosman B, Hellingwerf KJ. Growth-phase-dependent expression of the lipolytic system of *Acinetobacter calcoaceticus* BD413: cloning of a gene encoding one of the esterases. *J Gen Microbiol*. 1993;139(10):2329-2342. doi:10.1099/00221287-139-10-2329
244. Hooykaas PJJ, Heusden GPH Van, Niu X, et al. *Agrobacterium* -Mediated Transformation of Yeast and Fungi. doi:10.1007/82
245. Hwang H-H, Gelvin SB, Lai E-M. Editorial: "*Agrobacterium Biology and Its Application to Transgenic Plant Production*." Vol 6.; 2015. doi:10.3389/fpls.2015.00265
246. Sakalis PA, van Heusden GPH, Hooykaas PJJ. Visualization of VirE2 protein translocation by the *Agrobacterium* type IV secretion system into host cells. *Microbiologyopen*. 2014;3(1):104-117. doi:10.1002/mbo3.152
247. Kunik T, Tzfira T, Kapulnik Y, Gafni Y, Dingwall C, Citovsky V. Genetic transformation of HeLa cells by *Agrobacterium*. *Proc Natl Acad Sci*. 2001;98(4):1871-1876. doi:10.1073/pnas.98.4.1871
248. Bulgakov VP, Kiselev K V., Yakovlev K V., Zhuravlev YN, Gontcharov AA, Odintsova NA. *Agrobacterium*-mediated transformation of sea urchin embryos. *Biotechnol J*. 2006;1(4):454-461. doi:10.1002/biot.200500045
249. Petrunia I V., Frolova OY, Komarova T V., Kiselev SL, Citovsky V, Dorokhov YL. *Agrobacterium tumefaciens*-induced bacteraemia does not lead to reporter gene expression in mouse organs. *PLoS One*. 2008;3(6):2-6. doi:10.1371/journal.pone.0002352
250. Piers KL, Heath JD, Liang X, Stephens KM, Nester EW. *Agrobacterium tumefaciens*-mediated transformation of yeast. *Proc Natl Acad Sci U S A*. 1996;93(4):1613-1618. doi:10.1073/pnas.93.4.1613
251. Schrammeijer B, Risseuw E, Pansegrau W, Regensburg-Tuink TJG, Crosby WL, Hooykaas PJJ. Interaction of the virulence protein VirF of *agrobacterium tumefaciens* with plant homologs of the yeast Skp1 protein. *Curr Biol*. 2001;11(4):258-262. doi:10.1016/S0960-9822(01)00069-0
252. Soltani J, Van Heusden GPH, Hooykaas PJJ. Deletion of host histone acetyltransferases and deacetylases strongly affects *Agrobacterium*-mediated transformation of *Saccharomyces cerevisiae*. *FEMS Microbiol Lett*. 2009;298(2):228-233. doi:10.1111/j.1574-6968.2009.01723.x
253. Roushan MR, Zeeuw MAM De, Hooykaas PJJ, Heusden GPH Van. Application of

- phiLOV2 . 1 as a fluorescent marker for visualization of Agrobacterium effector protein translocation. 2018;685-699. doi:10.1111/tpj.14060
254. Gera N, Hussain M, Rao BM. Protein selection using yeast surface display. *Methods*. 2013;60(1):15-26. doi:10.1016/j.ymeth.2012.03.014
  255. Tzfira T, Li J, Lacroix B, Citovsky V. Agrobacterium T-DNA integration: Molecules and models. *Trends Genet*. 2004;20(8):375-383. doi:10.1016/j.tig.2004.06.004
  256. Liang Z, Tzfira T. In vivo formation of double-stranded T-DNA molecules by T-strand priming. *Nat Commun*. 2013;4:1-8. doi:10.1038/ncomms3253
  257. Fishburn J, Tomko E, Galburt E, Hahn S. Double-stranded DNA translocase activity of transcription factor TFIIH and the mechanism of RNA polymerase II open complex formation. *Proc Natl Acad Sci U S A*. 2015;112(13):3961-3966. doi:10.1073/pnas.1417709112
  258. Asturias FJ. RNA polymerase II structure, and organization of the preinitiation complex. *Curr Opin Struct Biol*. 2004;14(2):121-129. doi:10.1016/j.sbi.2004.03.007
  259. Müller CW. Transcription factors: Global and detailed views. *Curr Opin Struct Biol*. 2001;11(1):26-32. doi:10.1016/S0959-440X(00)00163-9
  260. Pelczar P, Kalck V, Gomez D, Hohn B. Agrobacterium proteins VirD2 and VirE2 mediate precise integration of synthetic T-DNA complexes in mammalian cells. *EMBO Rep*. 2004;5(6):632-637. doi:10.1038/sj.embor.7400165
  261. Gonçalves MAFV. Adeno-associated virus: From defective virus to effective vector. *Virology*. 2005;2:1-17. doi:10.1186/1743-422X-2-43
  262. Rivera-Torres N, Banas K, Bialk P, Bloh KM, Kmiec EB. Insertional mutagenesis by CRISPR/Cas9 ribonucleoprotein gene editing in cells targeted for point mutation repair directed by short single-stranded DNA oligonucleotides. *PLoS One*. 2017;12(1):1-18. doi:10.1371/journal.pone.0169350
  263. Kosicki M, Rajan SS, Lorenzetti FC, et al. *Dynamics of Indel Profiles Induced by Various CRISPR/Cas9 Delivery Methods*. Vol 152. Elsevier Inc.; 2017. doi:10.1016/bs.pmbts.2017.09.003
  264. Ivanov IP, Loughran G, Sachs MS, Atkins JF. Initiation context modulates autoregulation of eukaryotic translation initiation factor 1 (eIF1). *Proc Natl Acad Sci U S A*. 2010;107(42):18056-18060. doi:10.1073/pnas.1009269107
  265. Lovell, S., Mehzebeen, N., Battaile, K.P., Wood, M.G., Encell, L.P., Wood KV. PDB - 5IBO: 1.95Å resolution structure of NanoLuc luciferase. RCSB database only, unpublished. <https://www.rcsb.org/structure/5ibo>. Published 2016. Accessed January 8, 2022.
  266. Yaakov N, Barak Y, Pereman I, Christie PJ, Elbaum M. Direct fluorescence detection of VirE2 secretion by Agrobacterium tumefaciens. 2017:1-19.
  267. Ali Z, Shami A, Sedeek K, et al. Fusion of the Cas9 endonuclease and the VirD2 relaxase facilitates homology-directed repair for precise genome engineering in rice. *Commun Biol*. 2020;3(1). doi:10.1038/s42003-020-0768-9
  268. Dym O, Albeck S, Unger T, et al. Crystal structure of the Agrobacterium virulence complex VirE1-VirE2 reveals a flexible protein that can accommodate different partners. *Proc Natl Acad Sci U S A*. 2008;105(32):11170-11175. doi:10.1073/pnas.0801525105
  269. Dejonghe W, Sharma I, Denoo B, et al. Disruption of endocytosis through chemical inhibition of clathrin heavy chain function. *Nat Chem Biol*. 2019;15(6):641-649.

doi:10.1038/s41589-019-0262-1

270. Li X, Tu H, Pan SQ. Agrobacterium Delivers Anchorage Protein VirE3 for Companion VirE2 to Aggregate at Host Entry Sites for T-DNA Protection. *Cell Rep.* 2018;25(2):302-311.e6. doi:10.1016/j.celrep.2018.09.023
271. Pratheesh PT, Vineetha M, Kurup GM. An efficient protocol for the Agrobacterium-mediated genetic transformation of microalga *Chlamydomonas reinhardtii*. *Mol Biotechnol.* 2014;56(6):507-515. doi:10.1007/s12033-013-9720-2
272. Molino JVD, Carpine R, Gademann K, Mayfield S, Sieber S. Development of a Cell Surface Display System in *Chlamydomonas reinhardtii*. *Algal Res.* 2022;61(January). doi:10.1016/j.algal.2021.102570
273. Adair WS, Steinmetz S a, Mattson DM, Goodenough UW, Heuser JE. Nucleated assembly of *Chlamydomonas* and *Volvox* Cell Walls. *Assembly.* 1987;105(November):2373-2382.
274. Hyams J, Davies DR. The induction and characterisation of cell wall mutants of *Chlamydomonas reinhardtii*. *Mutat Res - Fundam Mol Mech Mutagen.* 1972;14(4):381-389. doi:10.1016/0027-5107(72)90135-2
275. Schmitz DJ, Ali Z, Wang C, et al. CRISPR/Cas9 Mutagenesis by Translocation of Cas9 Protein Into Plant Cells via the Agrobacterium Type IV Secretion System. *Front Genome Ed.* 2020;2(July):1-11. doi:10.3389/fgeed.2020.00006
276. Soltani J, Heusden GPH Van, Hooykaas PJJ. Chapter 18: Agrobacterium Mediated Transformation of Non-Plant Organisms. *Agrobacterium From Biol to Biotechnol.* 2008:649-675. doi:https://doi.org/10.1007/978-0-387-72290-0\_18
277. Hopfner KP, Hornung V. Molecular mechanisms and cellular functions of cGAS–STING signalling. *Nat Rev Mol Cell Biol.* 2020;21(9):501-521. doi:10.1038/s41580-020-0244-x
278. Yang YG, Lindahl T, Barnes DE. Trex1 Exonuclease Degrades ssDNA to Prevent Chronic Checkpoint Activation and Autoimmune Disease. *Cell.* 2007;131(5):873-886. doi:10.1016/j.cell.2007.10.017
279. Ablasser A, Hemmerling I, Schmid-Burgk JL, Behrendt R, Roers A, Hornung V. TREX1 Deficiency Triggers Cell-Autonomous Immunity in a cGAS-Dependent Manner. *J Immunol.* 2014;192(12):5993-5997. doi:10.4049/jimmunol.1400737
280. Pathare GR, Decout A, Glück S, et al. Structural mechanism of cGAS inhibition by the nucleosome. *Nature.* 2020;587(7835):668-672. doi:10.1038/s41586-020-2750-6
281. Vergunst AC, Schrammeijer B, Den Dulk-Ras A, De Vlaam CMT, Regensburg-Tuink TJG, Hooykaas PJJ. VirB/D4-dependent protein translocation from Agrobacterium into plant cells. *Science.* 2000;290(5493):979-982. doi:10.1126/science.290.5493.979
282. Pitzschke A. Agrobacterium infection and plant defense—transformation success hangs by a thread. *Front Plant Sci.* 2013;4(December):1-12. doi:10.3389/fpls.2013.00519
283. Madeira F, Park YM, Lee J, et al. The EMBL-EBI search and sequence analysis tools APIs in 2019. *Nucleic Acids Res.* 2019;47(W1):W636-W641. doi:10.1093/nar/gkz268
284. Mikaty G, Soyer M, Mairey E, et al. Extracellular bacterial pathogen induces host cell surface reorganization to resist shear stress. *PLoS Pathog.* 2009;5(2). doi:10.1371/journal.ppat.1000314
285. Fernández-Pérez EJ, Sepúlveda FJ, Peters C, et al. Effect of cholesterol on membrane fluidity and association of A $\beta$  oligomers and subsequent neuronal damage: A Double-Edged Sword. *Front Aging Neurosci.* 2018;10:1-14. doi:10.3389/fnagi.2018.00226

286. Biswas A, Kashyap P, Datta S, Sengupta T, Sinha B. Cholesterol Depletion by M $\beta$ CD Enhances Cell Membrane Tension and Its Variations-Reducing Integrity. *Biophys J*. 2019;116(8):1456-1468. doi:10.1016/j.bpj.2019.03.016
287. Mundhara N, Majumder A, Panda D. Methyl- $\beta$ -cyclodextrin, an actin depolymerizer augments the antiproliferative potential of microtubule-targeting agents. *Sci Rep*. 2019;9(1):1-12. doi:10.1038/s41598-019-43947-4
288. Hissa B, Pontes B, Roma PMS, et al. Membrane cholesterol removal changes mechanical properties of cells and induces secretion of a specific pool of lysosomes. *PLoS One*. 2013;8(12). doi:10.1371/journal.pone.0082988
289. Mañes S, Martínez-A C. Cholesterol domains regulate the actin cytoskeleton at the leading edge of moving cells. *Trends Cell Biol*. 2004;14(6):275-278. doi:10.1016/j.tcb.2004.04.008
290. Leitao SM, Drake B, Pinjusic K, et al. Time-Resolved Scanning Ion Conductance Microscopy for Three-Dimensional Tracking of Nanoscale Cell Surface Dynamics. *ACS Nano*. 2021. doi:10.1021/acsnano.1c05202
291. Ryoo D, Rydmark MO, Pang YT, Lundquist KP, Linke D, Gumbart JC. BamA is required for autotransporter secretion. *Biochim Biophys Acta - Gen Subj*. 2020;1864(7):129581. doi:10.1016/j.bbagen.2020.129581
292. Renn JP, Junker M, Besingi RN, Braselmann E, Clark PL. ATP-independent control of autotransporter virulence protein transport via the folding properties of the secreted protein. *Chem Biol*. 2012;19(2):287-296. doi:10.1016/j.chembiol.2011.11.009
293. Otto BR, Sijbrandi R, Luirink J, et al. Crystal structure of hemoglobin protease, a heme binding autotransporter protein from pathogenic Escherichia coli. *J Biol Chem*. 2005;280(17):17339-17345. doi:10.1074/jbc.M412885200
294. Wen X, Jiping L, Cai D, et al. Anticancer efficacy of targeted shikonin liposomes modified with rgd in breast cancer cells. *Molecules*. 2018;23(2):1-15. doi:10.3390/molecules23020268
295. Dang W, Wei Z ming. An optimized Agrobacterium-mediated transformation for soybean for expression of binary insect resistance genes. *Plant Sci*. 2007;173(4):381-389. doi:10.1016/J.PLANTSCI.2007.06.010
296. Shao S, Zhang X, van Heusden GPH, Hooykaas PJJ. Complete sequence of the tumor-inducing plasmid pTiChry5 from the hypervirulent Agrobacterium tumefaciens strain Chry5. *Plasmid*. 2018;96-97:1-6. doi:10.1016/J.PLASMID.2018.02.001
297. Chabaud NM, De Carvalho-Niebel · F, Barker · D G. Efficient transformation of Medicago truncatula cv. Jemalong using the hypervirulent Agrobacterium tumefaciens strain AGL1. *Plant Cell Rep*. 2003;22:46-51. doi:10.1007/s00299-003-0649-y
298. Van Der Fits L, Deakin EA, Hoge JHC, Memelink J. The ternary transformation system: constitutive virG on a compatible plasmid dramatically increases Agrobacterium-mediated plant transformation. *Plant Mol Biol* 2000 434. 2000;43(4):495-502. doi:10.1023/A:1006440221718
299. Kumar S, Morrison JH, Dingli D, Poeschla E. HIV-1 Activation of Innate Immunity Depends Strongly on the Intracellular Level of TREX1 and Sensing of Incomplete Reverse Transcription Products. *J Virol*. 2018;92(16). doi:10.1128/jvi.00001-18
300. Kumar SV, Misquitta RW, Reddy VS, Rao BJ, Rajam MV. Genetic transformation of the green alga - Chlamydomonas reinhardtii by Agrobacterium tumefaciens. *Plant Sci*. 2004;166(3):731-738. doi:10.1016/j.plantsci.2003.11.012

301. Brown A, Hormaeche CE, De Hormaeche RD, et al. An Attenuated AroA Salmonella Typhimurium Vaccine Elicits Humoral and Cellular Immunity to Cloned  $\beta$ -Galactosidase in Mice. *J Infect Dis.* 1987;155(1):86-92. doi:10.1093/infdis/155.1.86
302. Priebe GP, Brinig MM, Hatano K, et al. Construction and characterization of a live, attenuated aroA deletion mutant of Pseudomonas aeruginosa as a candidate intranasal vaccine. *Infect Immun.* 2002;70(3):1507-1517. doi:10.1128/IAI.70.3.1507-1517.2002
303. Mi Z, Feng ZC, Li C, Yang X, Ma MT, Rong PF. Salmonella-mediated cancer therapy: An innovative therapeutic strategy. *J Cancer.* 2019;10(20):4765-4776. doi:10.7150/jca.32650
304. Singer K, Shibolet Y, Li J, Tzfira T. Formation of Complex Extrachromosomal T-DNA Structures in Agrobacterium tumefaciens-Infected Plants. *Plant Physiol.* 2012;160(1):511-522. doi:10.1104/pp.112.200212
305. Pang Z, Raudonis R, Glick BR, Lin TJ, Cheng Z. Antibiotic resistance in Pseudomonas aeruginosa: mechanisms and alternative therapeutic strategies. *Biotechnol Adv.* 2019;37(1):177-192. doi:10.1016/J.BIOTECHADV.2018.11.013
306. Galle M, Carpentier I, Beyaert R. Structure and function of the Type III secretion system of Pseudomonas aeruginosa. *Curr Protein Pept Sci.* 2012;13(8):831-842. doi:10.2174/138920312804871210
307. Worstell NC, Singla A, Saenkham P, et al. Hetero-Multivalency of Pseudomonas aeruginosa Lectin LecA Binding to Model Membranes. *Sci Rep.* 2018;8(1):1-11. doi:10.1038/s41598-018-26643-7
308. Siryaporn A, Kuchma SL, O'toole GA, Gitai Z. Surface attachment induces Pseudomonas aeruginosa virulence. 2014;111(47):16860-16865. doi:10.1073/pnas.1415712111
309. Chung ME, Goroncy K, Kolesnikova A, Schönauer D, Schwaneberg U. Display of functional nucleic acid polymerase on Escherichia coli surface and its application in directed polymerase evolution. *Biotechnol Bioeng.* 2020;117(12):3699-3711. doi:10.1002/bit.27542
310. Huszczyński SM, Lam JS, Khursigara CM. The role of Pseudomonas aeruginosa lipopolysaccharide in bacterial pathogenesis and physiology. *Pathogens.* 2020;9(1). doi:10.3390/pathogens9010006
311. Wieland K, Chhatwal P, Vonberg RP. Nosocomial outbreaks caused by Acinetobacter baumannii and Pseudomonas aeruginosa: Results of a systematic review. *Am J Infect Control.* 2018;46(6):643-648. doi:10.1016/j.ajic.2017.12.014
312. Ivanov IE, Kintz EN, Porter LA, Goldberg JB, Burnham NA, Camesano TA. Relating the Physical Properties of Pseudomonas aeruginosa Lipopolysaccharides to Virulence by Atomic Force Microscopy †. *J Bacteriol.* 2011;193(5):1259-1266. doi:10.1128/JB.01308-10
313. Trunk T, S. Khalil H, C. Leo J. Bacterial autoaggregation. *AIMS Microbiol.* 2018;4(1):140-164. doi:10.3934/microbiol.2018.1.140
314. Tomlinson AD, Fuqua C. Mechanisms and regulation of polar surface attachment in Agrobacterium tumefaciens. *Curr Opin Microbiol.* 2009;12(6):708-714. doi:10.1016/j.mib.2009.09.014
315. Bafna JA, Sans-Serramitjana E, Acosta-Gutiérrez S, et al. Kanamycin Uptake into Escherichia coli Is Facilitated by OmpF and OmpC Porin Channels Located in the Outer Membrane. *ACS Infect Dis.* 2020;6(7):1855-1865. doi:10.1021/acsinfecdis.0c00102

316. Newman JR, Fuqua C. Broad-host-range expression vectors that carry the L-arabinose-inducible *Escherichia coli* araBAD promoter and the araC regulator. *Gene*. 1999;227(2):197-203. doi:10.1016/S0378-1119(98)00601-5
317. Warren L, Manos PD, Ahfeldt T, et al. Highly Efficient Reprogramming to Pluripotency and Directed Differentiation of Human Cells with Synthetic Modified mRNA. *Cell Stem Cell*. 2010;7(5):618-630. doi:10.1016/J.STEM.2010.08.012
318. Vick JE, Johnson ET, Choudhary S, et al. Optimized compatible set of BioBrick™ vectors for metabolic pathway engineering. *Appl Microbiol Biotechnol*. 2011;92(6):1275-1286. doi:10.1007/s00253-011-3633-4
319. Cong L, Ran FA, Cox D, et al. Multiplex genome engineering using CRISPR/Cas systems. *Science*. 2013;339(6121):819-823. doi:10.1126/SCIENCE.1231143
320. Yang F, Naqvi NI. Sulfonyleurea resistance reconstitution as a novel strategy for ILV2-specific integration in *Magnaporthe oryzae*. *Fungal Genet Biol*. 2014;68:71-76. doi:10.1016/j.fgb.2014.04.005
321. Barger CJ, Chee L, Albahrani M, et al. Co-regulation and function of foxm1/ rhno1 bidirectional genes in cancer. *Elife*. 2021;10:1-48. doi:10.7554/ELIFE.55070
322. Hoang TT, Karkhoff-Schweizer RR, Kutchma AJ, Schweizer HP. A broad-host-range F1p-FRT recombination system for site-specific excision of chromosomally-located DNA sequences: Application for isolation of unmarked *Pseudomonas aeruginosa* mutants. *Gene*. 1998;212(1):77-86. doi:10.1016/S0378-1119(98)00130-9
323. Hajdukiewicz P, Svab Z, Maliga P. The small, versatile pPZP family of *Agrobacterium* binary vectors for plant transformation. *Plant Mol Biol*. 1994;25(6):989-994. doi:10.1007/BF00014672
324. Lindbo JA. TRBO: A High-Efficiency Tobacco Mosaic Virus RNA-Based Overexpression Vector. *Plant Physiol*. 2007;145(4):1232-1240. doi:10.1104/PP.107.106377
325. Katoh Y, Terada M, Nishijima Y, et al. Overall architecture of the intraflagellar transport (IFT)-B complex containing cluap1/IFT38 as an essential component of the IFT-B peripheral subcomplex. *J Biol Chem*. 2016;291(21):10962-10975. doi:10.1074/jbc.M116.713883
326. Sokurenko E V., Courtney HS, Ohman DE, Klemm P, Hasty DL. FimH family of type 1 fimbrial adhesins: Functional heterogeneity due to minor sequence variations among fimH genes. *J Bacteriol*. 1994;176(3):748-755. doi:10.1128/jb.176.3.748-755.1994
327. Chao G, Lau WL, Hackel BJ, Sazinsky SL, Lippow SM, Wittrup KD. Isolating and engineering human antibodies using yeast surface display. *Nat Protoc*. 2006;1(2):755-768. doi:10.1038/nprot.2006.94
328. Feng S, Varshney A, Coto Villa D, et al. Bright split red fluorescent proteins for the visualization of endogenous proteins and synapses. *Commun Biol*. 2019;2(1):1-12. doi:10.1038/s42003-019-0589-x
329. Stanton BC, Nielsen AAK, Tamsir A, Clancy K, Peterson T, Voigt CA. Genomic mining of prokaryotic repressors for orthogonal logic gates. *Nat Chem Biol* 2013 102. 2013;10(2):99-105. doi:10.1038/nchembio.1411
330. Daeffler KN-M, Galley JD, Sheth RU, et al. Engineering bacterial thiosulfate and tetrathionate sensors for detecting gut inflammation. *Mol Syst Biol*. 2017;13(4):923. doi:10.15252/MSB.20167416
331. Meisner J, Goldberg JB. The *Escherichia coli* rhaSR-PrhaBAD Inducible Promoter

- System Allows Tightly Controlled Gene Expression over a Wide Range in *Pseudomonas aeruginosa*. *Appl Environ Microbiol*. 2016;82(22):6715-6727. doi:10.1128/AEM.02041-16
332. Keeble AH, Turkki P, Stokes S, et al. Approaching infinite affinity through engineering of peptide-protein interaction. *Proc Natl Acad Sci U S A*. 2019;116(52):26523-26533. doi:10.1073/pnas.1909653116
333. R S, U P, Puhler A. A broad host range mobilization system for in vivo genetic engineering: Transposon mutagenesis in gram negative bacteria. *Biotechnology*. 1983;(1):784-790.
334. Baba T, Ara T, Hasegawa M, et al. Construction of *Escherichia coli* K-12 in-frame, single-gene knockout mutants: The Keio collection. *Mol Syst Biol*. 2006;2. doi:10.1038/msb4100050



# Xavier Pierrat

Final year PhD candidate

[xavier.pierrat@epfl.ch](mailto:xavier.pierrat@epfl.ch)

+41 76 817 92 36

rue pré-du-marché 41  
CH-1004 Lausanne

Nationality: French, B permit

Age: 31

[linkedIn/xavierpierrat](https://www.linkedin.com/in/xavierpierrat)

## CURRICULUM VITAE

### Professional experience



2022-  
2017

**PhD candidate** in Prof. Persat's lab, Ecole Polytechnique Fédérale de Lausanne

Title: Rewiring *Agrobacterium tumefaciens*' DNA transfer machinery to mammalian cells

Summary: using **synthetic bacterial and mammalian display** of adhesins, I am adapting a natural bacterial DNA transfer machinery to build a **new DNA vector** with enlarged therapeutic options such as delivery of CRISPR-Cas9 gene editing to cure monogenetic diseases or treat solid tumors.

We also **crystallized** a protein acting as a mechanosensory in *Pseudomonas aeruginosa*. I study the structure and function by random **mutagenesis with high-throughput microscopy screen**.

Finally, I enjoyed **managing projects** of undergraduate students and **teaching** practical work in molecular biology.



2020

**Merck Innovation cup, winning team** (1-week boot camp)

Team drug discovery technologies: next generation targeted protein degradation



2017

**Research assistant** at Nanobiotix, a French nanomedicine SME (3 months)

*In vitro* immuno-oncology: innate immune activation by irradiation stimulated by nanoparticles.



2016

**Research intern** at Roche innovation center Zürich (6 months)

Tasks: cloning, transfection protocol optimization, targeted and stable integration, FACS

Results: Discovery pipeline enhanced using synthetic biology and high throughput cell engineering



2015

**Master's thesis** in Prof. Fussenegger's lab, Biosystems Science Department (12 months)

Tasks: cell culture, cloning, transfection, dimerization and tetracycline-like systems, microscopy

Results: built a **synthetic biocomputer in a 3D culture of mammalian cells**



2014

**Bachelor's thesis** in Prof. Elisseff's lab at Johns Hopkins School of Medicine (5 months)

Tasks: *in vitro* and *in vivo* studies, drug encapsulation, immunohistochemistry, real-time PCR

Results: induced thermogenesis in adipose tissue by drug-loaded PLGA microparticles, report awarded by Ecole Polytechnique



2013

**Business development intern** (2 months)

Tasks: market study and epidemiology in dermato-oncology and radiotherapy areas

Results: elaboration of a 30-pages business plan enabling a strategic decision



2013-  
2012







**Group science project** at Ecole Polytechnique, awarded top 3 best in 100 (4h/week)

Tasks: Study of the bacterial biosequestration of atmospheric CO<sub>2</sub> into limestone

Results: Discovery and isolation of an autochthon bacteria having this property

## Education

---

	2021	<b>PhD in bioengineering</b>
	2017-	Relevant PhD courses: <ul style="list-style-type: none"> <li>• Introduction to technology transfer - from invention to market</li> <li>• Drug/Device Product Development and Regulation – Europe and US</li> <li>• “Smovie” workshop: created a 3-min movie of my project for a broad audience</li> <li>• Recombinant protein expression in animal cells for medicine and structural biology</li> <li>• Cancer biology I, pharmacokinetics (Lausanne University)</li> <li>• Image processing and analysis for life scientists</li> </ul>
	2020	<b>Strategy consulting training</b> (online, 1 week)
	2017	<b>Synthetic biology in action: Programming bacteria to do amazing things</b> (1 week) EMBO practical course, which also includes lectures by pioneers in the field.
	2016	<b>Drug Discovery and Development (D3) Project simulation</b> (2 days) This course gives a complete overview of the drug discovery and development pipeline in the pharmaceutical industry, from drug discovery scientist to full development clinician.
	2016-	<b>MSc in Biotechnology</b>
	2014	Bioengineering, bioprocess, mathematical modeling, bioinformatics and synthetic biology
	2014-	<b>MSc in engineering, Ecole Polytechnique</b> , Paris: one of France’s leading universities
	2011	Specialization in <b>bioengineering</b> (genetic engineering, disease-, cell-, immuno- and neurobiology) Included a military training as student officer at Gendarmerie Nationale
	2011-2009	<i>Classes Préparatoires</i> , two years of intensive tertiary level study (mathematics, physics and chemistry) for the nationwide competitive examination to the French <i>Grandes Ecoles</i>

## Publications

---

2022	<a href="#">bioRxiv</a> : <i>Engineering Agrobacterium tumefaciens adhesion to target cells</i> , <a href="#">Pierrat et al.</a>
2021	<a href="#">mBio</a> : <i>The membrane microenvironment regulates the sequential attachment of bacteria to host cells</i> . <a href="#">Pierrat et al.</a>
2021	<a href="#">PNAS</a> : <i>Mechanotaxis directs Pseudomonas aeruginosa twitching motility</i> . Kühn, Talà, Inclan, Patino, <a href="#">Pierrat, et al.</a>
2021	<a href="#">ACS nano</a> : <i>Time-resolved scanning ion conductance microscopy for three-dimensional tracking of nanoscale cell surface dynamics</i> . Leitao, Drake, Pijusic, <a href="#">Pierrat, et al.</a>
2021	<a href="#">iScience</a> : <i>The wall-less bacterium Spiroplasma poulsonii builds a polymeric cytoskeleton composed of interacting MreB isoforms</i> . Masson, <a href="#">Pierrat, et al.</a>
2021	<b>Talk</b> : EMBL Symposium: <i>Life at the Periphery: Mechanobiology of the Cell Surface</i> .
2021	<a href="#">YouTube</a> : <i>Il cherche des bactéries contre le cancer</i> , 7-min video with “Antoine vs Science”.
2021	<b>Poster (elected best poster)</b> : <i>Targeted adhesion and VirE2 delivery into heterologous hosts using a synthetic adhesin display system in A. tumefaciens</i> . Agrobacterium conference 2021, online.
2017	<a href="#">Nature methods</a> : <i>Programmable full-adder computations in communicating three-dimensional cell cultures</i> . D. Ausländer, S. Ausländer, X. <a href="#">Pierrat, et al.</a>
2017	<a href="#">eLife</a> : <i>Biofilms: Flipping the switch</i> . X. <a href="#">Pierrat</a> and A. Persat.

## Languages and IT

---

- **French:** native language
- **English:** fluent
- **German:** upper intermediate (Goethe-Zertifikat C1 in 2014)
- **IT:** Advanced level in Matlab, ImageJ, Prism, Office and Python. Basic level in Java, FlowJo.

## Interests

---

- Biotechnology Student Association's board member: organization of social events
- Captain of my volley-ball team
- Former organizer of the Ecole Polytechnique's career fair and of oenological wine tastings